FINAL REPORT

Project Title: Materials and Process Design for High-Temperature Carburizing: Integrating Processing and Performance

Covering Period: September 1, 2002 – March 31, 2007

Date of Report: July 31, 2007

Recipient:
Worcester Polytechnic Institute
100 Institute Road
Worcester, MA 01609-2280

Award Number: DE-FC36-01ID14207

Subcontractors: Northwestern University

Other Partners: Industrial Participants as Indicated in Proposal

Contact(s):
Diran Apelian
WPI
100 Institute Road
Worcester, MA 01609-2280
(508) 831-5992; dapelian@wpi.edu

Project Team:
Dibyajyoti Aichbhaumik
U.S. Department of Energy
Golden Field Office
1617 Cole Blvd.
Golden, CO 80401
(303) 275-4706
debo.aichbhaumik@go.doe.gov

Distribution Notice: No limits on distribution.

Executive Summary:

The objective of the project is to develop an integrated process for fast, high-temperature carburizing. The new process will result in an order of magnitude reduction in cycle time compared to conventional carburizing

and represents significant energy savings in addition to a corresponding reduction of scrap associated with distortion free carburizing steels. In addition to the above accomplishments, alloys were developed Gearmet® C61 and C69 in collaboration with Questek Corp. These alloys have demonstrated high performance and have been used in a variety of applications – i.e., GM, NASCAR, knife blades, etc. The project has demonstrated energy reduction, process optimization, and the value of working together within an industry-university alliance such as CHTE. The latter has allowed the researchers at WPI, Northwestern and Questek to be able to take the laboratory results and developments to commercial use.

Accomplishments: See Appendix A, which contains three key publications:

- Optimization of High Temperature Vacuum Carburizing: *Process Simulation, Experiment and Validation.*
- Performance Optimization and Computational Design of High-Strength Gear Steels (page 21)
- Residual Stress Control and Design of Next Generation Ultra-hard Gear Steels (page 229)

Project Activity:

ID Number	Task / Milestone Description	Planned Completion	Actual Completion	Comments
1a	ThermoCalc Modeling	7/31/05	7/31/05	100%
1b	Process Experiments	7/31/05	7/31/05	*100%*
1c	Industrial Experiments	7/31/05	12/31/06	*100%*
1d	Hardenability	10/31/03	7/31/05	*100%*
2a	Redesign Alloys	10/31/04	4/29/05	*100%*
2b	Grain Stability	10/31/04	7/31/05	*100%*
3a	RCF and Wear	7/31/05	12/31/06	*100%*
3b	Residual Stress	7/31/05	12/31/06	*100%*
3c	Redesign for Performance	7/31/05	4/29/05	*100%*
3d	Forming Dies	7/31/05	7/31/05	*100%*
3e	Forging/Casting Dies	7/31/05	7/31/05	*100%*

Products Developed:

The experimental Cu-bearing alloys aimed at reducing material cost through decreased Co content have been evaluated and subsequent heat treatment studies were completed. Local Electrode Atom Probe (LEAP) tomographic microanalysis was utilized to analyze the microstructure of M_2C strengthening dispersions. Data were collected from the carburized case of all four experimental Cu-bearing alloys at tempering times of 12 and 48 hours, corresponding to two observed hardness peaks. Tomographic reconstruction and 3D analysis of has been completed for one of four experimental Cu-bearing alloys as a function of tempering time. At typical peak hardness tempering conditions for M_2C precipitation strengthening, the M_2C carbides have reached an over-aged state and are over 50% larger than the optimal size assumed in the alloy design process. A reduced precipitated M_2C volume fraction was also observed. This larger size, reduced volume fraction as well as a strong interaction and co-location with the Cu strengthening dispersion have been identified as the main causes of the discrepancy between designed and achieved hardness values for the Cu-bearing alloys. Maximum hardness was ultimately achieved with further aging, where the M_2C strengthening dispersion both increased in volume fraction and coarsened to a rod-shaped morphology, diminishing the effective co-location between precipitate phases. Using revised microstructural parameters as quantified with LEAP analysis, alloy design models were recalibrated, providing close agreement with measured hardness levels. Preliminary calculations using the revised design models by an undergraduate materials design team suggested a maximum achievable surface hardness of 65 Rc is possible within design constraints for this microstructural approach.

Spur gears of four experimental Cu-bearing alloys have been machined for single tooth bending fatigue studies. Carburization cycles are developed to ensure proper surface carbon and case depth requirements. Heat treatment is currently underway, with preliminary testing on puck samples to be used for refinement of carburization cycles including carbon and microhardness measurements. Preliminary isotropic superfinishing (ISF) studies on experimental Cu-bearing alloys have demonstrated an increased response to common ISF slurry chemistries compared to high Ni-Co C61 and C67 alloys.

For newly designed alloy prototypes aimed at extremely high surface hardness accessible only through low case transformation temperatures,

process optimization including vacuum carburizing, cryogenic deformation and tempering has been performed on newly designed alloy prototypes. Two runs of vacuum carburization have been carried out with process cycles designed through CBPWIN2 and DICTRA simulation. The surface carbon content after the second run was measured as 0.9%, showing good agreement with the predicted carbon content. The carbon content profile also shows a desired carbon level of 0.8% at a depth of 50μm where the volume fraction of retained austenite was confirmed as 22% through X-ray diffraction, confirming the designed alloy is well suited for planned cryogenic deformation to complete martensitic transformation in the outer case.

Cryogenic deformation including cryogenic shot peening and cryogenic compression has been optimized for reduced retained austenite levels. Specimens were cut from vacuum carburized samples and 50um was ground off the surface so the exposed surface has the designed carbon content of 0.8%. Two runs of cryogenic shot peening have been completed at Purdue University. In the first run, the surface with 0.8wt% carbon was subject to shot peening at the temperature range of -110^{o}C~-80^{o}C. A lower temperature of -130^{o}C was obtained and a prolonged peening time applied in the second run for specimens resolutionized and liquid nitrogen treated. Three levels of peening intensity (low, medium and the highest available) were selected in both runs according to prior Almen tests. Conditioned hard cut wire steel shot media (hardness of 58~62 Rc) was chosen to ensure the plastic deformation in specimens during peening. X-ray diffraction shows that retained austenite content at the carbon level of 0.8% was slightly reduced after shot peening at -110 ^{o}C/-130^{o}C with low peening intensity, which suggest that a temperature closer to -196 ^{o}C and more energy are probably needed to complete martensitic transformation. Cryogenic uniaxial compression was then employed to meet requirements for temperature and deformation extent. The 3×3×6 mm and 4×3×7 mm specimens were aligned with the 0.8wt% carbon case parallel to the compression axis, subjecting case and core to parallel deformation. The compression test was conducted at -196 ^{o}C to a plastic strain of 4-5%. Consistent with transformation kinetic model predictions, X-ray diffraction confirmed the amount of austenite on the surface was reduced from 22% to 8%. To explore a possible industrial process for cryogenic compression, collaboration with DesignMecha, Co. Ltd. in Korea was established to perform ultrasonic surface modification at -196 ^{o}C on vacuum carburized cylindrical specimens. The amount of austenite reduction demonstrated was intermediate between that of cryogenic shot peening and the cryogenic uniaxial compression.

Subsequent tempering at 482 ^{o}C has been performed to the cryo-compressed specimens. To minimize austenite during tempering, the specimen was cyclically treated in liquid nitrogen 1hr for every 8 hrs of tempering. Prolonged tempering (56 hrs) has shown a hardness of 976 Hv at 80um depth and a hardness of 512Hv in the core. The experimental case hardness is within 8% of the design goal.

Patents: None

Publications/Presentations: (*: presenting author)

B. Tiemens*, G.B. Olson and A.K. Sachdev, *Design and Microstructural Validation of Cu-Bearing Ultra-Hard Gear Steels*, Materials Science and Technology 2006, Cincinnati, OH, October 17, 2006.

Y. Qian*, J. Almer, U. Lienert, B. Tiemens, G.B. Olson, *Non-destructive Residual Stress Distribution Measurement in Nano-structured Ultra-high Strength Gear Steels*, Presentation and Proceedings, the Fifth International Conference on Synchrotron Radiation in Materials Science, Chicago, IL, July 30 - August 2, 2006.

B. Tiemens*, G.B. Olson, *Design and Optimization of High Power Density Gear Steels,* Poster Presentation (2nd place Student Poster Competition - Ph.D. section), ASM Chicago chapter Monthly Meeting, April 11, 2006.

Y. Qian*, J. Almer, U. Lienert, B. Tiemens, G.B. Olson, *Non-destructive Residual Stress Distribution Measurement in Ultra-high Strength Gear Steels*, Poster Presentation, ASM Chicago chapter Monthly Meeting, April 11, 2006.

B. Tiemens*, G.B. Olson, *Performance Optimization of Ultra-Hard Gear Steels,* Presentation, Materials Technology Laboratory/Steel Research Group 22nd Annual Meeting, March 21, 2006.

Y. Qian*, G.B. Olson, *CryoPeen 70: Future Ultra-high Strength Gear and Bearing Steel*, Presentation, Materials Technology Laboratory/Steel Research Group 22nd Annual Meeting, March 21, 2006.

X. Gao* and G.B. Olson, “DOE-OIT High Temperature Carburizing Steels: Process Modeling”, MTL/SRG 2005, the Materials Technology

Laboratory (Steel Research Group) 21th Annual Meeting, Evanston, IL, March 14-15, 2005.

Y. Qian* and G. B. Olson, “High Performance Gear Steels: Controlling Residual Stress”, MTL/SRG 2005, the Materials Technology Laboratory (Steel Research Group) 21th Annual Meeting, Evanston, IL, March 14-15, 2005.

B. L. Tiemens* and G. B. Olson, “Materials and Process Design for High-Temperature Carburizing: Gear Performance”, MTL/SRG 2005, the Materials Technology Laboratory (Steel Research Group) 21th Annual Meeting, Evanston, IL, March 14-15, 2005.

Y. Qian, J. Almer, B. L. Tiemens, G. B. Olson, Residual stress Analysis for advanced gear steels using synchrotron radiation, manuscript in preparation.

Y. Qian*, J. Almer, B. L. Tiemens, G. B. Olson, Residual Stresses in Advanced Gear Steels – Analysis and New Design, poster session for Argonne researchers, Evanston, IL, December 13, 2005.

X. Gao, B.L. Tiemens, Y. Qian, G.B. Olson and F. Stavehaug, “Findings of high temperature vacuum carburizing during process simulations, experiments and validation, surface treatment, and performance tests,” manuscript in preparation.

D. Apelian, G.B. Olson, B.L. Tiemens*, X. Gao and Y. Qian, “Materials and Process Design for High-Temperature Carburizing: Integrating Processing and Performance,” The 2004 Fall Meeting of CHTE, the Center for Heat Treating Excellence of WPI, Columbus, OH, Nov. 3-4, 2004.

D. Apelian, G.B. Olson, B.L. Tiemens*, X. Gao and Y. Qian, “Materials and Process Design for High-Temperature Carburizing: Integrating Processing and Performance,” The 2004 Spring Meeting of CHTE, the Center for Heat Treating Excellence of WPI, Worcester, MA, May 12-13, 2004.

B.L. Tiemens* and G.B. Olson, "High Temperature Carburizing Steels - Gear Performance," The 2004 Spring Meeting of PMRC, the Powder Metallurgy Research Center of WPI, Worcester, MA, April 28-29, 2004.

X. Gao*, H.J. Jou and G.B. Olson, “Development of Versatile and Multi-Constraint Carburizing Process Simulation and Optimization Software Using Thermo-Calc/DICTRA and Their C++ TCIPC Interface,” MTL/SRG

2004, the Materials Technology Laboratory (Steel Research Group) 20th Annual Meeting, Evanston, IL, March 22-23, 2004.

B. Tiemens* and G.B. Olson, "High Temperature Carburizing Steels - Gear Performance," MTL/SRG 2004, the Materials Technology Laboratory (Steel Research Group) 20th Annual Meeting, Evanston, IL, March 22-23, 2004.

X. Gao, G.B. Olson, F. Stavehaug and C. Scharer. "Process Design and Optimization for High-Temperature Vacuum Carburizing," In: Modeling, Control and Optimization in Nonferrous and Ferrous Industry, F. Kongoli et al. eds, pp. 381-395, 2003

"Materials and Process Design for High-Temperature Carburizing: Integrating Processing and Performance." **CENTER FOR HEAT TREATING EXCELLENCE FALL MEETING**, Cincinnati, OH, Oct. 29-30, 2003

"Materials and Process Design for High-Temperature Carburizing: Integrating Processing and Performance." **CENTER FOR HEAT TREATING EXCELLENCE SPRING MEETING**, Worcester, MA, May 28-29, 2003

"Controlling High Temperature Carburizing." **MATERIALS TECHNOLOGY LABORATORY/ STEEL RESEARCH GROUP ANNUAL MEETING**, Evanston, IL, March 24-25, 2003

Budget Data (03/31/07):

Phase / Budget Period			Approved Spending Plan			Actual Spent to Date		
			DOE Amount	Cost Share	Total	DOE Amount	Cost Share	Total
	From	To						
Year 1	9/01	9/02	339,849	343,000	682,849	262,722	422,958	685,680
Year 2	9/02	9/03	371,424	348,217	719,641	387,251	366,000	753,251
Year 3	9/03	9/04	400,123	470,963	871,086	274,975	419,605	694,580
Year 4	9/04	9/05	258,248	505,560	763,808	313,825	486,800	800,625
Year 5	9/05	3/07	150,784	178,974	329,758	281,654	152,300	433,954
		Totals	1,520,428	1,846,714	3,367,142	1,520,428	1,847,663	3,368,090

Appendix A:

Key Publications- *accomplishments*

- Optimization of High Temperature Vacuum Carburizing: *Process Simulation, Experiment and Validation.*
- Performance Optimization and Computational Design of High-Strength Gear Steels (page 21)
- Residual Stress Control and Design of Next Generation Ultra-hard Gear Steels (page 229)

Optimization of High-Temperature Vacuum Carburizing - Process Simulation, Experiment and Validation

Xiujie Gao†, Benjamin L. Tiemens†, Yana Qian†, Frode Stavehaug* and Gregory B. Olson†

† Department of Materials Science & Engineering, Northwestern University, Evanston, IL 60208

* QuesTek Innovations LLC, 1820 Ridge Ave., Evanston, IL 60201

Abstract

Compared to conventional gas carburization, the optimization of vacuum carburization at elevated temperatures offers an order of magnitude savings in process cycle time with corresponding reductions in processing cost and energy consumption. This paper summarizes work aimed at such optimization by quantifying the vacuum carburizing behavior of two case-hardened steels, GearMet® C61 and C69. Optimum boost and diffuse cycle times as well as carburization temperatures were determined through a combination of weight gain, microhardness measurements and surface carbon measurements iteratively combined with computational modeling. The effect of carburization on the residual stress state as well as the bending fatigue properties was also studied.

1 Introduction

In current carburizing practice, gas carburizing under atmospheric or slightly higher pressure is most commonly used. Vacuum carburizing was first introduced two decades ago (Herring and Hughton, 1995) and consists of repeated boost and intermediate diffuse cycles followed by a final diffuse. The furnace is usually maintained at a relative low pressure (around 1 kPa) except during boosts when the pressure is raised to about 10 kPa. Figure 1 shows schematically the change of surface carbon content (wt%) with time for gas and vacuum carburizing. Limited by soot formation, gas carburizing is a relatively slower process than vacuum carburizing where a higher carbon potential is maintained and is instead limited by the saturation of austenite and carbide formation. Due to a higher carbon potential (or higher availability of carbon), vacuum carburizing also provides a more homogeneous case depth and is more predictable and reproducible. Vacuum carburizing is often carried out at higher temperatures than regular gas carburizing, and this so-called "high-temperature" carburizing significantly reduces furnace cycle time.

Compared to conventional gas carburizing, the optimization and control of high-temperature vacuum carburizing would result in at least an order of magnitude reduction in cycle time and processing cost. This time reduction represents significant energy savings. Based on energy consumption statistics in the Process Heating Technology Roadmap (2001), conservative estimates reveal a 30% reduction in cycle time resulting in saving 20-24 trillion BTUs per year. High performance materials designed for high-temperature vacuum carburizing can enable higher power densities and increased life in transportation and die applications. The reduction of scrap associated with distortion-free and maximum uniformity steels achieved via high-temperature vacuum carburizing is yet another important source of energy savings. Reduced energy consumption would also greatly decrease environmentally harmful emissions.

In response to these potential productivity and quality improvements in heat treating technology, the Office of Industrial Technologies (OIT) division of the Department of Energy (DOE) has supported a multi-university project titled "Materials and Processes Design for High-Temperature Carburizing: Integrating Processing and Performance." The project addresses the technology for reduced process

cycle times of 50% or more and the achievement of distortion-free, maximum uniformity heat-treated parts. As part of this project, the work reported here focuses on the vacuum carburizing behavior at elevated temperature of two case-hardened steels, GearMet® C61 and C69. Response of the steels to high-temperature carburizing was investigated through their weight gains, surface carbon contents, microhardness and microstructures after carburizing. Residual stress and fatigue properties were also tested to verify the performance of steels that employ high-temperature carburizing.

2 Materials and Experimental Procedures

2.1 Materials

Two types of ultrahigh-strength case-hardened steels, GearMet® C61* and C69* from QuesTek Innovations LLC, have been chosen for this carburizing study because of their promising combination of strength and toughness (Kuehmann and Olson, 1998). GearMet® C61 provides unusual high strength/high toughness core properties for damage tolerant gearing. GearMet® C69 combines a ductile core with an ultra hard case that can achieve hardness levels up to 67 HRC, promoting high wear and contact fatigue life. GearMet® C69 is the product of an ongoing research and development program with the objective of reducing weight of components by as much as 50% over those manufactured using conventional high performance alloy steels. These case hardenable steel alloys have a carbon content in the range of about 0.05 weight percent to about 0.24 weight percent in combination with a mixture of about 15 to 28 weight percent cobalt, 1.5 to 9.5 weight percent nickel, 3.5 to 9.0 weight percent chromium, up to 3.5 weight percent molybdenum, and up to 0.2 weight percent vanadium. The nominal composition of GearMet® C61 is listed in Table 1 and the nominal composition of GearMet® C69 is referred to (Kuehmann and Olson, 1998).

Table 1: Nominal alloy composition of studied steels

Alloy	Fe	Co	Ni	Cr	Mo	V	C (core)
GearMet® C61	Bal.	18	9.5	3.5	1.1	0.08	0.16

2.2 Vacuum Carburizing

Two sample sizes were used in developing the vacuum carburizing process. One size was small pucks of 1.0 inch diameter and 1/3 inch thickness, and the other was larger discs of 5.25 inch diameter and ¼ inch thickness. All carburizing treatments were performed at Midwest Thermal-Vac (Kenosha, WI) using the patented Infracarb® process of ECM USA Inc.

The combined solutionizing/vacuum carburizing was carried out with varying boost times (bt) and carburizing temperatures (T). The chosen parameters were increased linearly, denoted with increasing integers (bt1 < bt2, T1<T2, etc.).

After the final diffuse cycle, samples were transferred to a separate chamber and quenched with oil or gas. All samples, except those used for surface carbon measurements, were then emersed in liquid nitrogen for one hour to promote complete martensitic transformation, followed by tempering from 1-16 hours at temperatures ranging from 200-510°C. To increase the residual stress level in the case, some components were shot-peened or laser-peened.

* US Patent Number 6,176,946 B1

To save time and cost in both process development and production, the boost/diffuse times were developed with the assistance of several diffusion simulation codes. The CBPWIN2 code (ECM-USA) was used for one dimensional (1D) carbon diffusion with temperature dependent diffusion coefficients. 2D and 3D diffusion was simulated using DEFORM HT (Scientific Forming Technologies Corporation) with diffusion coefficients dependent on both temperature and composition. DICTRA (Thermo-Calc Software) was also used to calculate the composition and temperature dependent carbon diffusivity used in DEFORM HT, as well as the activation energy and pre-exponential diffusion coefficient (D0) used in CBPWIN2.

2.3 Microhardness Measurement

Larger samples were first water-jet cut into smaller sizes. Before microhardness measurement, all samples were sectioned using a water-cooled cut-off wheel (Struers 456 CA). Proper sized samples were then mounted using Struers DuroFast powder for better edge retention and planeness. The samples were then ground and polished to 1 μm using a Struers RotoPol-11 grinder/polisher for flatness.

A computerized microhardness testing system (CLEMEX^{TM} CMT 3.0) was utilized to measure the Vickers hardness distributions of C61 and C69. A Knoop indenter was combined with Vickers when measurement closer to the sample edge was desired.

2.4 Microstructural Analysis

The alloy microstructure was observed through a Nikon Epiphot-TME microscope equipped with digital image acquisition software. A Hitachi 3500N Scanning Electron Microscope was utilized for electron microscopy. The microscope is also equipped with energy dispersive spectroscopy (EDS) for chemical analysis, including a light element detector for increased accuracy in carbon detection. Samples were etched before microstructural analysis. The compositions and properties of the etchants are given in Table 2.

Table 2: Metallographic etchants

Etchant	Composition (by volume)	Properties
Nital	2%-10% Nitric acid (HNO3) + 98%-90% Methanol (CH_3OH)	Emphasizes the carbides; Used for C61
Variant of Kalling's reagent 2 (Petzow, 1999)	33ml Hydrochloride (HCl, 32%) + 33ml Distilled Water (H_2O) + 1.5g Copper (II) Chloride ($CuCl_2$)	Fast etchant and good to show martensites and carbides; Used for C69

2.5 Weight Gain Measurement

The samples were marked and weighed before loading into the chamber. After the carburizing process was done, the samples were unloaded and weighed again. A milligram balance with a maximum capacity of 720g (ADP 720L) was used to measure the weight of large samples.

The weight gain data was used to obtain the average and instant carbon flux during carburizing.

2.6 Surface Carbon Content Measurement

Samples were sent to ASTON Metallurgical Services Co. Inc. for surface carbon content measurement. The combustion method following ASTM test procedure ASTM E415 was employed.

2.7 Residual Stress Measurement

Surface residual stresses of GearMet® C61 and C69 under different conditions were measured using x-ray diffraction at Northwestern University. The standard $\sin^2\psi$ method was employed to peak (211) for residual stress measurement and a value of 168GPa is used for $E/(1+\nu)$. Detailed parameters of the X-rayconditions are shown in Table 3.

Table 3: Parameters of X-ray facility

X-ray Source	Cr, K_α average λ=2.291Angstrom
Filter in incident arm	Vanadium
Point source size	1 mm
Collimator size	1 mm
Slit in incident arm	1 mm
Slits in detector arm	2 mm, 3 mm

2.8 Surface Roughness Investigation

Surface roughness values were measured with phase shift interferometry utilizing a MicroXAM Surface Mapping Microscope produced by ADE Phase Shift, Inc.

2.9 Single Tooth Bending Fatigue Performance Testing

For performance testing, a 5.25" diameter bar was hot-rolled from a forged, production-scale ingot of GearMet® C61. 1.25" thick blanks were then machined from which trial spur gears were cut (hobbed). The spur gears were carburized to a total case depth of 1mm. The heat treatment consisted of solutionizing/vacuum carburizing at T7 for 1.5 hours, cryogenic treatment in a liquid nitrogen bath and tempering at 500°C for one hour. After heat treatment, the gear sides were ground for alignment. Different surface treatments on the spur gears included grinding a targeted depth of 20μm from the root fillet, land and partway up the active profile, and a typical dual shot peening process. Single tooth bending fatigue testing on the spur gears was done on a MTS test frame operating at 40 Hz maintaining an R-value, or ratio of maximum to minimum applied load, of 0.01 using amplitude control. Tests ran until the applied load caused a tooth displacement exceeding 2 mm, which was classified as failure, or the selected endurance limit of 10 million cycles.

3 Results and Discussions

3.1 Boost Trends

3.1.1 Microhardness

Many factors have an impact on the accuracy and spatial resolution of microhardness measurement. For the materials studied, the mount material and mount configuration (i.e. the different sample geometries combined with the relative relationship between the mount surface and samples) made no significant difference in microhardness measurement. However, angled surfaces and variation in manual operation were seen to have a significant impact on measurement accuracy. For these reasons automatic

grinding/polishing machines and computerized microhardness testers should be employed whenever possible. The most important consideration for microhardness testing was discovered to be applied force and indent spacing. Figure 2 shows the dependence of Vickers' microhardness measurement on the applied force. When the applied force is below 200 grams, one can see that the apparent hardness increases significantly. This is mainly due to elastic recovery and non-elastic behavior of the indent, and can be generally avoided by maintaining a minimum indent diagonal of 25 μm.

The spatial resolution is usually limited by the minimum size of the indents (due to force dependence) and the interaction of an indent with another or the edge. Following ASTM E384 designations (ASTM, 1999), the closest allowable distance to the edge for Vickers is 63 μm and 13 μm for Knoop.

Following the above mentioned cautions and procedures, the microhardness profiles of GearMet® C61 samples were measured after a single boost cycle for different boost times for small samples at temperature T3 and large samples at temperature T5 and are shown in Figure 3a and b respectively. At temperature T3 the microhardness profiles expand continuously to higher hardness and deeper cases with increasing boost time. The flat region near the surface for bt13 is a sign of retained austenite, which lowers the hardness and is due to a lowering of the martensitic transformation temperature (Ms) caused by the increased carbon content. At the elevated carburizing temperature (T7), the effect of boost time is effectively reduced, as the microhardness profiles stop expanding after bt7. Retained austenite is also being formed at shorter boost times, as shown by the reduced surface hardness starting at bt10.

One may also notice that the maximum peak hardness at T3 is lower than that at T5. This is mainly because the 200C temper included after carburizing at T3 lowers the peak hardness and is not necessarily due to the different carburizing temperatures.

These hardness profiles obtained from boost experiments were mainly used to help estimate the carbon content needed to achieve certain surface hardness levels and at what surface carbon content retained austenite may exist for the various carburizing conditions,. Another very important use of the hardness profiles was to verify whether target case depth was achieved.

3.1.2 Weight Gain and Surface Carbon Measurement

The very important role of weight gain data obviously requires accurate measurement. Past experience has shown that the weight gain for the small pucks is on the order of the measurement error of a scale with a thousandth gram accuracy due to their small surface area,. Numerical rounding or handling errors (including air circulation) would also have a big impact on the measurement. In addition, the small pucks were rested on a grate during carburizing, which introduced a non-uniform carbon intake on the contacting surface. To overcome these disadvantages, larger pucks, hanging in the furnace, were used for weight gain measurements. The large pucks have a surface area and subsequent weight gain as much as 20 times that of the small pucks resulting in more consistent and accurate weight gain data.

The top plot in Figure 4 shows this weight gain data measured after a single boost cycle for different boost times for GearMet® C61 at T3 and T5. For T3, the weight gain increased with increasing boost time, with this increase beginning to diminish around bt10 and stopping at bt16. This slowing down of weight gain increase can be attributed to the formation of film carbides on grain boundaries and free surfaces which impede the inward diffusion of carbon. As these film carbides grow with increasing boost time, they form a continuous network that essentially prevents any additional carbon from diffusing, resulting in the observed weight gain "limit". . At the higher carburizing temperature of T5, the weight gain increase slows down at extended boost times (bt14) and did not exhibit an upper limit.

This delayed saturation can be attributed to the increased solubility and diffusion of carbon at the elevated temperature.

The most important use of weight gain information obtained from these boost experiments was to calculate the average or instant flux needed in the carburizing simulations. Boost times corresponding to the onset of constant weight gain were also used as a saturation limit for boost cycle simulation.

The middle plot in Figure 4 shows surface carbon content measurements after a single boost cycle for different boost times. For T3, the surface carbon content increased with increasing boost time until the saturation limit was reached and leveled out at bt16. At the elevated temperature of T5, the surface carbon content continued to increase for all boost times. The most important application of these surface carbon content measurements is to help determine the maximum carbon content that can be achieved prior to the formation of retained austenite. For both T3 and T5, the peak hardness moves from the surface to subsurface with increasing boost time. Using the boost time value at which this shift occurs, the corresponding surface carbon content without leading to retained austenite was found to be approximately 0.5wt%.

GearMet® C69 carburized at T7 exhibits similar trends in microhardness and weight gain to those of C61 at T5. The results are not repeated here and the reader is referred to (Gao et al., 2003) for details.

3.1.3 Residual Stress Measurement

The effect of boost time on the surface residual stress is presented in the bottom plot of Figure 4. Surface residual stresses were found to be all compressive and peak at a boost time of bt10 regardless of carburizing temperature. When the boost time is shorter than bt10, compressive stresses generally increase with boost time. When the boost time is further increased to bt13, the compressive stresses decrease attributed to the formation of retained austenite. The lower carburizing temperature T3 exhibited a larger peak in compressive residual stress than T5. This can be attributed to the relative slopes in carbon composition as observed through the associated hardness profiles near the surface. Due to the increased diffusion at the elevated temperature, the near surface hardness profiles for T5 are relatively shallow when compared to those of T3 as more carbon can diffuse further into the material. This shallower carbon gradient resulted in the lower peak residual stress value.

3.1.4 Surface Roughness

Examination of carburized surfaces under optical and scanning electron microscopes showed that high-temperature carburizing tends to produce a rough surface compared to conventional gas carburizing. To investigate the effect of the surface finish before carburizing on this final roughness, C69 pucks in both the as-machined condition and polished to 3um were carburized and then compared. As shown in Figure 5, the polished samples began with a much smoother surface (Rq=0.0066μm) than the as-machined (Rq=0.42μm). After carburizing, however, both surface conditions exhibited generally the same surface roughness (Rq=0.28μm in Figure 5c), which was on the order of the as-machined surface. Surface treatments prior to carburizing, therefore, are not believed to influence the surface roughness after carburizing.

3.1.5 Microstructural Analysis

Microhardness profiles, weight gain data, and surface carbon contents have shown evidence of non-monotonic time evolution for longer boost times. The non-monotonic behavior is attributed to the formation of carbides on grain boundaries and free surfaces, i.e., these carbides slow down the intake of carbon from free surfaces due to slow diffusion of carbon through these carbides. When the carbides

form a continuous network, the passage of carbon is fully blocked. In previous work (Gao et al., 2003), microstructural analysis using optical/electron microscopy and EDS has been performed to identify the composition, location and morphology of these carbides. The results for C69 carburized at a high temperature T7 using a long boost time bt10 are summarized below.

EDS line profile analyses and x-ray digital maps have shown that the carbides present in the microstructure are mainly Cr_7C_3 carbides. This result is consistent with the calculated phase diagram of GearMet® C69, which shows that at the carburization temperature, Cr_7C_3 is a stable carbide at a carbon content larger than approximately 0.95 wt%. Figure 6 is an optical micrograph showing carbides (white) and other phases. Most of the white carbides are on grain boundaries with only a few larger ones are within the grains. There are also carbides present on part of the free surface. The larger carbides can be classified as globular carbides (Totten and Howes, 1997) and other carbides on grain boundaries or free surfaces are forming a semi-continuous network and can be classified as film carbides (Ruxanda and Florian, 1995). The region enclosed by the white has a characteristic scale of around 20μm, corresponding to the general grain size (several tens of μm).

Another observation is that some larger regions in Figure 6 are most likely retained austenite and the martensite in the over-carburized region is mostly the plate morphology, contrasting to the lath martensite of the lower carbon core.

3.2 Diffuse Trends

For the high-temperature vacuum carburizing used in this study, the peak hardness position was seen to be offset from the surface due to surface retained austenite, with an intermediate diffuse cycle bringing the peak hardness closer to or onto the surface. Figure 7a shows typically observed hardness profiles illustrating this effect. Figure 7b shows the change of maximum case hardness with diffuse times for large C69 samples carburized for a boost time of bt4 at T7 and diffused for 2, 5, 10, 20 and 40 minutes respectively. The optimal diffuse time is identified as 10 minutes where the rate change of maximum hardness is moderate. Note a longer diffuse time would result in a more robust process but longer furnace time. For the final diffuse, which is often much longer than intermediate diffuse cycles, the peak hardness must be brought to the surface.

Figure 8 displays the influence of intermediate diffusion in the carburizing cycle on the surface residual stress. As expected, residual stress is somewhat reduced when diffusion is allowed since it levels the carbon gradient in the case.

3.3 Process Simulation and Optimization for High-Temperature Vacuum Carburizing

During the course of carburization process development, several notable features of high-temperature carburizing were found: flux variation with time, carbide formation and dissolution, diffusivity variation with carbon content and temperature, and multiple phase diffusion. The accuracy of carburization simulations depends on the ability of simulation software to account for these features. It was found that a minimum requirement for accurate simulation is the ability to handle variable flux and diffusivity. Currently available simulation software and their features are listed in Table 4.

Table 4: Simulation software comparison

	Simple 1D	DICTRA 1D	DEFORM HT 2D/3D
Flux J	Constant	J(Time)	J(Time)

Diffusivity D	D(Temp)	D(Carbon,Temp)	D(Carbon,Temp)
Carbide formation and dissolution	No	Yes	Maybe
Multiple phase diffusion	No	Yes	No

The simple 1D software (CBPWIN2) with limited features was only used for preliminary simulations. DICTRA 1D has all needed features and is the ideal tool since it can simulate carbide formation and dissolution with variable flux. So far, the variation of diffusivity with carbon content and temperature is considered, and an averaged constant flux is used. Other features will be considered in future work.

To simulate a complex component geometry, one needs to use 2D/3D software. DEFORM 2D has limited geometry/meshing capacity as it can only create or import polygons, cannot import nodes and elements and can only generate a linear triangular mesh. DEFORM 3D allows the user to import a surface and then mesh a solid into linear tetrahedral mesh with limited mesh seeding and control capacity, or import a linear hexahedron mesh which is better and faster than tetrahedral. A survey has been conducted to identify preprocessing software that can be interfaced to DEFORM-HT 3D seamlessly. So far the PATRAN software has been identified as the best candidate, as it may be able to simulate carbide formation and dissolution by assuming the carbide-forming rate is much greater than that of carbon diffusion (Dupen, 1994).

During the practice of process development and optimization it was very desirable to have a process simulation and optimization code that has the features of DICTRA, considers many constraints, and generates a set of boost and diffuse cycles once the material, carburizing temperature and constraints are given. Some constraints arising from carburizing are: maximum surface carbon after boost/diffuse, minimum/maximum boost/diffuse time, boost/diffuse/total time as multiples of a specified time, etc. Although the simple 1D code considered constraints such as maximum surface carbon after boost/diffuse, it could not be used in an automated fashion due to the lack of consideration of other constraints (e.g., boost/diffuse/total time as multiples) and various other limitations (fixed flux, diffusivity not function of carbon content, fixed grid, etc.)

A versatile process design and optimization code considering all above features and constraints was developed to develop carburizing processes (Gao, 2004). The code uses the diffusion simulation capability of DICTRA and performs all necessary pre- and post- processing, automation, and housekeeping tasks via the inter-process communication interface of DICTRA. As a benefit of using DICTRA, another feature of this code is the integration with the specific materials design of the alloy being carburized, which uses the same thermodynamic database via Thermo-Calc. Currently a simple constant flux is used in the code, and the code can be run in either manual or automatic mode. For the manual mode, any number of boost and diffuse cycles can be specified, and in the automatic mode, in addition to the constraints mentioned above, one can also specify the desired carbon content at the desired case depth. The code can also be linked to iSIGHT, a complete design exploration tool, to perform efficient optimization of carburizing processes.

3.4 Temper Study

To find the optimal tempering parameters, pucks carburized with complete sets of boost and diffuse cycles (as would be done in conventional practice) as well as pucks that were intentionally over carburized using a boost time of bt19 have been combined to identify an optimal temper for C69 as

shown in Figure 9. This optimal tempering condition led to a maximum surface hardness with an over-tempered and tougher core. The resultant hardness profile of commercially produced C61 after tempering is shown in Figure 10.

The evolution of surface residual stress with different tempering treatments was also investigated after the material was fully carburized using an optimal carburizing process. Laser peening, also called laser shock peening, is a novel surface processing technique to induce deeper and larger compressive residual stress into metals using high-power laser pulses (Montross et al., 2002). Figure 11 presents the surface residual stresses of C69 treated by liquid nitrogen (LN), stage I temper (200^{o}C), stage IV temper (482^{o}C) and laser peening, respectively.

From the graph, it can be seen that a high surface compressive residual stress is present after carburizing and quenching, and that laser peening is an effective way to compensate the residual stress relaxation of tempering, even raising the magnitude further to 1463MPa. Residual stress relaxed by ~50 MPa during stage I tempering from the as quenched status. The fact that the magnitude of surface compressive stress after stage IV tempering is not less than that after stage I tempering indicates that the residual stress relaxation during stage IV tempering is not greater than that during stage I tempering. This suggests that residual stress relaxation is not necessarily driven by increasing tempering temperature, but rather some similar mechanism for stress relaxation occurring during different tempering stages, such as volume changes associated with carbide precipitation (Brown et al., 1975).

It is noted that the compressive residual stress of C69 after laser peening can reach a very high value of 1463MPa on the surface, which matches expectations since previous studies show higher surface hardness can lead to higher compressive residual stress (Qian, 2003). Such a high surface compressive residual stress hasn't been achieved in other current materials and can greatly benefit fatigue performance (Schlicht et al., 1988).

3.5 Performance Trends

Stress versus cycles to failure plots, or S-N diagrams, are shown for four surface conditions of C61 in Figure 12. Solid symbols denote runs prematurely terminated prior to failure at the designated endurance limit of 10 million cycles. Curves were generated using a least squares exponential fit.

Significant performance gains were seen from all surface modifications. SEM images of the corresponding surfaces shown in Figure 13 reveal distinct surface morphologies and associated root mean square (RMS) roughness values (also denoted as Rq). The as heat-treated surface displayed substantial grooving along prior austenite grain boundaries, a phenomenon possibly caused by increased diffusivity and transport present at the elevated carburizing temperatures. Specimen failure was seen to follow along these grooves, and the poor performance demonstrated by gears with the as heat-treated surface can be attributed to grain boundary grooving initiating and accommodating fatigue fracture. Surface modification either through grinding or shot peening eliminated any grain boundary grooving and resulted in the observed performance gains.

Further performance gains were also seen with the addition of shot peening. Shot peening is an established way of improving gear performance through generating compressive residual stress at the surface that counteracts applied tensile loads (Parrish, 1980; Scholtes and Macherauch, 1984). For the spur gears in this study, the surface compressive residual stress was raised from roughly 300 MPa to 1100 MPa using shot peening, subsequently increasing bending fatigue performance. As was shown in Figure 13, shot peening also changes the surface topography. While it does slightly increase the overall

surface roughness, shot peening also compacts the surface and "smears out" the detrimental grain boundary grooving.

Detailed observations were also made on the locations of fatigue crack initiation. Besides the grooved prior austenite grain boundaries of the as heat-treated gears, a predominant location for fatigue crack initiation was specimen corners. Figure 14 shows one such corner-initiated failure as well as the corresponding microhardness cross-sectional map. As shown in the microhardness map, a region of excess hardness in the corner corresponds very closely to the location of fatigue initiation. This excess hardness can be attributed to over-carburization of specimen corners, as the very high fluxes associated with vacuum carburizing at high temperature coupled with the geometric constraint of specimen corners result in carbon accumulation and in this case excess hardness. Corner over-carburization has been previously shown to negatively affect bending fatigue performance (Cohen et al., 1992). The flux boundary condition of vacuum carburizing, compared to the fixed potential boundary of conventional gas carburizing, excacerbates this corner effect. Ongoing tests eliminating the overcarburized corners have already demonstrated a further 15% improvement in fatigue strength.

4 Conclusions

High-temperature vacuum carburizing processes have complex features such as variable flux with time, variable carbon diffusivity with composition and temperature, carbide formation and dissolution and multi-phase diffusion. A minimum requirement for accurate simulation is that the software is able to handle variable flux and/or diffusivity. DICTRA 1D is the ideal tool for 1D simulation since all features can be considered. A versatile carburizing process design code built on DICTRA has been developed and is also able to consider many constraints observed during real process development. The code is also able to be linked to iSIGHT to perform efficient optimization of carburizing processes. For 2D/3D simulations, DEFORM-HT is shown to be a good choice for fine tuning of component processing, and a survey has identified that PATRAN is the best candidate for seamless interfacing with DEFORM 3D.

Integration of simulation with materials characterization techniques such as microhardness testing, weight gain, surface carbon measurement, and microstructural analysis is essential to rapidly develop reliable carburizing processes. For microhardness measurements it was very important to adhere to ASTM E384, paying particular attention to the force dependence and distances between indents. It is also recommended to use an automatic grinding/polishing wheel for flatness and a microhardness tester with an image analyzer for consistent results. For weight gain measurement, samples with large surface areas are recommended for required precision.

A linear relationship between weight gain and boost time was observed prior to the formation of film carbides on grain boundaries and free surfaces. Once carbides form, the intake of carbon on the surface is slowed down (due to slow diffusion of carbon through these film carbides) resulting in the non-monotonic behavior seen in both weight gain and surface carbon measurement. Full blockage of carbon intake was seen once the carbide film forms a continuous network. In the high Cr steels C61 and C69, discrete Cr carbides precipitate on the surface and grain boundaries during the boost cycles and dissolve during the subsequent diffuse cycles. Using this information, boost cycles can then be chosen to avoid a continuous carbide network and corresponding diffuse cycles selected whose duration allows for robustness. Finally, a temper condition can be chosen such that surface hardness is maximized.

Examination of carburized surfaces under optical and scanning electron microscopes showed that high-temperature vacuum carburizing tends to produce a rough surface compared to conventional gas carburizing, with a potential adverse effect on fatigue strength if the surfaces are left unfinished. Over-

carburization of specimen corners, which is more prevalent in vacuum carburizing, was seen to initiate failure and reduce material performance. Masking of side surfaces is therefore recommended for gears vacuum carburized at high temperatures. It was found that tempering partially relives residual stress generated after cryogenic treatment, however a dramatic increase in residual stress can be achieved through shot peening or laser peening.

Single tooth bending fatigue performance was shown to be greatly affected by surface treatment. The as heat-treated surface had the lowest fatigue endurance limit, with both the ground finish and shot peening greatly benefiting the endurance limit. Shot peening produced the best bending fatigue performance due to large amounts of beneficial, compressive residual stress imparted to the surface.

Future Work

In the future, DICTRA will be used to investigate carbide formation and diffusion. For the developed simulation code based on DICTRA, a critical carbide fraction criterion during the boost cycle will be added to ensure that the carbide volume fraction is less than a critical value and the process is not controlled by carbon diffusion through films. An appropriate surface reaction kinetics model based on surface carbon and weight gain measurement will also be developed to model variable flux.

Acknowledgement

This project is subcontracted from the Center for Heat Treating Excellence (CHTE) at WPI under contract DE-PS07-01ID14026 from U.S. DOE (Idaho Operations Office) with matching fund support from GM at Northwestern University. The authors also wish to thank Caian Qiu, Brian Tufts, Herng-Jeng Jou and Jim Wright of QuesTek Innovations LLC for helpful discussions.

Reference

ASTM 1999. *Annual Book of ASTM Standards*, Philadelphia, PA: ASTM.

Brown, R.L., H.J. Rack and M. Cohen 1975. "Stress Relaxation During Tempering of Hardened Steel", *Mater. Sci. Eng.*, 21(1): 25-34.

Capital Surini Group International, I. and I. Energetics 2001. *Roadmap for Process Heating Technology*, Sponsored by the Industrial Heating Equipment Association and the U.S. Department of Energy Office of Industrial Technolgy.

Cohen, R.E., D.K. Matlock and G. Krauss 1992. "Specimen Edge Effects on Bending Fatigue of Carburized Steel", *J. Mater. Eng. Perform.*, 1(5): 695-703.

Dupen, B.M. 1994. "Modeling Vacuum Carburizing with the Finite Element Method", Thesis (Ph. D.), University of Connecticut, Storrs, CT.

Gao, X. 2004. "Versatile and multi-constraint carburizing process design and optimization software using Thermo-Calc/DICTRA and their TCIPC interface, Edison No. 6144601-04-0076, DOE Edison #: T-102834," Northwestern University, Evanston, IL.

Gao, X., G.B. Olson, F. Stavehaug and C. Scharer 2003. "Process design and optimization for high-temperature vacuum carburizing", Modeling, Control, and Optimization in Ferrous and Nonferrous Industry, F. Kongoli, B.G. Thomas and K. Sawamiphakdi, eds., Warrendale, PA: TMS, pp.381-395.

Herring, D.H. and R.L. Hughton 1995. "The influence of process variables on vacuum carburizing", Proceedings of the Second International Conference on Carburizing and Nitriding with Atmospheres, J. Grosch, J. Morral and M. Schneider, eds., Materials Park, OH: ASM International, pp.103-108.

Kuehmann, C.J. and G.B. Olson 1998. "Gear steels designed by computer", *Adv, Mater. Process.*, 153(5): 40-43.

Montross, C.S., T. Wei, L. Ye, G. Clark and Y.W. Mai 2002. "Laser shock processing and its effects on microstructure and properties of metal alloys: a review", *Int. J. Fatigue*, 24(10): 1021-1036.

Parrish, G. 1980. *The Influence of Microstructure on the Properties of Case-Carburized Components*, Metals Park, Ohio: American Society for Metals.

Petzow, G. 1999. *Metallographic Etching: Techniques for Metallography, Ceramography, Plastography*, 2nd ed., Materials Park, OH: ASM International.

Qian, Y. 2003. *Unpublished doctoral research at Northwestern University*.

Ruxanda, R. and E. Florian 1995. "Microscopic observations of the carbide/matrix interphasic interface in a low-alloyed hypercarburized steel", Proceedings of the Second International Conference on Carburizing and Nitriding with Atmospheres, J. Grosch, J. Morral and M. Schneider, eds., Materials Park, OH: ASM International, pp.117-121.

Schlicht, H., E. Schreiber and O. Zwirlein 1988. "Effects of material properties on bearing steel fatigue strength", Effect of Steel Manufacturing Processes on the Quality of Bearing Steels, J.J.C. Hoo, ed. Philadelphia, PA: ASTM, STP 987, pp.81-101.

Scholtes, B. and E. Macherauch 1984. "Residual stress determination", Case-Hardened Steels: Microstructural and Residual Stress Effects, D.E. Diesburg, ed. Warrendale, PA: Metallurgical Society of AIME, pp.141-159.

Totten, G.E. and M.A.H. Howes 1997. *Steel Heat Treatment Handbook*, New York: Marcel Dekker.

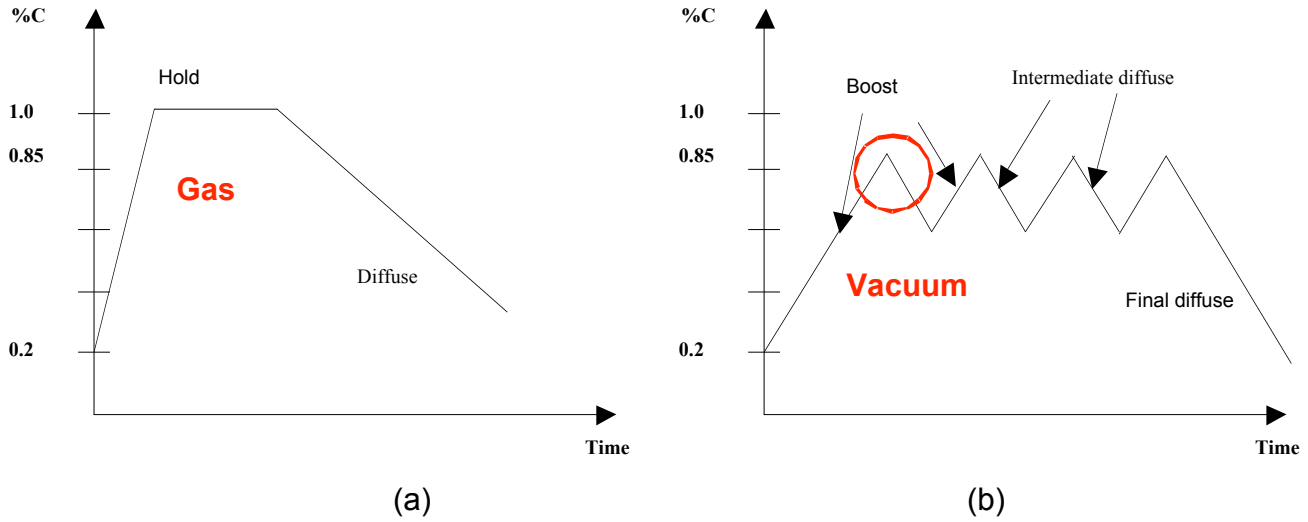

Figure 1: Schematics showing surface carbon content (wt%) changing with time in furnace for (a) Gas carburizing (b) High-temperature vacuum carburizing.

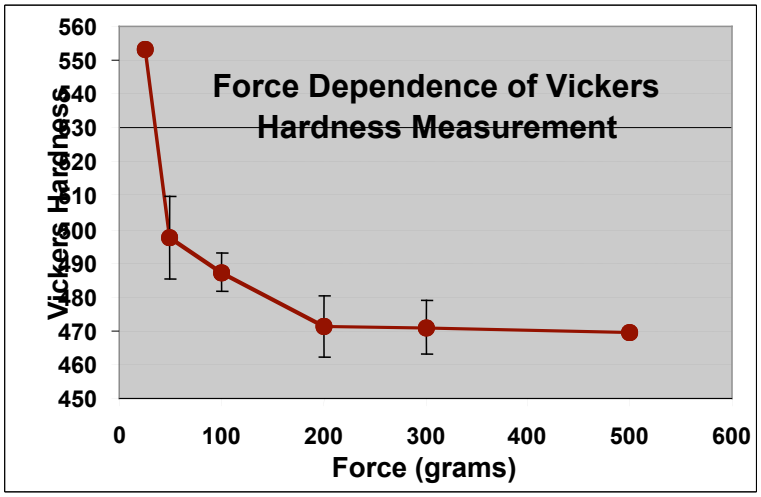

Figure 2: Dependence of Vickers' microhardness measurement on the applied forces. The material has a core hardness around 470 Vickers (HV).

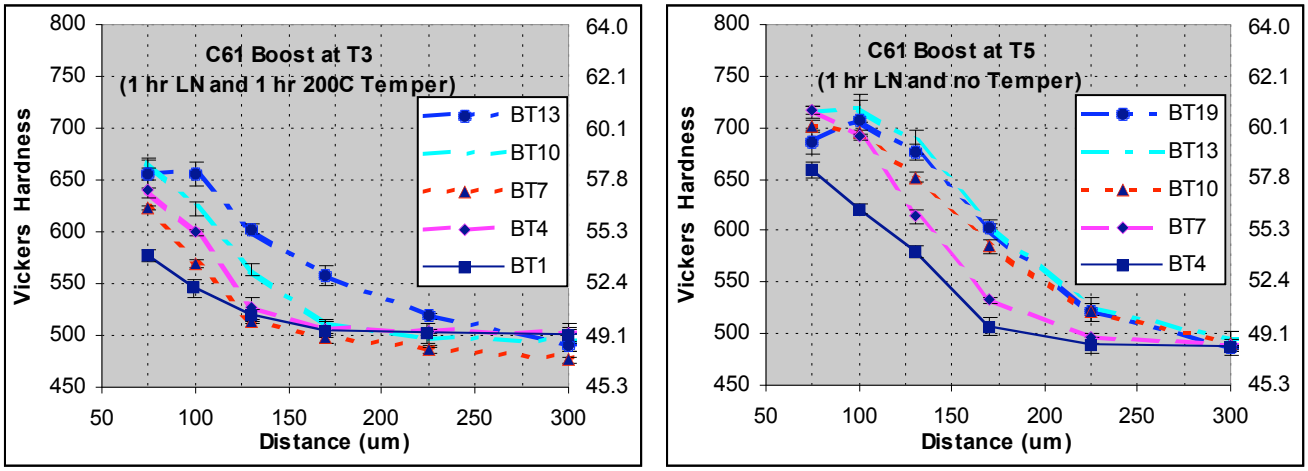

(a) (b)

Figure 3: Microhardness profiles for GearMet® C61 samples measured after different first boost times: a) using small samples at T3 and b) using large samples at T5.

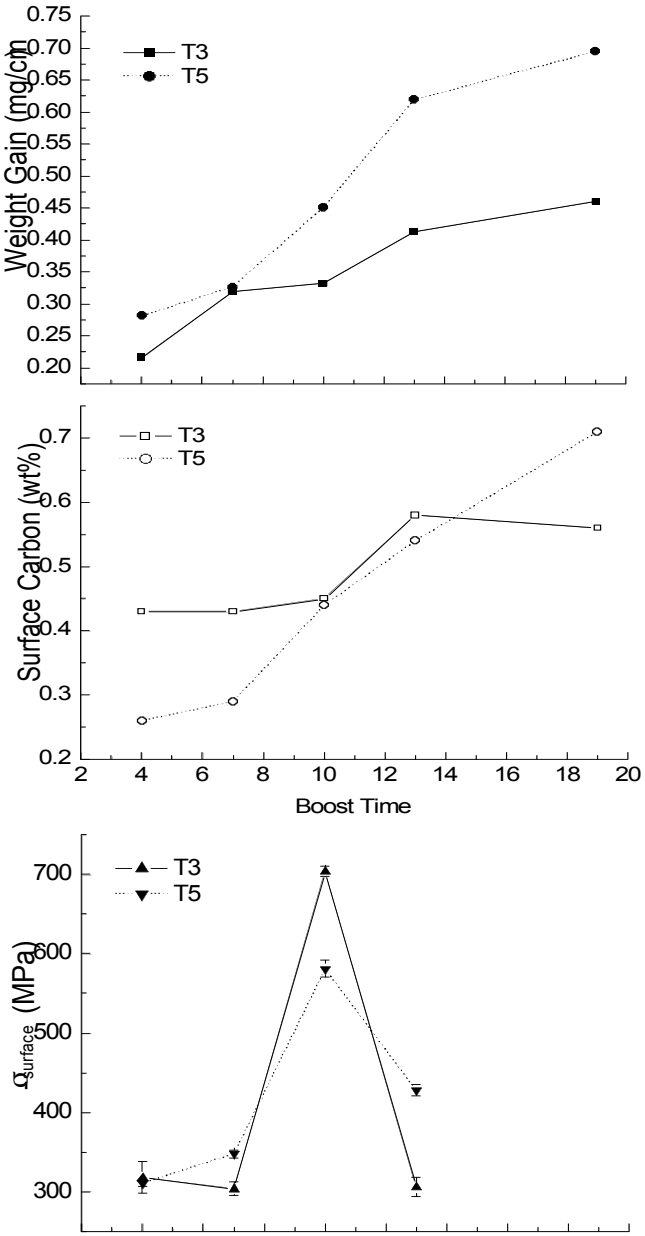

Figure 4: Weight gain, surface carbon content, surface residual stress after different first boosts for GearMet® C61 at temperature T3 and T5 (without any temper).

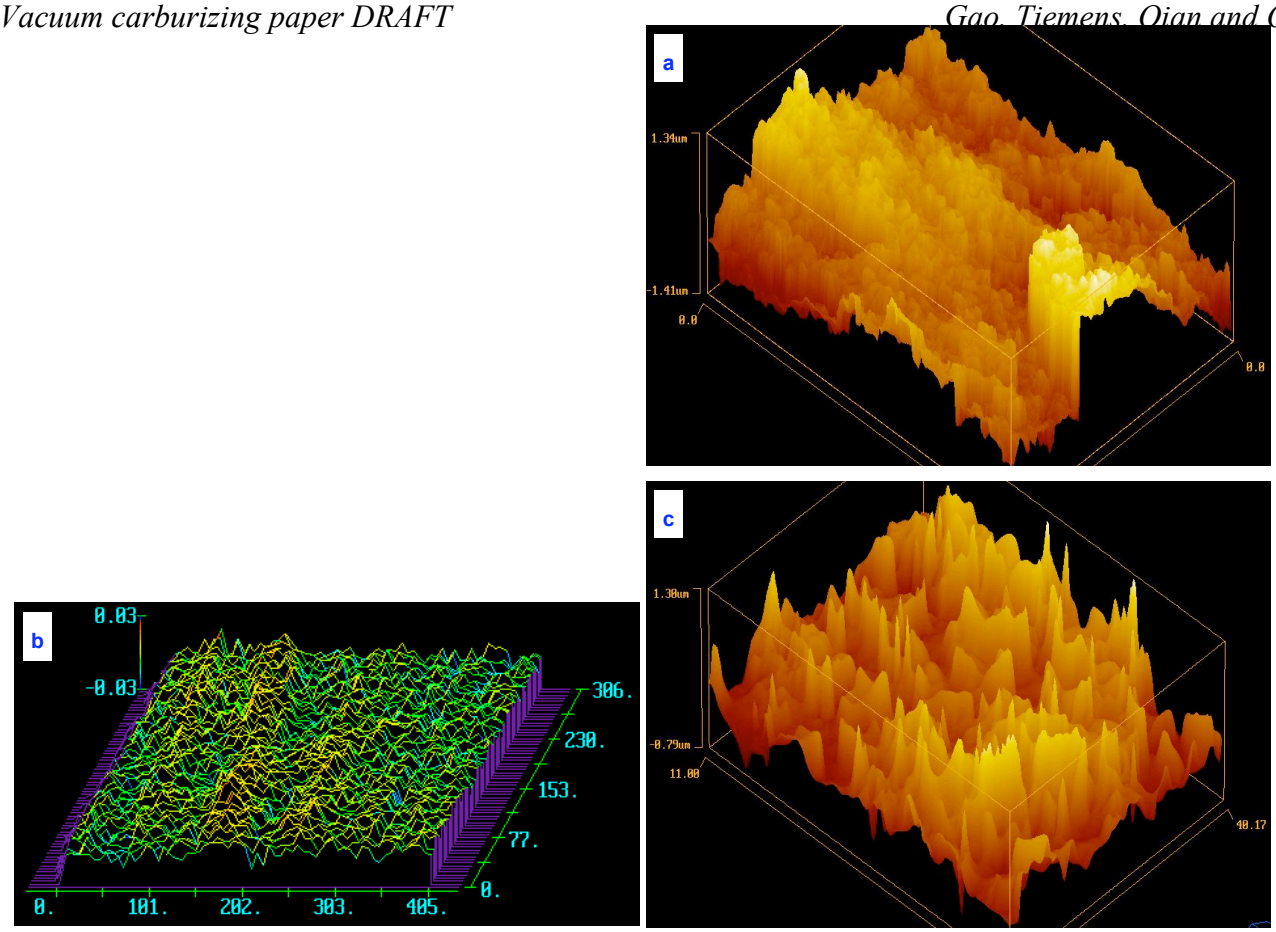

Figure 5: Surface roughness obtained from interferometer for a) As-machined sample after carburizing, b) Before carburizing with a pre-polishing down to 3 μm, and c) After carburizing with a pre-polishing down to 3 μm.

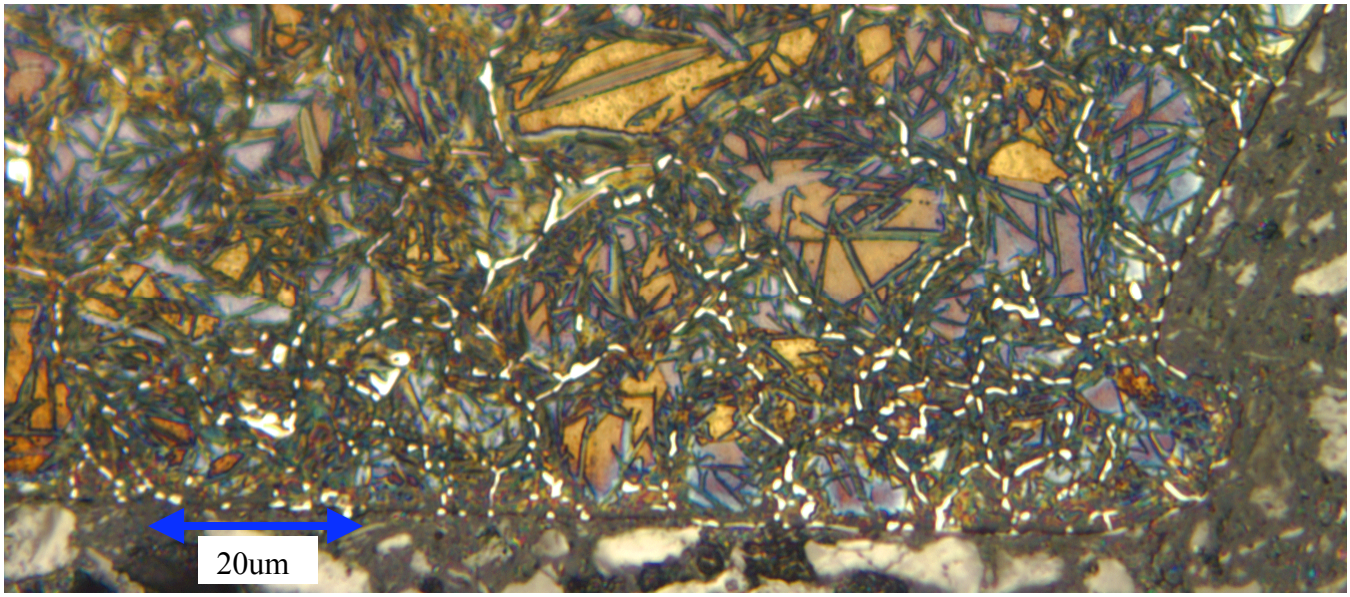

Figure 6: Optical micrograph of a GearMet® C69 sample showing locations and morphology of carbides (white) and other phases. Etched using a variant of Kallings' reagent 2. 1000x.

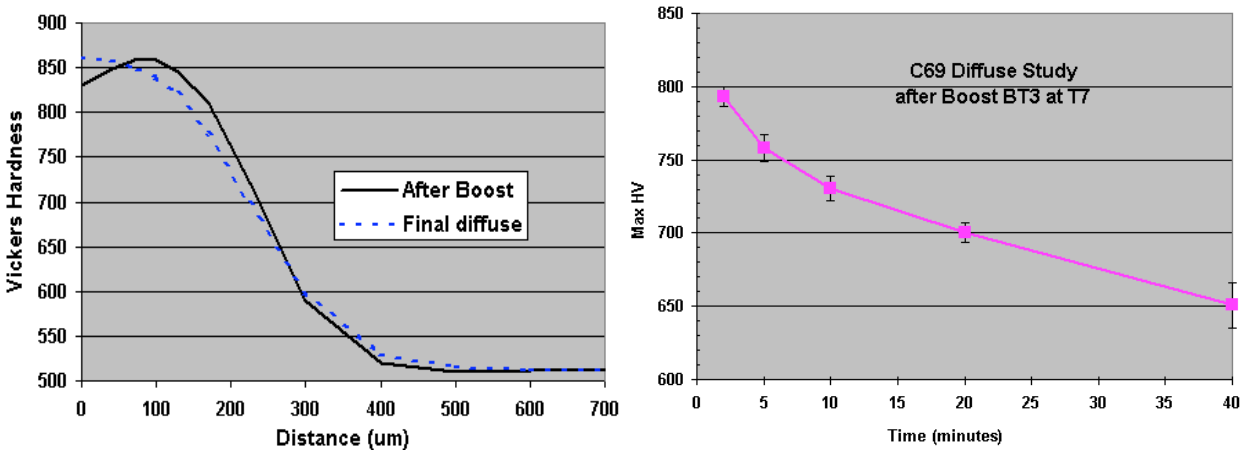

Figure 7: a) Schematic showing hardness profile after boost and diffuse respectively, b) Change of maximum case hardness with diffuse times for large C69 samples carburized for a boost time of bt4 at T7.

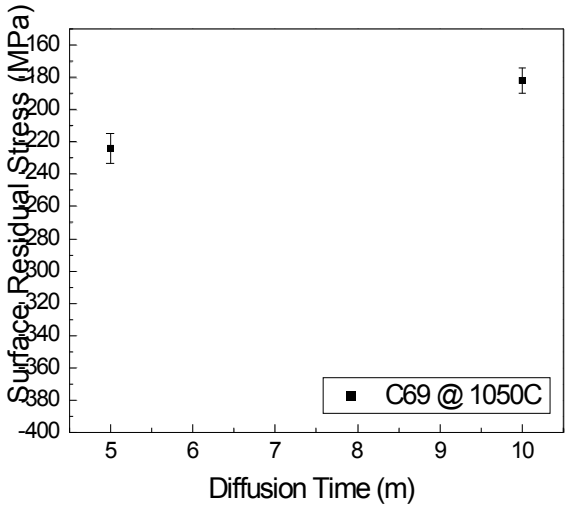

Figure 8: Surface residual stresses of C69 carburized at T7 with different diffuse time

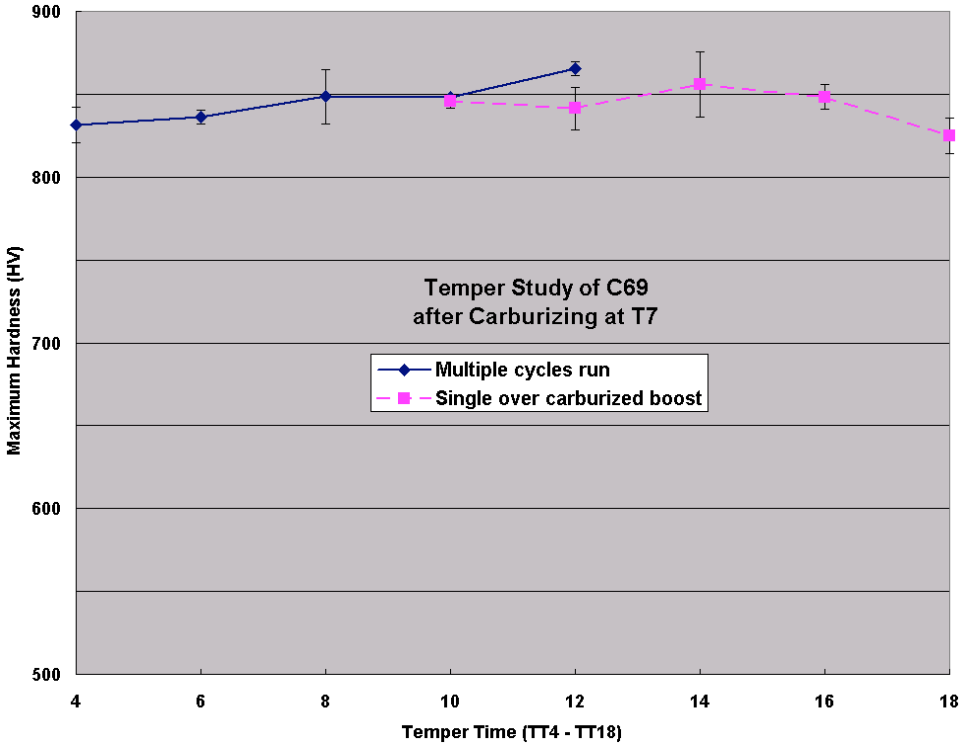

Figure 9: Optimal temper study for C69 using results from multiple cycle runs (real processes for components) and those that were intentionally over carburized using a boost time of bt19

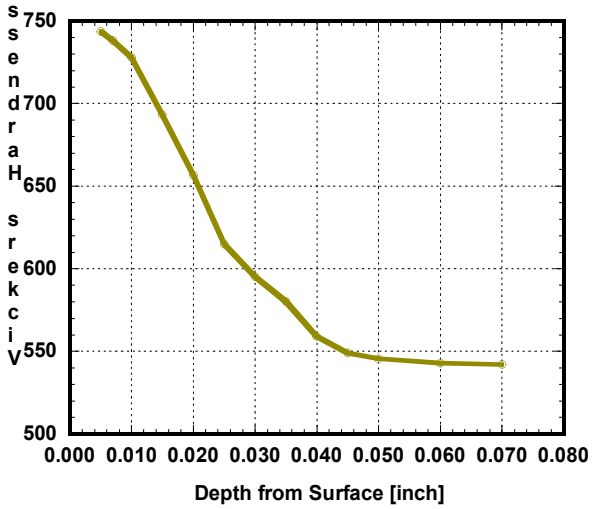

Figure 10: Specified hardness profile of commercial C61 alloy after temper.

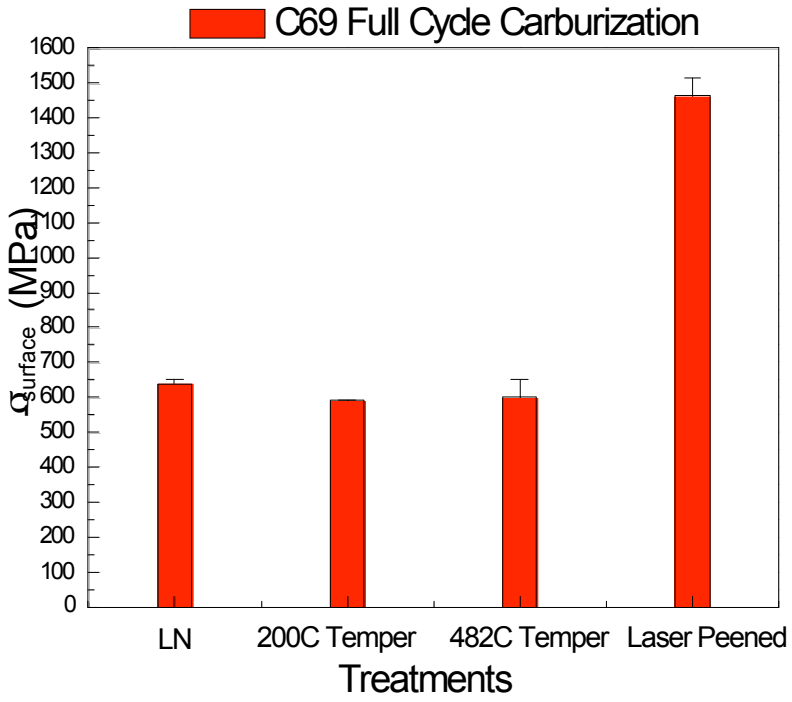

Figure 11: Surface residual stresses of fully carburized C69 after different treatments

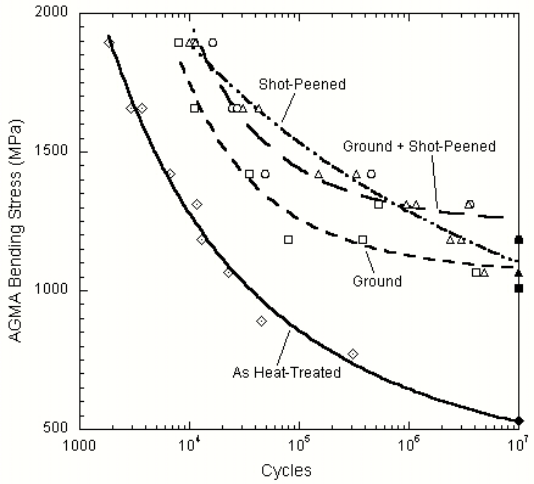

Figure 12: S-N curves for single tooth bending fatigue tests of the four surface conditions of C61.

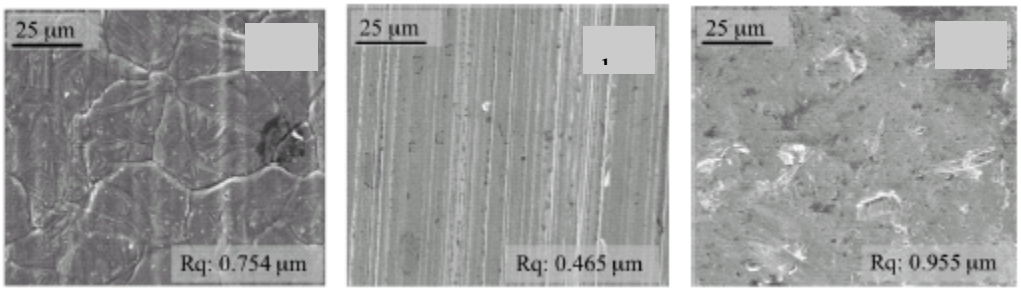

Figure 13: SEM micrographs with corresponding RMS (Rq) roughness values for the surface conditions of C61: a) As heat-treated b) Ground c) Shot Peened

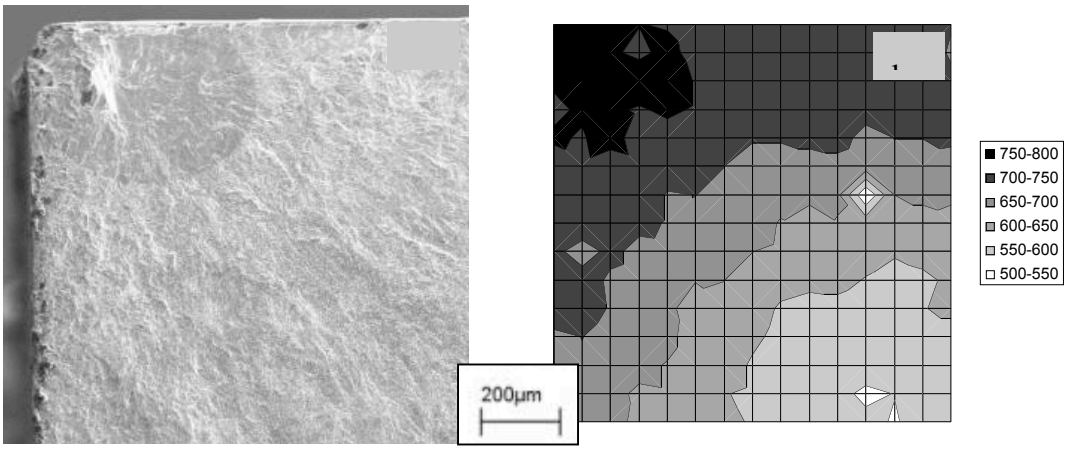

Figure 14: Correlation between location of a) corner fatigue initiation (SEM micrograph) and b) over-carburized corner (microhardness map)

NORTHWESTERN UNIVERSITY

Performance Optimization and Computational Design of Ultra-High Strength Gear Steels

A DISSERTATION

SUBMITTED TO THE GRADUATE SCHOOL

IN PARTIAL FULFILLMENT OF THE REQUIREMENTS

for the degree

DOCTOR OF PHILOSOPHY

Field of Materials Science and Engineering

By

Benjamin Lee Tiemens

EVANSTON, ILLINOIS

December 2006

ABSTRACT

Performance Optimization and Computational Design of Ultra-High Strength Gear Steels

Benjamin Lee Tiemens

Rising power density requirements in transmission gear applications are swiftly outpacing gear redesign alone and will ultimately depend on better materials. Ni-Co secondary hardening steels show great promise for these applications due to their optimized combination of strength and toughness.

The commercially available secondary hardening alloys GearMet® C61 and C67 have already demonstrated promising contact fatigue resistance, however bending fatigue is anticipated to be the primary failure mode limiting high power density gear applications. Single tooth bending fatigue testing was therefore completed on C61 and C67 spur gears to both assess the optimized performance of these alloys as well as identify defect populations currently limiting further advances. The resultant best-practice C61 spur gears in a shot peened and isotropic superfinished condition outperformed the top-ranking premium gear steel, demonstrating an approximate 15% improvement in bending fatigue endurance limit. Fatigue failures limiting further bending fatigue performance were identified to

primarily initiate at three defect classes: shot peening-induced surface damage, subsurface inter-granular cleavage facets and Al_2O_3 and La_2O_2S inclusions. C67 spur gears did not show increased performance despite elevated surface hardness levels due to the inability of current shot peening practices to achieve maximum compressive stress in ultra-high hardness materials.

In an effort to reduce the material cost of these alloys through minimization/elimination of cobalt alloying additions, BCC Cu precipitation was incorporated to offset ensuing losses in temper resistance by providing additional heterogeneous nucleation sites for the M_2C strengthening dispersion. Fifty-pound experimental heats were made of four designed compositions. Peak hardness levels achieved during tempering fell on average 200 VHN short of the 900 VHN designed surface hardness. 3-dimensional local electrode atom probe (LEAP) tomographic reconstructions of carburized samples demonstrated the heterogeneous nucleation of M_2C alloy carbides on Cu precipitates where peak strengthening occurred with overaged rod-shaped M_2C carbides. Recalibrated strengthening models accounting for the coarsened microstructure agreed well with measured hardness values with 2nd iteration designs predicting the maximum possible hardness to be 65 R_C.

Acknowledgements

No one person's work is ever done alone, and this holds especially true for my graduate studies and collaborations at both Northwestern and General Motors. The last several years have been a tremendous experience for me, which in large part is due to everyone I've had the chance to meet. It would be impossible to adequately express my gratitude to everyone, but I'd like to especially thank just a handful of people.

Professor G.B. Olson - People always say that by the time one leaves graduate school, he or she will know more on their thesis topic than their advisor. In my case, I can't see how that's possible and it doesn't bother me at all. It has truly been a privilege to work with you as your knowledge and intellect never ceased to impress me. You have set for me the ultimate example of how best to weld science and engineering, which I will undoubtedly strive to emulate for years to come.

Dr. Anil Sachdev - Thanks first of all for giving me the opportunities to interact and collaborate with General Motors, without which my graduate experience would be far different and much less rewarding. You have taught me many things, including the art of setting tough deadlines and pushing through to meet them while keeping a sense of humor. Thanks for everything.

Professor Morris E. Fine and Professor Mark Asta - Thank you for serving on my committee and for your helpful discussions.

Neil Anderson and James Bishar - I learned a lot from both of you on not only how to prepare for and run a gear test program, but more importantly on how to be a good engineer. I greatly value our past discussions and am very grateful to you for all your kind assistance. Roger Moore (007), Donald Nordeen, Tad Canning and Mark Paulicki - The only reason I was able to collect all that test data was because of you guys. It was great working with you and getting to know you as well. Don Maddock, Dr. Dale Gerard and Dr. Shekhar Wakade - I thank you and the rest of GM Powertrain for your generous support and enabling the collaboration crucial to this work.

Dr. Raj Mishra - Thank you for being my mentor at GM, including many helpful discussions as well serving as my culinary encyclopedia. Bob Kubic - You were invaluable to me at GM. I always appreciated your gracious assistance when you were in high demand, and greatly enjoyed our random conversations. Everyone else at GM R+D - My three summers in Warren were highly enjoyable but only because of all the great people I met along the way.

Dr. Dieter Isheim, Prakash Kolli, Rick Karnesky and everyone else atom probing at NUCAPT - The LEAP is an amazing tool, and my use of it was only made possible through your instruction, guidance and discussions. Dr. Stair and Rick Kraemer - You are truly under-appreciated yet vital members of Northwestern. Thanks for all your help. Peggy Adamson - Thanks for working red-tape miracles and keeping such a great sense of humor. Arup, Dave, Yana and Padmanav - Thanks for sharing an office and countless hours with me. May office basketball hopefully live in infamy. Olson Group Members - Past and present, you're a cool, laid-back bunch. I definitely made a good choice in

choosing the best group for me. Lynn Costanza - Thanks for all your help. Making all those samples was not easy, but you somehow made it seem so.

Friends - Too many to list as I've met a lot of amazing people over the last couple years. Andy, Les, Erik and Courtney - some of my best memories are with you, thanks for that. Nate - You were a great roommate for over four years, I couldn't have asked for better. James - You make me laugh more than anybody else, and although that scares me, I do appreciate it.

Stefan - I never could have guessed a summer internship roommate could have turned into such a good friend. I'll always remember our discussions and adventures and hope to have many more.

My Parents - You've always supported me to seemingly incredible lengths. I could not have asked for better role models on how to raise a family. I love you. The Brothers - I turn to you guys for reassurance that I'm not too weird and that genetics are truly to blame, and for this reason you are two of my favorite people.

Aleta - More than anything else, you have become the most important part of my life. Thanks for all your love and patience, as well as for your stubborness that helps keep mine in check. I can't imagine how life would be without you, and I hope I never have to. I love you with all my heart.

Zeus - King of cats. Last but not least, for your loving head-butts never failed to cheer me up.

Table of Contents

List of Tables

List of Figures

CHAPTER 1

Introduction

1.1. Motivation

Rising power density requirements in transmission gear applications are demanding significant technological innovation. In 2004, representative leaders of the gear industry, including members from the United States Army, Boeing, General Motors and John Deere, composed the Gear Industry Vision addressing these needs, specifically outlining strategic goals to be met by the year 2025 [**1**]. Among the stated objectives were ambitious goals for enhancing gear performance, calling for 25% increases in power density every 5 years as well as a 50% increase in power transfer efficiency. Such lofty aims will soon surpass performance gains possible through gear redesign alone and ultimately depend on better gear materials. The Gear Industry Vision identifies clean steels heat treatable to ultra-high hardness levels (RC70+) as leading candidate materials and the continuing development of such steels as a "key technological challenge" that must be addressed.

Based in Northwestern University, the Steel Research Group (SRG) is composed of various academic, industrial and government members spanning numerous disciplines and united in the advance of steel technology. The ultimate aim of the SRG is the ability to replace time-consuming empiricism in traditional alloy development with systems-based computational design of materials. Systems-based materials design focuses on the various interacting subsystems ultimately responsible for material performance. Drawing upon

the existing knowledge base of various materials systems, targeted microstructures can be engineered for specific applications through the iterative feedback between theoretical modeling of these subsystem interactions and state-of-the-art analysis of prototype alloys. Using this approach, an alloy family of Ni-Co secondary-hardening carburizing steels was developed that have shown great promise in addressing high performance gear applications. This work aims to utilize the same systems-framework used to create these alloys to now optimize their performance specifically to address rising power density requirements in transmission gear applications.

Yet another challenge acknowledged by the Gear Industry Vision is the rising competition to gears from other forms of power transmission, such as electric motors and hydraulic systems [**1**]. Economic viability of gears as well as the materials from which they are made will be increasingly important. In some instances, material cost must be reduced with minimal expense to performance, requiring creative solutions. A large portion of the raw material cost of the high performance Ni-Co steel alloys is the significant cobalt content typically employed to maximize secondary hardening during tempering. At approximately \$20-30 dollars per pound, cobalt is on average over ten times more expensive than other common steel alloying elements [**2**]. In response, second-generation secondary-hardening alloys will also be developed in this work aimed at reducing material cost through the minimization of cobalt. To achieve this, Cu precipitation will be incorporated into the alloy design to supplement and catalyze secondary hardening from M_2C alloy carbides. This novel microstructural modification is made possible by the adaptive capabilities afforded by the systems approach.

1.2. Systems Approach

In his review of systems-based engineering, Gwilym Jenkins stressed the importance of a unifying approach to combat increasing complexity of the world's problems [**3**]. Instead of optimizing individual factors within a complex system, Jenkins argued for the focused design of interacting subsystems aimed at collectively optimizing the overall system in the most efficient manner. This development process, as shown in Figure 1.1, takes the form of broad stages starting from the analysis of the system in question. Models and simulations are then utilized to design or synthesize an optimized system. This designed system is then implemented, with the observed results directing additional design iterations or being directly introduced into standard operation. The applicability of such thinking Jenkins felt was universal and urgent, requiring insertion "into industry, commerce, and into local and national government."[**3**]

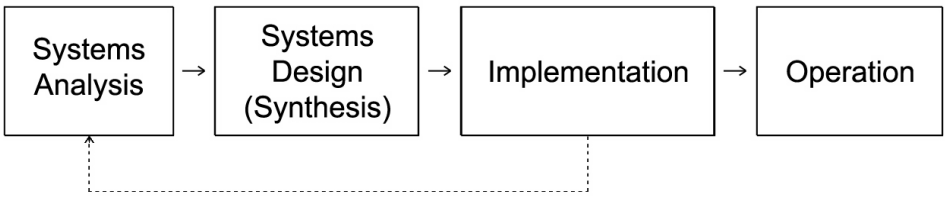

Figure 1.1. General stages for the systems engineering process [**3**]

Cyril Stanley Smith followed this mantra by applying the systems framework to materials science [**4**]. Here, each material is defined as a complex system controlled by a hierarchy of structural subsystems. Only through understanding the connections between these subsystems and the processes that lead to them can the overall material performance be optimized. Further expanding upon this vision, Gregory Olson has distinguished the

primary controlling subsystems as the central materials science components of processing, structure, properties and performance shown in Figure 1.2[**5**]. In turn, each of these primary subsystems can be expanded into an additional hierarchy of subsystems and interconnections.

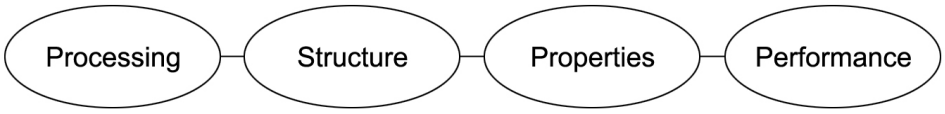

Figure 1.2. Linear structure of primary materials subsystems [**5**]

In following the linear chain of Figure 1.2, scientific understanding traverses left to right following "cause and effect" logic. By applying the systems framework and integrating scientific understanding of the interrelations governing the overall system, it becomes possible to follow a "goal/means" logic path traversing right to left. This approach pioneered by Olson first translates desired performance measures directly into quantitative property objectives. Microstructural elements can then be identified that are most instrumental in meeting these objectives, and through a combination of mechanistic and computational modeling, the corresponding composition and processing parameters can be derived. In this manner, materials transcend from experimental discoveries into inspired creations handcrafted for specific purposes.

The utility of this systems framework carries through initial alloy development into the operational performance optimization as well. Just as empirical approaches are traditionally used to develop alloy compositions, trial and error practices also commonly pervade efforts to tailor materials to specific applications. In this methodology, processing techniques and parameters are widely varied in the hopes of eventually capturing the

combination leading to "best practice" conditions. Not only are such procedures costly and time consuming, they neglect to ascribe the contribution of each processing step on the microstructural elements dictating material properties. Subsequently, these empirical practices most often yield non-transferable knowledge where the discovered optimal processing conditions only hold true for a specific alloy requiring the entire process to be repeated anytime a new alloy is introduced. By adopting the systems-based approach in process optimization, generated knowledge instead takes the form of key relationships between the structure-processing-property subsystems rather than alloy specific processing recipes. This allows not only for enhanced scientific understanding of the physical processes involved, but also for greater adaptability to the application of other alloy systems. The number of iterations required for processing/performance optimization is also greatly reduced with this approach. By incorporating the microstructural subsystems, direct links are generated between processing and observed properties, allowing for targeted optimization of key processing parameters.

1.3. Plan of Study

Guided by the systems-based approach, this work aims to address required gear material enhancements through both optimizing the performance of promising secondary hardening alloys as well as designing second-generation alloys to reduce material cost. Chapter 2 outlines the prevalent failure modes currently limiting high power density gear applications. The concepts behind secondary hardening steels are also discussed as well as an introduction on BCC Cu precipitation to be incorporated into new alloy designs. The various materials and experimental methods are covered in Chapter 3, as well as

the computational tools used in alloy design. Chapters 4 and 5 detail studies on existing alloys, starting with performance optimization driven by failure-inducing defect analysis of single tooth bending fatigue specimens. Chapter 5 follows with studies focused on intrinsic microstructural issues including grain coarsening, hardenability and carbide stability. Chapters 6 and 7 discuss the development of second-generation alloys incorporating nanoscale Cu dispersions to supplement and catalyze secondary hardening in lieu of expensive cobalt alloying additions currently used. Chapter 6 outlines the alloy design process for four experimental alloy compositions. Evaluation of resultant prototypes is discussed in Chapter 7 including hardness response during tempering and analysis of both nanoscale dispersions using 3D local electrode atom probe (LEAP) tomography. Microstructural parameters are then re-assessed to recalibrate alloy design models, and preliminary 2^{nd} design iterations were carried out. Chapter 8 summarizes both the performance optimization and alloy design, and Chapter 9 provides suggestions for future work.

CHAPTER 2

Background

2.1. High Power Density Gear Requirements

The use of gears is required in nearly all applications where power transfer is needed. Gears typically transfer power from one shaft to another, and can assume a myriad of geometries and configurations based on the specific application. During power transfer from one gear to another, stresses are generated between the mating gear teeth. The exact nature and magnitude of such generated stresses are dependent on the particular gear geometry being employed. The location of these stresses, however, is generally concentrated in two principal locations as demonstrated by the photoelastic stress analysis of polymer spur gears shown in Figure 2.1a [**6**]. Darkened bands in Figure 2.1a correspond to levels of constant stress formed by the interference between polarized light transmitted through the loaded spur gear and a reference beam. The first location is at the point of contact between two mating gear teeth. As the meshing gear teeth turn, sliding-rolling contact applies a load along the region of the gear tooth surface known as the active profile. The generated stress, called the surface contact stress, travels up and down the active profile as the gear teeth engage. At the midpoint of the active profile, or pitchline, these stresses are in general pure rolling as the applied load from one gear tooth is normal to the mating tooth. Both above and below the pitchline the applied load deviates away from normal,

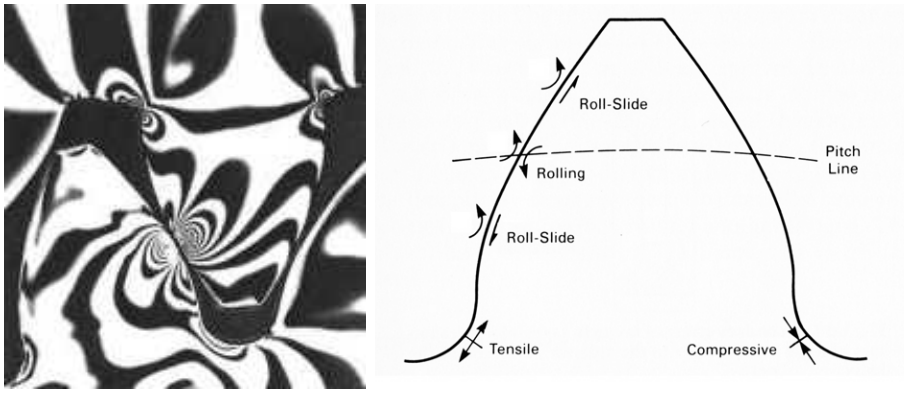

(a) (b)

Figure 2.1. a) Photoelastic stress analysis of polymer spur gears demonstrating principal locations of stresses generated during loading [**6**] and b) Schematic showing types of principal stress [**7**]

.

subsequently causing sliding and an associated shear stress component, shown schematically in Figure 2.1b [**7**]. The second principal stress location occurs at the gear tooth root radius or fillet, also shown in Figure 2.1b. This stress is generated as the loaded gear tooth acts as a cantilever beam, and is therefore commonly called the beam bending stress. This stress is tensile on the loaded side of the gear and compressive on the opposite side.

To determine the magnitude of these stresses, the American Gear Manufacturers Association (AGMA) has developed several detailed standards for various gear geometries [**8, 9, 10**]. In general, however, the AGMA stress calculations can be summarized by a basic stress formula consisting of three indices: a load index, a geometry index and a rating index [**11**]. The load index relates to the physical dimensions of the gear determining the transmitted load. The geometry index takes into account the effect of gear geometry on the generated stresses, including parameters such as the gear root fillet radius, the

number of gear teeth and the angle formed between the active tooth profile and a radial line through the pitchline, known as the pressure angle. The final index, the rating index, describes additional gear design considerations accounting for possible variations in operating conditions. These factors include allotted tolerances for gear manufacture and alignment, operating temperatures and the relative velocity between mating gears.

For the case of a generic beam tensile bending stress (St), the calculation takes the form of Equation 2.1:

$$S_t = U_L \times C_t \times R_a \tag{2.1}$$

where the load index is the unit load (U_L), the geometry index is the beam stress factor (C_t) and R_a the rating index or overall rating adjustment factor. The values for C_t and R_a can themselves be calculated from various other parameters pertinent to the specific gear geometry and configuration, with common combinations often listed in tables for reference [**12**]. For spur gear stress calculations, the value for U_L can be calculated with Equation 2.2:

$$U_L = W_t \times \frac{P_d}{F} \tag{2.2}$$

where W_t is the tangential load, F the face width of the gear in contact and P_d the diametral pitch. The diametral pitch is a measurement of the size of a tooth crossection normal to the gear axis found by dividing the number of teeth by a unit of pitch diameter. The surface contact stress (S_c) calculation has a slightly different general form as shown in Equation 2.3:

$$S_c = \sqrt{K} \times C_k \times \sqrt{R_a} \tag{2.3}$$

where the load index is now called the "K-factor" (K) and the geometry index denoted as C_k. The loading factor K is raised to power of one half to reflect the square root relationship between the applied tangential load (W_t) and the generated stress (S_c). The various parameters composing the rating index (R_a) are all related to load adjustments, therefore R_a is also raised to the one half power to calculate S_c. In many applications, the rating index is the same for both bending stress and surface contact stress calculations. The K-factor can be calculated by Equation 2.4:

$$K = \frac{W_t}{(F \times d_p)} \times \frac{(m_g + 1)}{m_g} \tag{2.4}$$

where d_p is the diameter of the pinion, or the smaller of the two contacting gears, and m_g is the ratio of gear teeth between the larger gear and the pinion.

As demonstrated by Equations 2.2 and 2.4 above, increasing power densities achieved either through increasing loads or decreasing gear dimensions translates directly into increased stresses. Consequently, both these primary stresses lead to related failures in high power density gear applications: sliding contact fatigue from repeated surface contact stresses and tooth bending fatigue from cyclical beam bending stresses.

2.1.1. Sliding Contact Fatigue

A common failure mode for any mechanical element subjected to rolling/sliding conditions is contact fatigue. In meshing gears, contact fatigue is generated due to cyclically applied contact stresses along the pitchline and surrounding active profile. Directly along the pitchline, the applied stress between the mating gear teeth is normal to the surface, generating pure rolling conditions. The contact between two rolling bodies generates

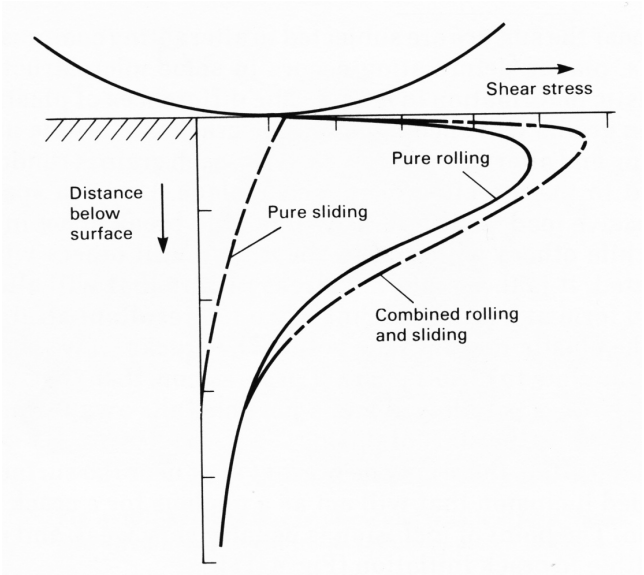

Figure 2.2. Schematic showing contact stress distribution due to combined rolling and sliding [**7**]

compressive elastic, or Hertzian, stress where the maximum shear stress occurs below the surface just ahead of the rolling contact point as shown in Figure 2.2. Subsurface damage occurs when this Hertzian contact stress exceeds the cyclical yield strength of the material or interacts with stress-rising defects such as inclusions. With further cyclical loading, the subsurface damage forms a crack that ultimately propagates to the surface and leads to damage ranging from micropitting to large-scale spalling. Above and below the pitchline on the active profile, an additional shear stress component is introduced due to sliding contact, as also shown schematically in Figure 2.2. The maximum combination of sliding and rolling stress components typically occurs just above and below the pitchline, making this portion of the gear tooth especially prone to pitting [**7**].

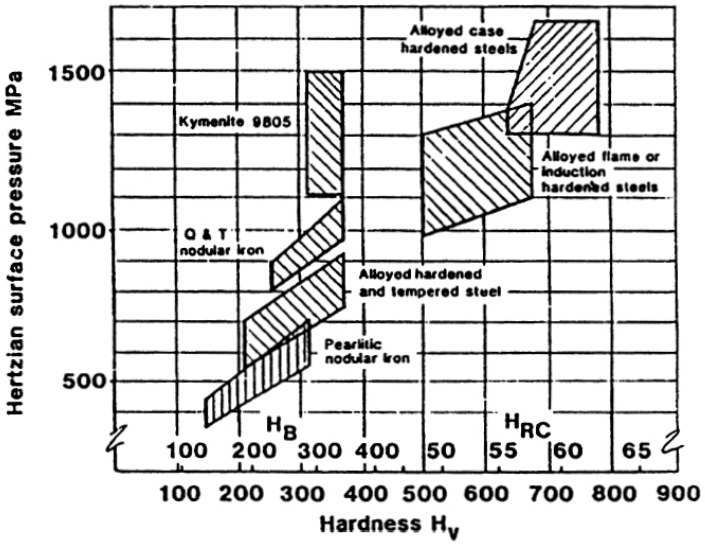

Figure 2.3. Trend of increasing hardness vs. maximum Hertzian contact pressure [**13**]

2.1.1.1. Effect of hardness. To counteract these contact stresses concentrated at or near the mating gear tooth surface, gear surfaces are commonly hardened through processes such as carburizing, nitriding and induction hardening. By only hardening the outer surface, overall toughness and impact resistance can be maintained through the softer core while the hardened case resists contact fatigue and general wear. Figure 2.3 demonstrates the ability of harder materials to withstand greater Hertzian contact stresses, with carburized alloy steels exhibiting the best performance [**13**].

As the applied Hertzian contact stress is increased, the depth at which the maximum shear stress occurs also increases. To properly resist contact fatigue, the hardened case must therefore be deep enough to counteract the applied stresses. Surface hardening through carburizing allows for adequately deep case depths, with typical carburized gear case depths ranging from 0.020" to 0.040" (0.5 - 1.0 mm).

2.1.1.2. Effect of residual stress. An additional benefit from surface hardening through carburizing is the generation of surface compressive residual stress. During the carburization process, hardening is achieved by diffusing carbon into the surface at solutionizing temperatures. The austenite-stabilizing ability of carbon creates a transformation temperature gradient between the carburized case and the core material. Upon quenching, the core transforms first due its lower carbon content and higher transformation temperature. The volume expansion associated with the martensitic transformation is accommodated by the softer austenite phase still present in the carburized case. With further cooling, the higher carbon case material transforms to martensite. The now martensitic core, however, resists the expansion of the carburized case transformation and leaves the surface material in a state of compression. This compressive stress acts to reduce the overall effective stress and allows for increased resistance to applied contact stresses.

2.1.1.3. Effect of carbide dissolution. Under heavy contact loads, the subsurface shear stress is of sufficient magnitude to cause localized deformation and associated microstructural transformations. This development, sometimes called "martensitic decay" or "altered martensite", is often located on shear planes around inclusions or primary carbides that act as stress risers and is commonly seen in bearing steels as well as carburized gears [**14**]. When chemically etched, such as with Nital, these bands appear white and are known as white etching bands (WEB's) or "butterfly wings", due to the way they spread out from the originating inclusion or carbide [**7**]. The microstructure of these WEB's or "butterfly wings" consists of heavily deformed, very fine-grained ferrite where all strengthening carbides have been partially or fully dissolved [**15**]. The interstitial carbon formerly composing the carbides subsequently diffuses out of the region,

leading to the observed white-etching behavior as well as causing strain-softening that in turn leads to further strain localization. The avoidance of these failure-inducing butterfly formations can in part be achieved by removing the stress risers from which they originate. Cleaner melt practices to reduce inclusions as well as optimized microstructures and heat treatments to avoid large primary carbides all benefit contact fatigue resistance. Steels strengthened through alloy carbides also show improved contact fatigue resistance than those strengthened by transition ϵ-carbides [**6**]. This is attributed to the increased thermodynamic stability of alloy carbides, which are more stable than cementite unlike transition carbides. Additionally, the dissolution of alloy carbides requires the diffusion of substitutional carbide forming elements of low mobility such as Cr and Mo, whereas dissolution of transition Fe-carbides only requires the diffusion of highly mobile interstitial C atoms. The size of strengthening carbides also plays a role in strain softening due to carbide dissolution. Under repeated heavy contact loads, the large subsurface shear stresses can with time shear and dissolve particles that under monotonic loading conditions would remain unshearable Orowan obstacles. The size at which strengthening carbides transition from particle shearing to particle bypass regimes is different, therefore, for monotonic and cyclic loading conditions, with the transition occurring later for cyclic loading. Overaging may therefore be a means of increasing the stability of strengthening dispersions to resist cyclic strain softening due to particle dissolution.

2.1.2. Bending Fatigue

Tooth bending fatigue has been found to be the most frequent of all gear failure modes [**7**]. Unlike surface contact stresses, bending stresses scale linearly with increasing load as well

as decreasing tooth thickness and will subsequently be a primary performance limitation in going to higher power densities. Bending fatigue failures occur due to the tensile beam bending stresses cyclically generated at the roots or fillets of loaded gear teeth, previously illustrated in Figure 2.1. The process of fatigue failure due to cyclic tensile stresses can be summarized by five stages as outlined by Fine [**16**]:

(1) Cyclic plastic deformation

(2) Microcrack initiation

(3) Formation of macrocracks due to microcrack propagation/coalescence

(4) Macrocrack propagation

(5) Final failure

Initially cyclic plastic deformation occurs through dislocation glide during each generated stress cycle. With continued glide, dislocations interact and form bundles or cells. Depending on the specific material and its initial microstructure, cyclic hardening, cyclic softening or a combination of the two may occur due to this evolution of the dislocation substructure. In certain materials, plastic deformation becomes severely localized and enhanced along certain slip bands known as "persistent slip bands" or PSB's. Microcracks are formed as obstacles impede dislocation motion, such as high angle grain boundaries and interfaces. At these obstacles, dislocation pileups accumulate until a critical level is reached and a dislocation avalanche process occurs, ultimately leading to localized plastic strain and microcracking. In cases where dislocation pileups do not occur, gliding dislocations emerge at the surface resulting in a slip step. With continued stress cycles, these steps accumulate where slip bands intersect the surface and the ensuing roughening of

the surface leads to the formation of a microcrack. The first microcracks to form in the fatigue process are often called Stage I fatigue cracks.

Once a microcrack has initiated, it will continue to grow assuming the stress or plastic strain cycling is above a threshold value. Below this threshold, known as the fatigue limit, microcracks may nucleate but fail to propagate. This phenomena may be in part due to interactions with obstacles such as phase boundaries or grain boundaries [**16**], however the exact nature of microcrack or "small crack" propagation is complicated and the focus of ongoing study [**17**]. Above the fatigue threshold, microcracks grow and/or coalesce until they have reached a sufficiently large size to be deemed a macrocrack, or Stage II fatigue crack. This transition can be generally approximated as the point where a microcrack has traversed an area exceeding several grain cross-sections [**16**]. The propogation of the larger macrocracks is a much better understood process with the advance of the crack tip generally following linear elastic fracture mechanics. The controlling parameter governing macrocrack propagation is the applied stress intensity range (ΔK) experienced at the crack tip during cyclical loading. Macrocrack propagation rates determined by change in overall crack length (c) per cycle (N) are usually observed to consist of three regimes based on ΔK. These three regimes manifest themselves as three regions in a log-log plot of $\frac{dc}{dN}$ vs. ΔK, as shown in Figure 2.4. The first region, Region I, centers around a threshold stress intensity range (ΔK_o) below which macrocracks will not propagate. At stress intensity ranges just above this threshold, crack propagation rates increase rapidly until leveling out into a region of steadily increasing crack growth, Region II. Crack propagation in this

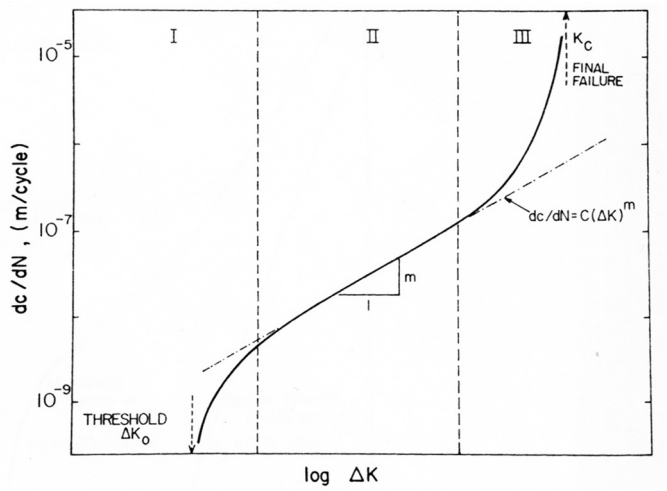

Figure 2.4. Schematic plot of fatigue crack propagation rate vs stress intensity range [**16**]

second region follows a power law known as the Paris relation shown in Equation 2.5:

$$\frac{dc}{dN} = C(\Delta K)^m \tag{2.5}$$

where C and m are constants. As the stress intensity range increases into Region III, the crack propagation rate once again increases very rapidly as the maximum stress intensity nears the critical stress intensity for fracture or critical fracture toughness (K_{IC}) and final failure occurs

In the specific case of surface hardened gears, the fatigue process is further complicated due to a gradient in microstructure and associated properties. Krauss outlined five stages of fatigue as manifested through five distinct regions on the fracture surface of a gear tooth that failed due to bending fatigue [**18, 19**]. Figure 2.5 shows example SEM micrographs of these five stages of bending fatigue in carburized gears [**20**].

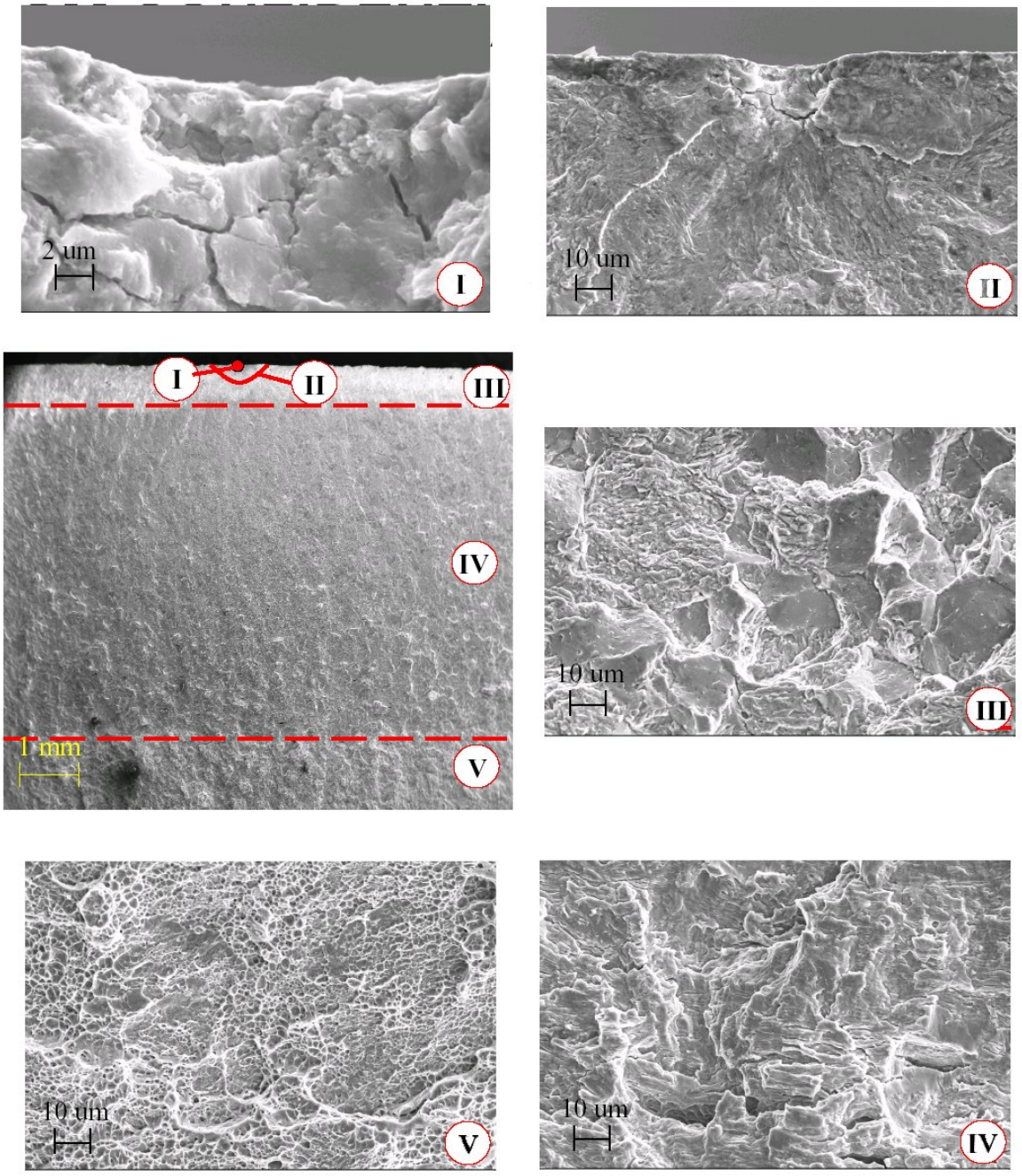

Figure 2.5. Five regions of bending fatigue crack propogation in case hardened steel [**20**]

Region I consists of fatigue crack initiation within the carburized case. Common defects where initiation occurs include intergranular oxidation from gas carburizing, embrittled prior-austenite grain boundaries and subsurface inclusions. Once initiated, the fatigue crack steadily propagates transgranularly through the carburized case in a radial fashion, outlining Region II on the fracture surface. If originating from the surface, the advancing fatigue crack will produce a semi-circular fracture path while subsurface initiated fatigue cracks radiate in all directions and form a circular fracture region around the initiating defect, a feature commonly referred to as a "fisheye". Once the advancing fatigue crack has reached the critical flaw size of the carburized case, it becomes unstable and rapidly advances, rupturing the length of the carburized case as seen in Region III. Further from the surface past the hardened layer, the advancing crack encounters the softer core, slows down and propagates once again in a stable manner. This region, Region IV, is characterized by a transgranular fracture surface with resolvable fatigue striations and secondary cracking[**18, 21**]. The crack steadily advances until reaching the critical flaw size of the softer core, eventually leading to ductile overload fracture (Region V).

2.1.2.1. Effect of hardness. The number of cycles spent in each of the aforementioned stages of fatigue failure depends greatly on the magnitude of the applied cyclic stress. If the maximum applied stress is low, the macroscopic strain state is predominantly elastic and a large number of cycles is required to cause failure. This high-cycle fatigue occurs near the fatigue limit, where the limiting stage of fatigue is the nucleation and propagation of Stage I microcracks. At higher stresses significantly above the fatigue limit, microcracks are able to initiate and propagate into macrocracks much more easily, and fatigue failure is accelerated. Most of the load cycles in this low-cycle fatigue then is spent in

the plastic deformation of advancing macrocracks. This behavior was shown experimentally for bending fatigue of carburized gears using acoustic emmision techniques, where crack initiation at high stresses composed approximately half of the cycles til failure, but increased to 89% of the total life near the endurance limit [**22**].

The transition between these two regimes is demonstrated during cyclical strain-controlled fatigue tests. Results from such tests are typically plotted on a log-log plot of the applied strain amplitude ($\frac{1}{2}\Delta\epsilon$) vs. cycles till failure (N_f), as shown schematically in Figure 2.6a. Here the total strain is a combination of the elastic strain range ($\Delta\epsilon_{el}$) and the plastic strain range ($\Delta\epsilon_{pl}$).

During low cycle fatigue where the large plastic strains dominate, the elastic strain component becomes negligible and $\Delta\epsilon \cong \Delta\epsilon_{pl}$. Near the fatigue limit in high-cycle fatigue, the total strain is predominantly elastic and $\Delta\epsilon \cong \Delta\epsilon_{el}$. General empirical relations correlate the cycles till failure with these two strain regimes and associated material parameters. For low-cycle fatigue, Equation 2.6 relates $\Delta\epsilon_{pl}$ and N_f:

$$\frac{1}{2}\Delta\epsilon_{pl} = \epsilon'_f(2N_f)^{-c} \tag{2.6}$$

where ϵ'_f and c are fitting parameters related to tensile ductility and work softening, respectively. Based on this relation, low-cycle fatigue life can be extended through increased ductility and enhanced work hardening, correlating with the ability to withstand increased plastic deformation from advancing fatigue macrocracks. This trend is shown schematically in Figure 2.6b where ductile materials perform better than harder and stronger materials in low cycle fatigue. This trend is reversed when going to high-cycle fatigue where elastic strains predominate. Here the empirical correlation with fatigue life follows

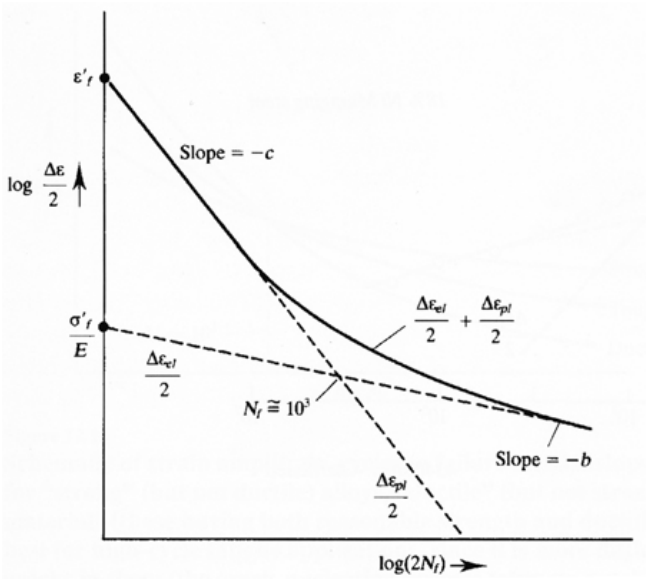

(a)

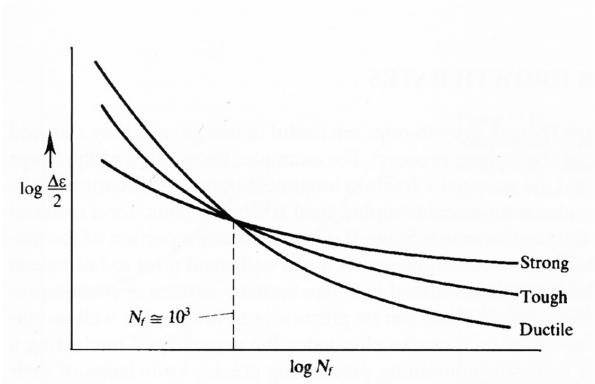

(b)

Figure 2.6. a) Schematic showing typical results of strain-controlled fatigue tests plotting strain amplitude vs. number of cycles til failure and b) relationship of general material properties on fatigue life [**23**]

the form of Equation 2.7:

$$\frac{1}{2}\Delta\epsilon_{el} = \frac{\sigma'_f}{E}(2N_f)^b \tag{2.7}$$

where the fitting parameters are now σ'_f, which relates closely with monotonic tensile strength, and b, which relates to cyclic work hardening. High-cycle fatigue life may then be

extended by increasing the tensile strength of the material, effectively resisting microcrack initiation and propagation. This behavior is also demonstrated schematically by Figure 2.6b, where stronger materials demonstrate improved high-cycle fatigue resistance than their more ductile counterparts. The total material response combining both elastic and plastic strain components would then be the combination of Equations 2.6 and 2.7:

$$\frac{1}{2}\Delta\epsilon = \frac{1}{2}\Delta\epsilon_{pl} + \frac{1}{2}\Delta\epsilon_{el} = \epsilon'_f(2N_f)^{-c} + \frac{\sigma'_f}{E}(2N_f)^b \tag{2.8}$$

As also demonstrated by Figure 2.6b, the ability of higher-strength materials to resist high-cycle fatigue ultimately translates into increased fatigue limits below which microcrack propogation and subsequent fatigue failure will not occur. Because this threshold marks the initial onset of plastic strain, the fatigue limit has long been linked with a material's tensile properties such as yield strength or ultimate bending strength. Murakami has shown that a better correlation exists with microhardness, which reflects a material's average flow stress or resistance to plastic deformation. An example of this trend is shown in Figure 2.7, where the fatigue limit (σ_{w0}) of various steels is shown to follow the relationship $\sigma_{w0} \cong 1.6HV$ [**24, 25**].

2.1.2.2. Defect sensitivity. The correlation between increased hardness levels resulting in increased fatigue limit is not observed at all strength levels. For the various steels shown in Figure 2.7, this trend holds true up to microhardness levels <400 Vickers (HV). Past this hardness level, the trend reverses and the fatigue limit is reduced with increased hardness. This phenomenon can be explained by the increased flaw sensitivity exhibited by harder materials. Figure 2.8 shows the relationship between the size of an artificial hole and the observed effect on fatigue strength for steels of two different hardness levels

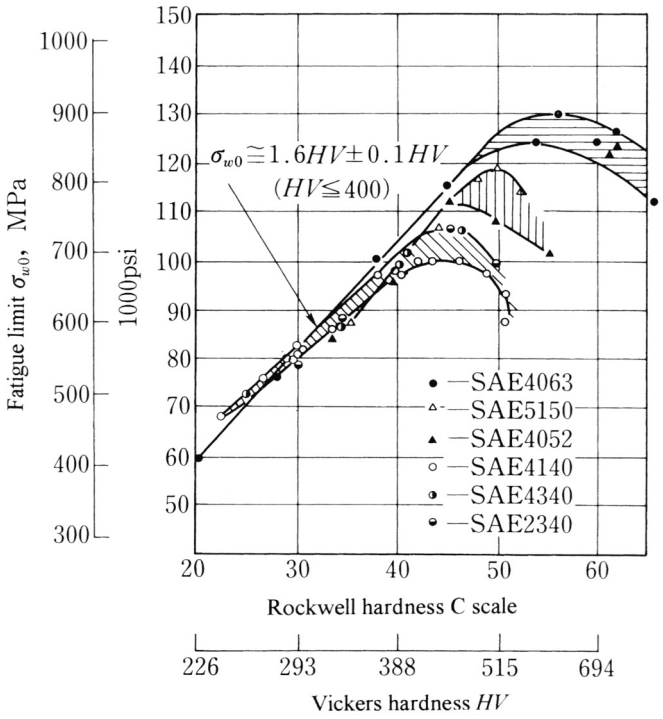

Figure 2.7. Correlation between microhardness and fatigue strength for various steels[**24, 25**]

achieved through different carbon contents [**25**]. Both steels exhibit a critical flaw size below which the impact of the flaw has a negligible or very small effect on the fatigue strength. Small microcracks were observed to form from these flaws but the effective rise in stress intensity due to these defects was not great enough to cause them to propagate. Once the imposed defects exceeded the critical diameter, the generated rise in stress intensity was great enough to cause microcrack propagation and ultimate fatigue failure. For the harder steel, this critical threshold occurs at a much smaller flaw size than the softer steel and the impact of flaws exceeding this critical dimension have a much larger impact on fatigue strength as well. For the steels shown in Figure 2.7, once the hardness level surpasses the 400 H_v threshold, the critical flaw size has reduced to the dimensions

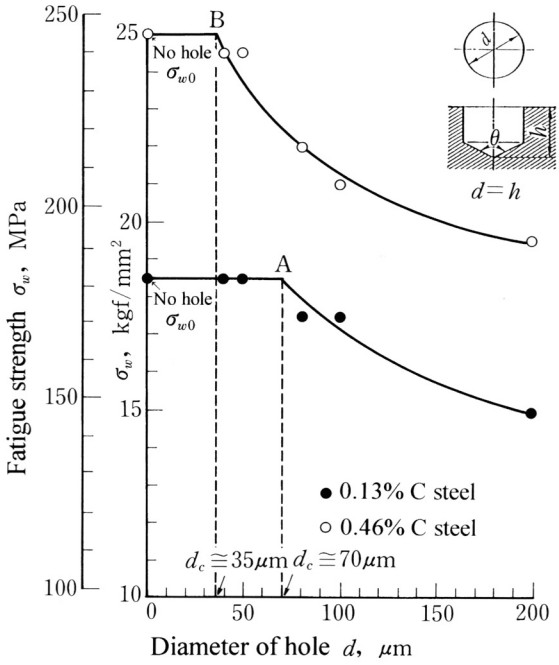

Figure 2.8. Relationship between artificial flaw size and fatigue strength [**25**]

of intrinsic flaws within the steels such as inclusions and surface defects. With increasing hardness, the detrimental nature of these flaws becomes more pronounced causing the reversed trend of diminishing fatigue strength.

One common method of minimizing the detrimental effect of defects is through shot peening. Shot peening imparts compressive residual stress into the surface and near subsurface through bombardment of hard media, including hardened steel, ceramic and glass. This compressive residual stress effectively acts as a mean stress counteracting applied tensile stress. Consequently, the use of shot peening greatly inhibits microcrack initiation and growth, both from the surface and near subsurface defects. This in turn elevates resistance to high cycle fatigue and the associated fatigue limit. The benefit of shot peening is not as great for low-cycle fatigue, where plastic strains predominant

and quickly overcome and dissipate compressive residual stresses. The magnitude of compressive residual stress that can be imparted to a material is largely a function of that material's yield strength [**26**]. Shot peening becomes increasingly important in the utilization of harder materials, therefore, as this residual stress advantage can be utilized to offset increased sensitivity to defects.

2.1.2.3. Microstructure limitations. Once extrinsic processing defects are addressed through such actions as cleaner melt practices and improved surface finishing techniques, the intrinsic microstructure becomes the limiting factor in fatigue failure. Statistical analysis of bending fatigue data for various carburized steels revealed that of all investigated parameters, prior austenite grain size had the largest correlation with endurance limit [**27**]. Grain size in general has been attributed to influence fatigue in different ways. Smaller grain size has been linked to increased resistance to high-cycle fatigue and improved fatigue limits. This grain size effect has been attributed to the increased strength from grain refinement (Hall-Petch strengthening) [**16**] as well as dilution of grain boundary phosphorus segregation believed to promote embrittlement by stabilizing cement [**19**]. Reducing grain size has also been shown to delay microcrack initiation and growth along intense slip bands by reducing the overall slip length[**28**]. As a result, the number of dislocations in a pileup is reduced as well as the associated stress concentration at the pileup-causing obstacle. The reduced slip length also limits the number of dislocations that can emerge at a free surface and cause surface roughening. In high carbon steels, grain size refinement has also been shown to increase fatigue resistance by minimizing detrimental microcracking formed by impingement of martensite plates during quenching[**29**].

Hardenability, or the lack thereof, can also influence a material's fatigue properties. Retained austenite formed by incomplete martensitic transformation upon quenching has been shown to increase low-cycle fatigue resistance [**30**]. This has been attributed to the improvement of ductility from the softer austenite as well as from crack impeding compressive stresses generated from the volume expansion of deformation-induced transformation to martensite [**19, 30**]. For high-cycle fatigue and the endurance limit, the reduction in hardness and tensile strength caused by retained austenite has been shown to be detrimental [**31**]. Small inhomogeneities due to limited hardenability such as Bainite patches have also been shown to act as fatigue initiation sites in ultra-clean steels [**25**].

2.2. Secondary Hardening Steels

To address rising power density requirements, steels must exhibit superior hardness to resist localized contact and bending stresses while at the same time sustain adequate toughness for sufficient flaw tolerance. One family of steels that has demonstrated the highest combination of strength and toughness is high-alloy secondary hardening martensitic steels. Secondary hardening steels get their name from a secondary hardening response exhibited by these alloys when aged at Stage IV (450-600°C) tempering temperatures. This hardening behavior arises from the formation of fine alloy carbide dispersions that replace coarse cementite particles during tempering. Because these alloy carbides are stable at higher temperatures, secondary hardening steels were first utilized as tool steels in order to maintain hardness at elevated temperatures, a phenomenon called "hot-hardness" or "red-hardness". The superior combination of strength and toughness

afforded through the fine alloy carbide dispersion was then utilized in high-strength high-toughness structural steels, leading to commercial alloys such as HY180 and AF1410 . It is this same optimized combination of strength and toughness that makes secondary hardening alloys well suited for high power density gear applications.

2.2.1. System Structure

Expanding upon the primary materials subsystems, the systems flow block diagram, or Olson diagram, for Ni-Co secondary hardening steels can be constructed for high power density gear applications as shown in Figure 2.9. The two performance objectives correspond to the two limiting failure modes in high power density gears, specifically bending fatigue and sliding/rolling contact fatigue. Top priority is placed on bending fatigue, as it is the most common failure mode as well as anticipated to be the primary limitation when attempting elevated power densities in transmission gear applications. Most important in meeting these objectives is the optimization of the properties hardness and toughness, as previously discussed. Additional resistance to both bending and contact fatigue is generated through compressive residual stress at the surface and mechanical stability of the strengthening dispersions. Structure is divided into two main subsystems: the matrix or base steel and the carburized case. Being the ultimate creation of the materials designer, microstructural elements composing these structures are the central link connecting processing and properties and will be discussed in later sections.

Processing subsystems begin with the creation of the actual gear from raw material, which is conventionally accomplished using one of three different methods. The most common of these methods is machining the gear from a cast ingot that has been forged

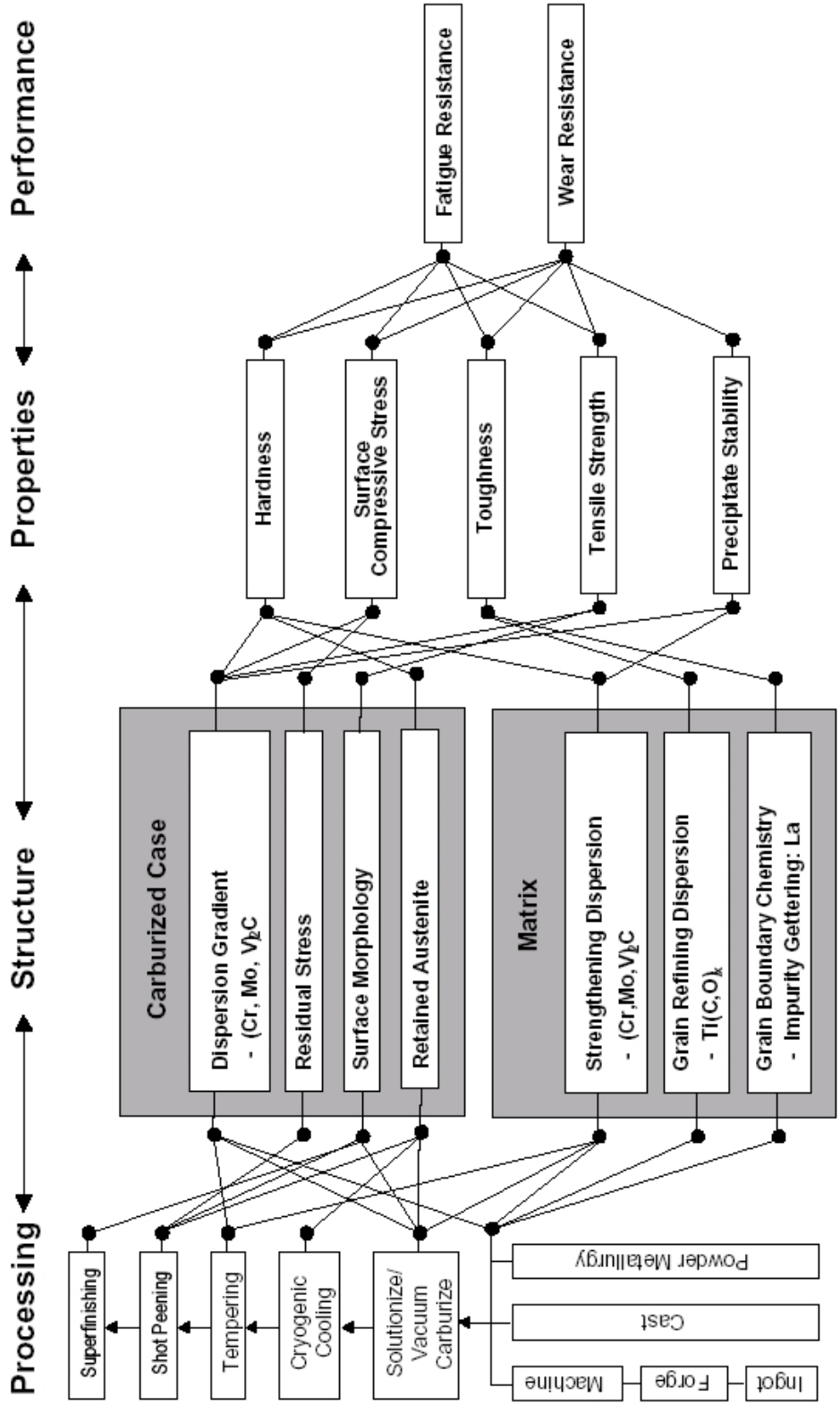

Figure 2.9. Systems flow block diagram of high power density gear applications

into stock. Additional gear manufacturing methods include direct casting and powder metallurgy techniques such as powder forging. Once the gear is formed it is typically heat treated to harden the surface through a process such as carburizing. Carburization treatments consist of a solutionizing heat treatment to dissolve primary carbides and bring the material to an austenitic state for increased carbon solubility. There are various methods of carburizing to diffuse carbon into the surface, ranging from simple pack carburizing to conventional gas carburizing. High temperature vacuum carburizing is desirable for high power density gear applications by avoiding intergranular surface oxidation common to conventional gas carburizing which commonly initiates bending fatigue failures [**19**]. Once carburized the gears are quenched and often subjected to cryogenic treatments to ensure complete martensitic transformation. Tempering treatments are then performed to achieve secondary hardening through the precipitation of alloy carbides. Various surface treatments can then be performed. Shot peening is commonly employed to impart compressive residual stress to the surface of gear teeth and root notches. Different means of improving the surface finish of the gear to rid of stress rising asperities include honing, grinding and burnishing [**12**]. Isotropic superfinishing combines chemical slurries with vibrating abrasive media to achieve very low surface roughness values shown to enhance gear performance in both bending and contact fatigue [**32**].

2.2.2. Matrix

2.2.2.1. Microstructure. The base microstructure of Ni-Co secondary hardening steels typically consists of a tempered lath martensite matrix, with the Ni and Co in solid solution. The lath martensitic structure occurs in steels with low to medium carbon contents

and is composed of groups or packets of very fine and parallel board-shaped crystals, or laths. This lath structure is formed upon quenching from the FCC austenite phase through a diffusionless shear transformation, resulting in a highly dislocated substructure due to accommodation of the associated lattice invariant deformation. The fine structure of the martensitic laths as well as the associated high dislocation densities gives this microstructure an excellent combination of strength and toughness. At higher carbon contents, the martensitic transformation temperature (M_s) is suppressed, causing the martensitic transformation mechanism to occur through twinning instead of dislocation motion. The resultant structure is composed of nonparallel plates and is usually accompanied by significant amounts of untransformed, or retained, austenite phase. The nonparallel nature of plate martensite often causes the impingement and subsequent brittle cracking of plates formed upon quenching. This propensity for microcracking, as well as a decreased dislocation density and softening from retained austenite make the plate martensite morphology less favorable to optimize strength and toughness than the lower carbon lath martensite microstructure.

Suspended in solid solution within this lath martensite microstructure are both the Ni and Co alloying additions. Ni is a common alloying element utilized in steels to enhance toughness. Similar to other BCC metals, brittle fracture of Fe tends to occur along {100} cleavage planes. Work by Krasko and Olson has attributed this behavior to a reduction in the overall ferromagnetic contribution to the total surface energy due to the presence of Ni at or near the surface of {100} planes [**33**]. Because the ferromagnetic contribution is negative, its reduction increases the total surface energy and the associated Griffith work of brittle separation, subsequently resisting cleavage fracture.

Cobalt alloying additions were originally added to tool steels in order to maintain hardness at elevated temperatures, a phenomenon known as "hot hardness" or "red hardness". This behavior arises as, besides from being a modest solid solution strengthener, Co is attributed to retard dislocation recovery at elevated temperatures [**34**]. This phenomenon is believed to occur through hindering the self-diffusion of Fe and associated dislocation climb through atomic short-range ordering between Co and Fe [**35, 36, 37**]. For secondary hardening steels, preserving this dislocation substructure during tempering at elevated temperatures sustains more locations for the heterogeneous nucleation of strengthening alloy carbides. By aiding heterogeneous nucleation, cobalt additions subsequently accelerate secondary hardening and allow for peak hardness to be achieved at significantly reduced tempering temperatures where the thermodynamic driving force for precipitation is increased. Cobalt additions, therefore, enable the precipitation of finer, more efficient strengthening dispersions and maximize the secondary hardening response. Figure 2.10 demonstrates this effect of Co on secondary hardening, where after 1 hour of tempering, the addition of Co both raises the peak hardness by 10 R_C and reduces the peak hardness tempereature by over 200°F (100°C) [**38**]. To ensure equivelant martensite transformation temperatures (M_S) between the two alloys, 10 wt% Ni was added as an austenite stabilizer to offset the martensite stabilizing effect of Co. In further studies of both alloys in Figure 2.10 comparing the isothermal hardnening response at 500°C, the Co-Ni steel demonstrated an accleration of secondary hardening by 2 to 3 orders of magnitude [**38**].

Another benefit of secondary hardening is that M_2C alloy carbides are thermodynamically more stable than cementite. Given sufficient tempering time, it then becomes

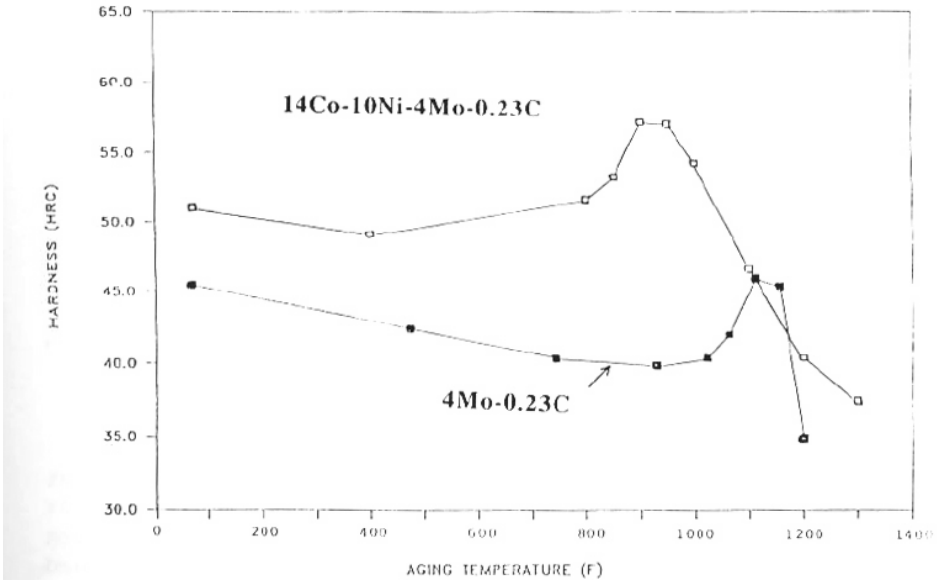

Figure 2.10. Hardness response after 1-hr temper at various temperatures for secondary hardening steels with and without 14Co-10Ni (wt%) [**38**]

possible to fully dissolve coarse, embrittling cementite particles and replace them with much finer and more stable alloy carbides. Work done by Speich on secondary hardening alloys demonstrated a doubling of the measured Charpy V-notch energy through complete dissolution of coarse cementite particles, as shown by the tempering-toughness trajectories in Figure 2.11 [**34**].

2.2.2.2. Grain refining dispersion. In order to resist grain coarsening during high temperature heat treatments, fine submicron secondary dispersions are often incorporated to pin grain boundaries. Small additions of Ti are frequently added to form Ti carbides and nitrides, as well as Ti oxides in powder-forged steels. With further gains in heat cleanliness reducing the role of large primary inclusions, however, these secondary grain pinning particles can become sites for microvoid nucleation and detrimentally impact toughness. Although typically strongly bonded to the surrounding matrix, secondary particles can

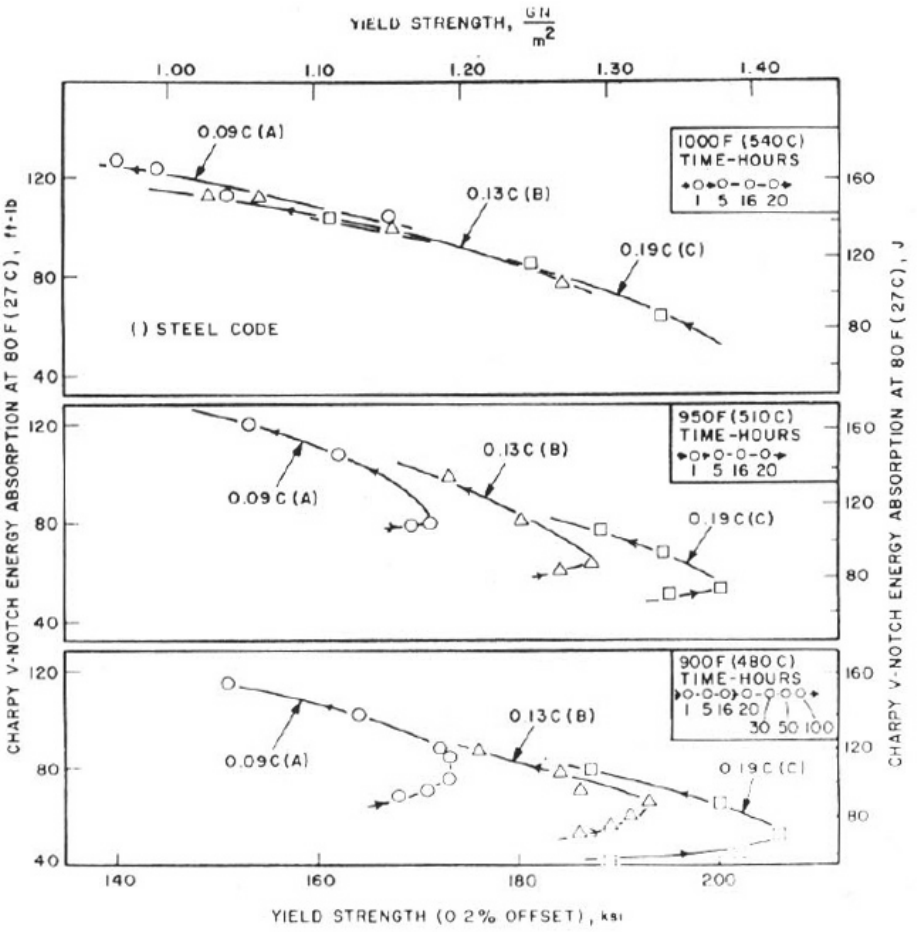

Figure 2.11. Effect of time and tempering temperature on Charpy v-notch energy in 10Ni-2Cr-1Mo-8Co steels (wt%) [**34**]

de-bond under high strains, subsequently forming microvoids. Localized shear occurs between microvoids and eventually leads to void coalescence and ductile fracture. To minimize the effect of this microvoiding behavior, the size and volume fraction of these particles likewise needs to be minimized. The grain pinning ability of secondary particles is also a function of the average particle size (d_{bar}) and particle volume fraction (f_v), with the maintained grain size proportional to the ratio of d_{bar}/f_v. Microvoid resistance, therefore, can be enhanced by reducing the volume fraction and size of secondary particles

without impairing their grain pinning ability by maintaining the proper size to volume fraction ratio. Additionally, grain pinning particles can be designed to have increased interfacial strength with the surrounding matrix to resist particle debonding.

2.2.2.3. Grain boundary chemistry. For ultra-high strength steels, a common factor limiting toughness is hydrogen embrittlement. Embrittlement due to hydrogen occurs through brittle decohesion of grain boundaries, a phenomena aggravated by impurity segregation [**39**]. The role of various impurity elements on grain boundary decohesion is directly related to their various effects on the work required to pull the boundary apart, specifically the Griffith work of brittle cleavage ($2\gamma_{int}$). This work of separation scales with the amount of solute at the boundary, Γ as shown in Equation 2.9:

$$2\gamma_{int} = (2\gamma_{int})_o - (\Delta g_b^o - \Delta g_s^o)\Gamma \tag{2.9}$$

where $2\gamma_{int})_o$ is the work of interfacial separation in the absence of impurities and Δg_b^o and Δg_s^o are the solute free energies of segregation to a boundary and to a free surface, respectively. The difference in free energies of a solute between a boundary and a free surface therefore reflects the embrittling potency of the specific impurity, with elements that have a lower energy at a free surface reducing the work of interfacial separation and causing brittleness. Besides H, common impurities such as P and S are two other such embrittling elements. To minimize the effect of these embrittling impurities, cleaner melt practices can be employed as well as incorporation of impurity gettering elements such as La that form stable compounds. Conversely, elements can be added that increase the work of interfacial separation by having lower free energy at boundaries compared to

free surfaces. Small additions of B are used for this purpose and work to enhance grain boundary cohesion to resist hydrogen embrittlement.

2.2.3. M_2C Carbide Precipitation Strengthening

Secondary hardening steels garner most of their strength through a fine dispersion of alloy carbides. The level of precipitation strengthening achieved is highly dependent on the interaction mechanism between a gliding dislocation and a precipitate. When precipitates are small and coherent with the surrounding matrix, dislocations are able to cut into and shear the precipitate given sufficient energy. Depending on the particular system, the resistance to particle shearing and the associated strengthening is due to several mechanisms, including coherency strains between precipitates and matrix (coherency strengthening), disruption of atomic ordering within precipitates (order strengthening) and additional surface area created from particle shearing (chemical strengthening). With all of these strengthening mechanisms, larger particles provide more resistance to shearing than smaller ones, resulting in the general strengthening behavior for particle shearing illustrated in Figure 2.12 [**40**]. With continued growth, precipitates become increasingly difficult to shear due to their larger size as well as loss of coherency with the surrounding matrix. Eventually particles become non-shearable and gliding dislocations must bow around the particles. The Orowan bypass regime than dominates where a gliding dislocation must bow completely around a particle until touching to form a contained loop, thereby allowing the remaining reconnected dislocation segment to continue gliding. Unlike particle shearing, Orowan bypass is driven by interparticle spacing where increasing the number of obstacles impedes dislocation motion. For a given particle volume fraction,

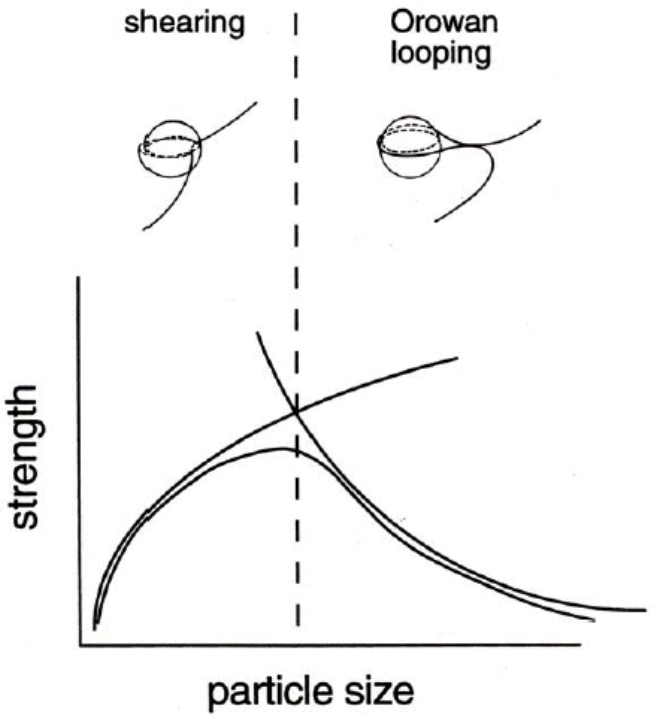

Figure 2.12. Schematic representation of precipitation strengthening as a function of particle size at constant volume fraction [**40**]

fewer larger precipitates are less efficient Orowan strengtheners than a larger number of smaller precipitates. This difference in the particle size dependency for strengthening through particle shearing and by particle bypass results in the maximum precipitation strengthening occurring at the transition between these two mechanisms, as also shown schematically in Figure 2.12. Optimization of precipitation strengthening thus requires the refinement of the utilized precipitate strengthening dispersion to a sufficiently fine size scale.

Ni-Co secondary hardening steels achieve very fine dispersions of alloy carbides in part due to their large Co alloying additions. As previously discussed, the added temper

resistance provided by the Co allows for increased heterogeneous nucleation sites for alloy carbides. By easing nucleation, the driving force for precipitation is increased resulting in finer precipitate dispersions. Additionally, the type of carbide utilized in precipitation also plays a role. Carbides capable of maintaining high coherency with BCC Fe are able to precipitate at a much finer size scale. These carbides correspond to close packed structures, namely the FCC MC carbide (M=Nb, Ta, Ti, V) and HCP M_2C carbide (M=Fe, Cr, Mo, W)[**41**]. Other alloy carbides such as M_6C, M_7C_3 and $M_{23}C_6$ are more thermodynamically stable but less coherent with BCC Fe, resulting in coarser particle dispersions of reduced strengthening efficiency, as well as reduced toughness due to incoherent precipitation on interfaces.

The precipitate dispersion of choice in Ni-Co secondary hardening steels is M_2C alloy carbides, where strong carbide forming elements (M) include Cr, Mo, V and W. Although metastable, M_2C carbides exhibit the strongest driving force for precipitation from martensite as well as display the aforementioned coherency with the BCC tempered martensite matrix, resulting in the ability to form exceedingly fine strengthening dispersions. The transition between particle shearing and particle bypass marking the point of maximum precipitation strengthening has been shown to occur at an M_2C precipitate diameters of 3 nm [**42**]. In order to reach dispersions on such a fine size scale, the thermodynamic driving force and kinetics for precipitation are controlled through alloying to compose mixed alloy carbides of $(Cr, Mo, V, W)_2C$. Due to the increased stability of Mo_2C over Cr_2C, Mo increases the precipitation driving force when substituted for Cr but is ultimately limited for solidification segregation considerations. Small additions of

V and W also greatly increase the driving force for M_2C precipitation, however both are also constrained, this time due to limited solubility in FCC Fe.

2.2.4. Current Alloys

A family of ultra-high strength, secondary-hardening carburizing steels were chosen as candidate materials to address high power density gear applications due to their optimized combination of strength and toughness. Using the previously discussed systems-based materials design approach, the first prototypes of these alloys were developed by John Wise at Northwestern University, successfully achieving surface hardness values of 69 HRC [**40**]. These prototypes were further developed and then commercialized as GearMet® C69 and C67 by QuesTek Innovations in Evanston, IL [**43**]. Designed for maximized surface hardness, this alloy has shown great promise in contact fatigue, outperforming M50 bearing steel in NTN ball-on-rod rolling contact fatigue (RCF) screening tests [**43**] as well as outperforming any material to date in recent re-circulating spur gear contact fatigue tests run at the NASA Glenn Research Center [**44**]. Again using the same materials design approach, QuesTek developed an additional secondary-hardening carburizing steel, this time designed for conventional gear steel surface hardness levels (58-61 HRC) but with a harder, yet flaw-resistant, core. Carburized to 61 HRC, this alloy is commercialized by QuesTek as GearMet C61 and due to its harder core, has successfully been implemented in racing applications at reduced gear widths with no impact on performance.

The optimized combination of strength and toughness exhibited by ultra-high strength secondary hardening steels has already been demonstrated to enhance contact fatigue resistance. Currently, however, the bending fatigue properties and resultant suitability

for high-power density gear applications, of these steels has not been assessed. Both GearMet C61 and C67 will be investigated in this study to both assess and optimize their bending fatigue performance.

Brian Tufts also expanded on Wise's alloys and developed a powder metallurgy variant designed for continuously variable transmission (CVT) applications [**45**]. Aimed at reducing cost, Tufts explored the possibility of a hybrid design consisting of a lower cost base steel serving as a substrate for high alloy steel employed at the surface to counteract highly localized stresses generated in CVT components. Materials formed through powder metallurgy (PM) have been also shown to exhibit greater high temperature coarsening resistance than their wrought counterparts when modified with stable-oxide forming elements that form grain pinning dispersions [**46**]. As a means of counteracting significant grain coarsening observed in C69 alloys, Tufts designed PM variants containing small Ti additions to getter increased oxygen levels intrinsic to powder processing. The resultant grain-pinning oxide dispersions could be explored as a means of providing grain coarsening resistance during heat treatments at elevated temperatures. The ensuing alloy was subsequently named PMC69-Ti and will be used in this work to study its potential increased resistance to grain coarsening.

2.3. BCC Cu Precipitation

One possible alternative to Co-assisted M_2C precipitation strengthening is the incorporation of BCC Cu precipitates. Strengthening with Cu precipitates is commonly used for achieving strength where carbon additions are limited due to weldability concerns,

such as in high strength, low alloy (HSLA) steels used in applications like shipbuilding, pressure vessels and pipelines [**47, 48, 49**].

2.3.1. Cu Precipitation Strengthening

BCC Cu precipitation strengthening in steels is due to so-called "modulus strengthening" as outlined by Russell and Brown [**50**], where the softer Cu particles have a lower shear modulus than the harder ferrite matrix. This modulus mismatch of the coherent Cu particles results in an "attractive" interaction with matrix slip dislocations, with the energy needed to "pull" the dislocation out of the sheared particle resulting in the observed increase in yield strength. The amount of strengthening provided by modulus strengthening is dependent on the critical angle at which a dislocation can cut softer precipitates, specifically the angle formed between the portion of dislocation in the matrix to the portion inside the particle being sheared. This angle is ultimately related to interparticle spacing and in turn particle radii and volume fraction (f). The maximum value of this strengthening increment occurs when the precipitate radius equals twice that of the dislocation core (r_o) and for Cu particles in a Fe matrix can be described by Equation 2.10:

$$\tau_{max} = 0.041 \frac{Gbf^{1/2}}{r_o} \tag{2.10}$$

As shown in Equation 2.10, the dependency of modulus strengthening on interparticle spacing results in the same general form as that of Orowan bypass of nonshearable particles where strength is proportional to the square root of precipitate volume fraction. This dependency is demonstrated in Figure 2.13 where the maximum hardening increment

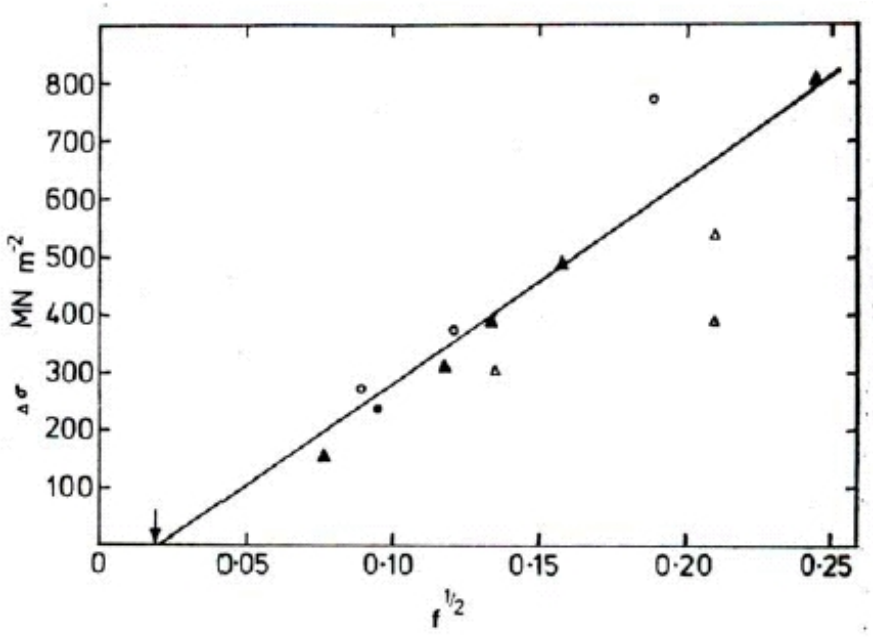

Figure 2.13. Strengthening increment due to Cu precipitation showing relationship to phase fraction to the one-half power [**50**]

from various studies is plotted vs. phase fraction to the one-half power [**50**]. Alternative strengthening mechanisms have been proposed [**51, 52**], however, recent work by Deschamps supports the Russell-Brown model for these systems [**53**].

Peak strengthening occurs as the metastable, spherical BCC Cu precipitates reach a critical diameter of 2.3 to 3.0 nm [**54**]. Upon further aging and growth they begin to lose coherency through an intermediate martensitic transformations to a 9R structure[**55, 56**], ultimately evolving into the incoherent rod-shaped morphology of the equilibrium FCC ϵ-phase [**57**]. BCC Cu precipitation is known to occur at Stage IV tempering temperatures (450-600°C) making it fully compatible with the heat-treating regime used in M_2C precipitation for secondary hardening as shown by Saha [**58**]. In his development of blast-resistant plate steel, carbon restrictions due to weldability considerations limited

the necessary M_2C phase fraction, and BCC Cu precipitation was successfully employed as an alternative strengthening agent to achieve targeted strength goals.

2.3.2. Heterogeneous Nucleation on Cu Particles

Besides providing a supplemental source of strength, Cu precipitation has additional attributes that can be potentially utilized to catalyze M_2C precipitation. Cu is known to precipitate out of solution very rapidly on grain boundaries and dislocations, restricting their mobility and resulting in temper resistance and grain refinement [**59, 60, 61, 62**]. Additionally, Cu precipitates themselves have been shown to act as heterogeneous nucleation sites for other phases, such as Laves phase in high Cr ferritic steels [**63, 64**], Ni_3(Ti,Al) intermetallics in maraging steels [**65**], and α-Fe in iron-based amorphous glass [**66, 67**], examples of which are shown in Figure 2.14. Much like the role of Co additions, therefore, Cu precipitation has been shown to provide increased locations for heterogeneous nucleation, both on additional dislocations provided through temper resistance and on the actual Cu particles themselves. Evidence of this behavior is also supported by the aforementioned work of Saha in Cu-bearing, low carbon steels [**58**]. Using 3-dimensional atom probe (3DAP) tomography, Saha demonstrated the ability of Cu precipitates to act as heterogeneous nucleation sites for Ni-rich austenite precipitates desired for transformation toughening. Additionally, targeted secondary hardening strength levels were successfully achieved from M_2C precipitation even in the absence of Co, suggesting a secondary hardening enhancement effect from the incorporation of Cu precipitation similar to that achieved through Co alloying additions.

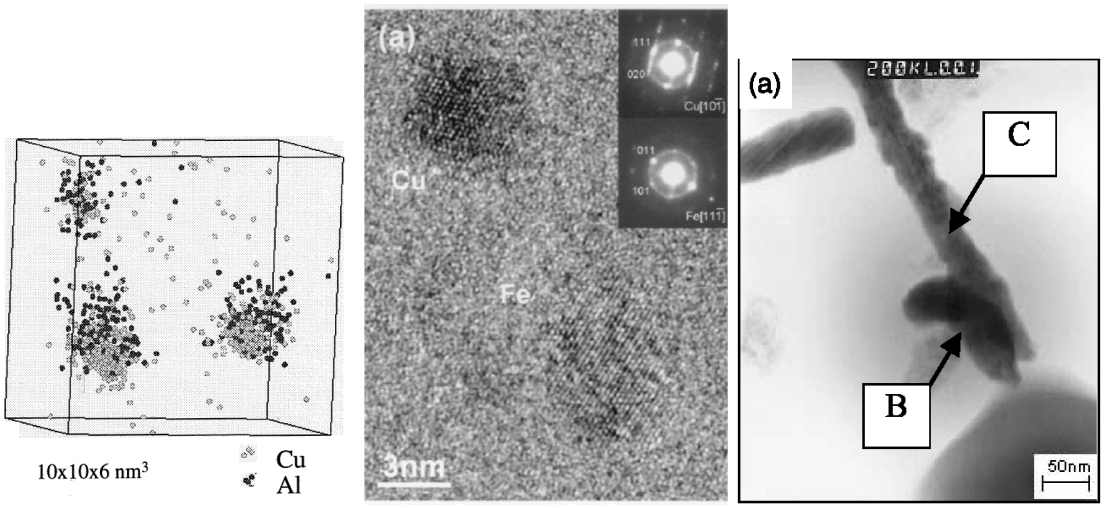

Figure 2.14. Examples of heterogeneous nucleation of various precipitates on Cu particles: a)3DAP reconstruction of Al-rich intermetallics in maraging steels [**65**], b)HREM and NBD patterns of α-Fe in amporphous glasses [**67**] and c) TEM micrograph of laves phase in stainless steel (B=Cu, C=laves phase) [**63**]

CHAPTER 3

Materials and Methods

3.1. Materials

3.1.1. GearMet® C61/C67

The C61 and C67 materials used for bending fatigue testing and performance optimization studies were produced by QuesTek Innovations with the compositions listed in Table 3.1. Both materials originally came from production-scale ingots cast using vacuum induction melting (VIM) followed by vacuum arc remelting (VAR). Small alloying additions were also included of La (0.01-0.03 wt%) to getter impurities, B (0.001-0.003 wt%) for grain boundary cohesion enhancement and Ti (0.01-0.03 wt%) to form grain pinning dispersions. Ingots were forged to 7.2" diameter bar and then machined down to a diameter of 5.25".

3.1.2. Premium Gear Steel

When assessing the bending fatigue performance of the C61/C67 alloys, it is important to be able to accurately compare results with previously acquired data from other alloys. To ensure proper data comparison, "control" gears remaining from previous GM Powertrain experiments were also tested to verify reproducibility of past results. The material was provided by GM Powertrain in the form of single tooth bending fatigue spur gears samples ready for testing. The spur gears were made from a premium gear steel and were conventionally heat treated consisting of gas carburization followed by a Stage I temper.

The roots of the spur gears were ground to remove inter-granular oxidation intrinsic to the gas carburization process. Because previous bending fatigue results are unpublished and material sensitive, alloy designation and composition were withheld.

3.1.3. C69M3B

C69M3B is an earlier prototype of the C69 alloy originally designed to avoid embrittling Sigma phase seen in previous prototype alloys. The composition of C69M3B is listed in Table 3.1. QuesTek Innovations formerly donated cast and wrought C69M3B material to Brian Tufts for rolling contact fatigue testing and tempering studies [**45**]. Remaining, untested RCF samples will be used in this work to study the effect of overaging heat treatments on carbide stability.

3.1.4. PM C69-Ti

PMC69-Ti will be used in this work to study potential grain coarsening resistance from Ti oxide dispersions. Table 3.1 lists the nominal composition. Two powder-forged bars 5/8" in diameter and 7" long were received from researcher Brian Tufts. Seven disks approximately 2 mm thick were sectioned from one of the bars using an abrasive cut-off saw and used as specimens for heat treatment and grain size analysis.

Table 3.1. Composition of investigated materials in weight percent.

Alloy	Co	Cr	Ni	Mo	W	V	Ti	C	Fe
C61	18.0	3.5	9.5	1.1	-	0.08	-	0.16	Bal.
C67	16.0	4.5	4.4	1.8	0.1	0.1	-	0.071	Bal.
C69M3B	19.6	4.9	2.6	2.1	-	0.1	-	0.071	Bal.
PM C69-Ti	19.6	4.9	2.6	2.1	-	0.1	0.05	0.071	Bal.

3.1.5. Prototype Cu-bearing alloys

Prototype heats for each of four experimental Cu-bearing alloy compositions were produced following processing steps typical of comparable commercial high strength gear steels. High purity 30-pound ingots were first cast using a combination of vacuum induction melting (VIM) and vacuum arc re-melting (VAR) at Special Metals Corporation in New Hartford, New York. Very small additions of La (0.03 wt.%) and Ti (0.01 wt.%) were also included to getter impurities and form grain pinning dispersions, respectively. The cast ingots were then shipped to the Technology Processing Center (TPC) of Special Metals (also known as Huntington Alloys) in Huntington, West Virginia to work the ingots into geometries more suitable for sample sectioning. The ingots were first homogenized at 1250°C for 12 hours, hot rolled to 0.75" thick plate and air-cooled to room temperature. Once cooled, the plates were normalized at 1050°C for 1 hour and once again air cooled to room temperature. A final annealing step at 700°C for 2 hours was performed to soften the rolled plate for ease of machining. Chemical analysis was obtained with x-ray fluorescence (XRF) and combustion infrared measurements. Designed and measured compositions of the four experimental alloys will be included and discussed in Chapters 6 and 7.

3.2. Experimental Procedures

3.2.1. Heat Treating

High temperature carburizing for experimental Cu-alloy samples was performed at Midwest Thermal-Vac using a single solutionizing/vacuum-carburizing step at 1000°C for 1.5 hours, followed by a cryogenic treatment in a liquid nitrogen bath to ensure complete

martensitic transformation. Two sample geometries were sent for carburization, the first of which were gear tooth-sized blocks to simulate the carburization of gear teeth and allow for evaluation of both carburized case and core microstructures. The second geometry consisted of thin slices 1.5 mm thick which were through-carburized and then used for carburized case carbon measurement. Carburized samples were then encapsulated in evacuated Pyrex tubes at Northwestern University to avoid oxidation during further heat treatment. Encapsulated samples were tempered in a box furnace at either 482°C or 510°C for various times. After tempering, samples were air cooled to room temperature.

Solutionizing studies of Cu-bearing experimental alloys were performed on carburized samples at Northwestern University using an upright Argon furnace. Samples were suspended in a steel wire basket within the furnace and solutionized at temperatures ranging from 1050-1200°C in an inert Argon atmosphere to prevent significant oxidation. Samples were then oil quenched, rinsed with water and cooled in liquid nitrogen to avoid retained austenite. A 1 hour Stage I temper at 200°C was then performed to eliminate autotempering effects after quenching.

3.2.2. Microhardness Testing

Microhardness testing was used to measure carburized case hardness gradients as well as generate 2-D hardness maps of spur gear tooth cross-sections. Prior to measurement, specimens were mounted in Bakelite and then ground and polished up to 1μm finish. Measurements were made using a Buehler Micromet II Micro Hardness Tester following ASTM standard E92 [**68**]. Indentions are made using a diamond Vickers pyramidal indenter with face angles of 136° applying a 500-gram load for 10 seconds. The resultant

indentation is then measured at 400× magnification, with the Vickers hardness (VHN) calculated according to Equation 3.1:

$$VHN = \frac{1.854P}{d^2} \tag{3.1}$$

where P is the applied load in kg and d is the average value of the two measured indent diagonals in μm. With the exception of microhardness maps, all hardness values are the average of at least three measured indents. For purpose of comparison, surface measurements were taken at a depth of 100μm for the carburized case hardness measurements and three equidistant interior points were selected for the core hardness measurements.

3.2.3. Microscopy

Light microscopy was employed to study microstructure of C61/C67 carburized spur gear teeth crossections and sectioned samples of carburized experimental Cu-bearing alloy specimens. Sectioned samples were first mounted in Bakelite and polished down to 1μm finish. A 5-10% Nital etchant (5-10% nitric acid in ethanol) was swabbed on the polished specimen surface for 10 second increments to etch the surface and reveal microstructural components. Imaging was done using a Nikon EPIPHOT-TME microscope at various magnifications.

Light microscopy was also employed to measure prior austenite grain size for grain coarsening resistance studies of PMC69-Ti. Conventional chemical etchant methods to reveal grain boundaries are often unsuccessful in high purity materials, due to the lack of impurity segregation and associated localized chemical attack at grain boundaries. An alternative method utilizing oxidation was subsequently used to delineate the prior

austenite grain boundaries of heat-treated PMC69-Ti samples. The oxidation method, or oxygen etching, involves slightly oxidizing the sample surface while at a elevated solutionizing temperatures. At elevated temperatures (below 1200°C), grain boundary diffusivity dominates bulk diffusivity, thereby causing oxide to first form at the grain boundaries. After quenching, this oxide can then be observed and used to distinguish prior austenite grain boundaries. For this study, an upright argon furnace was used for the solutionizing heat treatments. Although designed to operate under an inert atmosphere, trace amounts of oxygen are inherently present in the system, a problem that lends itself quite nicely to oxygen etching. Heat treatments were done for one hour at 50°C intervals between 900°C and 1200°C and then terminated by an oil quench. The samples were then slightly polished to varying degrees using 1μm diamond polish at 2-5 second intervals. An etchant of 15% HCL and 85% ethyl alcohol was swabbed at 10-second intervals to provide increased contrast. Both polishing and etching were done to varying degrees depending on sample condition. The linear intercept method was used to measure grain size, as outlined by ASTM E112-96 [**69**].

3.2.4. Single Tooth Bending Fatigue Testing

3.2.4.1. Gear machining. 1.25" thick gear blanks were first cut from the 5.25" diameter C61 and C67 bar stock at Roll-A-Matic Inc. in Walled Lake, MI. Spur gears were then cut from the blanks using a hobbing procedure, where the cutting tool, or hob, progressively forms the gear teeth through a series of cuts as it is fed across the gear blank. Table 3.2 gives relevant dimensions of the spur gear geometry.

Table 3.2. Selected spur gear geometry values for single tooth bending fatigue specimens

Number of teeth	24
Module	4.500
Diametral Pitch	5.6444
Pressure Angle	20.0
Pitch Diameter	108.000
Major Diameter	118.300
Minor Diameter	98.150
Circular Tooth Thickness	7.483

3.2.4.2. Heat treatment. Heat treatment of spur gear specimens was completed at Midwest Thermal-Vac consisting of a single solutionizing/vacuum-carburizing step, cryogenic treatment in a liquid nitrogen bath and vacuum tempering. Three batches of C61 spur gears were solutionized/carburized at either 950, 1000 or 1050°C and tempered at 500°C for 1.5 hours, while one batch of C67 gears was solutionized/carburized at 1050°C and tempered at 500°C for 52 hours. Post heat treatment grinding of gear tooth sides to remove allotted excess material of up to 0.3mm (0.12") was employed to counteract any distortion and/or cracking caused by the heat treatment and subsequent quenching as well as remove potentially over-carburized material at gear teeth corners. Due to the observed lack of distortion observed after heat treating C61/C67 spur gears, the final batch of C61 spur gears was ground to the final face width prior to heat treatment with grinding in the hardened post-heat treated state omitted. For this batch of C61 spur gears, over-carburization of gear tooth corners was achieved by applying "stop-off paint" to the gear sides prior to heat treatment. Stop-off paint acts as a barrier to carbon diffusion and allows for an even carburized case layer achieved by preventing excess carbon to diffuse in from the gear sides.

3.2.4.3. Shot peening. The shot peening process used was a standard dual-peening process employed by GM Powertrain and performed by the Metal Improvement Company at their Romulus, MI facility. Dual peening consists first of a high-intensity application of peening media to maximize and deepen compressive residual stress at the target surface, followed by a less-intense saturation of softer media intended to smooth out asperities and raise the compressive stress at the near surface. For the C61/C67 spur gears, the first peening operation consisted of high-intensity application of hardened steel (60-64 HRC) cut-wire shot media conditioned to remove sharp edges. The second peening operation was performed using a glass bead media. Detailed shot peening parameters, including shot size, intensity and saturation levels are proprietary.

3.2.4.4. Isotropic superfinishing. To increase the surface finish of shot peened spur gears, isotropic superfinishing (ISF) was employed. The ISF process consists of chemically accelerated vibratory polishing where parts are placed in a vibrating bin containing a slurry of abrasive media and chemical etchants. Surface roughness is gradually reduced as the chemical etchant attacks surface asperities that are subsequently eroded by the abrasive media. The resultant surface created by the ISF process is non-directional, or isotropic, and can approach average surface roughness values (R_a) down to a mirror-like finish of R_a <0.15 μm (4-6 μ-in) [**32**]. This process was initially developed by REM Research Group, Inc and all preliminary alloy reactivity studies as well as final polishing of spur gear specimens was conducted at their headquarters in Brenham, TX.

3.2.4.5. Testing. Stress-controlled single tooth bending fatigue testing was done on a 100kN MTS test frame outfitted with a top-loading actuator as well as a fixture used to support the spur gear test specimens . As illustrated in Figure 3.1, single tooth bending

fatigue testing consists of the use of two anvils. An upper anvil connected to the top-loading actuator through a 100kN load cell applies the cyclical load to the end of the tested tooth. A lower stationary anvil located on the attached fixture braces a support, or anchor, tooth to prevent the spur gear from rotating during loading. A support dowel aligns the spur gear with the stationary figure as well as providing additional support. The cantilever effect created by the offset upper anvil concentrates the generated tensile stress at the root notch of the tested tooth, corresponding to the location of failure. The anchor tooth is fully supported by the stationary lower anvil and is assumed to experience negligible stress.

A cyclical compressive load is applied at 40 Hz maintaining an R-value, or ratio of minimum to maximum applied load, of 0.01 through software amplitude control. Tests were run until either the selected endurance limit of 10 million cycles was achieved or until the total upper anvil displacement exceeded 2mm, at which point the tested gear tooth was deemed failed due to significant macroscopic cracking or often total gear tooth fracture. Ultimate bending strength testing was also performed with the same experimental setup with a linearly increasing load applied at a rate of 1.7 kN/sec. Increasing loads were applied until failure, chosen as the point where the upper anvil displacement rate rapidly exceeded 0.4mm/sec due to cracking of the loaded gear tooth. Pressure sensitive tape was place between the upper loading anvil and test tooth to ensure even loading along the full width of the gear tooth.

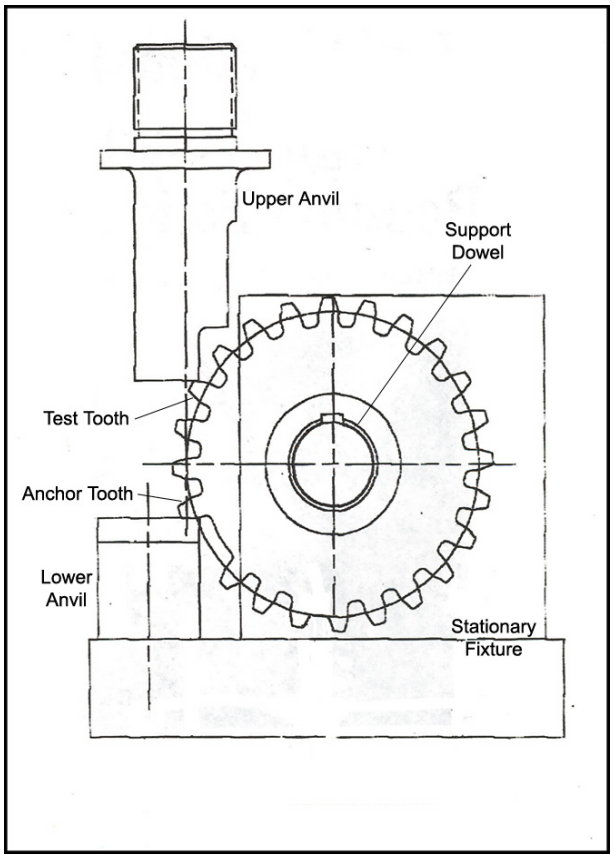

Figure 3.1. Schematic of single tooth bending fatigue test (courtesy of James Bishar - GM Powertrain)

3.2.5. Interferometry

Light interferometry was used to study surface topography of C61 and C67 spur gear teeth. A WYKO interferometer set in vertical scanning mode was utilized at various magnifications. Corrections for specimen tilt and curvature were included when necessary. Surface roughness was calculated as expressed by the average surface roughness (R_a), root mean square (RMS) roughness (R_q), maximum height of the measured profile (R_t) and average maximum height of the profile (R_z).

3.2.6. Electron Microscopy

Scanning electron microscopy (SEM) was employed to study surfaces of the fracture surface of failed spur gear teeth as well as the topography and features of various spur gear surface conditions. A Hitachi S-3500 microscope with tungsten hairpin filament was used at Northwestern University with a 20kV electron beam while the specimen chamber maintained a vacuum level of 10^{-4} torr. A secondary electron (SE) detector was used to image topographic features while a backscatter electron (BSE) detector was used to achieve chemical contrast of inclusion phases located on fracture surfaces. Qualitative chemical analysis and mapping of inclusion phases was performed using a PGT energy dispersive x-ray (EDS) analyzer.

3.2.7. Dilatometry

Dilatometry is the method of observing phase transformation during heating and cooling by measuring the associated volume change. For this work, an MMC quenching dilatometer was used for hardenability studies measuring the martensite start temperature (M_S) of C61/C67 at different quench rates. Cylindrical samples 1mm long and 3mm in diameter were prepared using electro-discharge machining (EDM). Samples are heated using an induction furnace at 1.6°C/sec up to a solutionizing temperature of 1000°C, where the samples were held for 10 minutes. Quenching at various cooling rates was then achieved through the use of helium jets. Specimen temperature is measured by a Pt / Pt-10% Rh thermocouple spot-welded onto the sample. The change in specimen length caused by volume change due to phase transformations and thermal expansion is measured by a LVDT transducer connected to quartz platens touching both ends of the sample. To

prevent interference from oxidation, the sample chamber is maintained at vacuum levels $<10^{-4}$ torr.

3.2.8. Rolling Contact Fatigue Testing

Rolling contact fatigue (RCF) testing was performed on C69M3B specimens to study effects of overaging on carbide stability. Tests were performed using an NTN 3-ball-on-rod dual-head rolling contact fatigue tester as outlined by Glover [**70**]. Specimens consist of 3/8" diameter rods radially loaded by three 1/2" diameter test balls. The load is supplied by compression springs through tapered bearing cups, as shown in Figure 3.2. A bronze retainer equally spaces the balls and sits within the tapered cups. Rolling contact is generated as a spindle rotates the sample at 3600 RPM, with the three loaded balls causing 2.389 test track loading cycles per revolution of the cylindrical sample. The radial load between one ball and the cylindrical specimen is 1084 N (244 lb), calculations for which are also shown in Figure 3.2.

During testing, the system is lubricated by Exxon Turbo Oil 2380 applied at rate of 4 drops per minute. Tests are run until pitting-induced vibration triggers a magnetically attached vibration sensor that stops the test. An attached timer accurate up to 0.1 hours recorded the duration of each test run, with the total cycles to failure calculated by Equation 3.2:

$$\#Hours = \frac{60\ min}{hr} \times \frac{3600\ rev}{min} \times \frac{2.389\ cycles}{rev} = 0.516 \frac{million\ cycles}{hour} \qquad (3.2)$$

Up to eight tests per sample may be run by shifting the cylindrical sample up and down within the spindle grip, ensuring a minimum distance of 1 mm between test wear tracks.

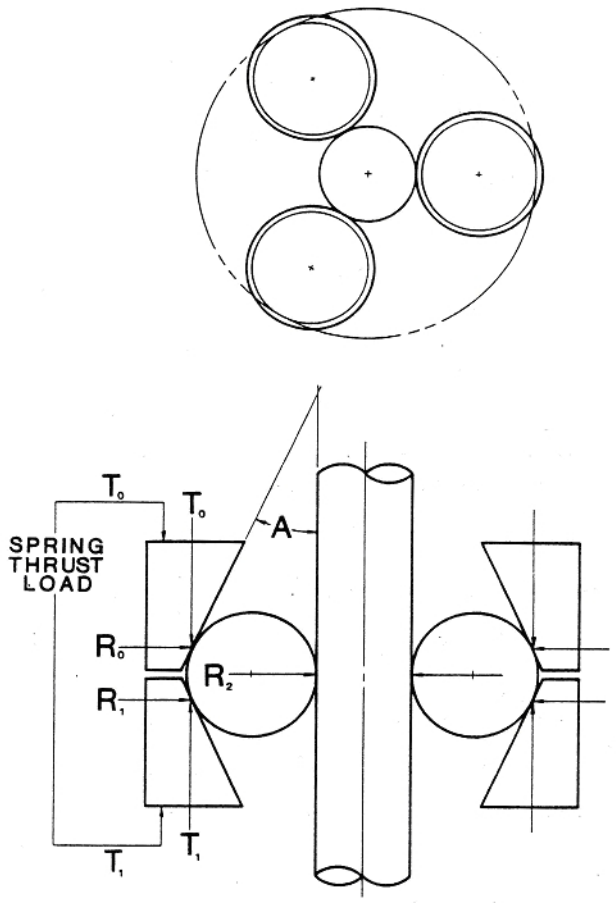

	English Units	ISO Units
A = cup angle	25.083 deg	25.083 deg
$T_0 = T_1$ = spring thrust load	57 lb	253.65 N
R_0 = radial load between upper cup and ball		
$R_0 = \frac{T_0}{\tan A}$	121.79 lb	541.97 N
R_1 = radial load between lower cup and ball		
$R_1 = \frac{T_1}{\tan A}$	121.79 lb	541.97 N
R_2 = radial load between one ball and specimen		
$R_2 = R_0 + R_1$	243.59 lb	1083.98 N

Figure 3.2. Schematic of NTN 3 ball-on-rod rolling contact fatigue test including load calculations [**70**]

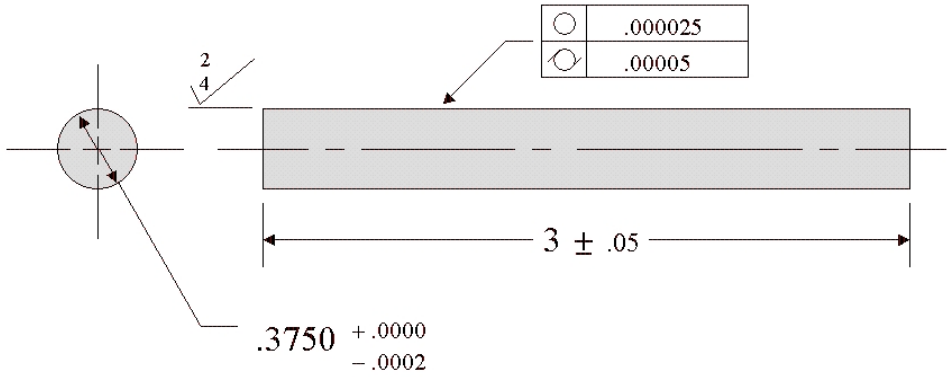

Figure 3.3. Schematic of NTN 3 ball-on-rod rolling contact fatigue test specimen. All dimensions in mm.

C69M3B RCF cylindrical samples were previously heat treated and centerless-ground to the dimensions shown in Figure 3.3 by Brian Tufts [**45**]. Two heat treatments were selected. A one hour temper at 550°C was used to achieve peak hardness, and a second temper of 5 hours at 550°C was used to overage the material and drop the hardness by 1-2 Rockwell C, as previously shown by Tufts [**45**]. Heat treatments were performed at Northwestern University in a box furnace with samples encapsulated in evacuated pyrex tubes. Because NTN tests are extremely sensitive to surface finish, tantalum foil was included inside the pyrex tube to getter remnant oxygen and avoid any surface oxidation. Test balls and tapered bearing cups were from the NTN Company and made from SAE 52100 bearing steel. Both test balls and bearing cups were replaced every three test iterations.

3.2.9. X-Ray Diffraction

Residual stress and retained austenite profiles of C61 and C67 spur gear roots were measured using x-ray diffraction by Proto Manufacturing Ltd. In Ontario, Canada. Measurements were done using a CrK_α radiation source. Residual stress measurements were done using the peak shift of {211} crystallographic reflections adhering to standard SAE J784a [**71**]. The x-ray elastic constant used in stress calculations was assumed to be 168.9 MPa (24,500 ksi), a typical value for high strength gear steels. Retained austenite measurements were done using a 4-peak collection method taking into account possible convolution of M_2C carbide peaks and adhering to the standards SAE SP-453 [**72**] and ASTM E975-84 [**73**].

X-ray diffraction was also used at Northwestern University to detect the presence of retained austenite in carburized Cu-bearing alloy samples. A Scintag diffractometer equipped with CuK_α radiation source was used for wide angle scans with a 2Θ range of 40-90°. Qualitative assessments of austenite content were then made by examining for the presence of {220} reflections.

3.2.10. 3-D Local Electrode Atom Probe (LEAP) Tomography

In order to analyze the microstructure of these nanoscale precipitates, 3-dimensional atom probe (3DAP) tomography will be employed. Atom probe tomography utilizes a combination of time-of-flight mass spectrometry and point-projection microscopy to chemically identify and locate individual atoms within a bulk sample. As shown schematically in Figure 3.4, atom probe specimens are needles or tips sharpened to <100nm in diameter.

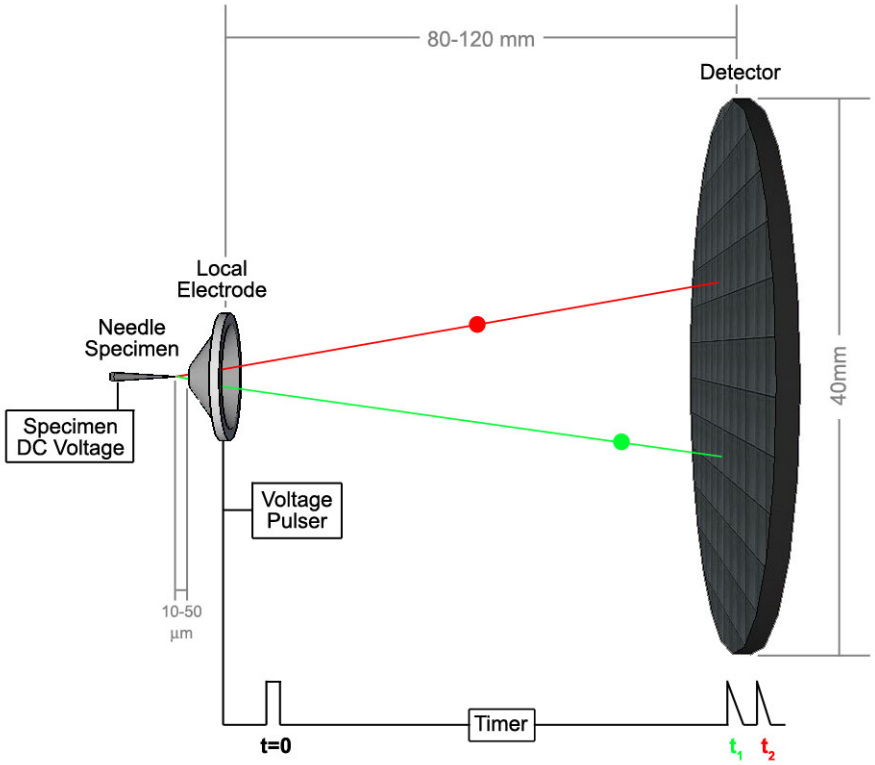

Figure 3.4. Schematic representation of 3-dimensional local electrode atom probe (LEAP^{TM})

A positive voltage pulse is applied to the sharpened tip, causing field evaporation of positively charged metal ions that are subsequently drawn to a detector plate along a voltage differential. The chemical identity of each ion is revealed through the mass-to-charge ratio as determined by the time-of-flight between the applied pulse and point of detection. The x and y coordinate of each ion within the sample is then determined from the point of impact on the 2-D detector, and the depth or z coordinate is determined by the sequence number or absolute time of impact.

For this research, a new generation atom probe will be employed called a local electrode atom probe (LEAP^{TM}). The LEAP improves upon conventional 3DAP by generating the

electric field through a localized extraction electrode, also illustrated in Figure 3.4. Due to the close proximity of the electrode to the specimen tip, the voltage requirements for field evaporation are much smaller and can be pulsed at much faster frequencies (2×10^5 Hz), significantly raising the data collection rate. The electrode also serves to shield evaporated ions from the effect of the cycling electric field near the specimen tip, providing for increased mass resolution (greater than 1/500 full width at half maximum (FWHM)) at large field-of-views up to 40°. The practical result of these improvements is the ability to reconstruct significant volumes of material ($>10^6$ nm^3) in a matter of hours instead of days, making the LEAP comparable to other conventional forms of microscopy used to study the nanoscale [**74**]. The LEAP tomograph at the Northwestern University Center for Atom Probe Tomography (NUCAPT) will be used to study the nanoscale dispersions of both BCC Cu and M_2C carbide in order to recalibrate alloy design models with updated microstructural parameters.

Atom probe samples were created by first sectioning "posts" 300mm×300mm in cross-section and approximately 25mm long directly from the surface of carburized and tempered samples using a precision saw. A two-step electropolishing procedure was then used to sharpen the posts into tips. Initial polishing was done with a 10% perchloric acid in butoxyethanol solution at room temperature applying a DC voltage of 15-20V. Final polishing and necking was done in a second, weaker solution of 2% perchloric acid in butoxyethanol at a reduced DC voltage of 8-12V, with the final specimen achieving a tip radius <100nm.

Atom probe tomography was performed using a LEAP^{TM} 3000 tomograph manufactured by Imago Scientific Instruments Corporation in Madison, WI. Analyses were

performed after cooling specimens to a temperature of 100 Kelvin (-173°C) to minimize atomic motion while under ultra-high vacuum (residual pressure $<10^{-8}$ Pa). Field evaporation of atoms from the specimen tip was achieved through applying high voltage pulses at a frequency of 200kHz. Voltage is applied to the specimen tip through a standing DC voltage with voltage pulses applied through the extraction electrode at a pulse-to-DC voltage ratio of 15%. The voltage levels required for field evaporation is dependent on the radius of curvature of each specimen tip, with the standing DC voltage ranging from 500V for very sharp tips (diameter<10nm) to 15,000V for larger tips (˜100nm diameter). Steady field evaporation rates of 400-10000 atoms/second were maintained through software-controlled manipulation of the voltage levels, with applied voltage steadily increased to account for tip blunting with continued specimen evaporation.

Reconstruction and quantitative analysis of collected data sets was performed with the IVAS software from Imago Scientific Instruments. The volume of the analyzed material (v_{total}) was calculated from the total number of ions in the reconstruction (n) using Equation 3.3:

$$v_{total} = \frac{n\Omega}{f} \tag{3.3}$$

where the average atomic volume,Ω, is set equal to that of BCC Fe (1.18×10^{-2} nm^3) and the overall detection and reconstruction efficiency (f) is estimated at 0.6. Standard deviations (σ) of measured compositions through the LEAP analysis were calculated using Equation 3.4 [**75**]:

$$\sigma = \sqrt{\frac{c(1-c)}{n}} \tag{3.4}$$

where c is the measured composition of the particular element. To quantify the two precipitate dispersions, two tools were used in the IVAS software: isoconcentration surfaces and 1-dimensional (1D) composition profiles. Isoconcentration surfaces are essentially 3-dimensional compositional contour maps, where a threshold composition is selected for one or a combination of elements and a surface is drawn connecting the selected concentration[**75**]. 1D compositional profiles were generated through a cylindrical selection volume 1 nm in diameter at various lengths. Composition profiles are generated by counting the number and type of each atom contained within the cylinder over increments 0.1nm thick.

3.3. Computational Tools

3.3.1. Thermo-Calc^{TM}

Two software programs were utilized in the computational design of these alloys: Thermo-Calc^{TM} and Computational Materials Dynamics, or CMD^{TM}. Thermo-Calc is a thermodynamic database and calculation package developed by the Royal Institute of Technology in Stockholm, Sweden (KTH) [**76**]. In order to extrapolate to higher order systems, Thermo-Calc uses sublattice models [**77, 78**] to describe existing experimental data from mostly binary and ternary systems. Equilibrium and metastable equilibrium thermodynamic values are then calculated as a function of chemical composition, temperature and pressure by solving for the state of lowest Gibbs free energy. Two databases were utilized for these thermodynamic calculations. The solution (SSOL) database was created by the Scientific Group Thermodata Europe (SGTE), a consortium of various European research centers, and consists of free energy data for over 150 binary, 70 ternary and 20 higher

order systems. The SSOL database was used for all thermodynamic calculations except for martensite start temperature (M_S) calculations, where the high temperature data used to compile the SSOL database doesn't accurately describe the lower temperature thermodynamics. M_S calculations were done using the MART5 database, an updated version of the MART4 database developed by Ghosh and Olson [**79**] that includes modified low temperature parameters for Fe-based FCC and BCC phases for more accurate M_S predictions.

3.3.2. Computational Materials Dynamics (CMD^{TM})

The other software program used, CMD^{TM}, was developed by QuesTek Innovations LLC in Evanston, IL [**80**] and consists of a collection of mechanistic models linked to Thermo-Calc to calculate relevant thermodynamic parameters as well as to the companion DICTRA (Diffusion Controlled TRAnsformation) program to calculate applicable kinetic mobility parameters [**81**]. Mechanistic model calculations that were utilized in CMD include the Ni-Co secondary hardening steel strength model, martensite start temperature model and Scheil microsegregation model, all of which are discussed further in Chapter 6.

CHAPTER 4

Bending Fatigue Performance Optimization

In order to assess the bending fatigue performance of secondary hardening ultra-hard steels, single tooth bending fatigue tests on GearMet C61 and C67 spur gear were completed at the GM Powertrain Gear Center in Wixom, MI. The use of standard GM performance validation techniques is important as it allows for comparison with existing unpublished data as well as incorporates relevant gear manufacturing processes that ultimately affect material performance. Additionally, the utilization of such accepted practices to demonstrate the performance of perceived "nontraditional" gear steels provides a visible and practical example to industry on the merits of such materials and the design methodology from which they were born. Bending fatigue testing and analysis consisted of two primary stages. The first stage involved addressing processing factors identified as directly causing bending fatigue failures. This process optimization was carried out through targeted analysis and remedy of fatigue inducing defects instead of empirical performance optimization achieved by surveying a wide range of processing variables. Once optimized, the second stage of testing assessed prevailing factors limiting performance to provide a quantitative estimate of "best practice" bending fatigue resistance of these materials as well as provide direction for ongoing research and development.

4.1. Process Optimization

4.1.1. Effect of Surface Condition

Due to the highly localized nature of the generated bending stresses at the surface of gear tooth notches, the most pertinent processing parameters for bending fatigue are often the various surface treatments performed on carburized gear teeth. In order to assess the impact of these surface treatments on C61, four surface conditions were first investigated: as heat-treated (AHT), ground (GR), shot-peened (SP) and a combination ground and shot peened (GR+SP). Post heat treatment grinding of gear root notches is commonly employed for gears carburized using conventional gas carburization methods where significant intergranular and surface oxidation can occur. Shot peening is employed in certain applications to increase resistance to fatigue crack initiation and propagation through creation of compressive residual stress.

Applied stress versus cycles to failure plots, or S-N diagrams, are shown in Figure 4.1 comparing the measured single tooth bending performance for the four surface conditions of C61 spur gear specimens. For comparison, curves were generated using a least squares exponential fit of the form shown in Equation 4.1:

$$\sigma = a\ exp^{(-(log\ n))} + b \tag{4.1}$$

where σ is the maximum bending stress experienced in the gear tooth root notch for the particular applied bending load, n the number of cycles to failure and a and b fitting parameters governing the shape and endurance limit for each curve, respectively. Hollow symbols with adjoining arrows indicate runs achieving the designated endurance limit of

10 million cycles and thus stopped prior to failure. Because these interrupted test runs do not represent actual cycles to failure they were not included when fitting S-N curves.

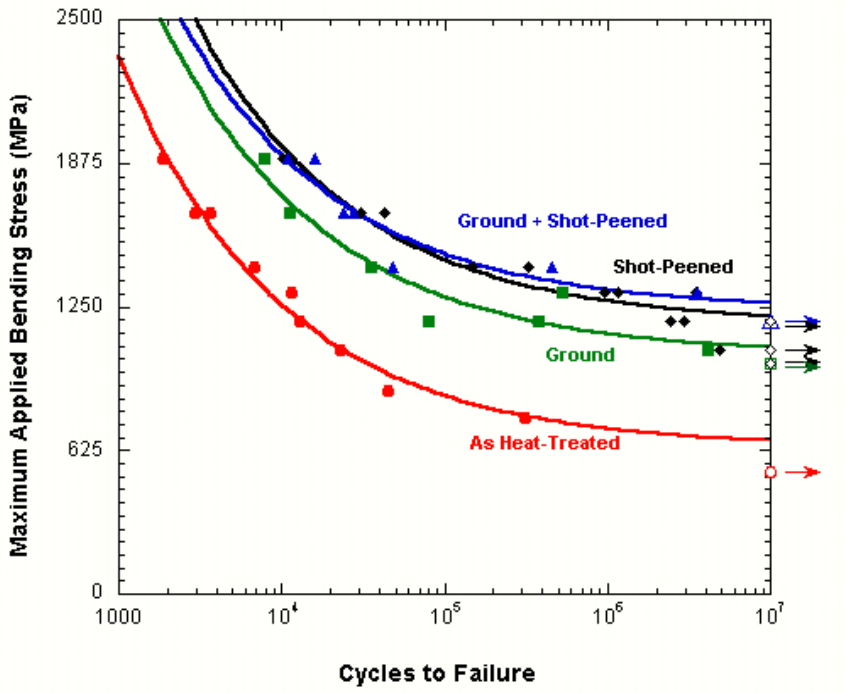

Figure 4.1. S-N curves for four different surface conditions of C61 spur gears

Surface condition was seen to have a significant effect on the single tooth bending fatigue resistance of C61, with the as heat-treated surface resulting in the poorest performance. Figure 4.2 shows SEM images of the four surfaces as well as their RMS roughness (R_q) values as measured by light interferometry. The as heat-treated surface exhibits significant grooving or etching along the prior austenite grain boundaries, with pronounced grooving occurring where grain boundaries coincide with remnant machining grooves. This grooving phenomena is believed to be caused by the high temperature vacuum carburizing process used for the C61 spur gears, where temperatures are elevated to sufficient levels to cause enhanced diffusion at grain boundaries. Additionally, pitting can also be

observed along the grain boundary grooves of the AHT surface. Early in the carburization process, transient carbides of similar spherical dimension are observed to form at the surface during high carbon flux boost cycles, and it is believed these pits are left behind as the carbides eventually dissipate during subsequent low carbon flux diffuse carburization cycles. Light interferometry of untested gear teeth root notches measured the depth of these grooves and pits to exceed 1 μm, at which point the groove width diminished below the resolution of the interferometer. The poor fatigue resistance of the AHT C61 spur gears can be directly attributed to these grooved prior austenite grain boundaries that effectively act as pre-initiated fatigue cracks. SEM analysis of gear teeth fracture surface demonstrate the detrimental effect of grain boundary grooving, where fatigue initiation and final fracture propagation path closely coinciding with grooved grain boundaries on the specimen surface, where in some instances entire grains were observed to decohere upon final rupture.

Grinding the gear roots removed the grain boundary grooving, resulting in a ridged topography of reduced surface roughness, as shown in Figure 4.2b. Removing the etched surface layer resulted in significant improvement in bending fatigue performance, as shown in Figure 4.1. Comparing the fitting parameter b, which defines the improvement in endurance limit, grinding the gear roots resulted in over a 60% improvement in bending fatigue performance compared to the AHT surface (1040 vs. 640 MPa). The process of grinding was also shown to impart approximately 100 MPa of beneficial compressive residual stress to the immediate surface, as shown in Figure 4.3.

Bending fatigue failures were still seen to originate at the surface, this time associated with the grinding ridges that run parallel to the gear tooth root. Additionally, in a

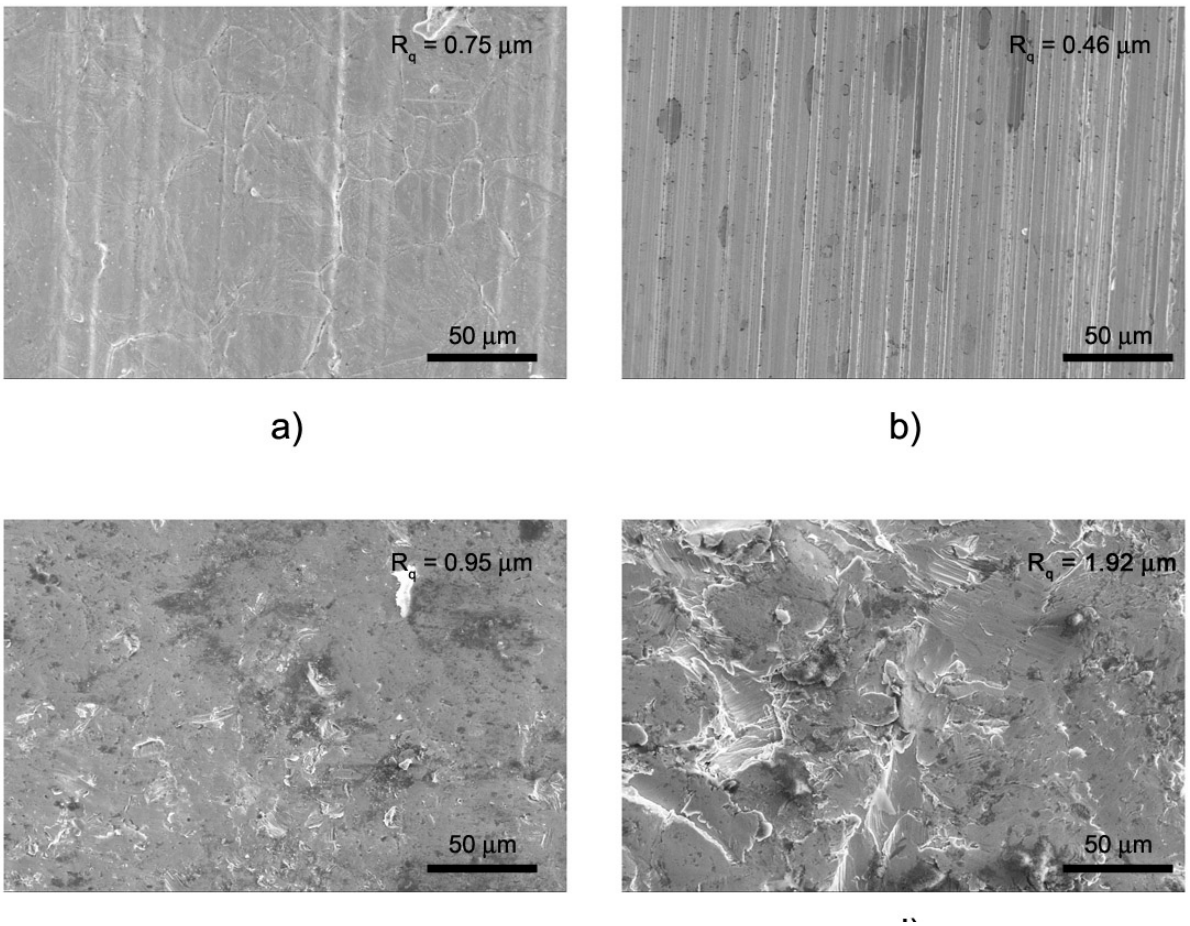

Figure 4.2. SEM micrographs and RMS (R_q) surface roughness measurements of C61 spur gear surface treatments: a) As heat treated, b) Ground, c) Shot peened and d) Ground and shot peened

portion of gear teeth the grinding of gear roots was observed to be incomplete and regions of the AHT grooved topography remained, an example of which is shown in Figure 4.4. In several instances, fatigue failures initiated at the more detrimental grooved grained boundary locations, even when occurring ˜200 - 300 μm away from the point of maximum applied stress where most failures occurred, such as the typical failure location shown by the fracture surface in Figure 4.4.

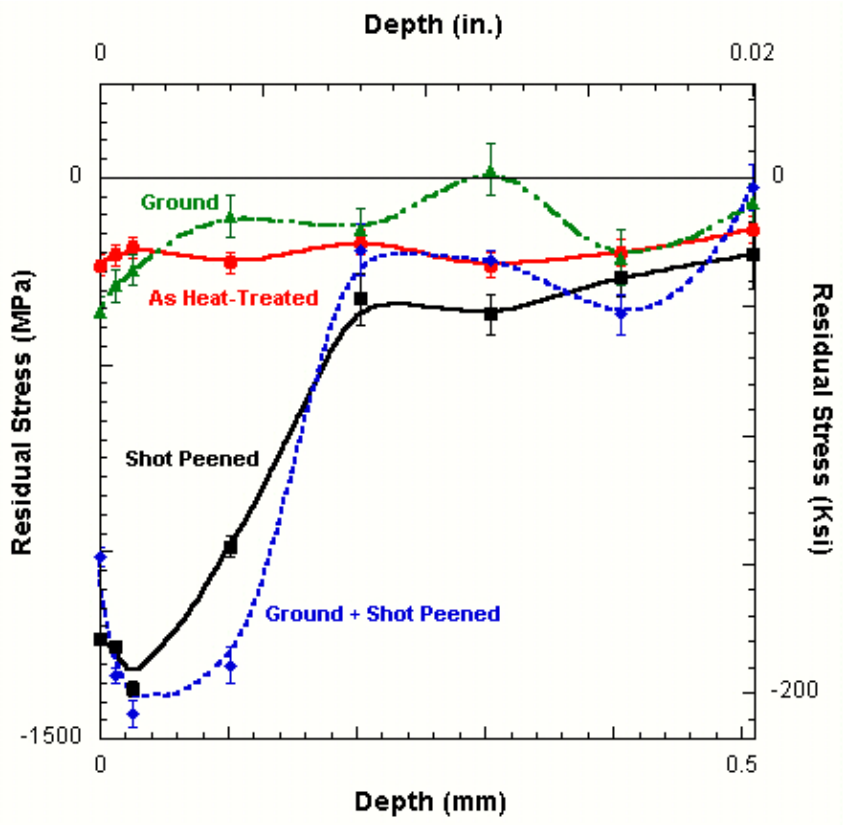

Figure 4.3. Measured residual stress profiles for C61 surface treatments

Shot peening was seen to further improve the bending fatigue performance, raising the approximate endurance limit (as defined by the b fitting parameter) by around 10%. This can largely be attributed to the large amounts (~1000 MPa) of compressive residual stress imparted to the surface, as shown in Figure 4.3. Even though the shot peening process increased the overall surface roughness, this roughening was compressive in nature and essentially "smoothed out" and eliminated the detrimental grain boundary grooving. Additionally, even though the SP surface has approximately twice the overall surface roughness of the GR surface, it is nondirectional and subsequently less detrimental than

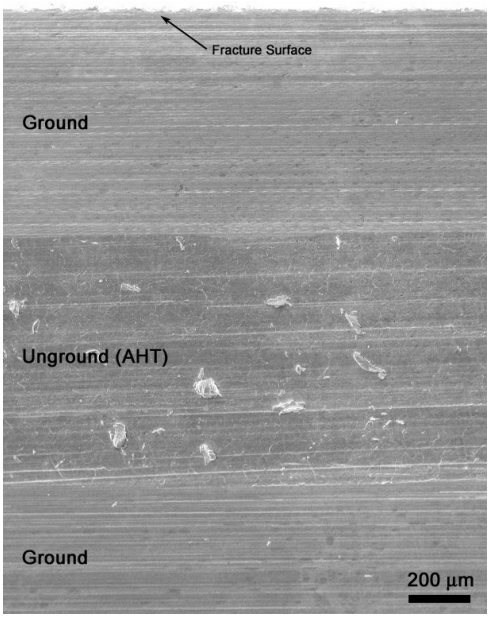

Figure 4.4. SEM micrograph showing region of grooved topography remaining in C61 gear roots after grinding

the grinding ridges that, by nature of the grinding process, are oriented transverse to the applied load in the direction of maximum impact on fatigue.

As shown in Figure 4.1, the effect of grinding before shot peening results in negligible difference when compared with the SP-only S-N curve. This further demonstrates the ability of shot peening to fully eradicate grain boundary grooving as well as the importance of nondirectionality over overall surface roughness. The roughness of the GR+SP surface is significantly elevated to an RMS value of 1.92 μm, corresponding to an increased experienced shot peening intensity, as also suggested by its residual stress profile in Figure 4.3 where the surface stress is slightly lowered but the total depth increased. This may be due to a number of factors such as reduced surface hardness from material removal via grinding, different interaction between the shot peening media and the relative topographies of the AHT and GR surfaces and process variability of the shot peening process as

performed by the actual shot peening vendor, which will be further discussed in Section 4.2.1.

4.1.2. Corner Over-carburization

In the case of shot-peened gears, sub-surface initiation was also seen at high cycle fatigue failures approaching the endurance limit. Figure 4.5 shows a typical sub-surface initiation site where fatigue was observed to initially originate from a flat, cleavage surface and then propagate radially outward creating a smooth, transgranular area. These features, or "fisheyes" as they are commonly called, were always located roughly 200-300 μm below the surface and always in the corner. Such subsurface initiation sites and corresponding "fisheye" morphology have been observed in other carburized gear steels to nucleate on inclusions [**82, 83, 84**]. The flat, cleavage planes centered in the "fisheye" fractures were also observed in non-subsurface initiated fractures, predominately in the same corner region where the fisheye features were observed.

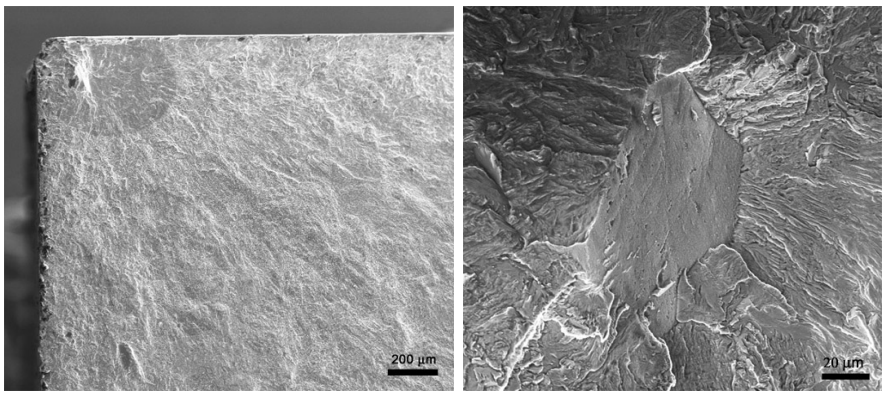

(a) (b)

Figure 4.5. SEM micrographs of subsurface fatigue initiation in shot peened Batch A C61 spur gears showing a)"fisheye" fracture morphology and b)fatigue-initiated facet

The common corner location of the fisheye initiation sites and flat cleavage planes were also much harder than the rest of the case, as shown by the microhardness map in Figure 4.6. Each microhardness map grid point represents a microhardness measurement, with the first measurement located in the top left hand corner of Figure 4.6 taken at a distance 75 μm away from both neighboring edges. The excess hardness in the corner reached values up to 779 Vickers (approximately 63-64 R_C). Such over-carburization of specimen corners has been shown to occur as carbon introduced at the surface cannot readily diffuse from the corner into the bulk[**85, 86**].

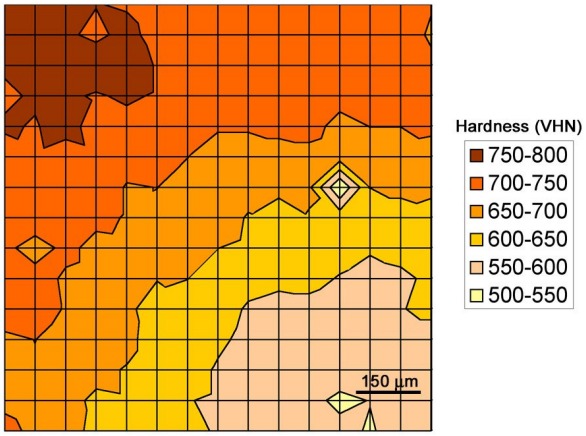

Figure 4.6. Microhardness map of overcarburized C61 spur gear corner (Batch A)

Carbon accumulation in specimen corners has been also been demonstrated with 2D carburization diffusion simulations by Gao ([**87**]). Figure 4.7a shows a 2D carbon diffusion simulation for a single boost and diffuse carburization cycle for C61, demonstrating carbon accumulation in specimen corners. Gao also analyzed C61 samples subjected to boost carburization cycles and observed the formation of Cr-carbide films at the prior austenite grain boundaries, as shown in Figure 4.7b. With subsequent diffuse cycles, these carbide

films were observed to dissociate and the carbon diffuse deeper into the material. However at specimen corners where diffusion is limited but carbon flux is enhanced, this dissociation of film carbide is much more difficult and likely plays a role in the smooth facets observed in the overcarburized specimen corners.

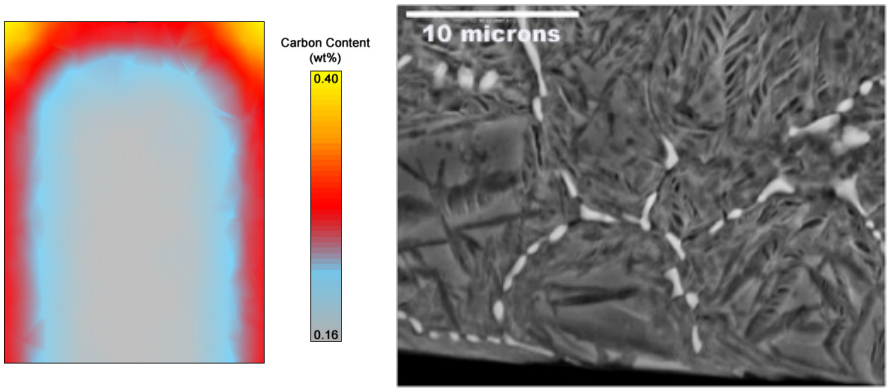

(a) (b)

Figure 4.7. a) Carbon accumulation in specimen corners in 2D carburization simulations and b) SEM micrograph of grain boundary Cr carbide in C61 formed during carburization boost cycles, courtesy of Gao [**87**]

Such accumulation is not as severe in conventional gas carburizing because of the constant potential boundary conditions. In contrast, high temperature vacuum carburizing involves elevated levels of carbon flux into the material and maintains this flux during each boost cycle, enabling the introduction of additional carbon even in the presence of accumulation. This increased carbon content subsequently changed the microstructure in the corner of C61 spur gears relative to the rest of the carburized case, as seen by the white-etching retained austenite and midrib-bearing plate martensite visible in the light micrograph of Figure 4.8a relative to Figure 4.8b.

The change in microstructure also resulted in a change in the residual stress. Figure 4.9 shows that the altered corner microstructure resulted in a less compressive residual

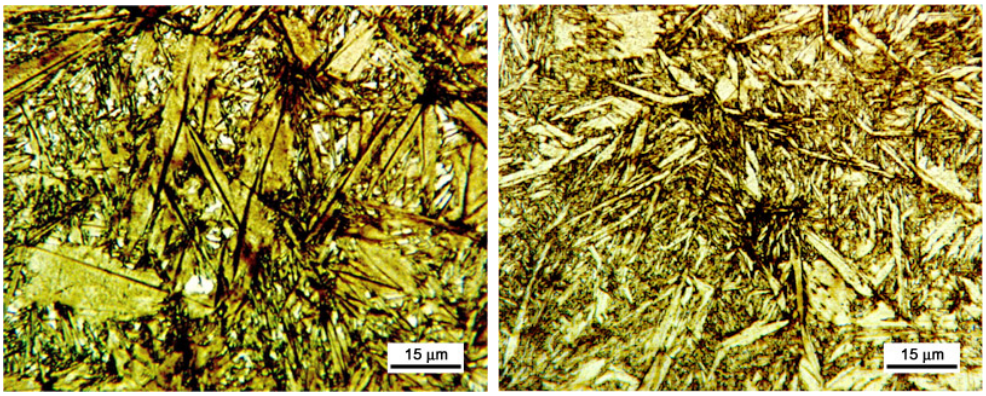

(a) (b)

Figure 4.8. Light micrographs of C61 spur gear teeth cross-sections (Batch A) showing microstructure for a) overcarburized corner and b) root center-line of carburized case

stress at the surface, as well as a much shallower compressive residual stress depth. This corner residual stress deficit becomes large around a depth of 0.3 mm, promoting the subsurface fatigue crack initiation that was observed around the same depth.

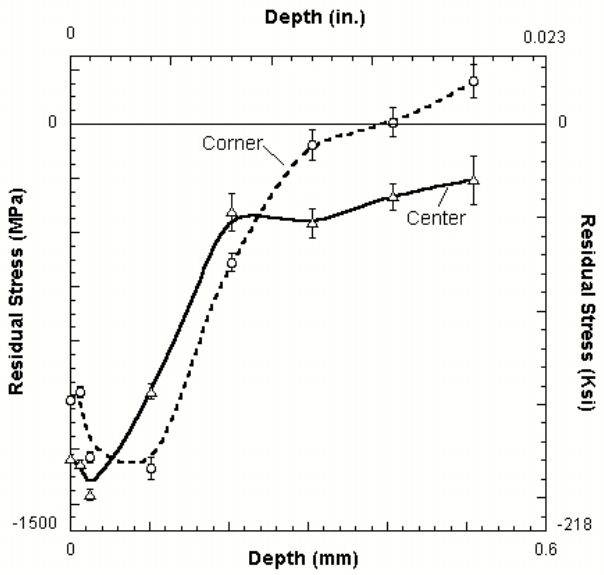

Figure 4.9. Batch A shot peened C61 residual stress profiles measured at the root center and edge at gear corner

A second batch of C61 spur gears, designated C61 Batch B, were then prepared in an effort to avoid overcarburization caused by high temperature vacuum carburizing through two processing alterations. The first was to reduce the solutionizing/carburizing temperature from 1050°C to 950°C to lower the magnitude of carbon flux into the surface. Additionally, post heat-treatment grinding of the gear sides was used to remove the outer 0.3mm (0.012 in.) of material on each side that is most prone to carbon accumulation. Due to the 5% reduction in face width from grinding the gears, applied bending loads were correspondingly reduced by 5% from values used previously in order to achieve equivalent bending stresses. After taking these preventative measures, single tooth bending fatigue performance of C61 was seen to increase, as shown in Figure 4.10. The fitting parameter b defining fatigue endurance limit was raised by over 200 MPa over the previous SP and GR+SP Batch A gears to 1450 MPa.

Similar performance gains were observed in previous studies by Krauss and coworkers where a 10% increase in bending fatigue life was achieved by rounding off specimen corners prior to gas carburizing to achieve a uniform case microstructure [**86**]. A larger performance increase is also expected for specimens subjected to high temperature vacuum carburizing where the fixed carbon flux boundary conditions are more prone to accumulate carbon in specimen corners [**85, 86**]. Based on these previous studies, the observed 17% increase in bending fatigue endurance limit of C61 Batch B gears can reasonably be attributed to the avoidance of over-carburized specimen corners. Figure 4.11 shows a microhardness map for the corner of a Batch B C61 spur gear cross-section.

Compared with those previously tested, the corners of Batch B gears do not show elevated hardness levels indicative of carbon accumulation/over-carburization and when

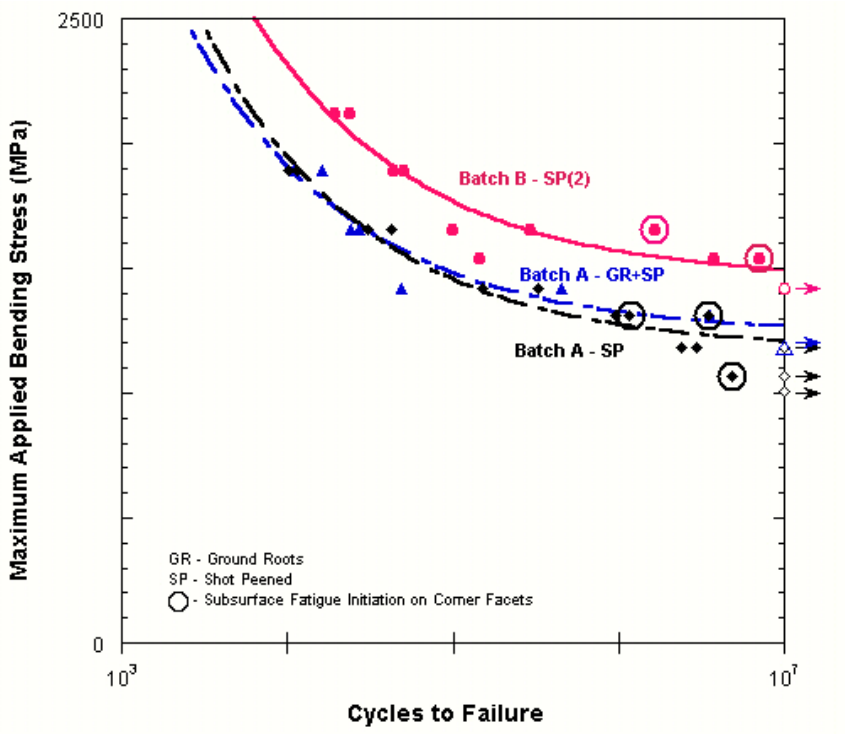

Figure 4.10. S-N curves for C61 Batch A and B spur gears showing performance 17% improvement in bending fatigue performance due to avoidance of overcarburized corners

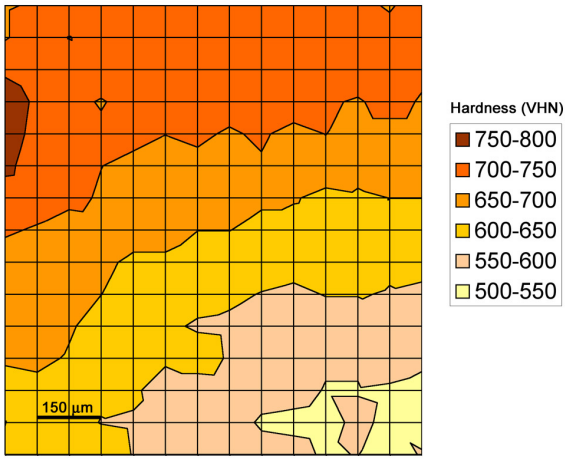

Figure 4.11. Microhardness map of Batch B C61 spur gear corner

analyzed using light microscopy, likewise show increased microstructural uniformity with the rest of the gear root edge. Figure 4.12 shows measured residual stress profiles for C61 Batch B gears. Again unlike Batch A gears, there is no distinguishable difference between measurements taken near specimen edges and away from the corner in the center of the gear root, suggesting uniform microstructure and avoidance of excessive retained austenite, plate martensite and reduced compressive stress in gear teeth corners.

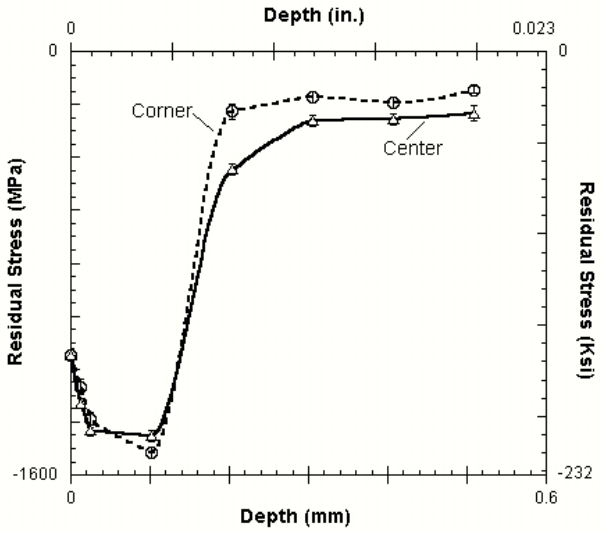

Figure 4.12. Batch A shot peened C61 residual stress profiles measured at the root center and edge at gear corner

4.2. Process Limitations

As seen in the process optimization stage of single tooth bending fatigue testing, maximizing compressive residual stress is critical for fatigue resistance [**88, 89**]. Additionally, surface finish and microstructural uniformity are also important factors for bending fatigue. The second stage of single tooth bending fatigue testing focused on the current

limitations of these parameters, specifically shot peening variability and associated limitations, surface finish improvement through isotropic superfinishing and microstructural defects in the form of inclusions. This second stage of testing utilized Batch B C61 spur gears, an additional batch of C61 spur gears (Batch C) and a set of C67 spur gears.

4.2.1. Shot Peening

S-N curves for shot peened Batch C C61 spur gears are shown in Figure 4.13 along with results for previous batches of shot peened C61 gears for comparison. In the high cycle fatigue regime ($>10^6$ cycles), Batch C more closely resembled Batch B due to complete avoidance of overcarburized corners shown to limit high cycle fatigue performance of Batch A C61 spur gears. Although no failures were recorded in this region for Batch B gears, a runout at 10^7 cycles was achieved at over 1300 MPa, which was over 100 MPa greater than the highest run-out achieved with Batch A gears. In the low cycle fatigue regime, however, Batch C fell short of the performance exhibited by Batch B gears and closely mirrored that of Batch A.

Figure 4.14 shows measured residual stress profiles for all three batches of shot peened C61 gears. The first observation that can be made is that there is significant variation between batches even though specified shot peening parameters were supposedly identical. This variability reflects the inconsistency in the actual shot peening procedure and was seen to primarily affect the stress at the surface as well as the maximum achieved compressive stress, with the effective compressed layer staying essentially constant around 0.2 mm. The observed variation in residual stress was not seen to directly correlate to

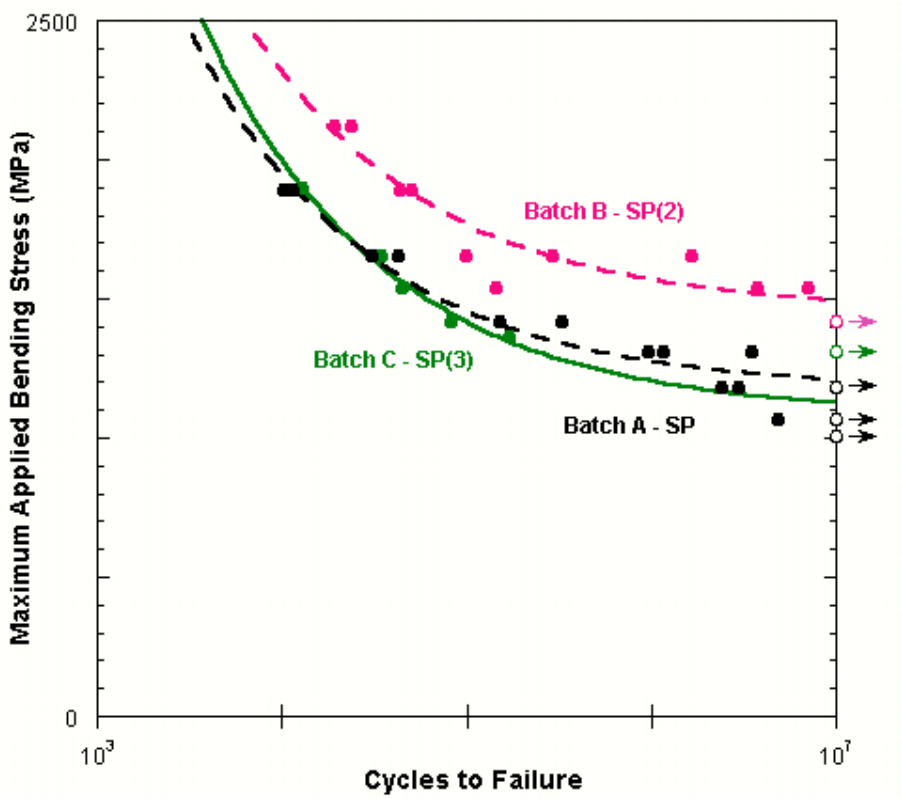

Figure 4.13. S-N curves for shot peened C61 spur gears

single tooth bending fatigue properties, however. Batch B, the best performing in bending fatigue, did achieve the greatest maximum compressive stress, but not the greatest surface compressive stress. The lowest values of compressive stress both at the surface as well as overall, were shown by batch C, however its bending fatigue results were almost identical to that as batch A that demonstrated the highest surface compressive stress and a maximum stress very close to batch B.

Another aspect of shot peening possibly affecting low-cycle fatigue performance is effective damage caused by the impact of peening media on the gear tooth surface. Figure 4.15a shows an SEM micrograph of the shot peened surface of a shot peened batch C C61

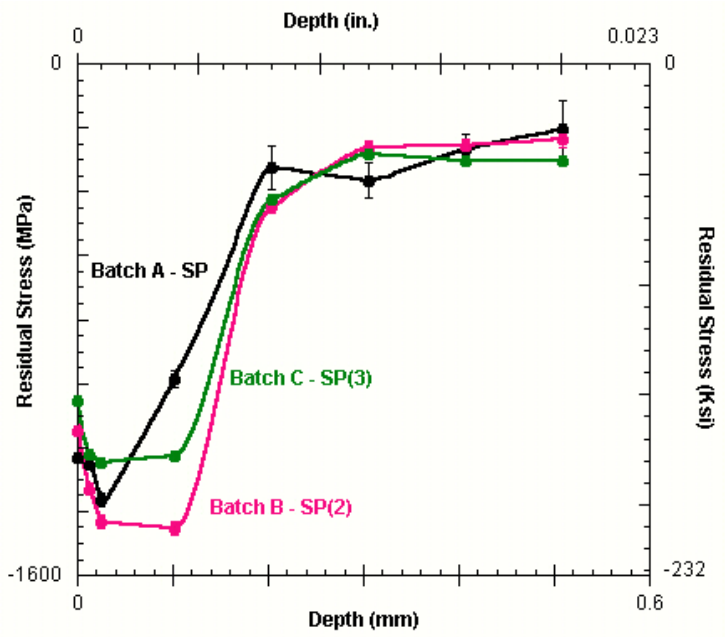

Figure 4.14. Measured residual stress profiles for shot peened C61 spur gears

spur gear showing a surface crack caused by significant plastic deformation during the peening process. Figure 4.15b shows a light micrograph of a corresponding cross-section where white etching bands or crescents were observed near the shot peened surface, further suggesting severe plastic deformation on the surface due to repeated high energy impact from the spherical peening media. Such features are consistent with a phenomena known as "overpeening", where excessive shot peening damages the surface to a sufficient degree to offset the imparted beneficial compressive stresses and reduce fatigue resistance. The occurrence of observed surface and subsurface damage due to shot peening was more evident on batch C gears compared to batch B gears, and is the most likely factor causing the reduced low-cycle fatigue resistance.

To study the effect of increased hardness on bending fatigue, C67 spur gears were fabricated for single tooth bending fatigue testing. Harder materials are desired to resist

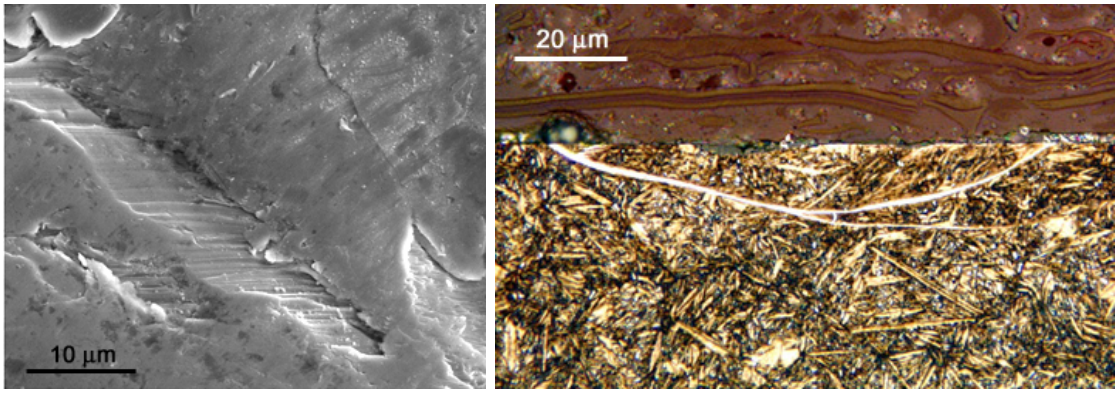

(a) (b)

Figure 4.15. Surface damage caused by shot peening on batch C C61 spur gears as evidenced by a)SEM micrograph showing shot peened induced fissure on gear tooth surface and b) light micrograph of corresponding cross-section showing white-etching crescent indicative of severe plastic deformation (5% Nital etch)

contact and bending fatigue stresses, and although they are generally more sensitive to flaws, they also have increased capacity to sustain larger strains prior to yielding and subsequently can achieve greater compressive residual stresses with shot peening [**90**]. C69 spur gears were ground after heat treatment along with Batch B C61 spur gears to remove potentially overcarburized material. Single tooth bending fatigue S-N curves for shot peened C69 spur gears are shown in Figure 4.16 along with corresponding shot peened Batch B C61 results for comparison. Even with the increased hardness of C67, its single tooth bending fatigue resistance was significantly below that of C61, with an approximate endurance limit around 150 MPa below that of the 1450 MPa of shot peened Batch B C61 gears.

One possible factor for the reduced performance of C67 was an amount of remnant grain boundary carbides in excess of that observed in the carburized case of corresponding

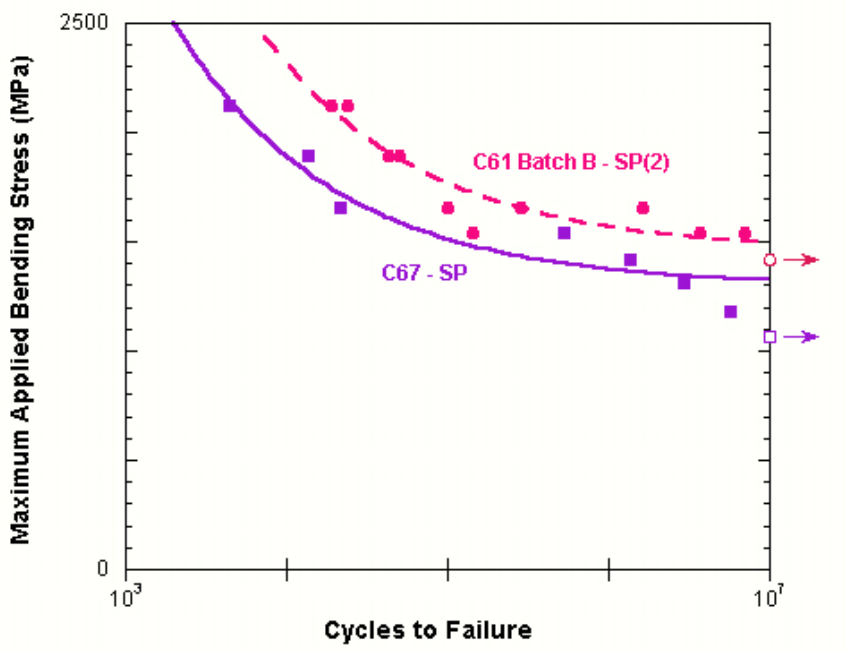

Figure 4.16. S-N curves for shot peened C67 and shot peened Batch B C61 spur gears

C61 Batch B spur gears. More importantly, however, was the response of C67 to shot peening. Figure 4.17 shows the measured residual stress profiles for both shot peened C67 and Batch B C61 spur gears. Only measurements taken along the center of the gear root are displayed, as those taken near specimen corners at the root edge showed no significant difference. Although the compressive stress achieved at the surface of the C67 spur gears was slightly higher than that of C61, the overall maximum value was reduced. Additionally, the generally shape of the residual stress profile exhibited by C67 does not demonstrate the characteristic sigmoidal curve as shown by C61, suggesting the compressive stress saturation point was not achieved.

In an effort to maximize compressive residual stress in C67, various shot peening process variants were explored on carburized C67 puck samples, with the resultant residual

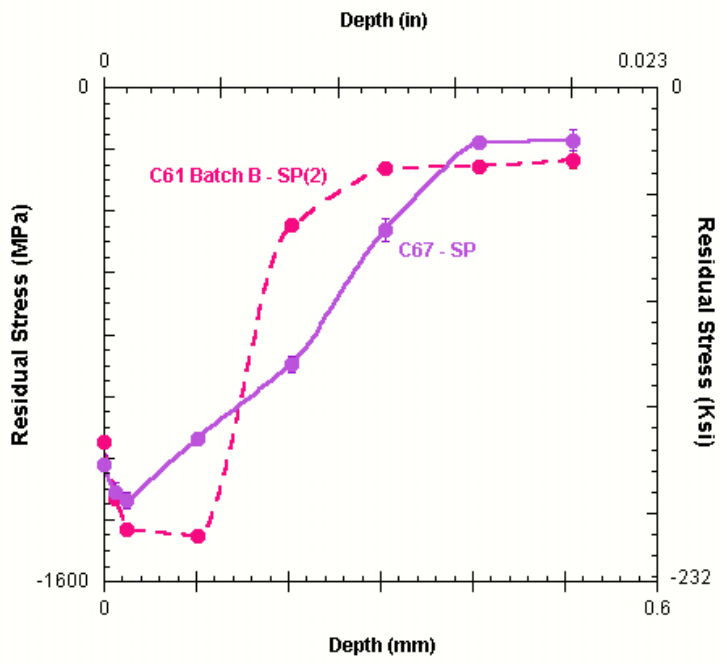

Figure 4.17. Residual stress profiles for shot peened C67 and shot peened Batch B C61 spur gears

stress profiles shown in Figure 4.18. A slight gain in the maximum compressive stress to around 1400 MPa was achieved in one of the test pucks, however achieved compressive stress levels did not surpass those achieved in C61.

The inability of the shot peening process to achieve maximum compressive residual stress in C67 spur gears can in large part be attributed to the excess hardness of C67 over the actual shot peening media. At a hardness of 60-64 R_C, the hardened steel cut-wire shot medium used for the first stage of shot peening is actually softer than the surface hardness of carburized C67. Compressive stresses can still be generated with a shot media that is softer than the target material, however the maximum residual stress cannot be imparted as the shot media will deform against the harder target and absorb most of the projected energy. Based on the residual stress profiles of Figures 4.17 and 4.18, the upper

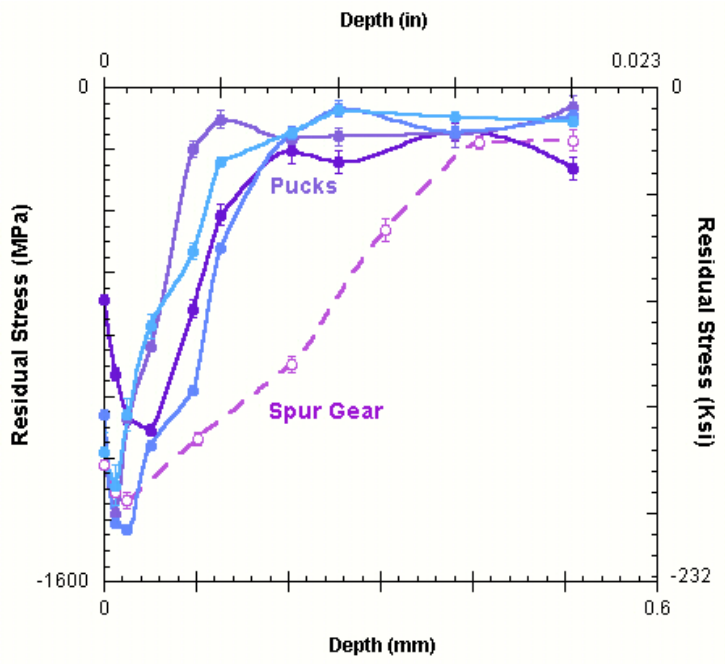

Figure 4.18. Residual stress profiles for C67 shot peening study

limit for current hardened steel cut-wire shot appears to be around 1300-1400 MPa when carburized C61 and C67 are used as targets.

Currently, hardened steel cut-wire shot is the hardest commercially available shot peening medium, therefore suggesting that maximization of C67 compressive residual stress may not be possible with current commercial practices. Laser peening is one method of imparting compressive residual stress that has potential for materials harder than standard shot peening media. Instead of through particle bombardment, laser peening imparts compressive stress through the interaction between an incident laser beam and an applied energy-absorbing surface coating. A thin layer of water contains the expansion along the surface, and the resultant compressive shock creates the compressive stress in the target material surface. Preliminary laser peening tests were completed on carburized

C67 test pucks to investigate possible benefits over conventional shot peening. Figure 4.19 compares the resultant residual laser peening stress profile compared to that measured from carburized C67 spur gears used in single tooth bending fatigue testing. Laser peening did produce a much deeper compressive stress layer, however the maximum compressive stress as well as the surface compressive stress was significantly less than achieved through conventional shot peening. Previous laser peening studies have shown significant residual stress enhancement over conventional shot peening [**91**], and these results indicate that further optimization of the laser peening process for C67 is required. Relaxation of residual stress may also have occurred due insufficient sample thickness of the carburized C67 pucks used in the study.

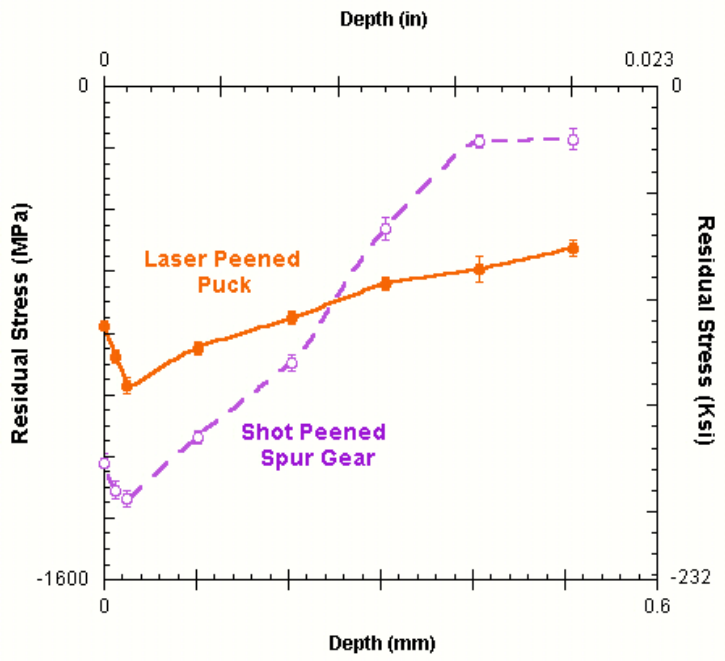

Figure 4.19. Measured residuall stress profile for laser peened C67 compared to conventionally shot peened C67

4.2.2. Isotropic Superfinishing

Isotropic superfinishing (ISF) was investigated as a means of improving surface finish of shot peened batch B and C C61 gears as well as shot peened C67 spur gears. Resultant S-N curves showing single tooth bending fatigue results are shown in Figures 4.20 and 4.21 for C61 and C67, respectively. For both shot peened C61 and C67, isotropic superfinishing did improve resistance to bending fatigue, particularly the low-cycle fatigue life. C67 results in Figure 4.21 shows this benefit in the low-cycle fatigue region where under 100,000 cycles ISF improved bending fatigue life around a factor of 3. Beyond 100,000 cycles as fatigue initiation shifts from surface flaws to subsurface flaws, the benefit of ISF diminishes. ISF had a similar effect for C61, approximately doubling the low-cycle fatigue life (<100,000 cycles) for batch B C61 spur gears. Batch C C61 spur gears showed significant improvement after isotropic superfinishing, however they were also shot peened at a different time than their shot peened-only counterparts resulting in a slightly different residual stress profile.

Figure 4.22 shows the measured stress profiles for the two peening procedures used for batch C spur gears, with the shot peening procedure used for the ISF-conditioned gears resulting in a much deeper compressive stress layer as well as increased compressive stress at the surface. The near surface residual stress values for the two peening conditions are very similar however, suggesting the enhancement in surface residual compressive stress may be due to the ISF process. By removing surface asperities along with the very outer surface layer without relieving compressive stress, isotropic superfinishing effectively raises the surface compressive stress by eliminating tensile stress-causing defects and pushing the surface slightly closer to the maximum compressive stress point.

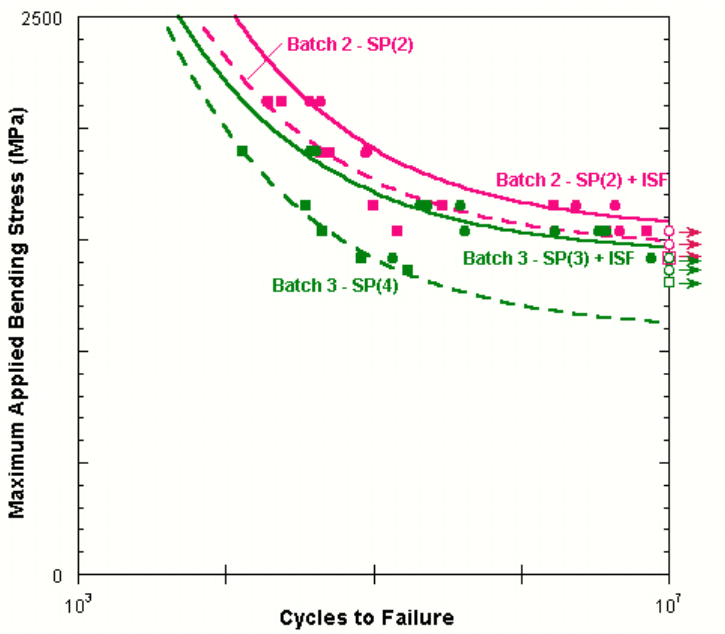

Figure 4.20. S-N curves for shot peened C61 showing effect of isotropic superfinishing

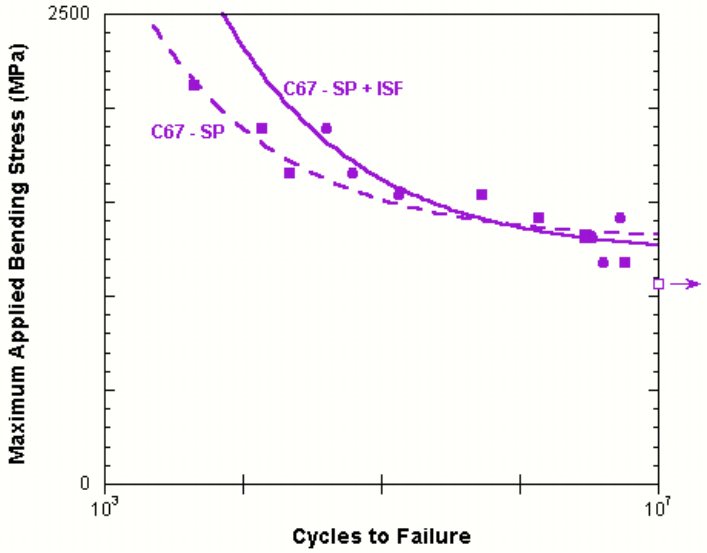

Figure 4.21. S-N curves for shot peened C67 showing effect of isotropic superfinishing

The surface finish after isotropic superfinishing was also much different for batch B gears compared to batch C gears. Figures 4.23 a and b shows SEM micrographs of the

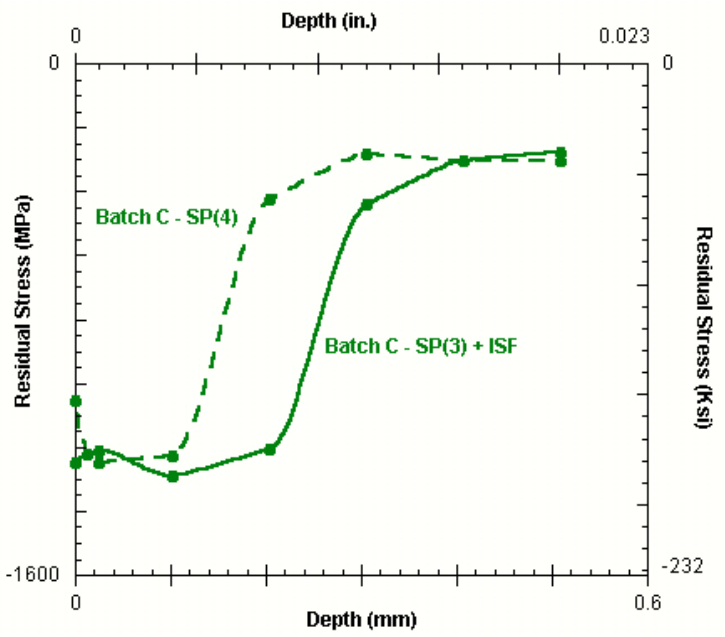

Figure 4.22. Measured residual stress profiles for both shot peening conditions of batch C C61 spur gears

ISF surfaces for shot peened batch B and C C61 spur gears, respectively. The surface of batch C gears was much rougher, with the frequent occurrence of what appears to be some form of pitting. C67 also displayed pitting following isotropic superfinishing that on some occasions was shown to initiate fatigue. For C67, these pits averaged around 50 μm in diameter and when found on tooth fracture surfaces delved approximately 50 μm beneath the surface. Pits observed in C61 were more frequent, but also approximately half the size, on average. From discussion with the isotropic finishing developers, these pits are not representative of chemical attack from the slurry used in the finishing process.

When investigating sectioned teeth from Batch C spur gears, however, the appearance of these pits very closely resembled that of the white etching crescents observed on the shot peened-only gears, as shown by the light micrographs of each in Figure 4.24. The

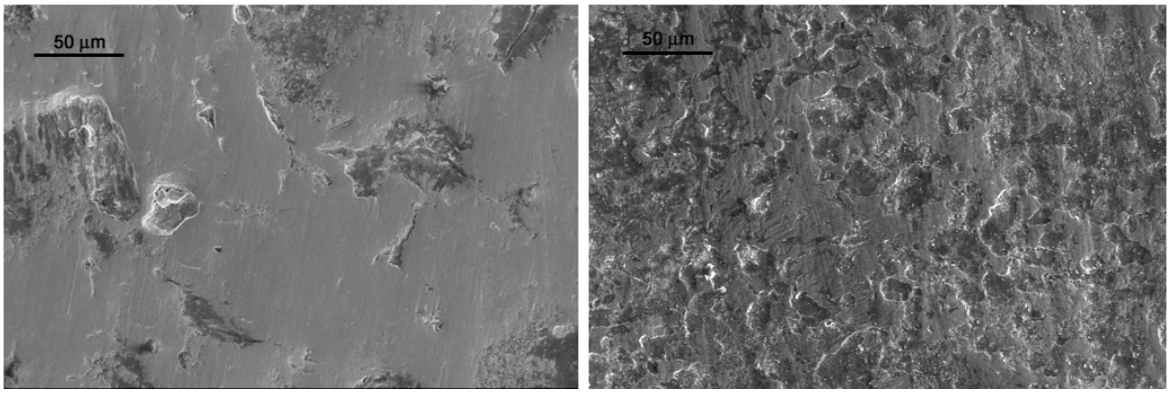

(a) (b)

Figure 4.23. SEM micrographs of isotropic superfinished surface for a)batch B and b) batch C C61 spur gears

"pitting" seen on the ISF surface of batch C C61 as well as C67 spur gears can most likely be attributed to the "plucking out" of damaged material caused by potential overpeening.

4.2.3. Mictrostructural Features

In shot peened C61 and C67 spur gears, subsurface fatigue initiation was observed to take place, primarily in the high cycle fatigue region approaching the endurance limit. Microstructural features causing subsurface initiation fell into two classes: cleavage facets and inclusions.

4.2.3.1. Subsurface Corner Facets. As first observed in shot peened batch A C61 spur gears, cleavage facets occurred in high cycle fatigue failures $>10^6$ cycles near the endurance limit and always were located in specimen corners. Systematic preferential loading of specimen edges was not believed to be the cause, as pressure sensitive tape was used before each test to ensure even loading along the full width of each gear tooth and corner facets were observed to occur randomly at both edges of the loaded gear root.

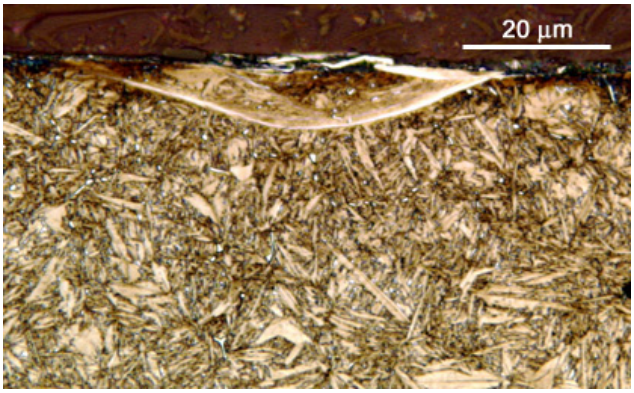

(a)

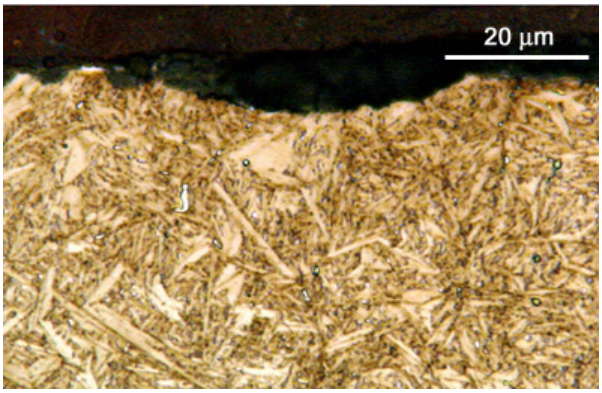

(b)

Figure 4.24. Light micrographs of batch C C61 spur gears comparing a)white-etching crescents in shot peened gears and b) "pitting" in shot peened gears after isotropic superfinishing

Despite the observed performance increase and enhanced microstructural uniformity, Batch B and C gears still demonstrated subsurface fatigue initiation on corner facets in high cycle fatigue failures, albeit at at elevated applied stress magnitudes. Facets seen in Batch B C61 gears had the same general appearance as Batch A gears, however, they were not as smooth as those previously seen and were always inclined to the fracture surface, an example of which is shown in Figure 4.25. Although successfully avoiding significant over-carburization, the reduction in solutionizing/carburizing temperature for Batch B gears

did result in remnant micron-sized grain boundary carbides that likely participated in the creation of these subsurface facets. The topological transition from completely smooth to sharp and ridged would also agree with the embrittlement mechanism changing from continuous retained austenite patches found in severe over-carburization of Batch A gear corners to the periodic, spherical carbides found in Batch B gears.

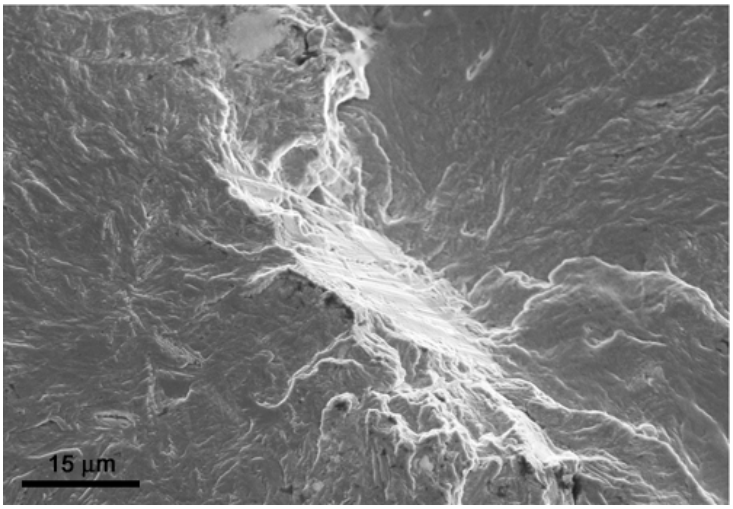

Figure 4.25. SEM micrograph of a batch B C61 spur gear tooth fracture surface showing fatigue-initiating facet

To achieve complete microstructural uniformity along the entire length of the carburized root notch, batch C C61 spur gears had stop-off paint applied to their sides prior to carburization to prevent excess carburization and subsequent carbon accumulation in specimen corners. The solutionizing/carburizing temperature was also raised to an optimized temperature of 1000°C to fully dissolve grain boundary carbides seen at the 950°C temperature used for batch B gears while avoiding excessive carbon flux experienced at the 1050°C temperature first used for Batch A gears. Additionally, batch C spur gears were ground to their final face width prior to carburization and all post-heat treatment

grinding omitted to completely avoid any detrimental effect of grinding in the hardened state. Figure 4.26 shows the resultant microhardness map taken of a batch C gear tooth corner cross-section, demonstrating the achieved uniform carburized case. Reduced hardness in the outer corner of the map is due to slight rounding of the corners caused by the isotropic superfinishing process. Microstructural uniformity as well as the absence of significant amounts of grain boundary carbides was verified by light microscopy and measured residual stress profiles confirmed equivalent compressive residual stress profiles in the corner compared to the root notch center.

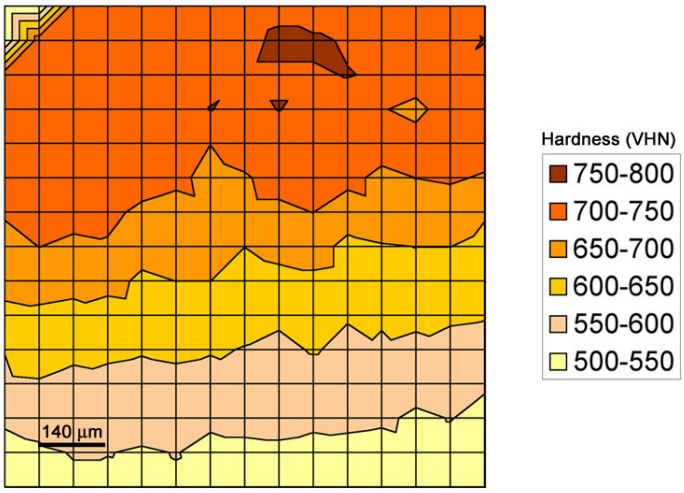

Figure 4.26. Microhardness map of batch C C61 spur gear tooth cross-section

Despite all these precautions, subsurface initiation was still observed to occur in the corners of batch C spur gears. The appearance of the fatigue-initiating features was very different from previous facets, however, this time assuming a "feathery" morphology not much different than the surrounding fracture surface, an example of which is shown in

Figure 4.27b. "Smeared" material along the root edge located just above the fisheye feature shown in Figure 4.27a is due to contact with the loading single tooth bending fatigue anvil during final fracture. The altered appearance of the fatigue-initiating feature does reflect the increased microstructural uniformity of the corner, and fatigue initiating facets have been previously observed in other microstructural systems containing no obvious microstructural inhomogeneities [**92, 93, 94, 95, 96**]. In these instances, grain boundaries and the presence of different phases and microstructures impeding dislocation motion are believed to cause fatigue inititiation.

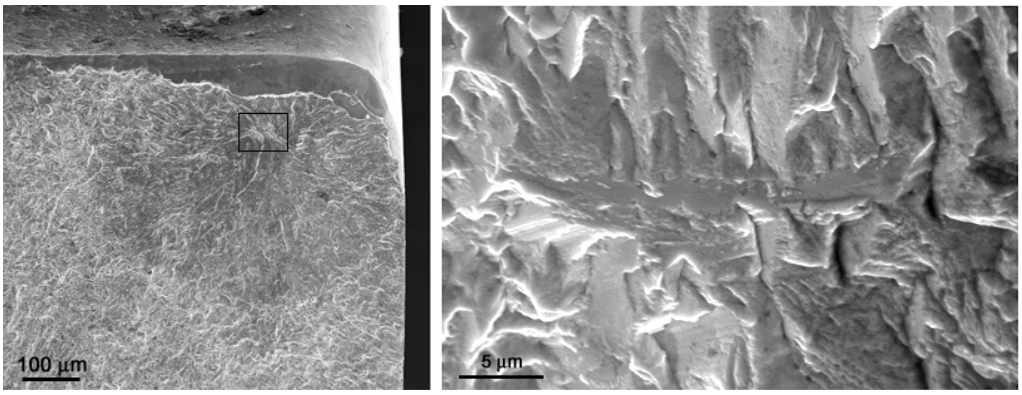

(a) (b)

Figure 4.27. SEM micrographs of a batch C C61 spur gear tooth fracture surface showing a) fisheye morphology of subsurface fatigue initiation and b)closeup of highlighted microstructural feature in a) causing initial fatigue nucleation in center of fisheye

The reoccurrence of subsurface fatigue initiation only in specimen corners, however, suggests the corner is still a "weak link" for high cycle fatigue. The common processing step for all three batches of C61 exhibiting corner facets was the application of shot peening after heat treatment. When shot peening gear root notches, it is common practice to shot peen around root edges and along the adjacent gear side to ensure complete

coverage and achieve fully compressive stresses. At the very high intensities and saturation levels used for shot peening the high strength C61 and C67 gear steels, this practice may in fact be detrimental by "overpeening" specimen corners. Similar to the 2D carburization effect causing carbon accumulation, specimen corners experience magnified shot peening coverage due to peening on both sides. This may be the root cause of the microstructural features causing corner subsurface initiation, and offers an explanation why subsurface facets were not observed in any region other than specimen corners. Over-carburization previously attributed to facet formation in batch A spur gears may have aggravated this phenomenon by weakening the microstructure prior to peening oversaturation. Further analysis as well as shot peening optimization is required to better understand this high cycle fatigue behavior.

4.2.3.2. Inclusions. The other microstructural features observed to initiate fatigue were inclusions. On the fracture surface, the same surrounding fisheye morphology as the corner facets was observed to radiate outward from each failure-inducing inclusion, however there was no preferential location for subsurface inclusion fatigue failures other than a common depth of 100-300 μm. Two classes of inclusions were observed as verified qualitatively by energy dispersive spectroscopy (EDS): Al_2O_3 inclusions in shot peened batch B C61 spur gears and La_2O_2S inclusions in shot peened batch C C61 and C67 spur gears. The switch from Al_2O_3 to La_2O_2S inclusions is a direct result of La additions to Batch C C61 (0.003 wt%) and C67 (0.01 wt%) alloy heats to specifically getter impurities.

Figures 4.28 and 4.29 show SEM micrographs of both classes of inclusions as seen on both the tooth fracture surfaces as well as the corresponding mating fracture surfaces remaining on the spur gear. Both Al_2O_3 and La_2O_2S inclusions were composed of clusters

of individual particles aligned along the hot working direction of the billets from which the gears were made. Individual inclusion particles composing each Al_2O_3 and La_2O_2S cluster were all between 1-10 μm in diameter. The arrangement and number of particles was very different between inclusion type. Al_2O_3 clusters were generally composed of only a couple individual inclusion particles tightly concentrated along a single line. In contrast, La_2O_2S clusters were composed of numerous particles and had a much larger cluster width.

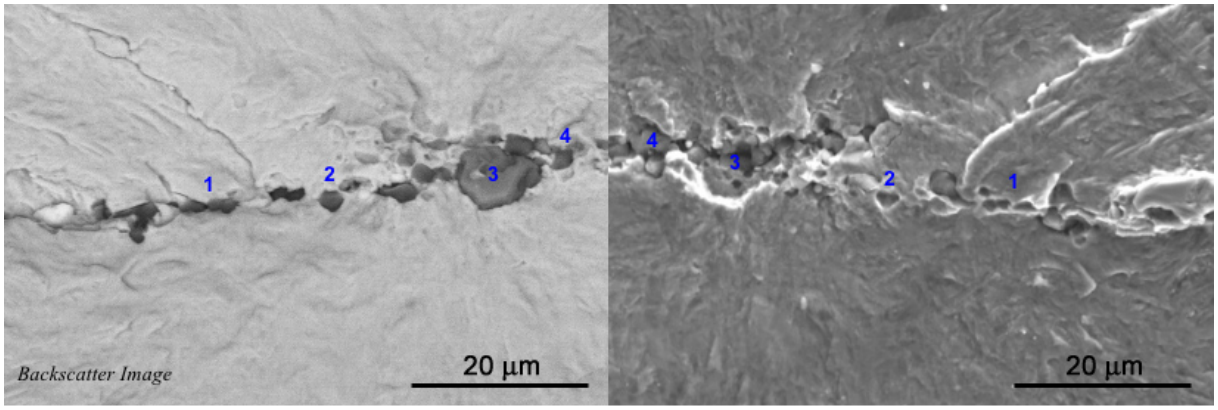

Figure 4.28. SEM micrographs of mating fracture surfaces of subsurface fatigue initiation on an Al_2O_3 inclusion

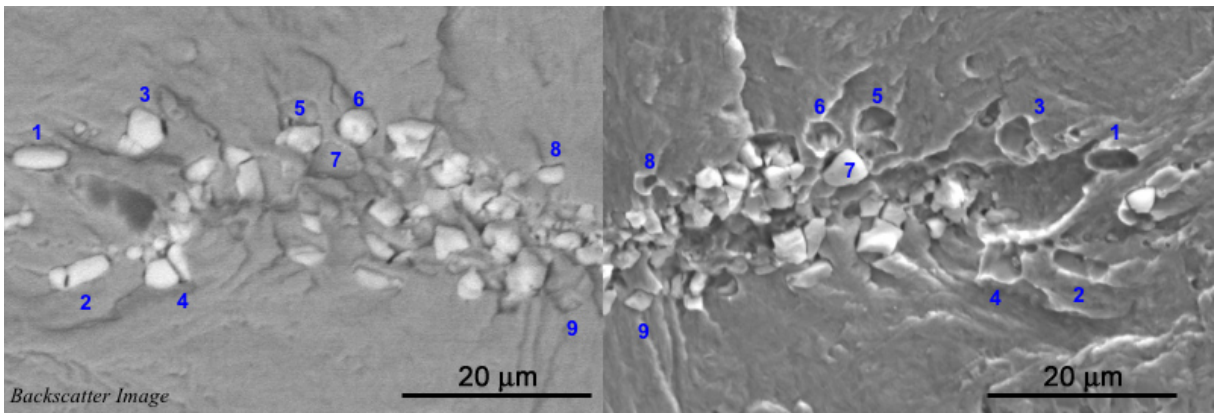

Figure 4.29. SEM micrographs of mating fracture surfaces of subsurface fatigue initiation on a La_2O_2S inclusion

The relative impact on single tooth bending fatigue was also much different between inclusion type. Figure 4.30 shows single tooth bending fatigue S-N curves for different shot peened C61 and C67 spur gears where at least one failure occurred due to subsurface inclusions. Al_2O_3 initiated failures, as denoted by circles in Figure 4.30, occurred in the high cycle fatigue range very near the endurance limit ($>10^6$ cycles) and were interspersed among other high-cycle fatigue failures at equivelent applied stresses. La_2O_2S initiated failures, however, caused failure at much earlier fatigue lives around 10^5 cycles and in the case of batch C C61 gears was clearly detrimental to fatigue life, occurring at an applied stress several hundred MPa below the other fatigue failures at equivalent fatigue lives. Due to limited data, the effect on C67 is less clear, however the comparatively frequent occurrence of two La_2O_2S-initiated inclusions, due to the alloy's relatively high La content, may be largely responsible for the underperformance of C67 in low-cycle fatigue.

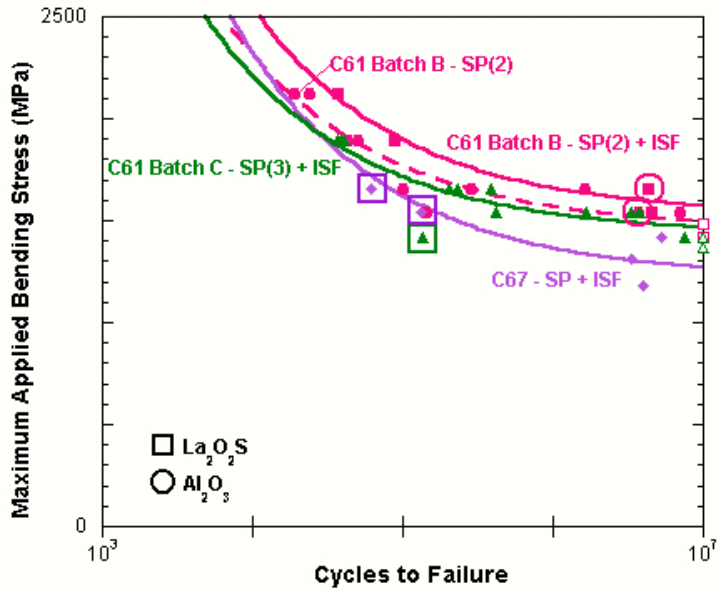

Figure 4.30. Occurance of subsurface fatigue initation on both Al_2O_3 and La_2O_2S inclusions in single tooth bending fatigue testing of shot peened C61 and C67

The increased defect "potency" of La_2O_2S inclusions compared to Al_2O_3 inclusions can also be seen by the depth at which they occurred relative to measured compressive residual stress profiles that were generated through shot peening. Figure 4.31 shows the location at which the observed inclusions initiated fatigue failure plotted against the corresponding residual stress profiles. With the exception of one La_2O_2S-initiated failure in C67, all La_2O_2S inclusions caused failure at much shallower depths where the compressive residual stress values were near their maximum values. In contrast, Al_2O_3 inclusions were only observed to initiate fatigue at depths corresponding to the effective depth of the compressive depth, where compressive residual stress levels were reduced by 75%.

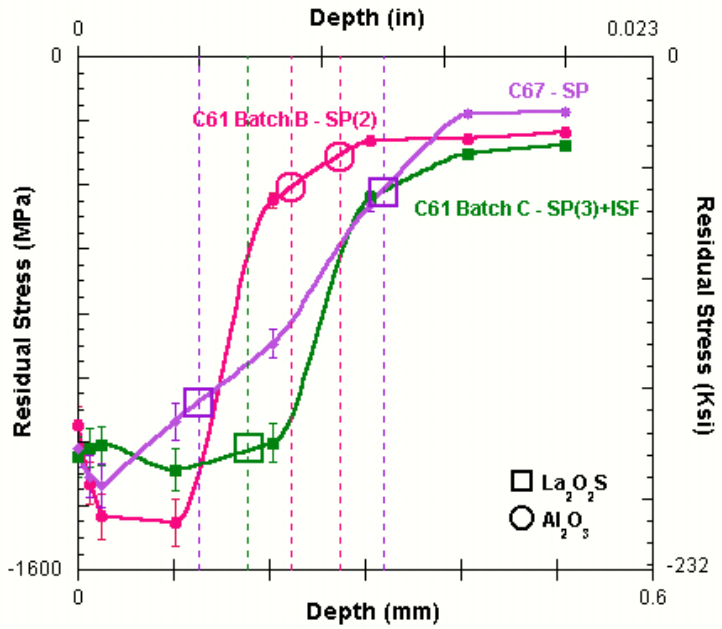

Figure 4.31. Location of subsurface fatigue initation on different inclusion types compared to corresponding residual stress profiles

Although the overall size of the inclusion clusters were not significantly different for Al_2O_3 and La_2O_2S inclusions, the nature of the individual particles composing them did show significant differences that most likely caused the dissimilarity in effective defect potency. As shown in Figure 4.29, La_2O_2S particles are located on both mating fracture surfaces with individual particles primarily de-cohering from the opposing fracture surface leaving behind a concavity. It is, however, unclear if numerous jumbled particles are in fact separate or the fractured remnants of a larger particle, and some single particles did show signs of fracture, such as annotated particle 8 in Figure 4.29. Al_2O_3 particles, in contrast, were primarily located and tightly bonded on only one mating fracture surface, displaying de-cohesion from the opposing surface with no discernable signs of particle fracture. McDowell and coworkers have shown similar results where cracked and de-bonded inclusions are more detrimental to fatigue than their bonded counterparts of equal size [**97**]. Additionally, recent and ongoing work by McDowell has shown that the specific locality between individual inclusion particles plays a large role in fatigue initiation, with particles placed adjacent to each other along the direction of applied stress being the most detrimental arrangement [**98**]. This agrees with the enhanced defect potency of the wider La_2O_2S inclusion clusters compared to the more compact Al_2O_3 clusters.

4.3. Structure/Property Relations

In an effort to summarize the effects of various observed defects, a comprehensive study was performed to identify fatigue-initiating features for all single tooth bending fatigue failures, when at all possible. Figure 4.32 summarizes identified fatigue-initiating defects for all three batches of C61 spur gears. When all the data is grouped together, several

trends can be observed. With the exception of La_2O_2S-initiated fatigue, all subsurface fatigue failures occurred in the high cycle fatigue region after 10^6 cycles. This is consistent with previous studies of high-cycle fatigue for other high strength steels, however the exact mechanics of this phenomenon are not entirely understood. The location of these subsurface fatigue failures was always at a depth 200-300μm below the surface at the point where compressive residual stress profiles taper off significantly. Because of their location along their respective S-N curves, it is these defects that ultimately control the fatigue endurance limit achieved by each C61 spur gear.

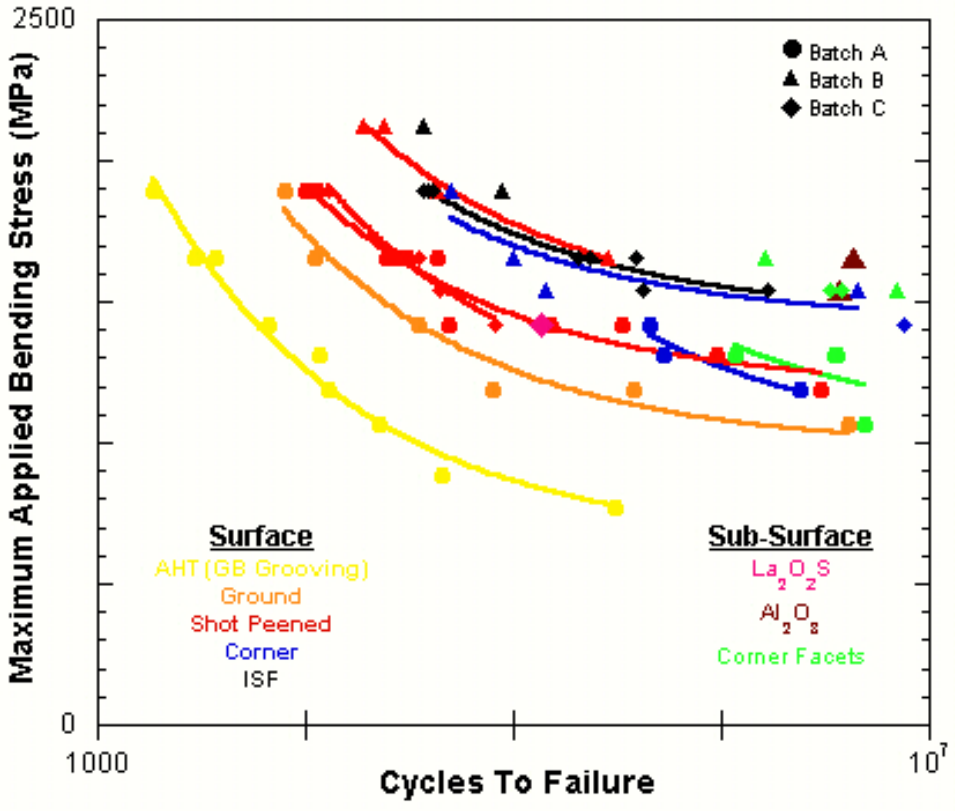

Figure 4.32. Fatigue-initiating defect identification for all three batches of C61 spur gear single tooth bending fatigue failures

Another observation is that surface initiated fatigue in shot peened gears tended to fall within two groups: one group composed of batch A and batch C shot peened gears and the other containing all batch B as well as batch C gears that had undergone isotropic superfinishing. As previously discussed, this variance is most likely due to surface damage caused by excessive shot peening in batch A and C spur gears, where in the case of isotropic superfinished Batch C gears, the ISF process counteracted this detrimental effect by raising the surface compressive stress.

Surface fatigue initiation was also observed to occur quite frequently at specimen corners, as shown in Figure 4.32. Many of these corner-initiated fatigue failures corresponded to equivalent applied stresses and fatigue lives as fatigue failures initiating on the surface away from the corners, however in some instances corner initiation appears as a separate defect class. Specifically in shot peened batch B C61 spur gears, surface initiation at specimen corners represented failures at the lowest applied bending stresses and several instances of surface corner initiation were also observed in the high-cycle fatigue range $>10^6$ cycles. Because a large portion of these failures occur either along the observed "lower band" of surface-initiated fatigue or along with subsurface corner facets, both phenomena of which are associated with over-peening, surface damage caused by over-peening of specimen corners is also a likely cause of this behavior. SEM analysis of fractured gear teeth did occasionally show corner surface such as shown in Figure 4.33 that corroborates this supposition.

One final observation can be made regarding the different inclusion types. Compared to Al_2O_3 inclusions, La_2O_2S inclusions appear to be more detrimental to fatigue as they are observed to cause fatigue failures at fewer cycles and lower applied stresses as well as

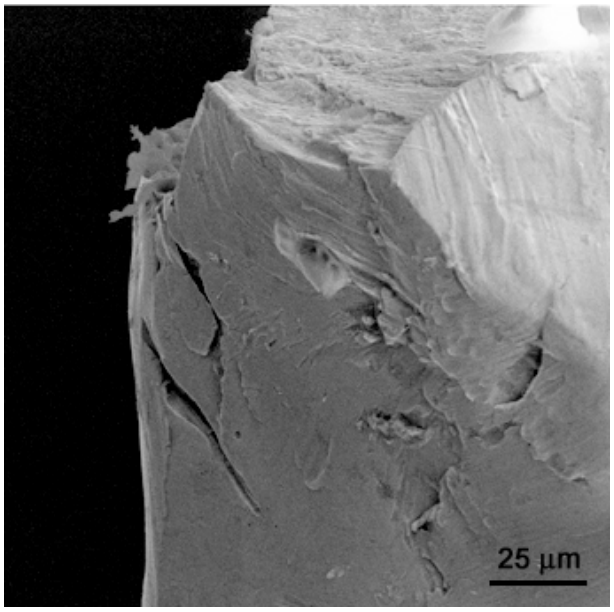

Figure 4.33. Example SEM micrograph of micracking at gear root corner

causing these failures at various depths seemingly regardless of compressive stress. A clear demonstration of the potency of La_2O_2S inclusions can be seen in the single S-N curve in Figure 4.34 for C61 Batch C gears that were shot peened and polished. In this instance, only one La_2O_2S inclusion was found to initiate fatigue, but it essentially was an outlier lying far below the fitted curve. A shift of the curve fit down to match the inclusion failure would result in a drop in the estimated endurance limit by over 250 MPa. Al_2O_3 inclusions, however, were observed more frequently not only when initiating fatigue but also in general inspection of gear tooth cross-sections, an example of which is shown in Figure 4.35. There seemingly exists a tradeoff therefore, between having numerous Al_2O_3 inclusions and few, but more potent La_2O_2S inclusions.

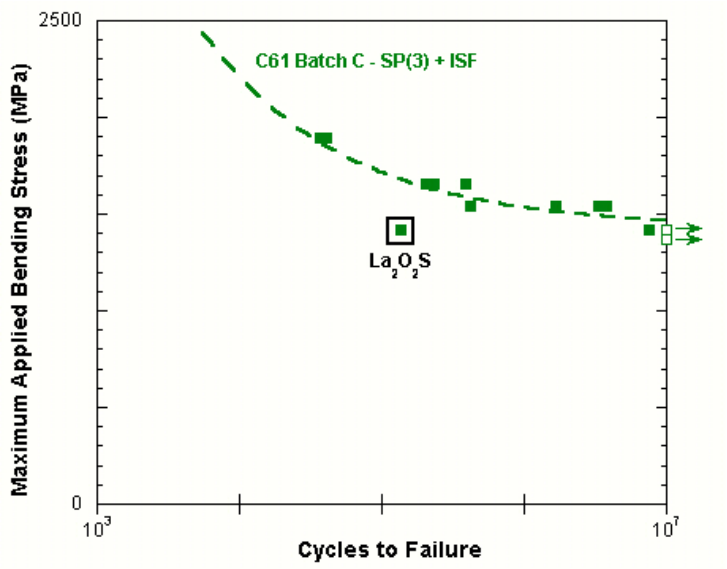

Figure 4.34. S-N curve for C61 Batch C spur gear showing detrimental effect of La_2O_2S inclusions on fatigue

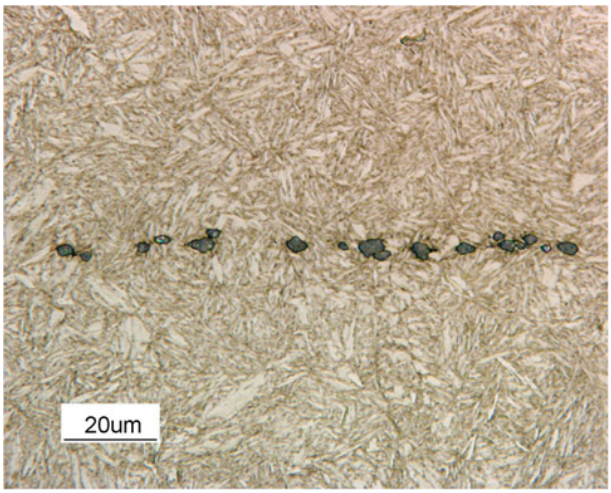

Figure 4.35. Light micrograph of Al_2O_3 inclusion observed in polished gear tooth cross-section. 5% Nital etch

4.4. Ultimate Bending Strength

The load versus displacement curves representing ultimate bending strength for the four investigated surface conditions in the preliminary process optimization stage of Batch

A C61 single tooth bending fatigue testing are shown in Figure 4.36. Curves are slightly offset for ease of comparison. Ultimate bending strengths are designated as the point where the measured displacement rates rapidly exceeded 0.4 mm/sec marking the onset of overload failure. Arrows highlighting dips in the load/displacement curves indicate catastrophic rupture of the carburized case, as suggested by corresponding, audible "pops" heard during testing, indicative of carburized case rupture [**99**]. Because the carburized case completely ruptures, the generated stress subsequently changes making all correlations between applied load and stress approximate. The point at which carburized case rupture occurs strongly depends upon the surface preparation of the tested gear, with increasing stress/displacement levels achieved by shot-peening and then further after grinding. A combination of grinding and shot peening resulted in no evident dip in the graph, suggesting simultaneous occurrence of case rupture and ultimate failure (also suggested by the audible "pop" heard only at failure). A distinct increase in total displacement and ultimate bending load was also seen for the gears that were at one point ground when compared to the gears that were not. Unlike bending fatigue, surface condition is shown to be the primary factor for monotonic overload bending where the sole benefit of shot peening is surface modification and not the generation of compressive residual stress.

Additional load versus displacement curves are shown in Figure 4.37 for Batch B and C C61 and C67 spur gears used for single tooth bending fatigue process limitation studies. Overload failure could not be achieved during initial testing of Batch B C61 spur gears, and additional tests were required to be run on a higher capacity test frame to achieve failure in one loading cycle. Unfortunately, all testable Batch B C61 gear teeth in the shot peened only condition had already been expended and could not be tested till failure

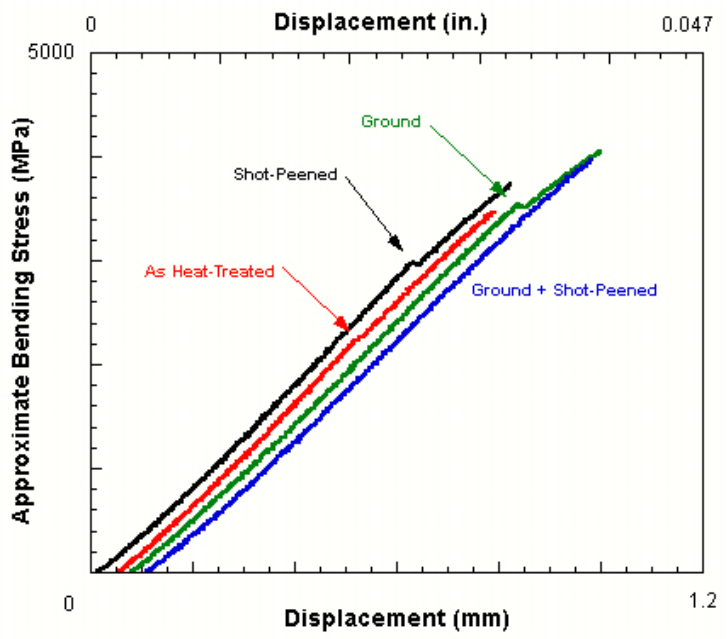

Figure 4.36. Ultimate bending strength curves for the four investigated surface finishes of Batch A C61 spur gears

on the higher capacity load frame. For these gears then, the load/displacement curve is shown up to the testing capacity of the previous machine, around 84 kN (approximately equivalent to a stress of 4.8 GPa in the gear tooth root). The occurrence of premature, catastrophic rupture of the carburized case seen in Batch A C61 gears as slight "dips" in the load/displacement curves was not seen in Batch B C61 gears. Audible "pops" associated with these dips were absent as well, further suggesting the carburized case remained intact throughout loading. The effect of isotropic superfinishing on Batch B gears cannot be determined because of the lack of comparable shot-peened only data.

Batch C C61 gears demonstrated reduced ultimate bending strengths compared to Batch B, most probably reflecting the surface damage caused by overpeening and related poorer isotropic superfinished surface. Curve dips signifiying case rupture were not easily

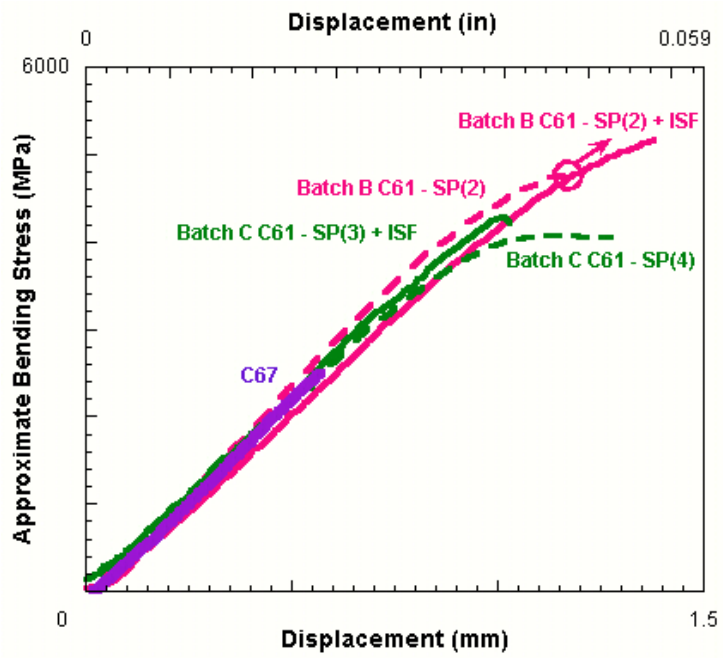

Figure 4.37. Ultimate bending strength curves for C61 and C67 spur gears. Circle denotes achieved test capacity.

determined due to significant data scatter, however it does appear that the carburized case of the shot-peened only Batch C spur gears did rupture around 4000 MPa, signified by the sudden change in slope of the curve and additional ductility characteristic of deformation of the softer core. For Batch C gears, isotropic superfinishing did appear to delay case rupture to higher applied stresses, however when case rupture did occur, overload failure occurred rapidly with negligible core deformation and associated ductility. C67 achieved an ultimate bending load around 43 kN without exhibiting any ductility. Isotropic superfinishing had no measurable effect on the ultimate bending strength of C67 and duplicate curves were not included. The reduced ultimate bending performance of C67 can most likely be attributed to both its enhanced sensitivity to surface finish and lower toughness relative to C61.

4.5. Performance Summary

In order to compare optimized C61 bending fatigue performance, representative S-N curves were provided by James Bishar of GM Powertrain to represent a baseline gear steel (L_{10} life) as well as a premium gear steel (L_{50} life). Figure 4.38 plots these representative curves agains best-practice C61 results, represented by batch B C61 shot peened and isotropic superfinished spur gears, as well as the starting C61 condition in the as-heat treated (AHT) condition for comparison. Starting well below the baseline gear steel in the AHT condition, targeted performance optimization was able to improve the bending fatigue resistance of C61 to above that of the representative premium gear steel as approximated by the fatigue endurance limit by around 15% and ultimately surpassing the baseline gear steel by over 40%. Figure 4.39 summarizes the single tooth bending fatigue performance optimization process for C61.

Ultimate bending curves for best-practice Batch B C61 spur gears as well as Batch A C61 and the representative premium gear steel, both of which are in the ground condition, are all shown in Figure 4.40. Ground Batch A C61 demonstrates improved yield strength over the premium gear steel, with a slight gain in ultimate bending strength. Best practice C61 gears show a significant improvement in ultimate bending strength, and further testing would need to be done with premium gear steels to investigate similar improvements. Based on shot peened-only Batch B and C gears however, a significant portion of the ultimate bending fatigue enhancement can be attributed to the C61 material and not entirely on the ISF processing, as the improved surface finish had only a slight benefit.

Total performance validation of C61, representing the three chosen metrics of single tooth bending fatigue endurance limit, surface hardness and ultimate bending strength is

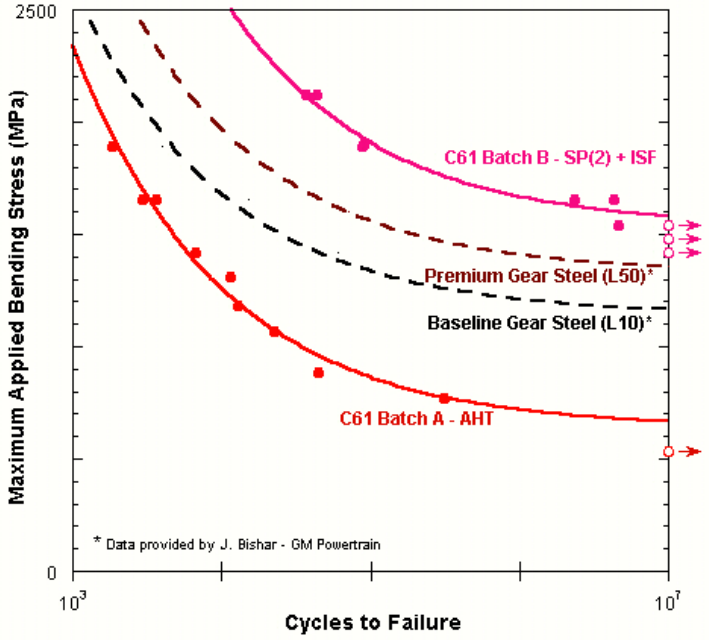

Figure 4.38. Comparison between C61 and representative baseline and premium gear steels in single tooth bending fatigue

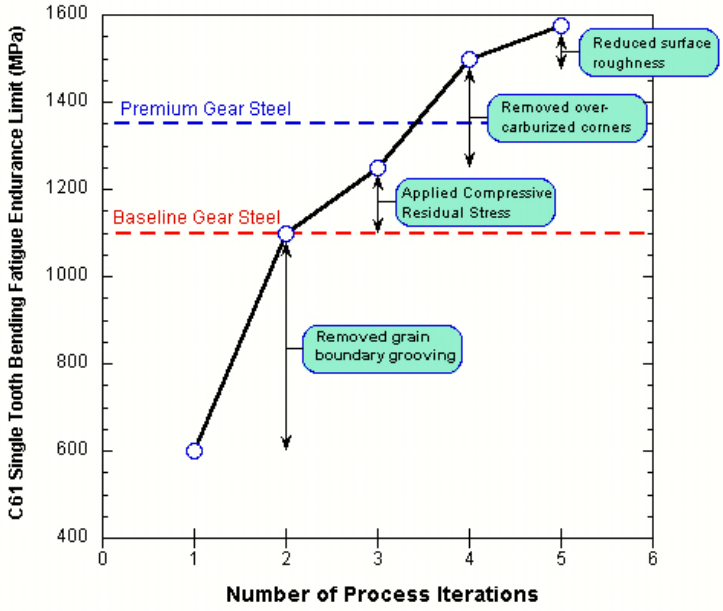

Figure 4.39. Summary of single tooth bending fatigue endurance limit optimizitaion for C61

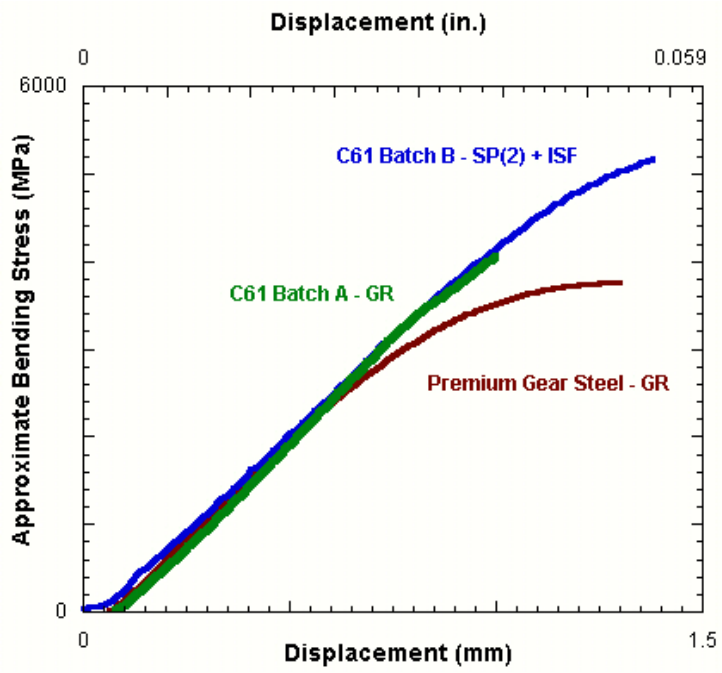

Figure 4.40. Ultimate bending strength comparison between C61 and a representative premium gear steel

summarized in Table 4.1. A range of ultimate bending strength improvement values are given to reflect the constrained comparison due to lack of isotropic superfinished data for other gear steels.

Table 4.1. C61 performance validation summary

	Baseline Gear Steel	Premium Gear Steel	C61	% Improvement over Premium
Bending Fatigue Endurance Limit (MPa)	1100	1375	1575	15
Surface Hardness (VHN)	668	668	715	7
Core Hardness (VHN)	410	410	510	24
Ultimate Bending Strength (MPa)	2975	3250	5190	25-60

The elevated hardness of C67 did not show any benefit in single tooth bending fatigue, in large part due to its un-optimized heat treatment and especially the inability of conventional shot peening to maximize compressive residual stress. Further development of heat

treatment as well as gear surface treatments such as shot peening and surface finishing is required get further bending fatigue performance from alloys much harder than C61.

CHAPTER 5

Microstructure Control Studies

As processing-induced defects are addressed through such measures as shot peening optimization and enhanced surface finishing techniques, microstructural limitations will become increasingly important for both bending and contact fatigue. Such limitations for high-strength gear steels include excessive grain coarsening, non-martensitic transformation products and dissolution of strengthening carbide dispersions. In the case of C61 and C67, coarsened grains in spur gear corners have already been observed to be involved in fatigue initiation and the predominant failure mode currently limiting high cycle fatigue resistance. The following three focus studies were completed to address these microstructural issues to investigate potential improvement methods as well as identify specific limitations or benefits intrinsic to the microstructure of the C61/C67 alloys.

5.1. Powder Metallurgy Grain Coarsening Resistance Study

As previously discussed in Chapter 2, prior austenite grain size has shown the highest statistical correlation with bending fatigue endurance limits of carburized gear steels [**100**], with grain size refinement leading to improved resistance to fatigue crack initiation and propagation. Grain coarsening is a potentially significant issue with the C61/C67 alloys as they are predominantly carburized at elevated temperatures using high temperature vacuum carburizing. Grain coarsening may already be influencing bending fatigue

performance of C61/C67 as evidenced by cleavage facets presumably along prior austenite grain boundaries causing subsurface fatigue initiation in shot peened spur gears.

In an effort to prevent grain coarsening during high temperature vacuum carburizing, several powder metallurgy (PM) variants of C69, a precursor alloy of the C67 used in single tooth bending tests, were investigated. Powder metallurgy materials have previously shown resistance to grain coarsening at elevated temperatures due to grain-pinning oxide dispersions [**46**]. Initial PM alloys, named C3L and C4, did not demonstrate enhanced grain coarsening resistance over wrought C69, subsequently attributed to a lack of stable oxide forming alloying elements [**45**]. Consequently, researcher Brian Tufts designed new alloy compositions incorporating sufficient Ti additions to getter typical oxygen levels intrinsic to the powder metallurgy process into a grain pinning oxide dispersion [**45**]. This Ti-bearing powder metallurgy alloy, named PM C69-Ti, was investigated in this work to study the possible benefit of the Ti addition on grain coarsening resistance.

Samples of PM C69-Ti were subjected to one-hour solutionizing treatments at temperatures ranging from 900-1200°C. The oxidation etching method outlined in Section 3.2.3 was utilized to delineate prior austenite grains, with resultant light micrographs taken and shown for all solutionizing temperatures in Figure 5.1. Average grain size measurements were then taken following ASTM E112-96 [**69**] consisting of ten linear intercept measurements per image, with the final value representing an average of two images from different locations. Figure 5.2 shows the average grain diameter and ASTM grain size measured for PM C69-Ti compared to previous results for wrought C9 as well as the initial C69 PM variants (C3L and C4) [**45**].

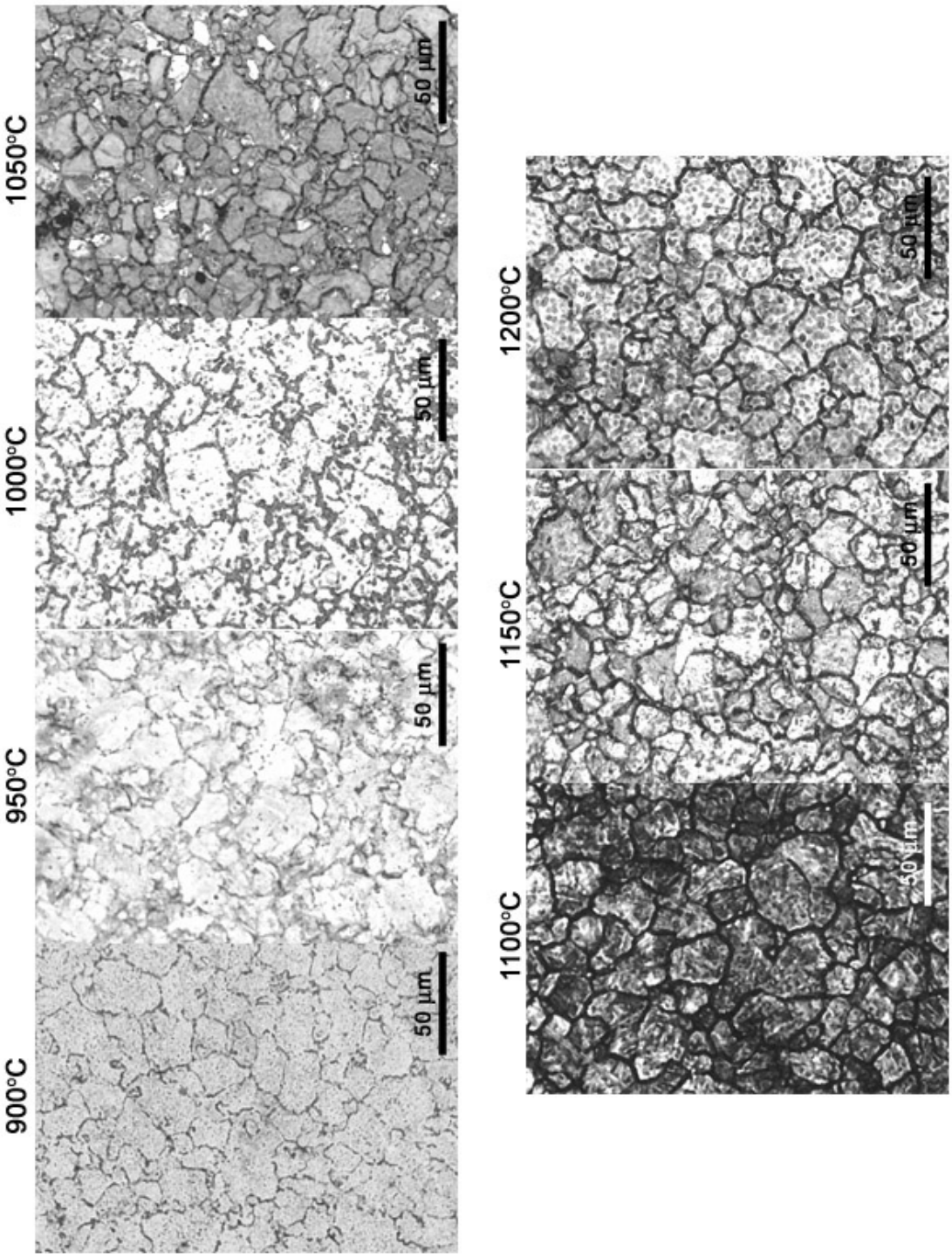

Figure 5.1. Light micrographs for PM 69-Ti solutionized at various temperatures

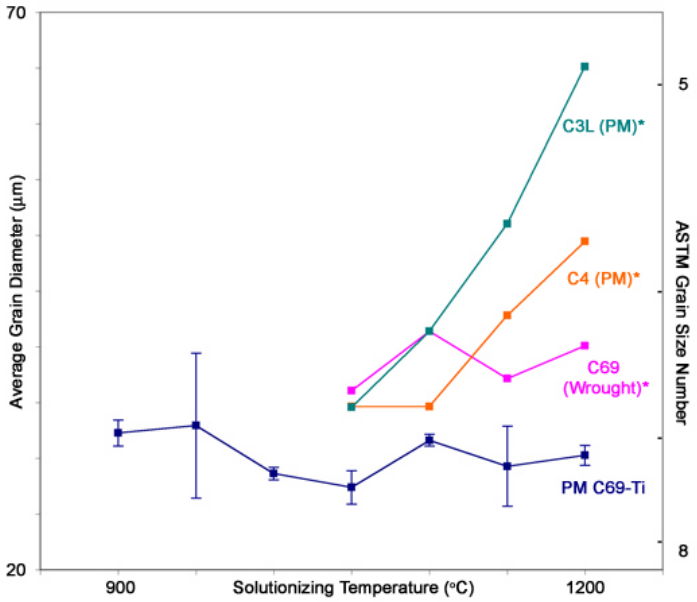

Figure 5.2. Measured average grain sizes for PM and wrought C69. *Data taken from Tufts [**45**]

The C69 PM material with added titanium does show resistance to grain coarsening, maintaining an approximate average grain diameter of 30 μm consistently up to 1200°C, well beyond normal solutionizing temperatures. Scatter within the data represents ± one standard deviation and can largely be attributed to varying degrees of grain boundary delineation during the oxidation etching process and associated difficulty of grain size measurement, particularly for samples solutionized at 950°C and 1050°C. Even considering this error and assuming similar scatter for the previous results, the Ti addition clearly demonstrates improved grain coarsening resistance over the previous PM alloys, C3L and C4, representing a reduction in average grain size after solutioning at 1200°C of approximately 40 and 50%, respectively. PM C69-Ti also displays a slightly finer starting grain size than both the wrought C69 and previous PM alloys by about 15%.

One potential source of error in these grain size measurements might be due to an intrinsic fault in the oxygen etching technique used to delineate prior austenite grain boundaries. Because oxidation was achieved through the trace oxygen levels present in the upright argonne furnace, the flow of oxygen and subsequent rate of oxidation was constant throughout the solutionizing heat treatment. Depending on how fast the oxidation took place, the presence of the oxide at the prior austenite grain boundaries could potentially obstruct coarsening of surface grains and mask the true coarsening behavior. Grain coarsening was observed in the C3L and C4 PM alloys using this technique, however subsequent alterations to the upright argonne furnace may have influenced the inherent oxygen content and related oxidation characteristics. For conclusive results on the grain coarsening resistance afforded by the Ti-bearing PM alloy, further study is required using either a different grain boundary etching process or a modified oxygen etching procedure where oxidation is limited to occur at the end of the solutionizing heat treatment.

5.2. Hardenability Assessment

Microstructural uniformity is critical in high power density gear applications as softer non-martensitic transformation products such as retained austenite and Bainite patches have been shown to reduce high-cycle fatigue performance [**31, 25**]. To study the hardenability of ultra-high strength secondary hardening steels, dilatometry was performed on C61 samples to measure the effect of cooling rate on transformation behavior and resultant microhardness levels. Samples were first heated to a solutionizing temperature of 1050°C and held for 5 minutes to ensure complete transformation to austenite and

dissolution of primary carbides. The samples were then cooled at different quench rates, at which point the microhardness was measured.

Figure 5.3 shows an example dilatometry plot showing the measured relative length change versus temperature. Upon heating, thermal expansion of the martensite causes steady expansion until around 800°C where the transformation to austenite is clearly visible by the associated volume contraction. The transformation continues with further heating until linear expansion is once again resumed, signifying complete transformation to austenite. Upon cooling, the thermal expansion of the austenite is reversed down to the martensite start temperature (M_S) signified by the associated volume expansion of the martensitic transformation.

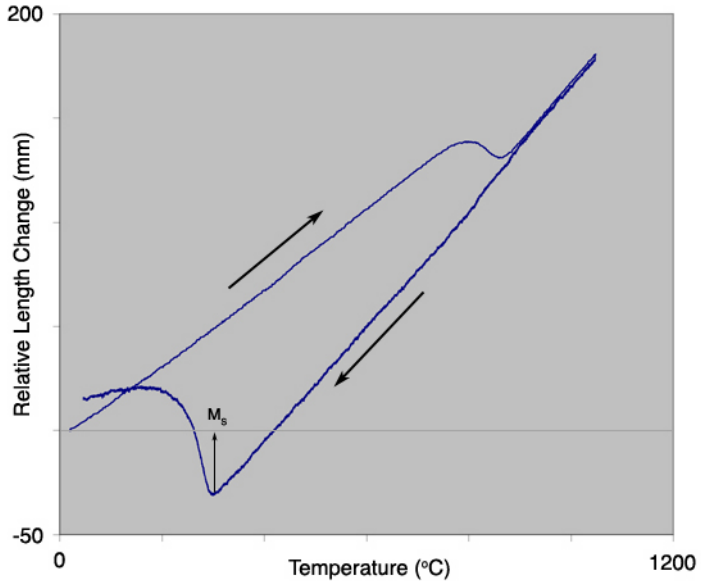

Figure 5.3. Example dilatometry curve showing relative length change versus temperature

Figure 5.4 shows the transformation response of C61 in the form of a time-temperature-transformation plot. Various cooling rates labeled as the time required to cool down to

room temperature. In each case, complete transformation from austenite to martensite occurred. No significant deviation of the martensite transformation temperature was observed nor the presence of any additional volume changes associated with other phase changes, verifying complete avoidance of Bainite.

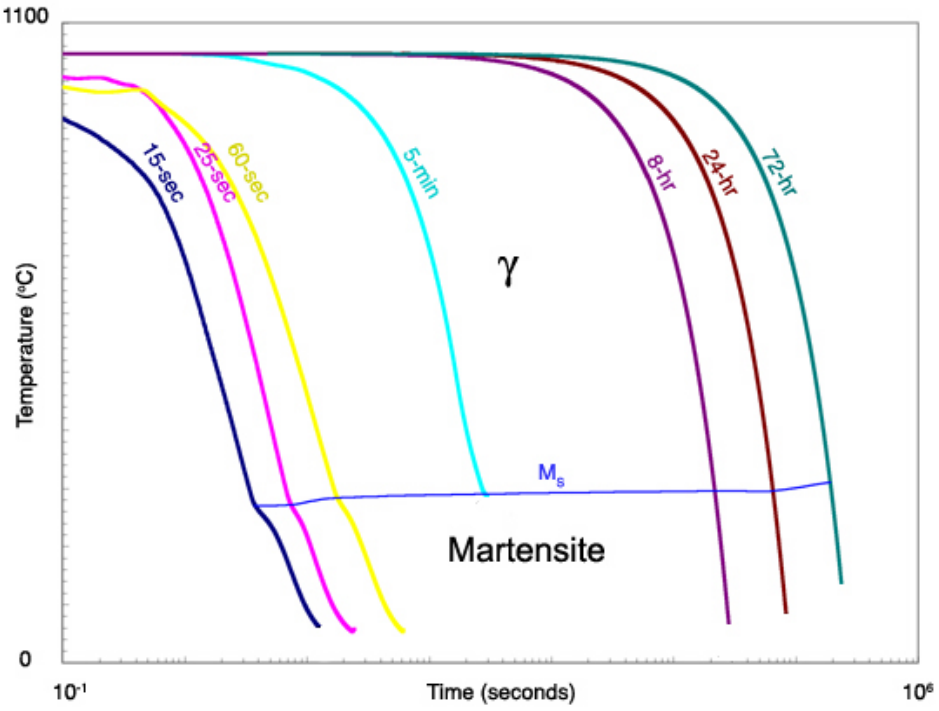

Figure 5.4. Time-Temperature-Transformation diagram for C61. Labeled quench rates designate time to reach room temperature from a starting solutionizing temperature of 1050°C.

In order to gauge the observed hardenability of C61 relative to other gear materials, corresponding hardenability data was obtained for the baseline gear steel and premium gear steel used for single tooth bending fatigue comparisons. Figure 5.5 shows this hardenability comparison where different cooling rates are now expressed as an equivalent air-cooled bar diameter and the shown hardness values correspond to the bar center at

the point of minimum cooling rate. Shown in this manner, the high hardenability of C61 enables the air-cooling of a bar exceeding 2 meters in diameter with minimal softening (~15%). In contrast, the premium and baseline gear steels demonstrate significant softening, demonstrating hardness reductions over 45 and 60% respectively at the center of a 2-meter diameter air-cooled bar.

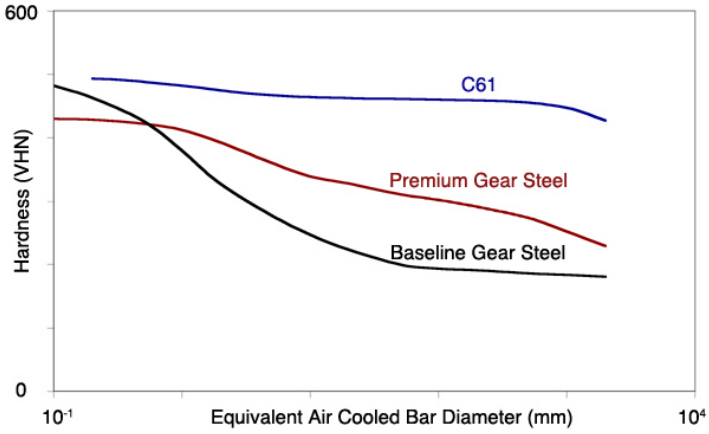

Figure 5.5. Hardenability comparison between C61, baseline and premium gear steels. Shown hardness corresponds to center of an air-cooled bar of given diameter.

5.3. Effect of Over-Aging on Carbide Dissolution

Ultimately a material's resistance to both bending and contact fatigue depends on the mechanical stability of its microstructural constituents. Dissolution of strengthening carbide dispersions, as discussed in Section 2.1.1.3, is one such mechanism for such microstructural degradation of secondary hardening steels strengthened by nanometer-sized M_2C alloy carbides. Overaging these fine carbides is one possible means of providing mechanical stability that might translate into fatigue resistance even considering the expense of strengthening efficiency.

To investigate the possible effects of overaging on mechanical precipitate stability, rolling contact fatigue (RCF) tests were performed on an extra sample of C69M3B, a precursor alloy of C69. Once fabricated and carburized (see Section 3.2.8), the C69M3B NTN rod was tempered at 550°C for one hour, corresponding to the peak hardness condition, and four RCF tests completed on one half of the rod. A second heat treatment was then performed at 500°C for 5 hours in order to overage the M_2C strengthening dispersion. Four additional RCF tests were then completed on the remaining half of the NTN rod. Table 5.1 records the rolling contact fatigue results for both temper conditions:

Table 5.1. Rolling contact fatigue data for C69M3B tempered at at 550° for different times

1-hr Temper			5-hr Temper		
Run #	Duration (hrs)	Cycles (10^6)	Run #	Duration (hrs)	Cycles (10^6)
1	41.2	21.3	5	22.75	11.7
2	54.7	28.2	6	9.1	4.7
3	60.1	31.0	7	26.4	13.6
4	52.85	27.3	8	4.2	2.17

Test runs 6 and 8 stopped at very short times and did not result in sample failure. A small amount of scorching and increased wear of the balls and bearing cups after run 6 suggested the premature failure was due to over-worn cups, which were subsequently replaced. The poor outcome of run 8 was most likely due to the spalling of one of the balls instead of the sample, as a pit was observed on a ball after the test. These two data points were not included in the final results.

Figure 5.6 displays the rolling contact fatigue results for the two temper conditions of C69M3B in a Weibull probability plot. Even with the removal of the two failed runs, the five-hour, over-aging temper showed about a 50% reduction in RCF life compared to the 1-hour peak aging heat treatment. This could be due to several different factors, the first of

which is just the reduction in hardness after the five-hour temper. Microhardness testing after over-aging found the hardness to be around 834 HV, or 65 HRC. This corresponds to the over-aged hardness reported by Brain Tufts at that temperature [**45**], and meets the desired hardness drop of 1-2 HRC from the peak hardness of C69M3B of 66 HRC. Another possible cause of this reduced performance may also be related to a significant level of oxidation that unfortunately occurred during the five-hour heat treatment. The oxide was carefully removed through spinning the sample on a lathe while lightly polishing with a 0.5-μm suspended alumina solution. This act of polishing may have altered the dimensions enough to have affected the test, or possibly the act of growing the oxide itself altered the sample surface.

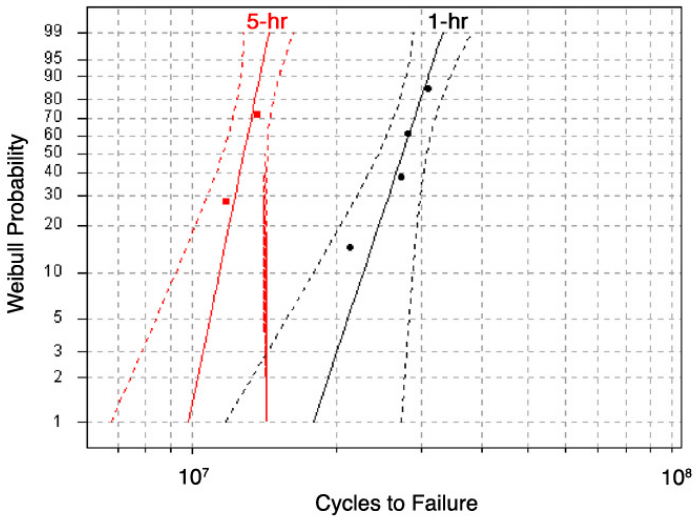

Figure 5.6. Weibull probability plot of C69M3B comparing peak and over-aged tempering conditions

Figure 5.7 compares the RCF results with previous results from the research of Brian Tufts[**45**]. The one-hour temper RCF tests match up fairly closely with those of Tufts, with a slight increase in life. This variation might be an additional reflection on the

extreme surface sensitivity of the NTN RCF test, with slight variations due to different sample heat treatment batches. When compared to standard M50 bearing steel, even the over-aged sample runs showed significant improvement over conventional alloys, however more runs and data points would be needed for any significant assessments to be made.

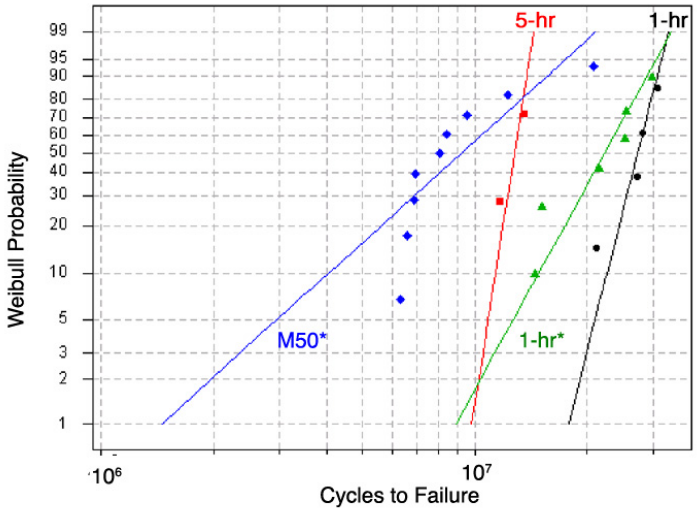

Figure 5.7. Weibull probability plot comparing new C69M3B RCF results with previous research by Tufts (denoted by *) [**45**]

No beneficial effect was therefore observed upon application of the overaging heat treatment, however the extreme nature of the NTN RCF test may render it unsuitable for observation of such phenomena. Roughened test balls used to accelerate failure in the interest of test time reduction effectively alter the nature of contact from one of pure rolling to one with a significant amount of impact loading from test ball asperities. The applied stresses from such loading are very localized to the specimen surface and would subsequently be much more sensitive to the absolute hardness, as observed by the decreased performance of the over aged C69M3B NTN bars. Any possible benefit

from over-aging of precipitate dispersions would more likely be observed in rolling/sliding conditions where maximum stresses occur below the surface.

CHAPTER 6

Cu-Bearing Alloy Design

For many applications, C61's extensive alloying additions make it too expensive. A large portion of this material cost is due to its high cobalt content, which at approximately \$20-30/lb is approximately 10 times more expensive than other common alloying elements such as nickel and chromium [**2**].

In an effort to reduce the material cost of these secondary-hardening steels, experimental alloys will be developed where the cobalt content is significantly reduced or eliminated. To counteract the subsequent loss in temper resistance previously provided by Co, BCC Cu precipitates will be incorporated to provide an additional means of precipitation strengthening as well as act as supplemental heterogeneous nucleation sites for the M_2C strengthening dispersion. Four compositions will be designed, aimed at exploring the Cu-Co composition space shown schematically in Figure 6.1.

The chosen levels of Cu alloying additions represent typical (0.9 at%) as well as elevated (3.3 at%) levels of Cu when compared to other Cu-bearing steel alloys. Explored cobalt contents correspond to completely eliminated levels (0 at%) for maximum cost savings as well as significantly reduced levels (5.8 at%) where material cost is still lowered yet maintaining sufficient Co content levels to observe its effect on secondary hardening. Using this design matrix, the relative effects of Cu and Co contents on secondary hardening can be observed.

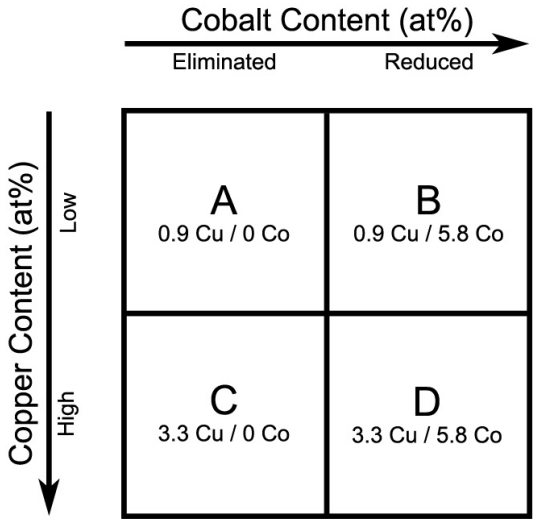

Figure 6.1. Co-Cu composition space as explored by four experimental alloy designs

Figure 6.2 outlines the system flow block (or Olson diagram) for secondary hardening gear steels where BCC Cu precipitation is now incorporated. The main microstructural subsystems consist of the lath martensite matrix and the dual strengthening dispersions of $(Cr,Mo,V)_2C$ alloy carbides and BCC Cu clusters.

6.1. Target Design Parameters

The design optimization process for such a microstructural system is illustrated in Figure 6.3 and consists of three main steps, the first of which is setting the strength level. Here the various strengthening contributions from the different microstructural systems are outlined and related to requisite alloy additions, specifically the carbon and copper levels required for the specified amounts of M_2C and BCC copper strengthening dispersions.

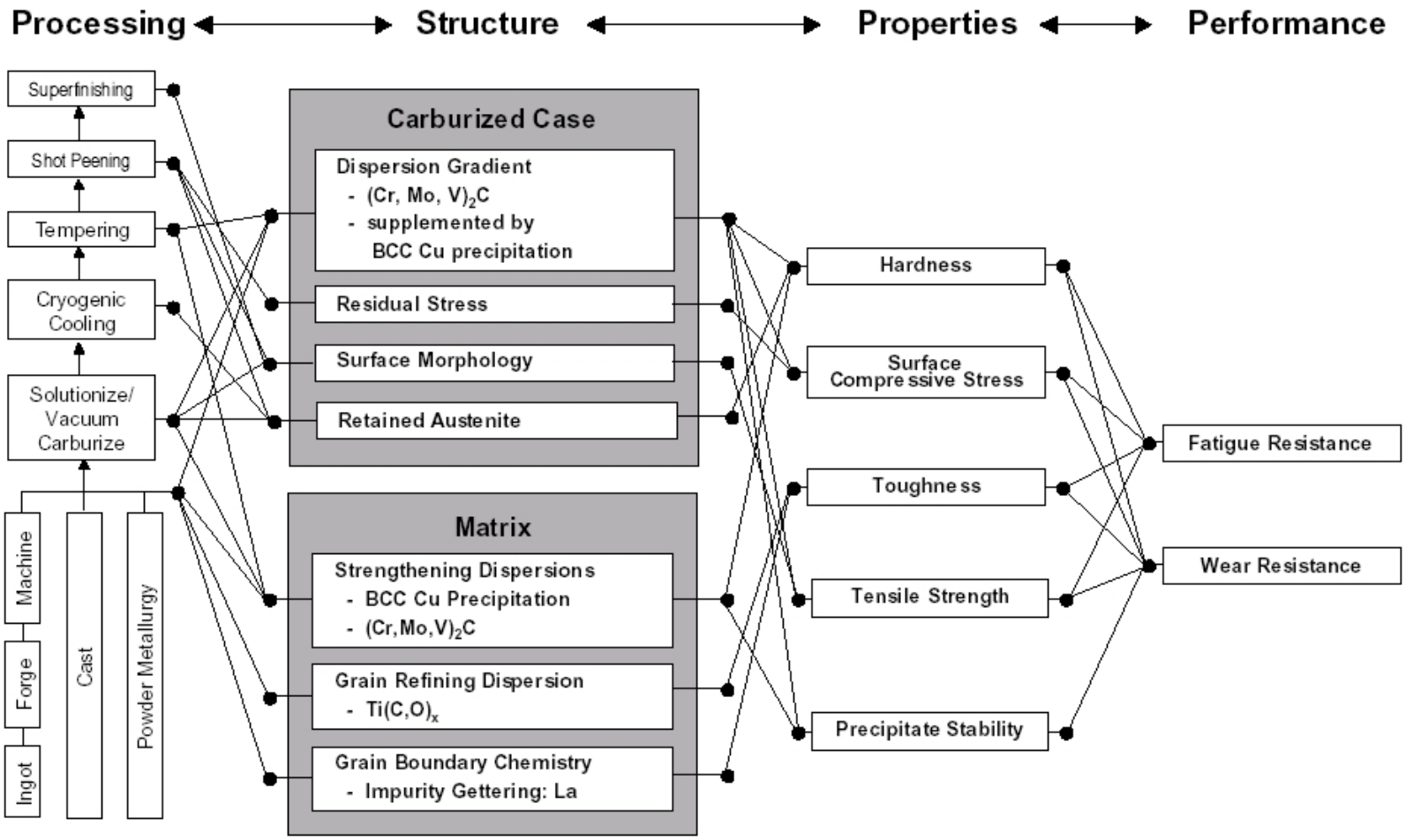

Figure 6.2. Systems flow block diagram of secondary hardening gear steel with incorporation of BCC Cu precipitation

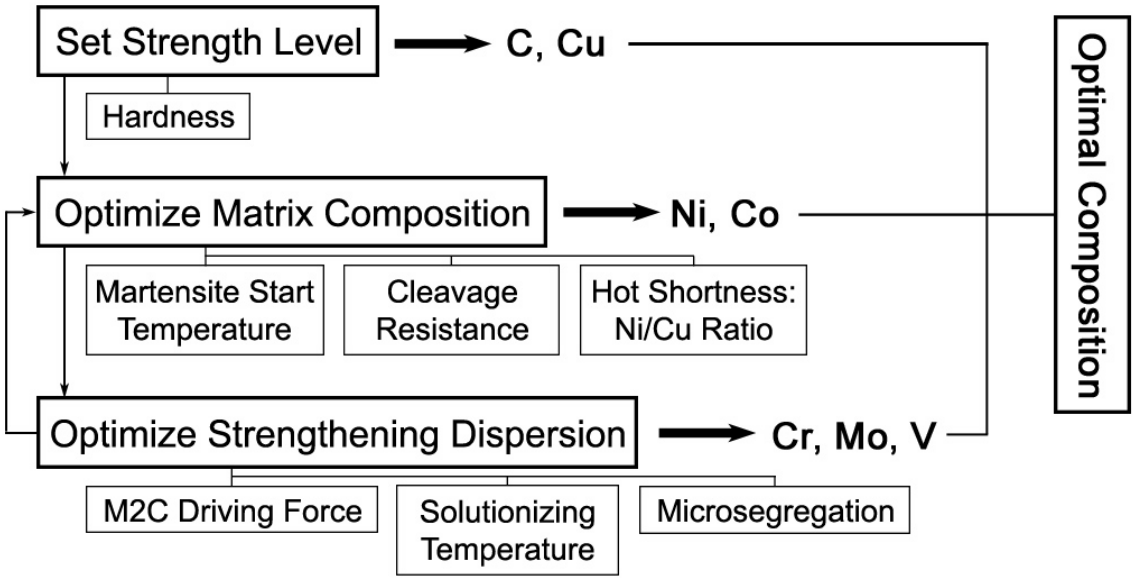

Figure 6.3. Design optimization process for Cu-bearing secondary hardening steels

The second step is to optimize the matrix composition through the additions of Ni and Co. The role of Ni in the tempered martensite matrix is to promote cleavage resistance by increasing the surface energy and associated Griffith work of brittle separation of {100} planes, where brittle fracture of BCC structures typically occur [**33**]. In the case of Cu-bearing steels, Ni has also experimentally been shown to prevent hot shortness when present in equal or greater amount than Cu [**101**]. However, as an austenite-stabilizing element, Ni strongly lowers the M_S temperature. Maintaining a sufficiently high M_S temperature ensures complete transformation to lath martensite, which not only exhibits superior toughness over plate martensite, but is also a highly dislocated structure conducive to M_2C carbide heterogeneous nucleation. An M_S temperature above 150°C ensures complete transformation to lath martensite upon quenching, but by increasing the

driving force for transformation through cryogenic treatments, a minimum temperature of 100°C is sufficient. As previously discussed, Co is added for temper resistance, but it also has the added benefit of raising the M_S temperature. Due to the emphasis on lowering material cost, however, Co contents will be fixed for the design of these alloys. Therefore, to optimize the matrix composition, one must balance the conflicting objectives of maximizing Ni for toughness and hot-shortness resistance and of maintaining a sufficiently high M_S temperature (>100°C) to ensure complete transformation to lath martensite. For alloys high in Co, care must be taken to avoid the embrittling Sigma phase, ensuring it is thermodynamically unstable ($-\Delta G_\sigma$).

The third step in the design optimization process focuses on optimizing the M_2C carbide strengthening dispersion by adjusting the relative amounts of the carbide forming elements Cr, Mo and V. The major objective is to maximize the thermodynamic driving force for M_2C precipitation (ΔG_{M_2C}). This must be balanced, however, against processing considerations, such as the solutionizing temperature (T_S) and microsegregation. Solutionizing is necessary to fully dissolve any primary carbides since, in addition to being deleterious to mechanical properties, they also tie up carbon and carbide forming elements that are needed for the M_2C strengthening dispersion. In the interest of reducing processing costs, it is desirable to minimize the temperature at which this takes place, preferably below 1050°C. Microsegregation can also occur during ingot solidification as certain elements, particularly heavy elements such as Mo, partition to either the liquid or solid phase. Prolonged homogenization treatments to eradicate this are an added cost, and these compositional fluctuations, as measured by the microsegregation amplitude (δ), are constrained to be less than a factor of 4.

Table 6.1. Targeted design parameters for experimental Cu-bearing secondary hardening steels

Parameter	Target
Case Hardness	894 VHN (67 Rc)
Core Hardness	392 VHN (40 Rc)
Case M_S	$> 100°C$
Core M_S	$> 300°C$
T_S	$< 1050°C$
Ni/Cu	≥ 1
ΔG_{M_2C}	Maximize (> 20 kJ/mol)
ΔG_σ	Minimize (<0)
δ_X	< 4

Once the appropriate combination of carbide formers has been found, a second iteration of matrix optimization calculations can be done to account for their effect on the M_S temperature. This iterative procedure is carried out until all of the design parameters have been optimized. Table 6.1 lists the target design parameters for the experimental Cu-bearing gear steels.

6.2. Design Models

6.2.1. Ni-Co Secondary Hardening Steel Strength Model

To model the strengthening contributions for both the lath martensite matrix as well as the M_2C carbide dispersions, the Ni-Co secondary hardening steel strength model developed by Wise will be used [**40**]. This approach models the strength as Equation 6.1:

$$\tau = \tau_{SS} + \tau_P + \tau_D + \tau_{\alpha'} \tag{6.1}$$

where τ is the total strength consisting of the linear superposition of solid solution strengthening (τ_{SS}), precipitation strengthening (τ_P), dislocation strengthening (τ_D) and

the intrinsic strength of the lath martensite substructure ($\tau_{\alpha'}$). To describe these various strengthening contributions, Wise applied relevant theories to model existing data. For solid solution strengthening, he used a model after Labusch [**102**] :

$$\tau_{SS} = 0.0078G\left(|\epsilon'_G| + 2\,|\epsilon_a|\right)^{\frac{4}{3}c^{\frac{2}{3}}} \tag{6.2}$$

where G is the matrix elastic modulus, ϵ'_G the solute modulus misfit and ϵ_a the solute size misfit at a specific solute atomic fraction denoted by c. The model specifically takes into account the matrix concentrations of Co, Ni, Cr and Mo, the equilibrium values of which are determined using Thermo-Calc incorporated through CMD.

The precipitation strengthening contribution has two forms, corresponding to shearable ($\tau_{P,shear}$) and non-shearable ($\tau_{P,Orowan}$) particles:

$$\tau_{P,shear} = 0.65\frac{Gb}{(L-2r)}\left(\frac{G_p r}{2\pi Gb}\right) \tag{6.3}$$

$$\tau_{P,Orowan} = 1.68\frac{Gb}{2\pi\sqrt{1-\nu}(L-2r)} ln\left(\frac{2r}{r_0}\right) \tag{6.4}$$

Shearable precipitates were modeled using Equation 6.3 following the modulus strengthening approach by Hornbogen [**103**]. Here, G is the shear modulus and b the Burger's vector of the matrix, and G_p, r and L the precipitate's shear modulus, radius and inter-particle spacing, respectively. For over-aged, incoherent M_2C carbides the strengthening contribution is described in Equation 6.4 by the Orowan-Ashby equation [**104**] with combined edge and screw dislocation effects [**105**], where ν is the Poisson's ratio of the matrix and r_0 the dislocation core radius.

Dislocation strengthening is modeled using Keh and Weissman's strength dependency relation on dislocation density (ρ) [**106**] adapted to include recovery effects that take place during tempering as outlined by Leslie [**107**] :

$$\tau_D = 0.38Gb\sqrt{\rho} \approx 145 - 60\left(\frac{V}{V_f}\right)_{M_2C} \quad (VHN) \tag{6.5}$$

In Equation 6.5, the degree of recovery is proportional to the fraction of M_2C precipitation relative to the final equilibrium volume fraction (V_f). Assuming a value of V/V_f of 0.8, the strength increment due to dislocations is 97 VHN. The final strengthening component is that provided by the lath martensite matrix itself, and is expressed by the Hall-Petch expression in Equation 6.6:

$$\tau_{\alpha'} = \tau_\alpha + kd^{-\frac{1}{2}} \equiv \ 65 \ \ (VHN) \tag{6.6}$$

The empirical value of 65 VHN has been found to agree well with typical grain sizes (d) and prefactor fitting values (k) for low carbon steels [**40**].

6.2.2. BCC Cu Precipitation Strength Model

To describe the strengthening increment provided by the BCC Cu precipitates, the general approach outlined by Russell and Brown [**50**] will be used, where the maximum precipitation strengthening is related to BCC Cu phase fraction by Equation 2.10. Based on the square-root strengthening dependence on particle volume fraction, Saha generated an empirical Cu strengthening model using an empirical correlation between hardness and yield strength for various steels as well as experimental data from Russell and Brown [**50**], as shown in Figure 6.4.

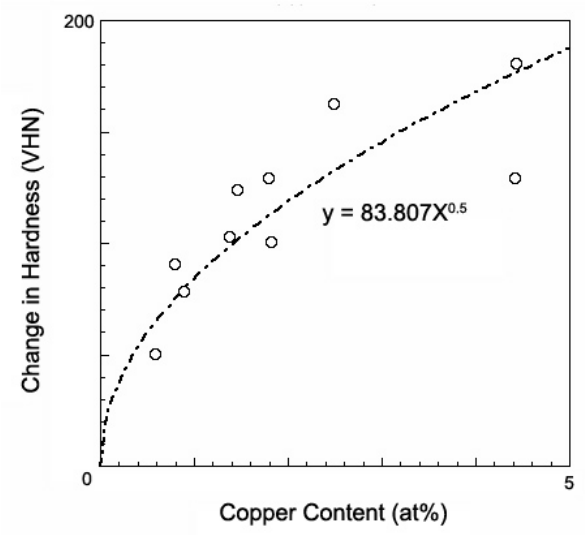

Figure 6.4. Empirical Cu precipitation strengthening model developed by Saha [**58**]

The resultant strengthening expression based on atomic percent (X) Cu shown is shown in Equation 6.7:

$$\Delta\tau_{(VHN)} = 83.807X_{Cu}^{\frac{1}{2}} \tag{6.7}$$

6.2.3. Martensite Start Temperature Model

The Ghosh and Olson model [**79**] was used to model the composition dependence of the martensitic transformation temperature (M_S). In this approach, the martensite nucleus is modeled as a set of coherency anti-coherency dislocations that must overcome a frictional force in order to propagate. Transformation is thus predicted to occur when the thermodynamic driving force to transform from FCC austenite to BCT martensite ($-\Delta G_{FCC\rightarrow BCT}$) is sufficient to overcome this frictional barrier (w_f) as shown in Equation 6.8:

$$-\Delta G_{FCC\rightarrow BCT} = w_f + K_1 \tag{6.8}$$

where K_1 is a constant including strain energy, interfacial energy and defect potency. The frictional work encountered by the propagating interface is a function of the composition of the matrix, specifically solid solution strengthening due to the various alloying elements, as expressed in Equation 6.9:

$$w_f = \sqrt{\sum_i \left(K^i X_i^{\frac{1}{2}}\right)} + \sqrt{\sum_j \left(K^j X_j^{\frac{1}{2}}\right)} + \sqrt{\sum_k \left(K^k X_k^{\frac{1}{2}}\right)} + K^{Co} X_{Co}^{\frac{1}{2}} \tag{6.9}$$

where values of K are solid solution strengthening coefficients and X the mole fractions for the respective subgroups of alloying elements: i=C, N; j=Cr, Mn, Mo, Nb, Si, Ti, V; k=Al, Cu, Ni, W.

6.2.4. Microsegregation Model

To ensure acceptable processability, microsegregation amplitudes of each alloy design are approximated using Scheil simulations [**108**]. By assuming infinite diffusion in liquid phases and no diffusion in solid phases, simulations can be quickly completed using solid/liquid equilibrium calculations that are repeatedly executed in Thermo-Calc with decreasing temperature. The resultant composition profiles are expressed as a function of calculated solid phase fraction and correspond to composition variation across dendrites during solidification.

6.3. Design Implementation

6.3.1. Strengthening Components

The first step in the actual design process is to determine the levels of carbon and copper needed to fulfill the strength requirements of 392 VHN (40 R_C) for the base alloy with

a carburized case reaching a maximum hardness of 894 VHN (67 R_C) at the surface. The strength of each base alloy is derived from three microstructural components: the tempered martensite matrix (τ_M), BCC Cu precipitates (τ_{Cu}) and M_2C carbides ($\tau_{M_2C}^{core}$). Additional M_2C carbides formed from carbon introduced during carburization provide the increased strength of the carburized case ($\tau_{M_2C}^{case}$). The total strength of each alloy (τ_{Total}) will thus be the combination of each of these strengthening increments, as expressed in Equation 6.10:

$$\tau_{Total} = \tau_M + \tau_{Cu} + \tau_{M_2C}^{core} + \tau_{M_2C}^{case} \tag{6.10}$$

The strength contribution from the tempered martensite matrix is derived by subtracting the precipitation strengthening contribution (τ_P) from the total secondary hardening strength model of Equation 6.1:

$$\tau_M = \tau - \tau_P = \tau_{SS} + \tau_D + \tau_{\alpha'} \tag{6.11}$$

From Equation 6.6, the value for the intrinsic strength of the lath martensite structure ($\tau_{\alpha'}$) is 65 VHN. The strength increment due to the dislocation density within this lath martensite structure (τ_D) is 97 VHN as given by Equation 6.5 assuming an 80% final M_2C volume fraction as compared to the equilibrium volume fraction. The final strengthening component of the martensite matrix comes from solid solution strengthening (τ_S) and will vary with composition according to Equation 6.2. Preliminary calculations for solid solution strengthening using the investigated Co content range of 0 to 5.8 at% and similar values for Ni and Mo resulted in an average value of approximately 30 VHN. The sum of

these three strengthening increments equaling 192 VHN was used as a first approximation for τ_M.

The value for τ_{Cu} corresponds to one of the two selected levels of Cu alloying additions of 0.9 and 3.3 at%. Using Equation 6.7, these levels of Cu translate into 80 and 151 VHN respectively.

The remaining increments of strength due to M_2C carbides were then translated to requisite carbon levels through Wise's model for secondary hardening steels [**40**]. First approximations for the required carbon contents were found using a generic form of the M_2C precipitation strengthening model showing the effect of carbon content on hardness, an example of which is shown in Figure 6.5. An M_2C particle diameter of 4nm was chosen to reflect over-aging heat treatments commonly employed to ensure complete dissolution of paraequilibrium cementite to maintain adequate toughness. The phase fraction of M_2C carbide utilized in precipitation strengthening was set to 80% of its ultimate equilibrium phase fraction ($V/V_f = 0.8$).

Based on these estimates, a preliminary composition was assumed by setting the carbide forming elements (Cr, Mo, V) to equal atomic concentrations that in sum equaled twice that of the atomic level of carbon in order to satisfy the M_2C stoichiometry. Nickel levels were set at twice that of copper and the M_2C radius and relative volume fraction (V/V_f) set to 4nm and 0.8, respectively. Based on these preliminary compositions, the calculated hardness values were determined as a function of carbon content to find the final carbon levels as shown in Figure 6.6.

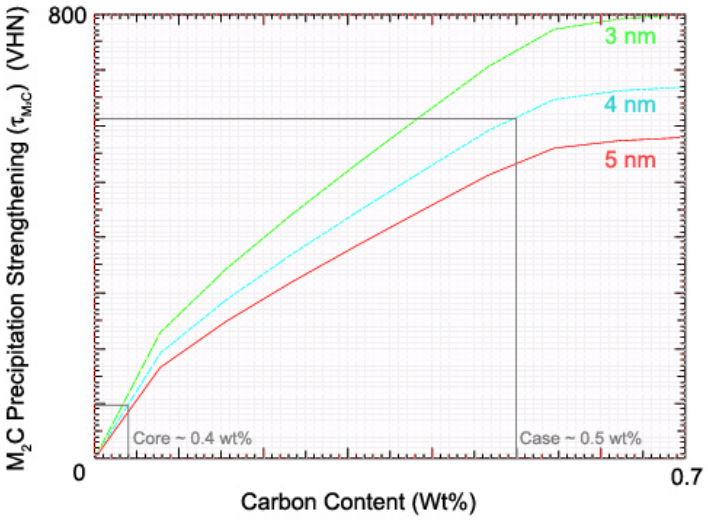

Figure 6.5. Prelimary carbon content requirement estimates using M_2C precipitation strengthening model

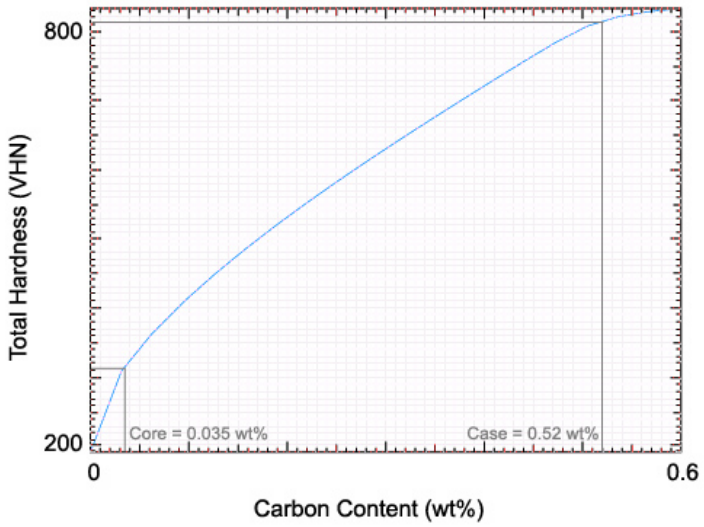

Figure 6.6. Final carbon content assessment

6.3.2. Matrix Optimization

The second step in the design methodology is to optimize the matrix composition. First the cobalt levels were set to pre-selected values 0 at.% for the low-Co alloys and 5.8 at.%

for high-Co alloys. Next, the effect on M_S due to Ni content was calculated to determine the maximum amount of Ni that could be added in order to resist brittle fracture. An example of this calculation is shown in Figure 6.7. A final calculation is done for the thermodynamic instability of the brittle Sigma phase ($-\Delta G_\sigma$) ensuring it is sufficiently avoided.

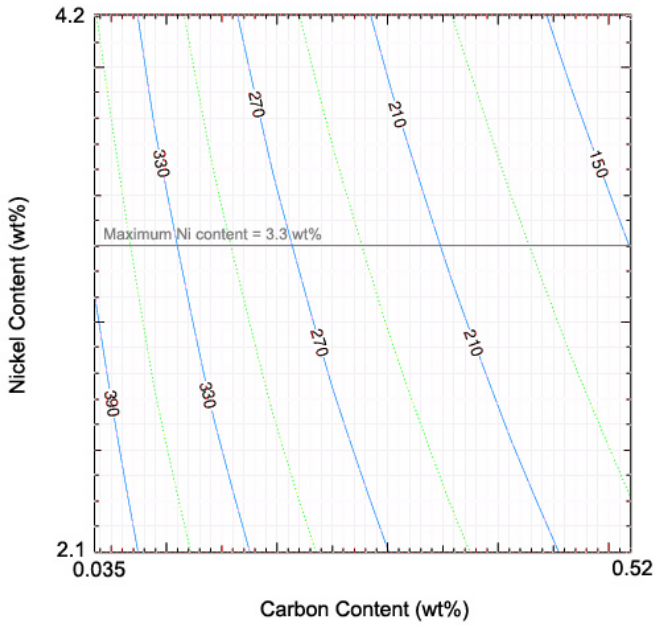

Figure 6.7. Maximum Ni content calculation for target case M_S temperature of 150°C

6.3.3. Carburized Case Optimization

The final design step was to optimize the M_2C strengthening dispersion while meeting processing requirements of a reasonable solutionizing temperature ($T_S < 1050$°C) and

minimum microsegregation ($\delta_x < 4$). Using Thermo-Calc, a pseudo-ternary phase diagram varying the carbide forming elements within the M_2C stoichiometric limits was calculated at the desired solutionizing temperature of 1050°C, as shown in Figure 6.8.

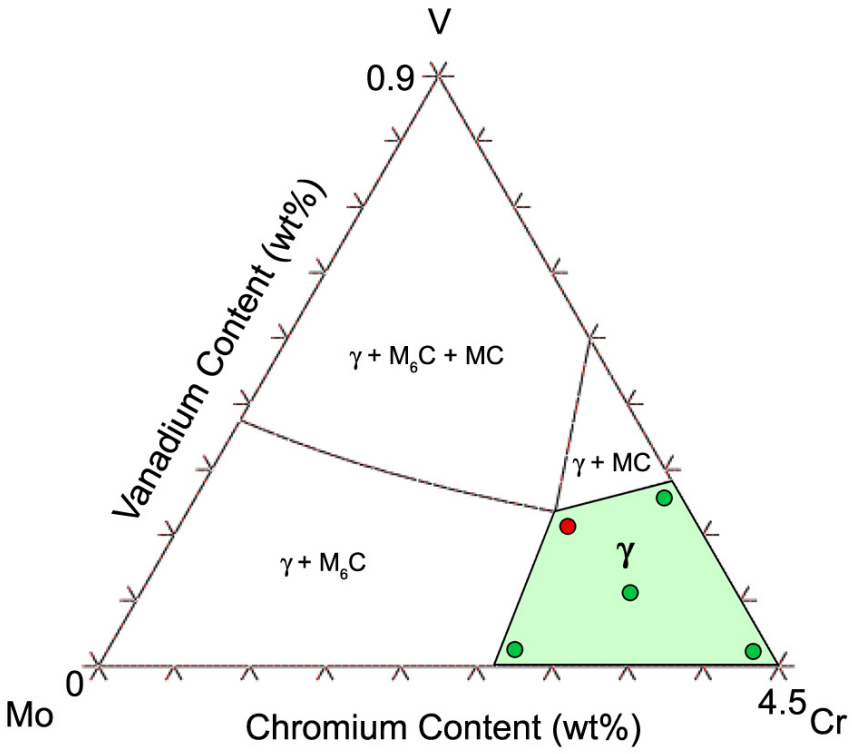

Figure 6.8. Calculated pseudo-ternary phase diagram at target solutionizing temperature of 1050°C. Five points are shown in austenite-only phase field marking investigated compositions, with the red, highlighted circle representating the composition with maximum M_2C driving force.

Within the observed austenite-only phase field, several exploratory compositions were selected for each of the four Cu-Co combinations and the M_2C driving force for precipitation was calculated using CMD. In each of the four alloy designs, the austenite-only phase field was found to be in the Cr-rich corner of the pseudo-ternary phase diagram,

and within this region, the maximum M_2C driving force was always found to correspond to the maximum vanadium concentration. Figure 6.8 shows five exploratory (Mo, Cr, V) compositions selected for one of the Cu-Co combinations with the optimum (Mo, Cr, V) combination located at the maximum V content within the austenite phase field.

Scheil simulations were calculated for each of these compositions, an example of which is shown in Figure 6.9. All composition amplitudes were found to be within acceptable levels.

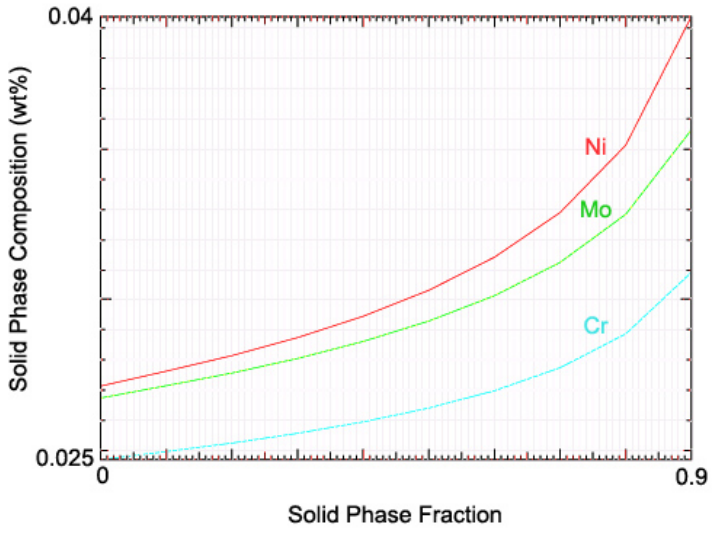

Figure 6.9. Example Scheil simulations for microsegregation amplitude calculations

6.4. Design Summaries

Design parameters were then re-calculated using the final compositions and were found to be within the required constraints. Table 6.2 summarizes the designed compositions for the four experimental alloys with corresponding predicted design parameters listed in Table 6.3.

Table 6.2. Designed compositions for experimental Cu-bearing alloys in weight percent

Design	C(Core)	C(Case)	Ni	Cr	Mo	V	Cu	Co	Fe
A	0.035	0.52	3.3	2.6	3.13	0.2	1.05	0	bal.
B	0.035	0.52	5.5	2.6	3.32	0.1	1.05	6	bal.
C	0.015	0.42	3.7	1.6	3.48	0.15	3.7	0	bal.
D	0.015	0.42	5.5	2.5	1.72	0.1	3.7	6	bal.

Table 6.3. Predicted design parameters for experimental Cu-bearing alloys

	A	B	C	D
Case Hardness (VHN)	894	910	890	868
Core Hardness (VHN)	396	408	426	427
Case M_S(°C)	115	118	92	113
Core M_S(°C)	327	365	277	333
T_S (°C)	1032	1040	1030	1016
Ni/Cu	3.1	5.2	1.0	1.5
ΔG_{M_2C}(kJ/mol)	20.4	21.7	20.4	19.0
ΔG_{σ}(kJ/mol)	-1.8	-1.6	-2.1	-2.8
δ_{Mo}	1.3	1.3	1.6	2.4

CHAPTER 7

Cu-Bearing Alloy Prototype Evaluation

For each designed composition, a prototype 30-lb ingot was prepared as outlined in Chapter 3. Table 7.1 compares the resultant measured composition of each ingot with its corresponding design. The most signficant composition discrepency was the Cu content of alloy B, where the measured Cu content was almost three times that of the designed 1.0 wt%. Carburized case carbon measurements were also much higher than designed levels for alloys C and D. Light micrographs taken from cross-sections of through-carburized specimens used for case carbon measurement revealed high levels of retained austenite and high-carbon plate martensite indicative of overcarburization. In the larger, gear tooth-sized specimens used for all other analyses, overcarburization was not observed to occur, however the measured effective case depth of 2 mm was approximately twice that of A and B alloy specimens, which achieved the targeted 1 mm case depth. The thickness of carbon measurement specimens was chosen to be 1.5 mm in order to achieve a through-carburized carbon content approximately equivalent to the surface, or maximum, carbon content of the targeted 1 mm carburization profile. Because of the constant carbon flux boundary conditions intrinsic to high temperature vacuum carburizing, this excess carbon introduced into C and D alloy specimens accumulated in the thin, through-carburized samples used for case carbon measurement with the subsequent overcarburization resulting in elevated carbon measurements not representative of larger specimens.

Table 7.1. Measured ingot compositions and designed compositions for experimental Cu-bearing alloys in weight percent. *Carburized case carbon measurements taken from through-carburized specimens.

	A		B		C		D	
	Design	Measured	Design	Measured	Design	Measured	Design	Measured
Ni	3.3	3.2	5.5	4.9	3.7	3.6	5.5	4.9
Mo	3.1	2.9	3.3	3.1	3.5	3.2	1.7	1.6
Cr	2.6	2.3	2.6	2.2	1.6	1.4	2.5	2.2
Co	0	0	6.0	5.5	0	0	6.0	5.5
Cu	1.0	1.0	1.0	2.7	3.7	3.3	3.7	3.9
V	0.2	0.2	0.1	0.1	0.1	0.1	0.1	0.1
C	0.035/0.52	NA/0.5*	0.035/0.52	NA/0.5*	0.015/0.42	NA/0.6*	0.015/0.42	NA/0.9*
Fe	bal.	bal.	bal.	bal.	bal.	bal.	bal.	bal.

7.1. Matrix Microstructure

Figure 7.1a shows a representative micrograph of the tempered lath martensite matrix achieved in all four experimental alloys. No retained austenite or primary carbides were visible in any of the alloys. X-Ray diffraction (XRD) of the carburized case verified the existence of a fully martensite matrix, as shown by the lone broadened BCC peaks characteristic of tempered martensite in Figure 7.1b. The apparent complete transformation to martensite suggests that the current M_S model is adequate for the design of Cu-bearing gear steels, and the avoidance of large primary carbides verifies the solution thermodynamics correctly predicted the austenite-only phase field of the pseudo-ternary phase diagram.

Additionally, all four alloys were successfully hot rolled, suggesting the minimum Ni/Cu ratio of 1 was sufficient to prevent hot shortness. This ratio may indeed represent a minimum allowable limit, since the hot rolled plate for alloy C, which did have the lowest Ni/Cu ratio of 1, was reported to exhibit patches that persistently glowed during cooling after the normalization heat treatment. Further analysis of the oxide scale is needed to see if this behavior is due to the same Cu segregation that induces hot shortness.

7.2. Solution Temperature

Solutionizing studies were conducted on the four experimental alloys to ensure complete compatibility with existing C61/C67 heat treatment regimens. Solutionizing heat treatments must be able to fully dissolve primary carbides and achieve a fully austenitic state to maximize carbon solubility during carburization. Carburized samples were solutionized in an argon furnace at various times for one hour, quenched in oil and then

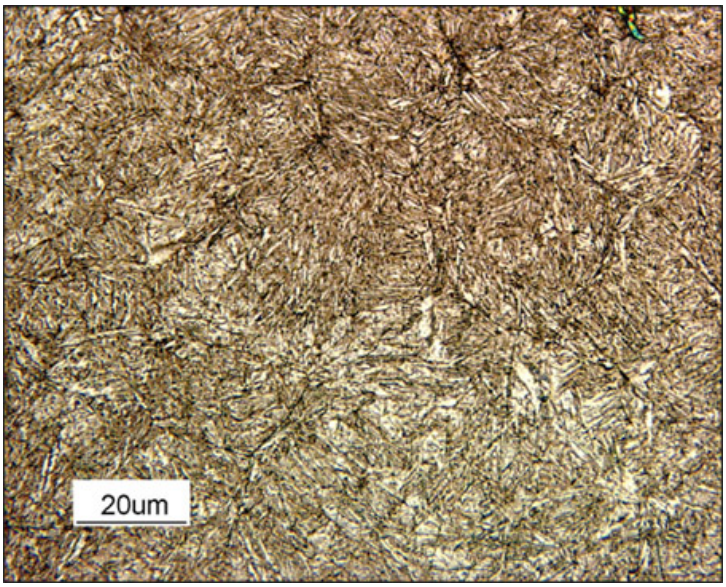

(a)

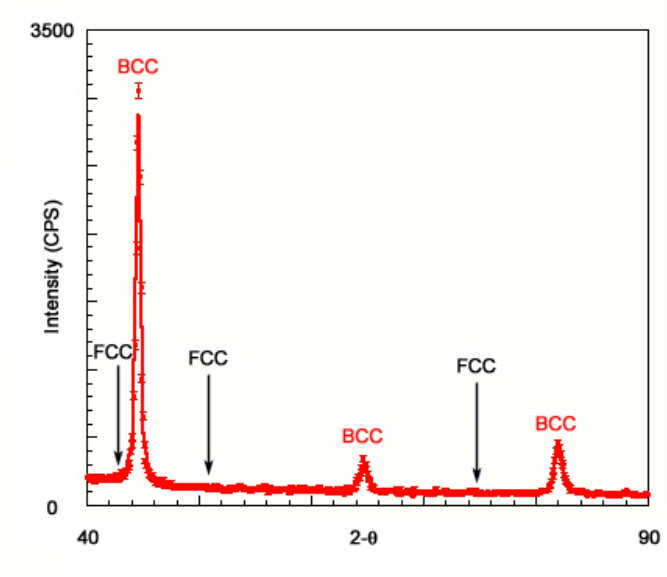

(b)

Figure 7.1. Lath martensite matrix exhibited by all four Cu-bearing alloys as shown by example a) light microscopy and b) x-ray diffraction

soaked in a liquid nitrogen bath for 30 minutes. A one-hour stage I temper (200°C) was then used to counter possible autotempering affects experienced during quenching. Figure 7.2 shows measured microhardness levels for the carburized case (100μm depth) for the four experimental alloys at solutionizing temperatures ranging from 1050 to 1250°C. Error bars represent ± one standard deviation of the averaged microhardness measurements. For reference, measured Cu and Co contents (wt%) are listed. Because representative case carbon measurements were not able to be obtained for alloys C and D, designed carbon contents (wt%) are listed instead. For all alloys, hardness generally decreased with increasing solutionizing temperatures, suggesting complete dissolution of primary carbides at or before the designed solutionizing temperature of 1050°C with slight softening occurring due to grain coarsening. Significant scatter in the hardness measurements arose due to uneven carburization of puck specimens, however average hardness values for all solutionizing temperatures exceeding 1050°C were either below or within the standard deviation of the 1050°C measurements. For the Cu-bearing alloys there is therefore no observed benefit for elevating solutionizing temperatures beyond the 1050°C currently used in existing heat treating regimes.

7.3. Tempering Response

Figure 7.3 shows the microhardness response for both the carburized case (100 μm depth) and the core of all four alloys at a tempering temperature of 482°C for up to 72 hours. Two distinct precipitation phenomena are observable, as represented by two hardness local maxima, one occurring around 12 hours and another later around 40 hours.

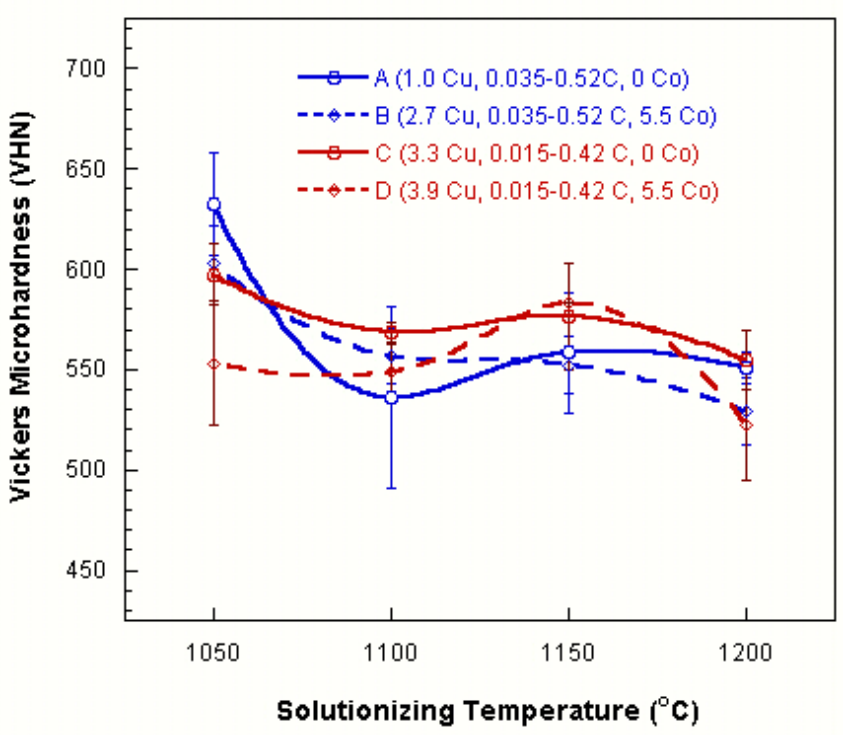

Figure 7.2. Solutionizing study for experimental Cu-bearing alloys

Comparing the peak hardness values with the hardness targets, all four alloys had a core hardness about 20-30 VHN lower than the target of 392 VHN, as shown in Figure 7.4. More important was the fact that the case hardness was approximately 200 VHN lower than the target case hardness of 894 VHN. Alloy B exhibited the highest hardness in both the case and core, however, it also had a measured Cu content over 2.5 times greater than its design due to chemistry control issues during melting. This additional Cu is predicted to provide an extra 50 VHN based on Equation 6.7 and correlates well with its increased strength over alloy A, which has equivalent carbon levels and Cu levels closer to the design. Considering this observed gain in hardness can be specifically attributed to excess Cu, as well as the fairly good agreement between the predicted and achieved hardness levels in

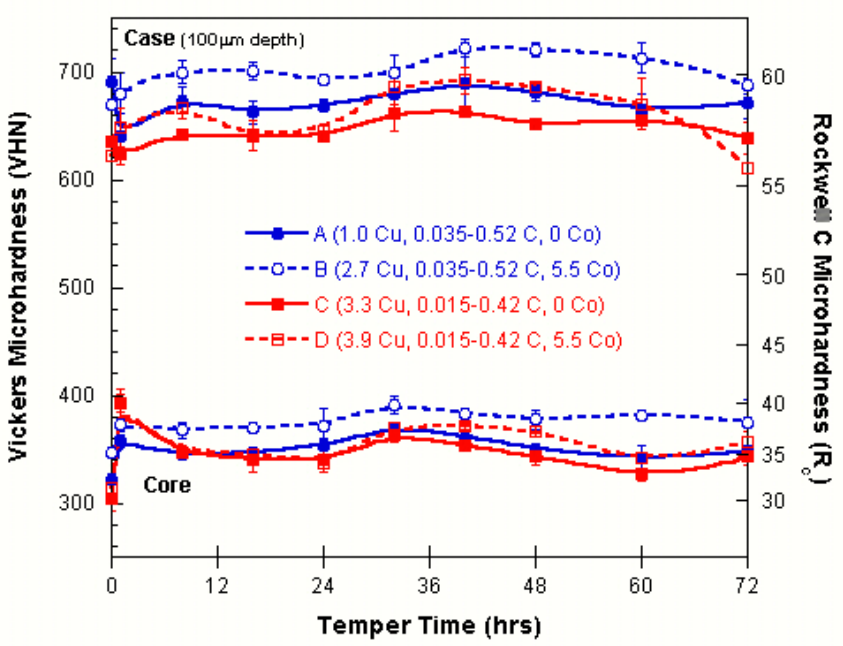

Figure 7.3. Microhardness response of the carburized case and core of the four experimental alloys tempered at 482°C

the predominantly Cu-strengthened core, preliminary assessment suggests predicted levels of Cu precipitation and related strength were for the most part achieved. The significant loss in strength in the case is greater than the anticipated strength increment due to the Cu alone and can most probably be associated with the M_2C strengthening dispersion.

An elevated tempering temperature of 510°C was also investigated as a means of possibly accelerating the M_2C precipitation kinetics. Figure 7.5 shows the resultant microhardness response for all four experimental alloys for both the carburized case (100 μm depth) and core tempered at 510°C. When compared to Figure 7.3, the same core hardness peak at 1-hr can be observed, corresponding to BCC Cu precipitation as well as the local hardness maxima around 12 hrs for the carburized case. At 510°C, however, this local case hardness maximum at 12hr is broader and is not followed up by a second

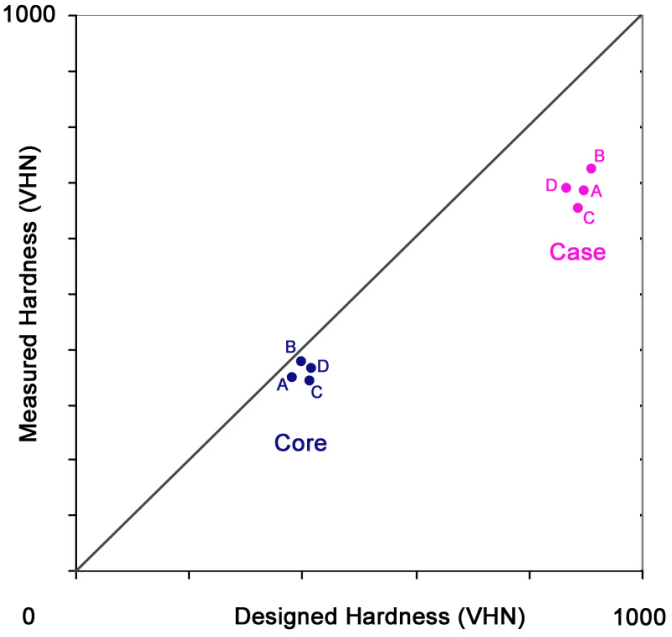

Figure 7.4. Comparison between designed and measured hardness levels for the carburized case and core for Cu-bearing experimental alloys

hardness peak around 48-hr such as was observed for tempering at 482°C. For tempering at 510°C the peak alloy case hardness was around the 12-16 hour range. The magnitude of the total peak hardness achieved by the four alloys was lower at the higher tempering temperature, with the exception of alloy B, as summarized in Table 7.2.

Table 7.2. Peak carburized case hardness comparison for tempering temperatures of 482°C and 510°C

	Peak Case Hardness (VHN)		Corresponding Core Hardness (VHN)		Hardness Difference (482°C-510°C)(VHN)	
Alloy	482°C	510°C	482°C	510°C	Case	Core
A	688.9	681.9	362.3	351.7	7	10.6
B	722.5	739	383.5	383.9	-16.5	-0.4
C	663.1	659.4	353.7	331.4	3.7	22.3
D	692.3	651.5	372.0	358.6	40.8	13.4

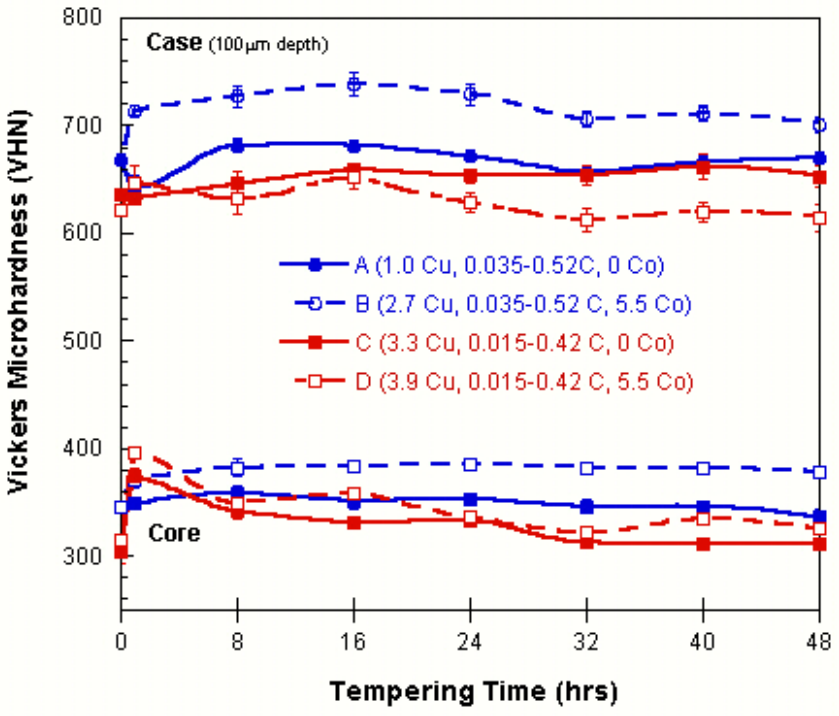

Figure 7.5. Microhardness response of the carburized case and core of the four experimental alloys tempered at 510°C

7.4. LEAP Microstructural Analysis

Figure 7.6 shows LEAP reconstructions for alloy B at tempering times of 1, 12 and 48 hours. Overall compositions for each dataset as well as the as-designed compositions and measured ingot compositions for alloy B are shown in Table 7.3. Calculated standard deviations of overall LEAP compositions using Equation 3.4 were all less than 0.5%. Overall compositions of LEAP datasets compared agreeably with the overall ingot composition measured with wet chemistry techniques. Reported Ni levels in LEAP datasets are inflated due to mass spectrum convolution with Fe. C, Co and Cu levels were systematically low as measured by the LEAP, suggesting preferential and/or anomalous field evaporation. To best reveal the precipitated phases in the reconstructions, only isoconcentration

surfaces for the Cu and M_2C precipitates are shown along with a 5% sampling of Fe atoms used to reveal the total analysis volume.

Table 7.3. Alloy B compositions (at%) for original design, wet chemistry measurements taken from ingot samples and the three overall compositions of LEAP datasets taken from samples of the three temper times

	Fe	Ni	Co	Cr	Mo	V	C (case)	Cu
Design	bal.	5.3	5.8	2.8	2.0	0.1	2.4	0.9
Measured	bal.	4.7	5.3	2.4	1.8	0.1	2.3	2.4
1-hr Temper	bal.	5.0	4.7	2.1	1.7	0.1	1.5	1.0
12-hr Temper	bal.	5.7	4.4	2.4	1.9	0.1	1.3	1.0
48-hr Temper	bal.	6.1	5.7	2.4	1.5	0.1	1.4	1.2

Each individual pink pixel represents one Fe atom. Isoconcentration surfaces used to outline Cu precipitates bound a concentration threshold chosen to be 5 at%. Threshold values for isoconcentration surfaces were chosen to be larger than intrinsic compositional variations to avoid noise while at the same time capture the clustering behavior and morphology of the precipitating species. The threshold value used to delineate the M_2C carbide precipitates included the combined levels of C, Cr, Mo and V set to a summed composition of 15 at%. Using these same isoconcentration threshold values to outline particles for each dataset, the number density for both Cu and M_2C precipitates was calculated by dividing the total number of observed precipitates by the respective analysis volume as calculated using Equation 1 as summarized in Table 7.4.

The volume of each constructed isoconcentration surface was used to calculate an equivalent sphere radius in order to quantify precipitate dimensions. Resulting size distributions for Cu precipitates and M_2C carbides are shown in Figure 7.7 and Figure 7.8 respectively. Asymmetry in the recorded size distributions can in part be attributed to the merging of nearby precipitates where isoconcentration surfaces touch and form a single

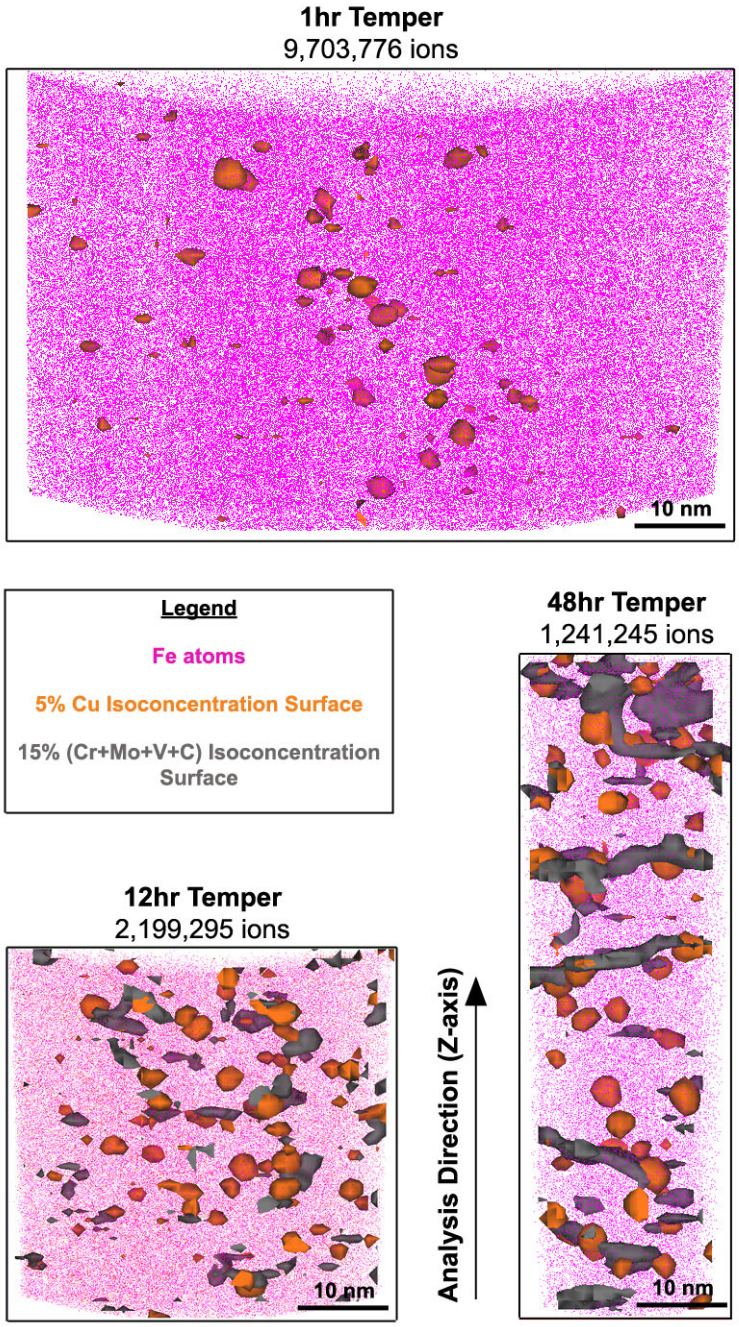

Figure 7.6. LEAP reconstructions for alloy B tempered at 1, 12 and 48 hours at 482°C

Table 7.4. Quantitative results from LEAP datasets taken from alloy B samples for the three tempering times

	Temper Time (hrs)	1	12	48
	Total # Ions	9703776	2199295	1241245
	Analysis Volume (nm^3)	190840.9	43252.8	24411.2
Cu	# precipitates	48	48	57
	Number Density (m^{-3})	2.5E+23	1.1E+24	2.3E+24
	$r_{typ.,1Dcomp.prof.}$ (nm)	1.0	1.0	1.2
	$r_{avg.,isoconc.surf.}$ (nm)	1.0±0.3	1.0±0.3	1.2±0.4
	$V_{f,typ.pptvol.}$	0.1	0.5	1.7
	$V_{f,isoconc.surfacevol.}$	0.1	0.6	2.4
M_2C-spheres	# precipitates	0	37	26
	Number Density (m^{-3})	0	8.6E+23	1.1E+24
	$r_{typ.,1Dcomp.prof.}$ (nm)	-	1.5	1.5
	$r_{avg.,isoconc.surf.}$ (nm)	-	1.1±0.3	1.2±0.4
	$V_{f,typ.pptvol.}$	0	1.2	1.5
	$V_{f,isoconc.surfacevol.}$	0	0.6	1.1
M_2C-rods	# precipitates	0	0	8
	Number Density (m^{-3})	0	0	3.3E+23
	$r_{typ.,1Dcomp.prof.}$ (nm)	-	-	4.0
	$r_{avg.,isoconc.surf.}$ (nm)	-	-	2.7±0.4
	$V_{f,typ.pptvol.}$	0	0	8.8
	$V_{f,isoconc.surfacevol.}$	0	0	2.7

volume. This resulted in a shoulder or secondary peak on the histograms at approximately double the radius upon which each distribution is centered. The M_2C carbide size distribution for the 48-hr temper condition also displayed a second population at larger sizes, corresponding to the over aged rod-shape morphology of several particles as seen in Figure 7.6. Two distinct precipitate morphologies, rod and sphere, were subsequently used to treat these different size distributions for the 48-hr tempering condition. The mean radius of each precipitate population ($r_{avg.,isoconc.surf.}$) for each temper time was then calculated and is reported in Table 7.4. The summed volume of all isoconcentration surfaces of each precipitate species was used to determine an approximation for the total precipitate

volume fraction ($V_{f,isoconc.surfacevol.}$) by dividing by the corresponding specimen analysis volume, also reported in Table 7.4.

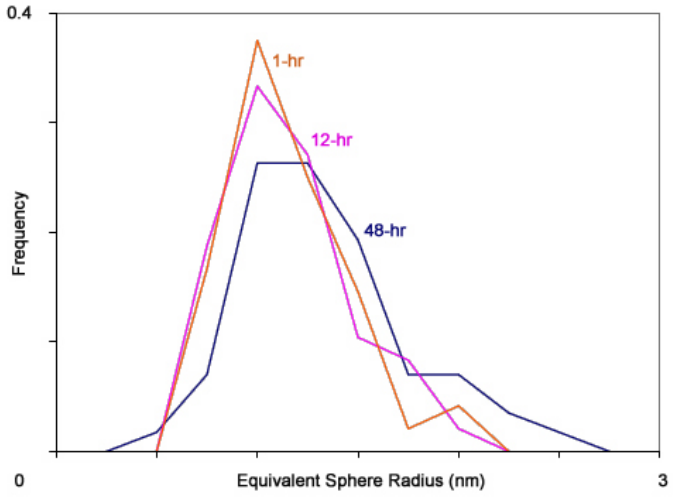

Figure 7.7. Size distribution of Cu precipitates in alloy B at three tempering times

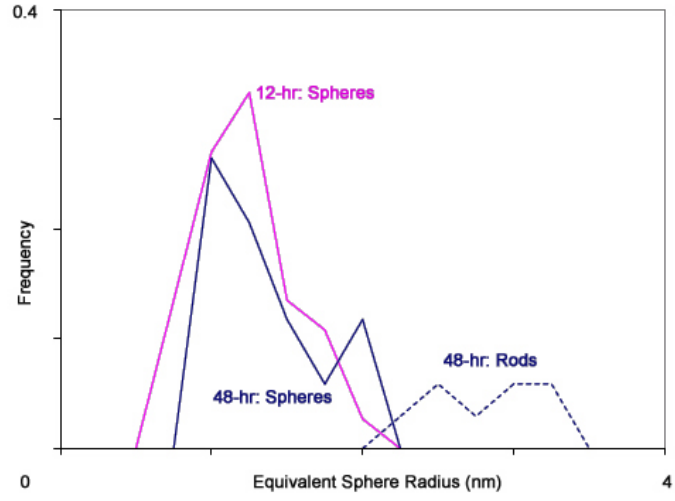

Figure 7.8. Size distribution of M_2C alloy carbides in alloy B at three tempering times

Care must be taken, however, when ascribing quantitative results to features observed in atom probe reconstructions due to localized magnification effects. Because of differences in the evaporation field for different phases, precipitates may preferentially protrude or recess from the specimen tip, causing distorted magnification in lateral (x-y) dimensions in the reconstruction. To ascertain dimensions independent of local magnification effects, additional measurements were done using 1-D composition profiles of precipitates taken along the analysis direction (z-axis) when possible. Figure 7.9 shows example LEAP reconstructions containing the 1-D concentration profile sampling cylinder as well as the resultant composition profiles used to determine the size of a rod-shaped M_2C carbide in the 48-hr temper condition. Using this method, typical particle radii ($r_{typ.,1Dcomp.prof.}$) were ascertained. For rod-shaped M_2C carbides, the reported typical radius is for a sphere of equivalent volume as the cylinder composed of the measured carbide length and width. Additional volume fraction estimates ($V_{f,typ.ppt.vol.}$) were also calculated by multiplying the number density of each precipitate species by the spherical volume associated with each typical radius. Table 7.4 lists these figures for comparison with values calculated with the isoconcentration surfaces.

As shown qualitatively by LEAP reconstructions in Figure 7.6 and quantitatively by Table 7.4, the chosen tempering times have distinctly different microstructures. Figure 7.10 contains side-by-side comparisons of representative 20x20x20 nm^3 volumes taken from each of the larger datasets for the three tempering times. Here three precipitation stages can clearly be identified: copper precipitation, M_2C precipitation and M_2C coarsening. After tempering for 1-hr, spherical Cu precipitates approximately 2 nm in diameter are present, corresponding to typical peak hardness conditions for BCC Cu precipitation

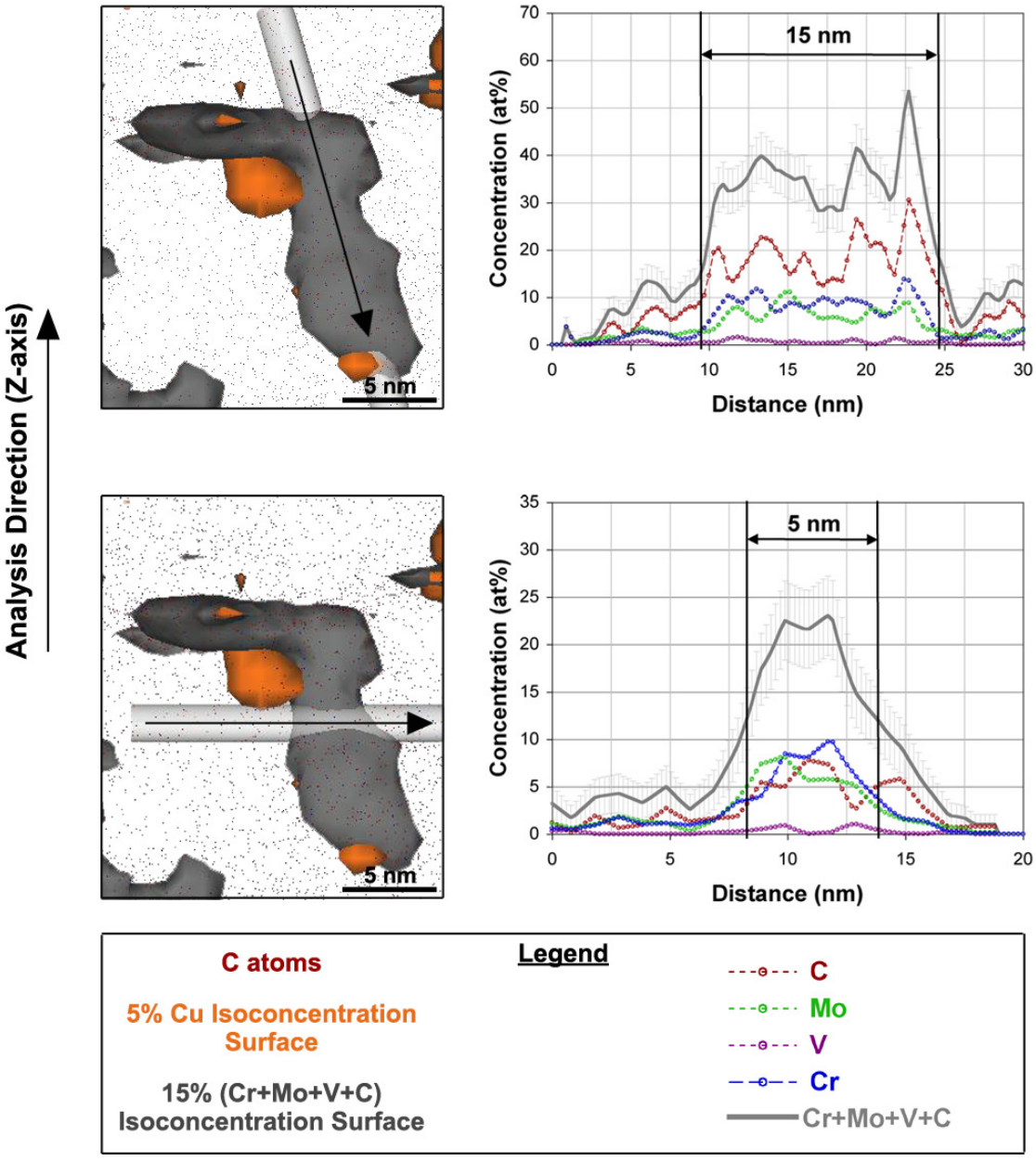

Figure 7.9. Example assessment of typical particle size using one-dimensional composition profiles through IVAS analysis software. Shown example is for a rod-shaped M_2C precipitate in alloy B tempered for 48 hours.

strengthening [**109**]. The tempering response of the core (as shown in Figure 7.3), where Cu precipitation is expected to account for 30-40% of the total strength, shows local hardness maxima at 1 hour, also supporting peak Cu strengthening conditions. The measured precipitate number density of $2.5\text{x}10^{23}$ m^{-3} is lower than is typically seen for peak Cu strengthening conditions of around 10^{24} m^{-3} [**109**], however the particle number density varies greatly over the total analysis volume of the LEAP specimen, with a large portion of the Cu precipitates residing in the middle third of the tip. Significant amounts of carbon segregation were observed on the boundary containing both sides of the region rich in Cu particles, suggesting the presence of un-dissolved cementite that could possibly be interfering with Cu precipitation. The Cu particle number density within the center region was very similar to LEAP reconstructions of other tempering times of around 10^{24} m^{-3}.

The second stage of precipitation seen at 12 hours of tempering consists of M_2C carbides nucleating on the Cu particles. The 2.5-3.0 nm average diameter of the carbides is indicative of peak M_2C precipitation strengthening efficiency, corresponding to the transition between particle shearing and particle bypass illustrated in Figure 2.12. Other secondary hardening steels of similar carbon contents, specifically GearMet C61, also reach peak M_2C precipitation strengthening conditions around 12 hours of tempering. The measured M_2C carbide phase fraction of approximately 1%, however, is significantly below that of the predicted equilibrium phase fraction of 6%. Even accounting for the carbon deficiency of the analyzed LEAP sample volume, the predicted equilibrium volume fraction of M_2C carbide of 3.5% is still much greater than what was measured, further indicating incomplete M_2C precipitation and not preferential loss of carbide during field

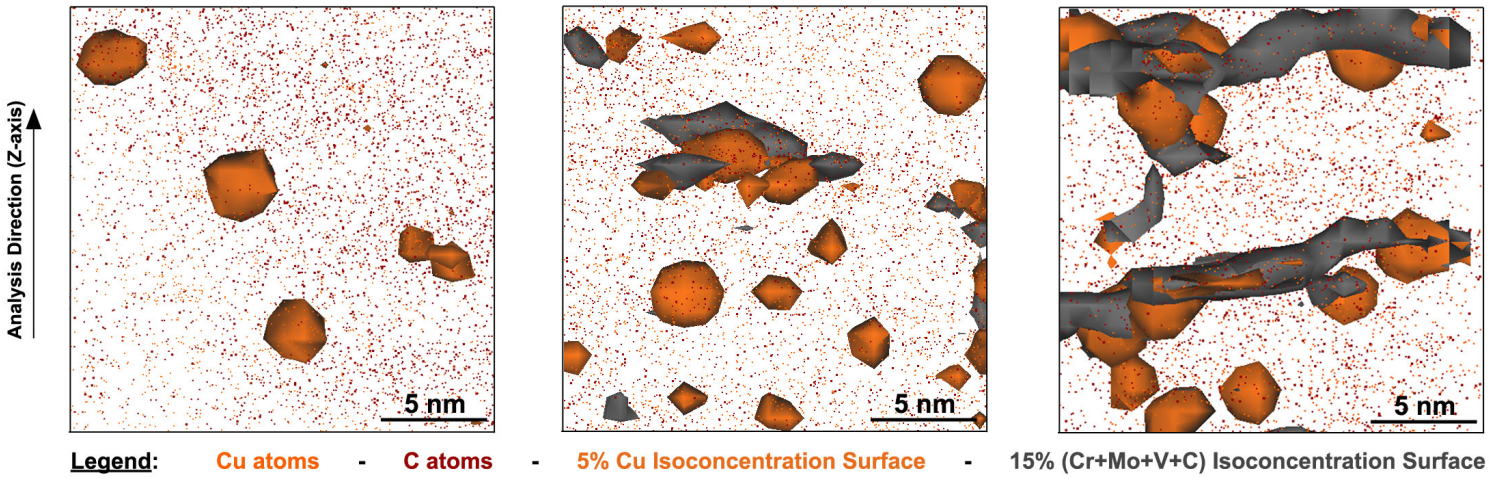

Figure 7.10. Representative LEAP reconstructions for alloy B at three different tempering times

evaporation. An analyzed LEAP specimen taken from the carburized case of an alloy A sample also tempered for 12 hours at 482°C contained a large cementite plate spanning the width of the tip specimen, further indicating incomplete M_2C carbide precipitation and associated cementite dissolution. The heterogeneous nucleation of strengthening carbide precipitates on Cu particles is thus shown to occur, however at a reduced effectiveness or potency when compared to nucleation on dislocations driven by Co-assisted temper resistance.

With further aging, however, peak hardness is achieved at 48 hours where two things are observed: 1)an increase in the M_2C volume fraction and 2)the coarsening of several M_2C carbides into rods. The increase in volume fraction comes from a 25-45% increase in the amount of 3nm spherical particles and in large part from the increased volume fraction from the coarsened rods, measured between 3-9%. The discrepancy between the two measuring methods for the carbide rods can be attributed to over and under-estimations intrinsic to the techniques. The cylinder created by measuring the length and width of M_2C rods using 1D composition profiles provides an upper bound by fully encasing the irregular carbide isosurfaces and slightly overestimating the total volume. The specific M_2C carbide used for measurement via 1D composition profiles was also one of the largest in the dataset but was chosen because of its orientation along the analysis direction (z-axis) preferred to minimize local magnification effects. Measurements using isoconcentration surfaces on the other hand slightly underestimated carbide rod dimensions due spatial aberation arising from different field evaporation properties of the alloy carbides, however using these values as a lower bound and the 1D composition profile measurements as an

upper bound, approximate values are found for the equivalent sphere radius and resultant rod volume fraction to be 3.5nm and 5.9% respectively.

Comparing the average M_2C carbide diameter (d) at the two tempering times (t), it is possible to approximate the precipitation kinetics, as shown in Figure 7.11. The rate constant of approximately 1/3 is indicative of precipitate coarsening following initial nucleation on the Cu precipitates, indicative of nucleation from supersaturated solutions where particle growth is suppressed allowing for fine precipitate dispersions, as described by Langer and Schwartz [**110**].

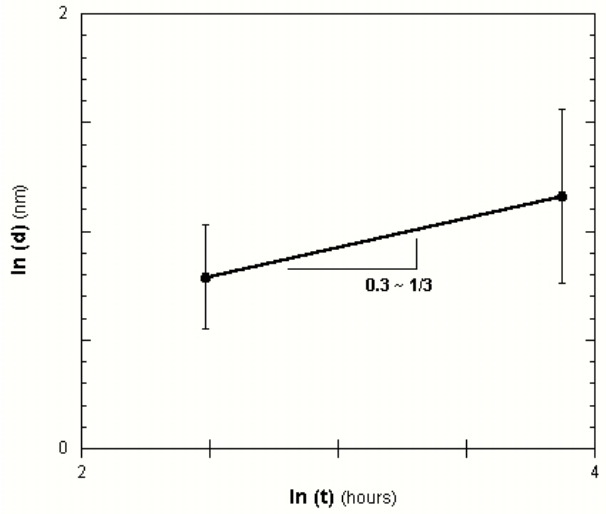

Figure 7.11. Precipitation kinetics for alloy B tempered between 12 and 48 hours at 482°C.

Chemical composition measurements of M_2C alloy carbides were difficult to accurately obtain from LEAP reconstructions. As shown in the 1-D composition profiles in Figure 7.9, M_2C carbides were primarly composed of roughly equal parts Mo and Cr, with significant measured Fe contents exceeding 50%. This can in part be attributed to matrix material contained within the 1-D sampling volume or "tube", where the sampling larger

sampling volume was required for sufficient statistical accuracy. 1-D composition profiles proved reliable for the measurement of BCC Cu precipitates in LEAP reconstructions of A and B alloy samples. Using 1-D composition profiles, the maximum Cu content of each precipitate was shown to strongly depend on the relative precipitate size. Figure 7.12 shows 1-D composition profiles taken along the analysis direction (z-axis) for three Cu precipitates in Alloy B after 48 hours of tempering at 482°C. Precipitates were chosen that corresponded to the observed average precipitate size as well as the lower and upper bounds of the measured size distribution. Significant amounts of Fe were observed in all Cu precipitates, with the maximum Cu content at the center ranging from 8 at% for the smallest Cu clusters (~2nm in diameter) to 30% in the largest precipitates (~3.5nm in diameter). This composition dependence on size was observed at all tempering times, with the largest Cu particles at 1 hour of tempering (~3nm in diameter) exceeding 25 at% Cu in their core. 1D composition profiles also revealed the presence of elevated Ni contents at the Cu particle interface, a known occurence in similar alloy systems [**58**], as well as elevated levels of Mo and C associated with M_2C carbides, an example of which is shown in Figure 7.13.

An additional way of analyzing the chemical composition of the spherical BCC Cu precipitates is through proxigram construction, where spherical shell sampling volumes are integrated for all Cu precipitates using the chosen isoconcentration surface as the reference interface [**75**]. Figure 7.14 shows an example proxigram calculated for all identified Cu precipitates in an alloy B specimen tempered for 48 hours. At distances greater than 1.2 nm from the reference interface towards the precipitate center, significant scatter results due to limited sampling from the largest of all precipitates. At the average

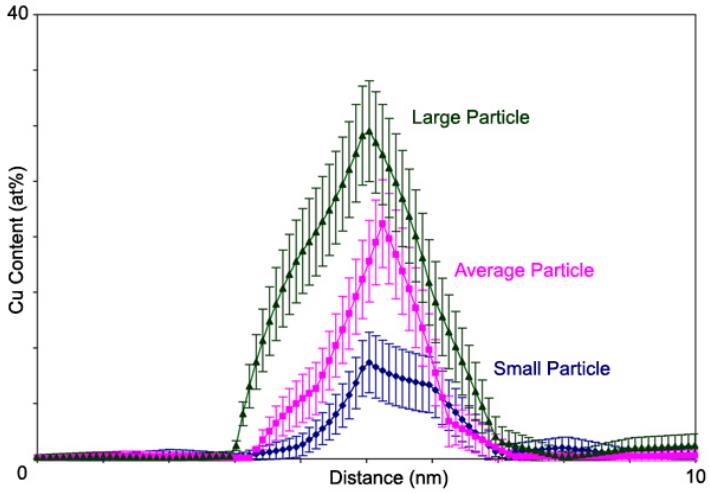

Figure 7.12. 1D Cu composition profiles for BCC Cu clusters in alloy B tempered for 48 hours at 482°C

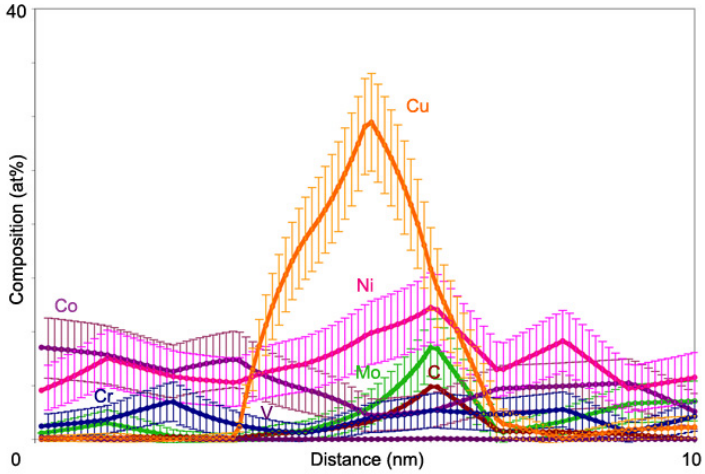

Figure 7.13. 1-D composition profile through a Cu precipitate in alloy B tempered for 48 hours at 482°C

particle radius of 1.2 nm, the observed Cu content of ~30-40 at% agrees well with 1-D composition profile measurements. Additionally, the Ni content is once again observed to be approximately 50% higher around the Cu precipitates than in the surrounding matrix. Similar proxigrams were observed for alloy B after tempering times of 1 and 12 hours.

Additionally, Cu precipitates in alloy A specimens demonstrated equivalent composition profiles and maximum Cu contents as alloy B even with a lower starting Cu content in the matrix. The main effect of the excess Cu content of alloy B can therefore be largely attributed to the observed increased number density and associated reduced interparticle spacing of Cu precipitates, further validating the general $f^{1/2}$ form of the Cu precipitation strengthening model utilized in the design.

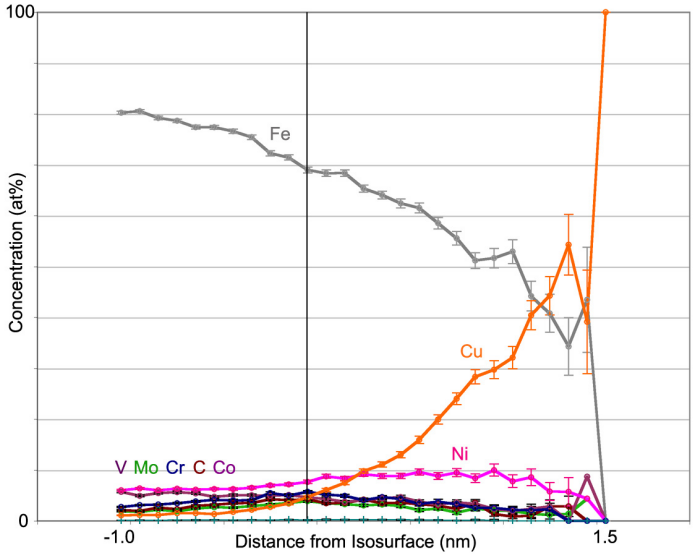

Figure 7.14. Calculated proxigram for Cu precipitates in alloy B tempered for 48 hours at 482°C

In order to explore secondary hardening in the absence of cobalt, LEAP analysis was also completed on carburized alloy A specimens. Figure 7.15 shows a LEAP reconstruction for alloy A tempered for 48 hours at 482°C with the measured composition listed in Table 7.5. The general microstructure was very similar to that of alloy B, with a mixture of spherical and rod-shaped carbides nucleating on Cu particles. Using the same procedure used for alloy B reconstructions, both Cu and M_2C precipitate dispersions were quantified as summarized in Table 7.6.

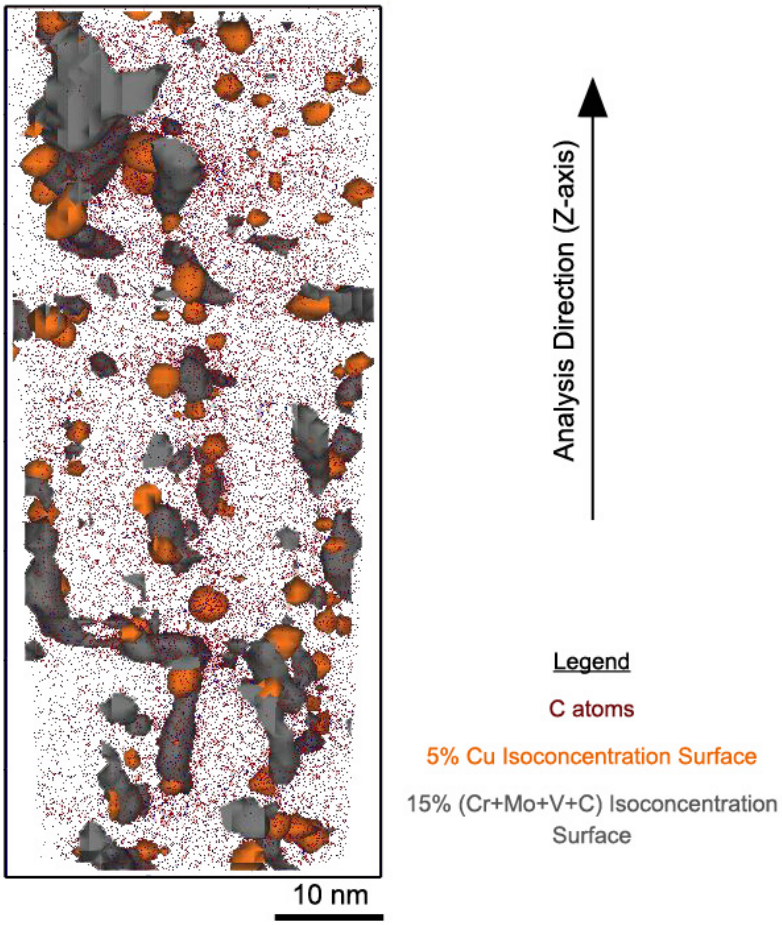

Figure 7.15. LEAP reconstruction of alloy A tempered for 48 hours

Table 7.5. Alloy A compositions (at%) for original design, wet chemistry measurements taken from ingot samples and the overall compositions of the LEAP datasets taken from the 48-hour temper sample

	Fe	Ni	Co	Cr	Mo	V	C (case)	Cu
Design	bal.	3.2	0	2.8	1.8	0.2	2.4	0.9
Measured	bal.	3.1	0	2.5	1.7	0.2	2.3	0.9
48-hr Temper	bal.	3.9	0	2.0	1.8	0.2	2.0	0.8

Comparing measurements in Table 7.6 to those of alloy B in Table 7.4, average precipitate dimensions are shown to be very similar. The number density of Cu particles is

Table 7.6. Quantitative results from LEAP dataset taken from an alloy A sample tempered for 48 hours

	Temper Time (hrs)	48
	Total # Ions	2569696
	Analysis Volume (nm^3)	50537.4
Cu	# precipitates	57
	Number Density (m^{-3})	1.1E+24
	$r_{typ.,1Dcomp.prof.}$ (nm)	1.2
	$r_{avg.,isoconc.surf.}$ (nm)	1.1±0.4
	$V_{f,typ.pptvol.}$	0.8
	$V_{f,isoconc.surfacevol.}$	1.1
M_2C-spheres	# precipitates	38
	Number Density (m^{-3})	7.5E+23
	$r_{typ.,1Dcomp.prof.}$ (nm)	1.5
	$r_{avg.,isoconc.surf.}$ (nm)	1.2±0.3
	$V_{f,typ.pptvol.}$	1.1
	$V_{f,isoconc.surfacevol.}$	0.6
M_2C-rods	# precipitates	14
	Number Density (m^{-3})	2.8E+23
	$r_{typ.,1Dcomp.prof.}$ (nm)	4.0
	$r_{avg.,isoconc.surf.}$ (nm)	2.9±1.2
	$V_{f,typ.pptvol.}$	7.4
	$V_{f,isoconc.surfacevol.}$	4.7

slightly reduced in alloy A and can most likely be attributed to the comparatively lower Cu content of alloy A (30% as captured in LEAP reconstructions). The number density of both spherical and rod-shaped M_2C carbides is also slightly reduced for alloy A compared to alloy B, however the overall carbide volume fraction is essentially equivalent, primarily due to the presence of two larger carbide clusters in the alloy A specimen effectively elevating the volume fraction as measured by isoconcentration surfaces($V_{f,isoconc.surfacevol.}$).

Combining the computed approximate volume fractions for both spherical and rod-shaped carbides at the 48-hour tempering time, the total volume fraction of ~6.9% for alloy A and ~7% for alloy B agree well with ThermoCalc equilibrium carbide volume fraction

calculations predicting 6.8% and 6.7%, respectively. Achieving this predicted equilibrium carbide phase fraction suggests complete dissolution of coarse cementite particles has been achieved along with anticipated gains in attendent fracture toughness levels. Along with increased toughness, complete dissolution of cementite and other transition carbides by the formation of stable alloy carbides provides mechanical and thermal stability when compared to Stage I tempered alloys of comprable hardness. Additionally, the ability to achieve equilibrium carbide volume fractions leading to peak strengthening while using a tempering temperature of 482°C indicates Cu precipitation does in fact mimic Co-assisted secondary hardening. As previously illustrated in Figure 2.10, secondary hardening in the absence of Co is not expected to occur until much higher tempering temperatures or at tempering times prolonged by magnitudes of order. As verified with LEAP reconstructions in zero Co alloys, Cu precipitation by itself has demonstrated the ability to initiate heterogeneous carbide nucleation necessary to both enhance and acclerate secondary hardening.

It is also interesting to note that peak alloy hardness occurred when the majority phase fraction of the predominant strengthening agent, the M_2C carbide dispersion, was largely in an over aged condition typically affiliated with decreases in strengthening efficiency instead of the observed increases. Because the interaction between dislocations and precipitate dispersions is dependent on interparticle spacing, coarser, over aged particles are typically less efficient strengtheners than finer particles as they have a larger interparticle distance at a constant volume fraction. The potential difference with this particular system, however, is that there is a strong interaction between two different strengthening dispersions, as designed into the microstructural approach. In this case,

as the M_2C carbides coarsen into rods, the effective center for each carbide begins to distance itself from its associated Cu particle, reducing the degree of co-location and approaching a more random dispersion. The volume fraction of precipitated carbide also increased when going from tempering 12 hours to 48 hours, suggesting the maximum volume fraction is most likely achieved after significant carbide coarsening has occurred. Therefore, in this scenario, the interparticle spacing might actually be minimized with some degree of over-aging. Additionally, the growth of these M_2C rods typically follows <100> habit directions [**41**], as shown clearly in the LEAP reconstructions in Figures 7.6 and 7.9. Oriented precipitate shapes such as rods and plates have in some cases been shown to be more efficient strengtheners than their randomly distributed spherical counterparts [**111, 112**]. Strengthening dispersion of rods oriented along <100> directions in theory would be favorable strengtheners in BCC Fe, as dislocations gliding along {110} slip planes would be transverse to 2 out of the 3 rod orientations, effectively acting as more efficient obstacles than a random distribution. This possible size/orientation effect coupled with the de-localization of the two strengthening dispersions provides a reasonable explanation for why a rod-shaped M_2C morphology is resulting in peak strength for these alloys.

7.5. Alloy Redesign

7.5.1. Model Recalibration

To determine if the deviation from the assumed optimal particle sizes observed with the LEAP at peak strength were responsible for the 200 VHN discrepancy between designed and measured hardness levels, design models were then recalibrated with updated

microstructural parameters. The Cu precipitation strengthening model used for first iteration designs assumed an optimal particle size of 1 nm in radius, however at peak alloy hardness average Cu precipitates were slightly over aged at an average radius of 1.2 nm. Previous experimental results reported approximately 20% less strengthening due to similar amounts of over aging after normalizing data to account for different volume fractions [**109**]. Applying this correction by simply multiplying the peak strength model by 80%, the size dependence of the Cu strengthening model was taken into account and recalibrated as shown in Figure 7.16.

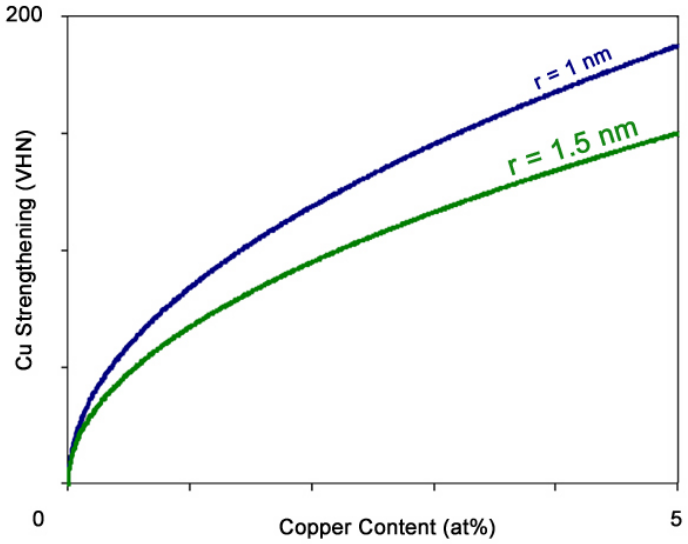

Figure 7.16. Recalibration of Cu precipitaiton strengthening model to account for overaging

For detailed recalibration of the M_2C strengthening model, more accurate size and volume fraction measurements must be made as well as further investigation into possible particle size effects and the nonlinear superposition of strengthening dispersions due to co-location. However, a preliminary model calibration could be made simply taking

into account the rod-shaped M_2C carbides since not only did they account for the majority of the M_2C volume fraction at peak strength, but as previously described they also were effectively decoupled from the Cu particles and their strengthening contribution could be added with simple linear superposition. To only consider the rods in the M_2C precipitation-strengthening model, the portion of the calculated equilibrium volume fraction converted into strength (V/V_f) parameter was set at 0.8 to reflect the approximate 80% that the rod-shaped carbides contributed to the total measured volume fraction of M_2C carbide. With this correction, the average precipitate size was set to the equivalent sphere radius previously found to be approximately 3.5 nm, recalibrating the strength model as shown in Figure 7.17. The end result of this recalibration is a significant loss in strength for a given carbon content. Taking the measured carbon content of alloy B, this recalibration caused a drop of approximately 200 VHN, correlating well with the discrepancy between measured and designed case hardness.

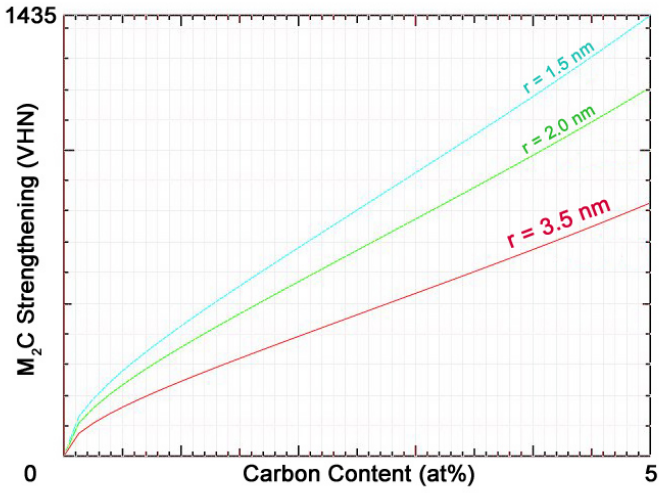

Figure 7.17. Recalibration of M_2C precipitaiton strengthening model to account for overaged rod-shape morphology

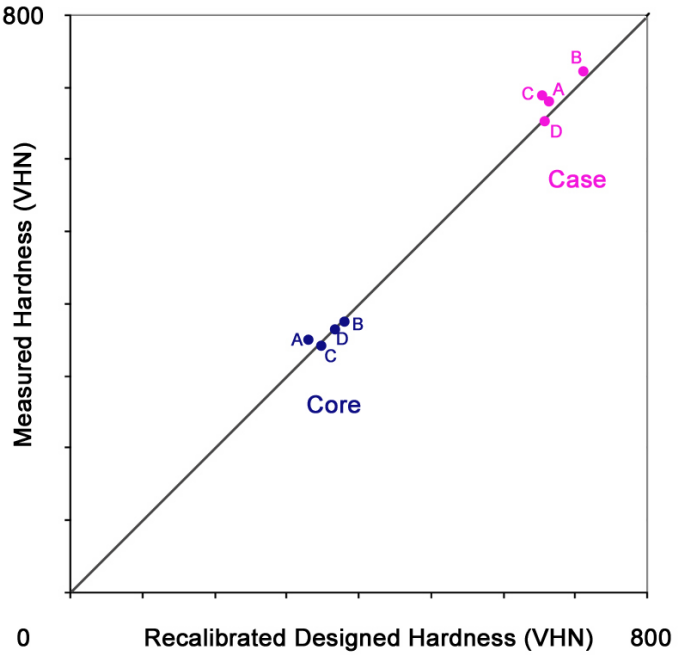

Figure 7.18. Comparison between recalibrated total strengthening model and measured hardness levels for the carburized case and core for Cu-bearing experimental alloys

Incorporating all strength model recalibrations to accurately reflect the microstructure observed at peak strength for alloy B, predicted strength levels were then recalculated for the measured compositions of all four experimental alloys. Figure 7.18 shows these recalibrated strength predictions plotted against measured hardness levels of both the carburized case and core for all four alloys, showing close agreement to less than 50 VHN.

7.5.2. Preliminary 2nd Design Iteration

Using these recalibrated strength models, new calculations were completed following the design approach previously outlined in Chapter 6. Due to the reduced strengthening efficiency of the larger M_2C carbides, the phase fraction of M_2C and associated levels of

C required for the target strength of 67 R_C (900 VHN) was significantly increased. This increase in carbon content in turn greatly suppressed the martensitic start temperature (M_S) and stabilized unwanted primary carbides. Design parameters were subsequently revised to a reduced target surface hardness of 65 R_C (832 VHN) and an increased target solutionizing temperature of 1100°C, enabling all other design parameters to be met or maximized. Table 7.7 outlines two resultant compositions, one with eliminated Co content and the other with reduced Co content for increased Ni, with the predicted design parameters outlined in Table 7.8. These preliminary calculations indicate that strengths up to 65 R_C are possible using Cu-nucleated M_2C strengthening in the absence of large cobalt contents.

Table 7.7. Preliminary compositions (wt%) for second iteration alloys derived using recalibrated design models

Alloy	C (case)	C (core)	Co	Cr	Cu	Mo	Ni	V	Fe
C10B	0.7	0.08	0	3.9	1.1	3.7	1.1	0.3	Bal.
C18	0.7	0.08	8.3	4.0	1.1	3.9	2.7	0.1	Bal.

Table 7.8. Predicted design parameters for second iteration alloys

Alloy	M_S Case (°C)	M_S Core (°C)	T_S (°C)	Strength (VHN)		M_2C Driving Force (kJ/mol)	δ_{Mo}	Ni/Cu
				Case	Core			
C10B	99.4	335.1	1087.7	825.2	392.3	27.6	1.6	1.1
C18	100.0	384.6	1090.7	826.2	393.0	28.8	1.6	2.6

CHAPTER 8

Conclusions

A systems-based approach was utilized in the optimization and design modification of secondary hardening steels to meet the demand of rising gear power density requirements. Single tooth bending fatigue tests were completed to both assess the optimized performance of existing secondary hardening gear steels as well as identify defect populations currently limiting further advances. Three focused microstructural studies were then completed on grain coarsening resistance, alloy hardenability and precipitate stability to address microstructural issues anticipated to limit fatigue performance. Finally, a second-generation alloy aimed at reducing material cost through incorporating Cu precipitation was successfully designed and resultant prototype alloys analyzed for design model recalibration.

8.1. Bending Fatigue Performance Optimization

Bending fatigue is the projected limiting failure mode for high power density gear applications and will require harder more flaw tolerant materials. Two commercialized secondary hardening gear steels, C61 and C67, were chosen for testing as they have demonstrated an optimized combination of strength and toughness as well as have shown promising contact fatigue resistance. Single tooth bending fatigue tests were first completed on a heat of C61 spur gears investigating the effect of different surface conditions on bending fatigue performance. Shot peening was shown to be an effective way to both

impart beneficial compressive residual stress to resist fatigue crack initiation and propagation but also as a means of eradicating detrimental grain boundary grooving caused by high-temperature vacuum carburizing.

A second phase of C61 single tooth bending fatigue tests of shot peened spur gears identified three major defect classes limiting fatigue. Low cycle fatigue was predominantly controlled by surface damage induced by shot peening, where observed adiabatic shear cracks both initiated fatigue as well as interfered with the isotropic superfinishing process utilized to enhance surface finish. High cycle fatigue failures approaching the endurance limit ($>10^6$ cycles to failure) were observed to largely initiate subsurface on intergranular cleavage facets. Overcarburization of specimen corners facilitated cleavage fracture and subsequently reduced the bending fatigue endurance limit by over 15%. The third defect class consisted of inclusions. Al_2O_3 inclusions were observed in high cycle fatigue failures near the endurance limit, while La_2O_2S inclusions were present in C61 spur gears containing La additions and occurred at lower applied stresses and cycles to failure. The increased defect potency of La_2O_2S inclusions can be attributed to the diffuse nature of the component particle clusters. Best-practice C61 outperformed the top-ranking premium gear steel, demonstrating an approximate 15% improvement in bending fatigue endurance limit.

The elevated surface hardness of C67 had no observable benefit for single tooth bending fatigue resistance. Various shot peening parameters were investigated to maximize compressive residual stress in C67, with no success. Standard shot peening practices are

concluded to be currently not sufficient to maximize compressive residual stress for materials possessing surface hardness levels exceeding the hardness of the hardest shot peening media.

8.2. Microstructural Limitations

8.2.1. Grain Coarsening

Complete resistance to grain coarsening up to solutionizing temperatures of 1200°C was demonstrated using a powder metallurgy alloy where a Ti addition was added to form stable grain-pinning oxide dispersions. Additionally, PM C69-Ti exhibited a starting grain size 15% smaller than its wrought counterpart. Neglecting any additional defects that may be introduced such as porosity, powder metallurgy may be a viable option to achieve microstructural refinement for increased bending fatigue resistance. Possible interference from the grain boundary oxidation utilized for optical delineation may be obscuring the true grain coarsening behavior, however, and further study utilizing a different grain boundary etching technique is needed.

8.2.2. Hardenability

C61 demonstrated a high level of hardenability through dilatometry measurements of transformation behavior for various cooling rates in conjunction with resultant microhardness measurements. When compared to the same gear steels used for single tooth bending fatigue performance comparisons, C61 softened only 15% at a cooling rate equivalent to that at the center of an air cooled bar 2-meters in diameter compared to a drop of 45 and 60% for baseline and premium gear steels, respectively. Based on the superior

hardenability of C61, nonmartensitic transformation products should in most cases be sufficiently avoided and would not be a concern for defect-driven fatigue initiation.

8.2.3. Carbide Dissolution

An overaging heat treatment aimed at increasing mechanical stability of strengthening carbide dispersions was not shown to benefit rolling contact fatigue life of C69M3B NTN RCF bars and actually decreased RCF life by about 50%. This deduction is only preliminary, however, as testing parameters were skewed by the possible deleterious effects caused by the growth of an oxide layer during the over-aging temper. Additionally, the roughened test balls used to accelerate the NTN RCF test appears to have accentuated sensitivity to surface hardness and may not be the most appropriate gauge of rolling/sliding contact fatigue behavior.

8.3. New Cu-Bearing Alloys

In an effort to reduce material cost through minimization/elimination of Cobalt alloying additions, BCC Cu precipitation was incorporated to offset ensuing losses in temper resistance by providing additional heterogeneous nucleation sites for the M_2C strengthening dispersion. Four designs were completed corresponding to four combinations of chosen Cu and Co composition restraints. Fifty-pound experimental heats were then made, of which samples were sectioned and heat-treated for prototype evaluation. Tempering hardness evolution studies revealed peak hardness to occur around 48 hours when tempering at 482°C, however peak surface hardness values were on average 200 VHN short of the designed value of around 900 VHN. Three-dimensional local electrode atom probe (LEAP)

tomography was utilized to study the nanoscale BCC Cu and M_2C precipitates located in the carburized case at various tempering times. BCC Cu was shown to act as a heterogeneous nucleation site for the M_2C strengthening dispersion at tempering temperatures comparable to high-Co alloys, however at a reduced nucleating efficiency. As a result, peak strength was achieved with over-aging where 80% of the M_2C carbide dispersion had reached a coarsened rod-shaped morphology at peak strength. Design models were recalibrated to account for the coarsened peak hardness microstructure, showing good agreement with measured strength values for both the carburized case and core of all four experimental alloys. Preliminary secondary design iterations were then completed using these recalibrated design models with resultant compositions achieving predicted surface hardness levels of 65 R_C.

CHAPTER 9

Suggestions for Future Work

Considerable progress has been achieved in the bending fatigue performance optimization of C61, however identified defects currently limiting fatigue can still be addressed. Additionally, BCC Cu was successfully incorporated into high strength gear steels and proven to catalyze secondary hardening, however much remains to be studied for proper model recalibration and full optimization of the microstructure.

9.1. Bending Fatigue

The shot peening process appears to be the current limiting factor for a majority of both low and high cycle bending fatigue failures. For C61 and materials of similar surface hardness levels, sufficient compressive stress can be generated with conventional shot peening practices, however surface damage due to high intensity shot peening needs to be addressed. Unlike chemical methods such as isotropic superfinishing, mechanical surface finishing processes may provide a means of removing damaged shot peened surface layers without being influenced by shot-peening induced damage features. Additionally, added protection or rounding of spur gear corners prior to shot peening could be used to avoid excessive peening and subsequent subsurface damage.

For C67 and other ultra-high hardness materials, conventional shot peening media does not possess sufficient hardness to impart the maximum possible compressive stress and alternative peening-type operations are necessary. Further development of laser peening,

ultra-high hardness shot media or other alternative peening operations are required to take full advantage of materials exceeding 60-63 R_C.

Fatigue-initiating inclusions are one defect class that may never be completely avoided. Continuing modeling on the effect of different inclusions and inclusion geometries should shed invaluable light on how to minimize the effect of intrinsic inclusion contents through selection of utilized gettering elements for less-detrimental inclusion phases as well as identification of possible melt processing and ingot hot working techniques to alter inclusions to specific morphologies.

One factor not currently well understood and vital to modeling efforts is the evolution of residual stress with applied loads. Interrupted test residual stress measurements or even non-destructive high energy x-ray diffraction methods could be utilized to gain insight into residual stress profile evolution during cyclical loading. This information would also help guide selection and tailoring of microstructures to better resist residual stress relaxation and improve fatigue properties.

Ultimately, processing variables optimized for bending fatigue must be reconciled and likewise optimized with rolling/sliding contact fatigue requirements. At the time of this publication, C61 sun gear samples were being fabricated for planetary gear contact fatigue pitting tests to be run at the GM Powertrain Gear Center in order to assess rolling/sliding contact fatigue resistance performance as a corollary metric to the obtained single tooth bending fatigue performance data.

9.2. Cu-Bearing Alloys

Additional microstructure analysis and quantification is needed to better understand and describe the precipitation and secondary hardening promotion of incorporated BCC Cu precipitation. The superposition law governing the BCC Cu and M_2C alloy carbide strengthening dispersions is needed to describe strengthening behavior at earlier tempering times prior to coarsening of the M_2C carbides into rods. Tempering studies at different temperatures as well as multi-step tempering procedures may reveal enhanced strengthening efficiency and/or tempering time reduction in these microstructures through manipulation of precipitation kinetics.

Ultimately the bending and contact fatigue resistance of these Cu-bearing alloys must be assessed to compare against existing secondary hardening alloys. At the time of this publication, spur gears have been fabrication out of the four experimental alloy heats and are awaiting heat treatment. A modified gear geometry was required due to limited dimensions of the starting raw material, however a sufficient number of testable teeth remains to generate approximate S-N curves for single tooth bending fatigue resistance comparison.

References

[1] Gear industry vision. In *Gear Industry Vision Workshop*, Detroit, Michigan, 2004.

[2] USGS. Metal prices in the united states through 1998. Technical report, U.S. Department of the Interior U.S. Geological Survey, 1998.

[3] G.M. Jenkins. The systems approach. In J. Beishon and G. Peters, editors, *Systems Behavior*. Open University Press, 1972.

[4] C.S. Smith. *A Search for Structure*. The MIT Press, Cambridge, MA, 1981.

[5] G. B. Olson. Materials design: An undergraduate course. In P. K. Liaw, J.R. Weertman, H.L. Marcus, and J.S. Santner, editors, *Morris E. Fine Symposium*, pages 41–48, Detroit, MI, 1991. The Minerals, Metals and Materials Society.

[6] D. Wright. Spur gears, Retrieved August 23, 2006 from: http://www.mech.uwa.edu.au/DANotes/gears/failure/failure.html.

[7] Lester E. Alban. *Systematic analysis of gear failures*. American Society for Metals, Metals Park, Ohio, 1985.

[8] Fundamental rating factors and calculation methods for involute spur and helical gear teeth (metric edition). Technical Report ANSI/AGMA 2101-D04, American Gear Manufacturers Association.

[9] Rating the pitting resistance and bending strength of generated straight bevel, zerol bevel, and spiral bevel gear teeth. Technical Report ANSI/AGMA 2003-B97 (R2003), American Gear Manufacturers Association.

[10] Rating the pitting resistance and bending strength of hypoid gears. Technical Report AGMA 932-A05, American Gear Manufacturers Association.

[11] E.E. Shipley. Failure modes in gears. In P. J. Guichelaar, Bernard S. Levy, and Niranjan M. Parikh, editors, *Gear Manufacture and Performance*, Materials/metalworking technology series, pages 107–136. American Society for Metals, Metals Park, Ohio, 1974.

[12] J. R. Davis. *Gear materials, properties, and manufacture*. ASM International, Materials Park, Ohio, 2005.

[13] M. Widmark and A. Melander. Effect of material, heat treatment, grinding and shot peening on contact fatigue life of carburised steels. *International Journal of Fatigue*, 21(4):309–327, 1999.

[14] A. Oila, B. A. Shaw, C. J. Aylott, and S. J. Bull. Martensite decay in micropitted gears. *Proceedings of the Institution of Mechanical Engineers Part J-Journal of Engineering Tribology*, 219(J2):77–83, 2005.

[15] R. Osterlund, O. Vingsbo, L. Vincent, and P. Guiraldenq. Butterflies in fatigued ball-bearings - formation mechanisms and structure. *Scandinavian Journal of Metallurgy*, 11(1):23–32, 1982.

[16] M. E. Fine. Fatigue resistance of metals. *Metallurgical Transactions A-Physical Metallurgy and Materials Science*, 11(3):365–379, 1980.

[17] K. S. Ravichandran, R. O. Ritchie, and Y. Murakami, editors. *Small fatigue cracks : mechanics, mechanisms, and applications : proceedings of the Third Engineering Foundation International Conference, Turtle Bay Hilton, Oahu, Hawaii, December 6-11, 1998*. Elsevier, Amsterdam ; New York, 1st edition, 1999.

[18] D. J. Medlin, G. Krauss, D. K. Matlock, K. Burris, and M. Slane. Comparison of single gear tooth and cantilever beam bending fatigue testing of carburized steel. *S A E transactions*, 1995.

[19] G. Krauss. Bending fatigue of carburized steels. In *ASM Handbook*, volume 19. ASM International, Metals Park, OH, 2002.

[20] B. Tiemens, A.K. Sachdev, and G. B. Olson. Performance of computationally designed ultra-hard steel for transmission gear applications. Collaborate Report CL - 04/41/MPL, GM Research and Development Center, August 2004 2004.

[21] R.D. Zipp and G.H. Walter. A fractographic study of high cycle fatigue fractures in carburized steel. *Metallography*, 7:77–81, 1974.

[22] A. Singh. An experimental investigation of bending fatigue initiation and propagation lives. *Journal of Mechanical Design*, 123(3):431–435, 2001.

[23] T.H. Courtney. *Mechanical behavior of materials*. McGraw-Hill series in materials science. McGraw Hill, Boston, 2nd edition, 2000.

[24] M. F. Garwood, H. H. Zurburg, and M. A. Erickson. Correlation of laboratory tests and service performance. In *Interpretation of tests and correlation with service*, pages 1–77. American Society for Metals, Cleveland, 1951.

[25] Y. Murakami. *Metal fatigue : effects of small defects and nonmetallic inclusions*. Elsevier, Oxford, 2002.

[26] Y. K. Gao, M. Yao, and J. K. Li. An analysis of residual stress fields caused by shot peening. *Metallurgical and Materials Transactions A-Physical Metallurgy and Materials Science*, 33(6):1775–1778, 2002.

[27] J. P. Wise, D. K. Matlock, and G. Krauss. Bending fatigue of carburized steels. *Heat Treating Progress*, pages 33–41, 2001.

[28] E.A Starke and G. Lutjering. Cyclic plastic deformation and microstructure. In *Fatigue and microstructure : papers presented at the 1978 ASM Materials Science Seminar, 14-15, October, 1978, St. Louis, Missouri*, pages 205–243. American Society for Metals, Metals Park, Ohio, 1979.

[29] C. A. Apple and G. Krauss. Microcracking and fatigue in a carburized steel. *Metallurgical Transactions*, 4(5):1195–1200, 1973.

[30] R. H. Richman and R. W. Landgraf. Some effects of retained austenite on fatigue resistance of carburized steel. *Metallurgical Transactions*, A 6(5):955–964, 1975.

[31] M. A. Zaccone and G. Krauss. Elastic limit and microplastic response of hardened steels. *Metallurgical Transactions A-Physical Metallurgy and Materials Science*, 24(10):2263–2277, 1993.

[32] G. Sroka and L. Winkelmann. Superfinishing gears - the state of the art. *Gear Technology*, (Nov/Dec):28–33, 2003.

[33] G.L. Krasko and G. B. Olson. Evaluation of decohesion mechanisms in iron by LMTO-ASA-Stoner cohesive energy calculations. In *Innovations in Ultrahigh-Strength Steel Technology*, volume 34 of *Sagamore Army Materials Research Conference*, pages 677–704, Lake George, N.Y., 1987.

[34] G. R. Speich, D. S. Dabkowski, and L. F. Porter. Strength and toughness of Fe-10Ni alloys containing C, Cr, Mo, and Co. *Metallurgical Transactions*, 4(1):303–315, 1973.

[35] S. Spooner, H. J. Rack, and D. Kalish. Neutron diffraction analysis of atomic arrangements in a maraging steel. *Metallurgical Transactions*, 2(8):2306–2308, 1971.

[36] A. F. Edneral, O. P. Zhukov, M. A. Kablukov, B. M. Mogutnov, and M. D. Perkas. Study of ordering process in iron-nickel-cobalt alloys with martensitic structure. *Fizika Metallov I Metallovedenie*, 36(4):727–734, 1973.

[37] V. Pierron-Bohnes, M. C. Cadeville, and G. Parette. Concentration-dependence of atomic short-range order in FeCo alloys (XCo 25%) from neutron diffuse-scattering. *Journal of Physics F - Metal Physics*, 15(7):1441–1448, 1985.

[38] G. B. Olson. Science of steel. In *Innovations in Ultrahigh-Strength Steel Technology*, volume 34 of *Sagamore Army Materials Research Conference*, pages 3–66, Lake George, N.Y., 1987.

[39] C.J. McMahon. Hydrogen embrittlement of high-strength steels. In *Innovations in Ultrahigh-Strength Steel Technology*, volume 34 of *Sagamore Army Materials Research Conference*, pages 597–618, Lake George, N.Y., 1987.

[40] J. P. Wise. *Systems Design of Advanced Gear Steels*. PhD thesis, Northwestern University, 1998.

[41] H. M. Lee and S. M. Allen. Coarsening resistance of M_2C carbides in secondary hardening steels .3. comparison of theory and experiment. *Metallurgical Transactions A-Physical Metallurgy and Materials Science*, 22(12):2877–2888, 1991.

[42] C. Knepfler. *Synthesis and Characterization of Molybdenum-Based M_2C Carbides*. PhD thesis, Northwestern University, 1994.

[43] C. J. Kuehmann and G. B. Olson. Gear steels designed by computer. *Advanced Materials And Processes*, 153(5):40–43, 1998.

[44] B.E. Tufts. Unpublished research, 2006.

[45] B.E. Tufts. Advanced steels for affordable cvt technology. Master's thesis, Northwestern University, 2001.

[46] G. B. Olson and R.G. Bourdeu. Rapidly solidified ferrous alloys. In *Rapidly Solidified Crystalline Alloys*. The Metallurgical Society of AIME, 1985.

[47] S. S. G. Banadkouki, D. Yu, and D. P. Dunne. Age hardening in a Cu-bearing high strength low alloy steel. *ISIJ International*, 36(1):61–67, 1996.

[48] D. P. Dunne, S. S. Ghasemi, and D. Yu. Isothermal transformation products in a Cu-bearing high strength low alloy steel. *ISIJ International*, 36(3):324–333, 1996.

[49] S. K. Dhua, D. Mukerjee, and D. S. Sarma. Influence of tempering on the microstructure and mechanical properties of HSLA-100 steel plates. *Metallurgical and Materials Transactions A - Physical Metallurgy and Materials Science*, 32(9):2259–2270, 2001.

[50] K. C. Russell and L. M. Brown. Dispersion strengthening model based on differing elastic-moduli applied to iron-copper system. *Acta Metallurgica*, 20(7):969–974, 1972.

[51] K. Osamura, H. Okuda, S. Ochiai, M. Takashima, K. Asano, M. Furusaka, K. Kishida, and F. Kurosawa. Precipitation hardening in Fe-Cu binary and quaternary alloys. *ISIJ International*, 34(4):359–365, 1994.

[52] M. Charleux, F. Livet, F. Bley, F. Louchet, and Y. Brechet. Thermal ageing of an Fe-Cu alloy: Microstructural evolution and precipitation hardening. *Philosophical Magazine A - Physics of Condensed Matter Structure Defects and Mechanical Properties*, 73(4):883–897, 1996.

[53] A. Deschamps, M. Militzer, and W. J. Poole. Precipitation kinetics and strengthening of a Fe-0.8wt%Cu alloy. *ISIJ International*, 41(2):196–205, 2001.

[54] G. M. Worrall, J. T. Buswell, C. A. English, M. G. Hetherington, and G. D. W. Smith. A study of the precipitation of copper particles in a ferrite matrix. *Journal of Nuclear Materials*, 148(1):107–114, 1987.

[55] P. J. Othen, M. L. Jenkins, G. D. W. Smith, and W. J. Phythian. Transmission electron-microscope investigations of the structure of copper precipitates in thermally-aged Fe-Cu and Fe-Cu-Ni. *Philosophical Magazine Letters*, 64(6):383–391, 1991.

[56] N. Maruyama, M. Sugiyama, T. Hara, and H. Tamehiro. Precipitation and phase transformation of copper particles in low alloy ferritic and martensitic steels. *Materials Transactions JIM*, 40(4):268–277, 1999.

[57] G. R. Speich and R. A. Oriani. Rate of coarsening of copper precipitate in an alpha-iron matrix. *Transactions of the Metallurgical Society of AIME*, 233(4):623–631, 1965.

[58] A. Saha. *Systems Design of Transformation Toughened Blast-Resistant Naval Hull Steels*. PhD thesis, Northwestern University, 2004.

[59] A. Takahashi and M. Iino. Microstructural refinement by cu addition and its effect on strengthening and toughening of sour service line pipe steels. *ISIJ International*, 36(2):241–245, 1996.

[60] M. Mujahid, A. K. Lis, C. I. Garcia, and A. J. DeArdo. HSLA-100 steels: Influence of aging heat treatment on microstructure and properties. *Journal of Materials Engineering and Performance*, 7(2):247–257, 1998.

[61] G. C. Hwang, S. Lee, J. Y. Yoo, and W. Y. Choo. Effect of direct quenching on microstructure and mechanical properties of copper-bearing high-strength alloy steels. *Materials Science and Engineering A - Structural Materials Properties Microstructure and Processing*, 252(2):256–268, 1998.

[62] Y. Futamura, T. Tsuchiyama, and S. Takaki. Strengthening mechanism of Cu bearing heat resistant martensitic steels. *ISIJ International*, 41:S106–S110, 2001.

[63] B. S. Ku and J. Yu. Effects of cu addition on the creep rupture properties of a 12% Cr steel. *Scripta Materialia*, 45(2):205–211, 2001.

[64] M. Hattestrand and H. O. Andren. Microstructural development during ageing of an 11alloyed with copper. *Materials Science and Engineering A - Structural Materials Properties Microstructure and Processing*, 318(1-2):94–101, 2001.

[65] K. Stiller, M. Hattestrand, and F. Danoix. Precipitation in 9Ni-12Cr-2Cu maraging steels. *Acta Materialia*, 46(17):6063–6073, 1998.

[66] K. Hono. Overview no. 133 - atom probe microanalysis and nanoscale microstructures in metallic materials. *Acta Materialia*, 47(11):3127–3145, 1999.

[67] T. Ohkubo, H. Kai, D. H. Ping, K. Hono, and Y. Hirotsu. Mechanism of heterogeneous nucleation of alpha-Fe nanocrystals from Fe89Zr7B3Cu1 amorphous alloy. *Scripta Materialia*, 44(6):971–976, 2001.

[68] ASTM E92-82 standard test method for vickers hardness of metallic materials, 2003.

[69] ASTM E 112-96 standard test methods for determining average grain size, 1996.

[70] D. Glover. A ball-rod rolling contact fatigue tester. In *Special Technical Publication*, volume 771, pages 107–124. ASTM, Philadelphia, 1982.

[71] Residual stress measurement by x-ray diffraction. Technical Report SAE HS-784, Society of Automotive Engineers, 2003.

[72] C.F. Jatczak, J.A. Larson, and S.W. Shin. Retained austenite and its measurement by x-ray diffraction. Technical Report SAE SP-453, Society of Automotive Engineers, 1980.

[73] Standard practice for x-ray determination of retained austenite in steel with near random crystallographic orientation. Technical Report ASTM E975-03, ASTM International, 2003.

[74] T.F. Kelly and A.A. Gribb. Atom probes leap ahead. *Microscopy Today*, September/October(September/October), 2003.

[75] M. K. Miller. *Atom probe tomography : analysis at the atomic level*. Kluwer Academic / Plenum Publishers, New York, 2000.

[76] B. Sundman, B. Jansson, and J. O. Andersson. The Thermo-Calc databank system. *Calphad-Computer Coupling of Phase Diagrams and Thermochemistry*, 9(2):153–190, 1985.

[77] B. Sundman and J. Agren. A regular solution model for phases with several components and sub-lattices, suitable for computer-applications. *Journal of Physics and Chemistry of Solids*, 42(4):297–301, 1981.

[78] M. Hillert, B. Jansson, B. Sundman, and J. Agren. A 2-sublattice model for molten solutions with different tendency for ionization. *Metallurgical Transactions A - Physical Metallurgy and Materials Science*, 16(2):261–266, 1985.

[79] G. Ghosh and G. B. Olson. Kinetics of FCC-BCC heterogeneous martensitic nucleation -1. the critical driving-force for athermal nucleation. *Acta Metallurgica et Materialia*, 42(10):3361–3370, 1994.

[80] H.J. Jou, L. Li, C. J. Kuehmann, and G. B. Olson. *User Guide for CMD^{TM} (Computational Materials Dynamics) Software*. QuesTek Innovations LLC, Evanston, IL, version 3/31/03 edition, 2003.

[81] J. O. Andersson and J. Agren. Models for numerical treatment of multicomponent diffusion in simple phases. *Journal of Applied Physics*, 72(4):1350–1355, 1992.

[82] T. Naito, H. Ueda, and M. Kikuchi. Fatigue behavior of carburized steel with internal oxides and nonmartensitic microstructure near the surface. *Metallurgical Transactions A-Physical Metallurgy and Materials Science*, 15(7):1431–1436, 1984.

[83] R. Murakami, D. Yonekura, and Z. D. Ni. Fatigue fracture behavior of high-strength steel in super long life range. *JSME International Journal Series A-Solid Mechanics and Material Engineering*, 45(4):517–522, 2002.

[84] H. Itoga, K. Tokaji, M. Nakajima, and H. N. Ko. Effect of surface roughness on step-wise S-N characteristics in high strength steel. *International Journal of Fatigue*, 25(5):379–385, 2003.

[85] K.D. Jones and G. Krauss. Effects of high-carbon specimen corners on microstructure and fatigue of partial pressure carburized steels. In *Heat treatment '79 : proceedings of an international conference organized by the Heat Treatment Committee of the Metals Society, in association with the Heat Treating Division of the American Society for Metals, and held at the Metropole Hotel, Birmingham, 22-24 May 1979*, page 237. Metals Society, London, 1980.

[86] R. E. Cohen, D. K. Matlock, and G. Krauss. Specimen edge effects on bending fatigue of carburized steel. *Journal of Materials Engineering and Performance*, 1(5):695–703, 1992.

[87] Jay Gao. Under review. 2006.

[88] Geoffrey Parrish. *The influence of microstructure on the properties of case-carburized components*. American Society for Metals, Metals Park, Ohio, 1980.

[89] M. Larsson, A. Melander, R. Blom, and S. Preston. Effects of shot peening on bending fatigue-strength of spring steel SS-2090. *Materials Science and Technology*, 7(11):998–1004, 1991.

[90] Richard C. Rice, B. N. Leis, Drew Nelson, and Society of Automotive Engineers. *Fatigue design handbook*. Ae ; 10. Society of Automotive Engineers, Warrendale, PA, 2nd edition, 1988.

[91] Y. Qian. Doctoral Research - Northwestern University, 2006.

[92] O. Umezawa and K. Nagai. Deformation structure and subsurface fatigue crack generation in austenitic steels at low temperature. *Metallurgical and Materials Transactions A-Physical Metallurgy and Materials Science*, 29(3):809–822, 1998.

[93] H. Yokoyama, O. Umezawa, K. Nagai, T. Suzuki, and K. Kokubo. Cyclic deformation, dislocation structure, and internal fatigue crack generation in a Ti-Fe-O alloy at liquid nitrogen temperature. *Metallurgical and Materials Transactions A-Physical Metallurgy and Materials Science*, 31(11):2793–2805, 2000.

[94] K Tokaji. Mean stress dependence of fatigue strength and subsurface crack initiation in Ti-15Mo-5Zr-3Al alloy. *Materials science and engineering. A, Structural materials*, 281(1-2):268–274, 2000.

[95] K. Tokaji, M. Kamakura, Y. Ishiizumi, and N. Hasegawa. Fatigue behaviour and fracture mechanism of a rolled AZ31 magnesium alloy. *International Journal of Fatigue*, 26(11):1217–1224, 2004.

[96] M. Hagiwara, A. Araoka, S. J. Yang, S. Emura, and S. W. Nam. The effect of lamellar morphology on tensile and high-cycle fatigue behavior of orthorhombic Ti-22Al-27Nb alloy. *Metallurgical and Materials Transactions A-Physical Metallurgy and Materials Science*, 35A(7):2161–2170, 2004.

[97] K. Gall, M. F. Horstemeyer, B. W. Degner, D. L. McDowell, and J. H. Fan. On the driving force for fatigue crack formation from inclusions and voids in a cast A356 aluminum alloy. *International Journal of Fracture*, 108(3):207–233, 2001.

[98] D.L. McDowell. Unpublished Research.

[99] Y. Q. Fu, Y. W. Gu, A. W. Batchelor, and W. Zhou. Investigation of fracture toughness of deep carburised M50NiL steel under different tempering temperatures. *Materials Science and Technology*, 14(5):461–465, 1998.

[100] J. P. Wise and D. K. Matlock. Bending fatigue of carburized steels: A statistical analysis of process and microstructural parameters. *S A E transactions*, 109:182–191, 2000.

[101] B. Mintz, R. Abushosha, and D. N. Crowther. Influence of small additions of copper and nickel on hot ductility of steels. *Materials Science and Technology*, 11(5):474–481, 1995.

[102] R. Labusch. A statistical theory of solid solution hardening. *Physica Status Solidi*, 41(2):659–669, 1970.

[103] E. Hornbogen and K. H. Z. Gahr. Distribution of plastic strain in alloys containing small particles. *Metallography*, 8:181–202, 1975.

[104] M.F. Ashby. *On the Orowan Stress*. M.I.T. Press, Cambridge, MA, 1969.

[105] P.B. Hirsch and F.J. Humphreys. *Plastic Deformation of Two-Phase Alloys Containing Small Nondeformable Particles*. The M.I.T. Press, Cambridge, MA, 1969.

[106] A.S. Keh and S. Weissman. *Deformation Structure in Body-Centered Cubic Metals*. Interscience, New York, 1963.

[107] W.C. Leslie, J.T. Michalak, and F.W. Aul. *The Annealing of Cold-Worked Iron*. Interscience, Detroit, 1961.

[108] E. Scheil. *Zeitschrift Fur Metallkunde*, 34:70–72, 1942.

[109] S. R. Goodman, S. S. Brenner, and J. R. Low. FIM-atom probe study of precipitation of copper from iron-1.4 at pct copper .1. field-ion microscopy. *Metallurgical Transactions*, 4(10):2363–2369, 1973.

[110] J. S. Langer and A. J. Schwartz. Kinetics of nucleation in near-critical fluids. *Physical Review A*, 21(3):948–958, 1980.

[111] J. F. Nie and B. C. Muddle. On the form of the age-hardening response in high strength aluminium alloys. *Materials Science and Engineering A-Structural Materials Properties Microstructure and Processing*, 319:448–451, 2001.

[112] J. F. Nie. Effects of precipitate shape and orientation on dispersion strengthening in magnesium alloys. *Scripta Materialia*, 48(8):1009–1015, 2003.

NORTHWESTERN UNIVERSITY

Residual Stress Control and Design of Next-Generation Ultra-hard Gear Steels

A DISSERTATION

SUBMITTED TO THE GRADUATE SCHOOL

IN PARTIAL FULFILLMENT OF THE REQUIREMENTS

for the degree

DOCTOR OF PHILOSOPHY

Field of Materials Science and Engineering

By

Yana Qian

EVANSTON, ILLINOIS

June 2007

ABSTRACT

Residual Stress Control and Design of Next-Generation Ultra-hard Gear Steels

Yana Qian

In high power density transmission systems, Ni-Co secondary hardening steels have shown great potential for next-generation gear applications due to their excellent strength, toughness and superior fatigue performance.

Study of residual stress generation and evolution in Ferrium C61 and C67 gear steels revealed that shot peening and laser peening processes effectively produce desired beneficial residual stress in the steels for enhanced fatigue performance. Surface residual stress levels of -1.4GPa and -1.5GPa were achieved in shot peened C61 and laser peened C67, respectively, without introducing large surface roughness or defects. Higher compressive residual stress is expected in C67 according to a demonstrated correlation between attainable residual stress and material hardness. Due to the lack of appropriate shot media, dual laser peening is proposed for future peening optimization in C67.

A novel non-destructive synchrotron radiation technique was implemented and applied for the first time for residual stress distribution analysis in gear steels with large composition and property gradients. Observed substantial residual stress redistribution

and material microstructure change during the rolling contact fatigue screening test with extremely high 5.4GPa load indicates the unsuitability of the test as a fatigue life predictor.

To exploit benefits of higher case hardness and associated residual stress, a new material and process (CryoForm70) aiming at 70Rc surface hardness was designed utilizing the systems approach based on thermodynamics and secondary hardening mechanisms. The composition design was first validated by the excellent agreement between experimental and theoretical core martensite start temperature in the prototype. A novel cryogenic deformation process was concurrently designed to increase the case martensite volume fraction from 76% to 92% for enhanced strengthening efficiency and surface hardness. High temperature vacuum carburizing was optimized for desired carbon content profiles using carbon diffusion simulation in the multi-component system. After cyclic tempering with intermediate cryogenic treatment, a case hardness of 68.5 ± 0.3Rc at 0.72 ± 0.2wt% carbon content was achieved. The design demonstrated the effectiveness of cryogenic deformation in promoting martensite transformation for high carbon and high alloy steels. Good agreement between achieved and predicted case and core hardness supports the effectiveness of the computational design approach.

Acknowledgements

I would like to take this opportunity to express my gratitude for the tremendous amount of support I received throughout my graduate study at Northwestern University. It is never adequate to say "thank you" to everyone. Here I would like to especially thank the following individuals, without whom, I would not have accomplished so much.

Professor G. B. Olson - You are indeed a role model for me. Your intelligence and knowledge, and your art in advising always amaze me. Thank you so much for your valuable advice on my research and my career.

Dr. Jonathan Almer - Thank you for your collaboration and help on my research. My study would not have been successful without you. I will never forget the days and nights I spent at the Advanced Photon Source, Argonne National Laboratory.

Professor Michael J. Bedzyk, Professor David C. Dunad and Professor Qian (Jane) Wang - Thank you for serving on my committee and for your helpful discussions.

Professor Christine L. Corum from Purdue University - Thank you for your collaboration on the Cryogenic Shot Peening project. My visit and experiment at Purdue were certainly enjoyable.

Mr. Jerry Carsello, Dr. Kathleen A Stair and Mr. Mark Seniw - Thank you for training me with the usage of various equipment. I would not have collected valuable data without your instruction and helpful discussions.

Dr. Benjamin Tiemens - Thank you for helping me with my synchrotron experiment. I can not imagine how I could get through the three-day beamtime without your help. And thanks for sharing an office and cheerful hours with me.

The 390 Extreme Dragonslayer Design Team, 2004 - Julian Benz, Young Chang, Akbar Naqvi and Kittichai Sojiphan - Thank you all for your hard work. You made this design possible.

Mr. Brian Tufts, Dr. Herng-Jeng Jou from QuesTek Innovations, Inc. - Thanks for your helpful discussions. Mr. Jeremy Hahn from Purdue University - Thank you for your help with the Shot Peener at Purdue. Professor Y. S. Pyoun from DesignMecha Co., Ltd. in South Korea - Thank you for the Ultrasonic Surface Modification treatment. Mr. Steven Lilagan from Metal Improvement Company, Inc. - Thank you for helpful discussions on shot peening.

Dave and Padmanav - Thanks for being my office mates. I certainly enjoyed your presence. Past and present Olson group members - Thank you all for your help. MSE staff members, especially Peggy Adamson - Thanks for making the graduate life easier.

The research work was originally sponsored by the Department of Energy, Office of Industrial Technologies. Thanks for the funding support.

Also I'd like to thank my parents for being so supportive. I have come such a long way and you are always there for me. Thank you. My sister - Thank you so much for taking care of mom and dad when I am far away from home. Your voice over the phone is always a comfort to me. My husband, Jun - You have become the most important part of my life. Thanks for all your love and patience, as well as for your encouragement when trouble finds me. I love you from the bottom of my heart.

I would like to thank my friends - too many to be listed - at Northwestern as well. Thank you all for sharing with me those wonderful memories.

Table of Contents

List of Tables

CHAPTER 1

Introduction

1.1. Motivation

High strength gear and bearing steels have been in rising demand for high power density transmission systems since the 1940's for their excellent performance under harsh working conditions. In aerospace, automobile, and heavy machinery industries, performance requirements become more and more demanding due to the increasing load, speed and temperature of the working environment. From the 1940's to 1990's, the lives of high strength gear and bearing steels for aerospace applications were improved by approximately 200 times, which was attributed to improved material cleanliness, controlled material microstructure, induced compressive residual stresses and improved fracture toughness [**1**]. Pyrowear 53 and M50NiL carburized steels have been recognized as the best gear and bearing steel, respectively, since the 1990's, because of their superior strength, toughness, wear and fatigue resistance. However, the development of new and better steels has been slowed down since then as the theoretical limit of property objectives is being approached.

The conventional steel alloy design heavily relied on empiricism. However, the high cost and time-consuming experimentation greatly impeded the development and commercialization of new advanced steels. To accelerate the development of new steel alloys by utilizing the valuable scientific information accumulated for centuries, the Steel Research

Group (SRG), a multi-institutional university/government/industry research team, was founded at MIT in 1985 and reorganized in 1988 at Northwestern University. SRG focused on the development of ferrous and non-ferrous alloys by establishing quantitative composition-structure-property models and necessary databases. By integrating computational modeling and the systems approach [**2**], the amount of experimentation for designing new materials can be reduced to 2∼3 single prototype iterations. Through the collaboration between multiple institutes and organizations, SRG has successfully accomplished the computer-aided design of new generation high performance steels, including the Ferrium® C61 and C67 steel families. Both families are named after the achieved case hardness, i. e., 61 Rc and 67 Rc, respectively. C61 has been proven to exceed AISI 9310 in fatigue performance and has been commercialized. The development of ultrahigh-strength steel, C67, is still ongoing.

To explore the performance potential of Ferrium C61 and C67 steels and the possibility of alloy redesign for higher hardness, a multi-disciplinary research project was carried out at Northwestern University. The project focused on the optimization of industrial processes, fatigue property demonstration for C61 and C67, and methods for residual stress control in these steels. Based on the research on C61 and C67 steels, the alloy redesign for higher hardness was proposed as higher hardness enables the achievement of higher contact fatigue strength and larger compressive residual stresses. Through the design, we also attempt to first understand the theoretical limit of case hardness in the C67 family and then to computationally design a new steel approaching this limit. In parallel, the Gear Industry specified in their vision for 2025 that an advanced gear steel with surface hardness of 70Rc is desired to improve the power density by 25% every five

years [**3**]. This vision also promoted our study on the design of next-generation ultra-hard gear steels.

1.2. Systems design of materials

The systems approach for new materials design mentioned in Section 1.1 originated from the general approach to solving complex problems in system engineering as reviewed by Jenkins [**4**]. Illustrated by Fig. 1.1 is the problem-solving flow from analysis, design, implementation to operation. The analysis of the system generates the design objectives. When designing the system, quantitative models describing relations between inputs and outputs of the system are established. Prediction of the overall system performance is also obtained from the outputs. Subsystems and conflicting objectives are often involved during this step when a system is complex. The goal of systems design is to improve the overall performance, even at the expense of sacrificing individual subsystems. After the system is designed, it is created and tested through implementation. If the objectives are not fully met, the information gathered through the design process will be fed back to the initial system analysis and the new iteration of design is started. Several iterations may be needed before the final design is demonstrated to be successful and put into operation.

After Smith recognized the complexity of materials and the feasibility of treating materials as a hierarchy of structures which can be optimized for overall performance [**5**], Olson extended his idea to the four elements in material science. Processing, structure, properties and performance are four essential elements for materials science and their linear relationship is described in Fig. 1.2 [**6**]. Each element can be treated as a system

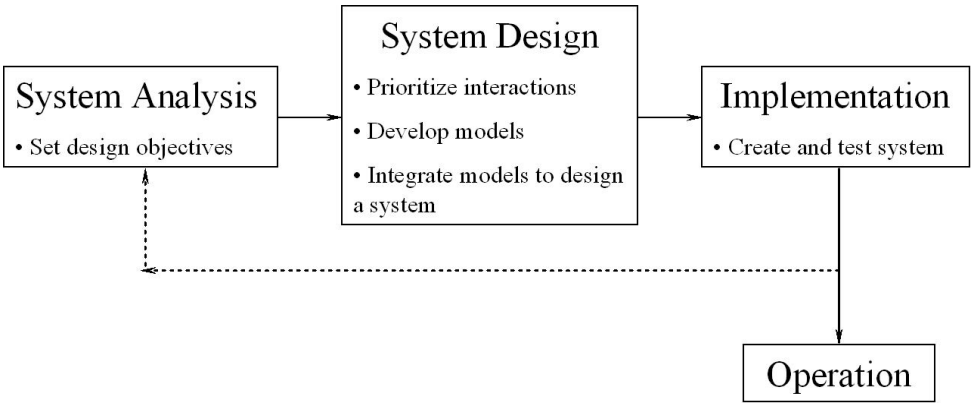

Figure 1.1. Problem solving flow using system approach.[**4**]

and broken down into subsystems. Subsystems interact with one another within one element and with subsystems belonging to other elements. A system design diagram can be drawn to elaborate relations between these subsystems and thus guide the design of materials. Such a diagram is explained in detail in Chapter 5.

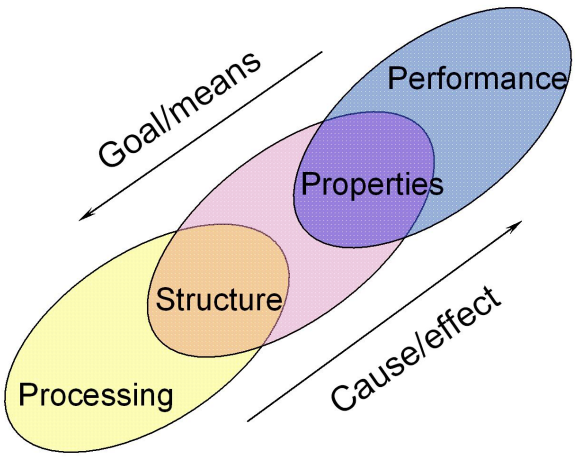

Figure 1.2. Four elements in Materials Science and their relationship.[**6**]

1.3. Project overview

The 5 year DOE-OIT supported research project titled *Materials and Process Design for High-Temperature Carburizing: Integrating Processing and Performance* consisted of three major parts. Dr. Jay Gao focused on high temperature carburizing process design. Graduate student, Benjamin Tiemens participated in industrial process optimization and fatigue testing for C61 and C67 steels. Coordinated study on residual stress control in high strength steels and on alloy redesign for higher hardness is the subject of this dissertation.

1.3.1. Process simulation

A detailed procedure of carburizing process simulation was developed by Dr. Jay Gao to reduce the number of experimental carburization trials and therefore lower the cost of process development [**7**]. The software Thermo-Calc/DICTRA was selected due to its ability of including necessary features in high temperature carburizing of complex multicomponent alloys. Dr. Gao also developed a new process optimization software system built on Thermo-Calc/DICTRA and the QuesTek TCIPC interface [**8**].

1.3.2. Performance demonstration

Graduate student Benjamin Tiemens performed industrial fatigue testing for spur gears of Ferrium C61 and C67 steels at the General Motors Research and Development Center. Superior performance of C61 was demonstrated but C67 still needed further process optimization for improved fatigue performance. Building on this research, principles and methods for residual stress control were further studied in this thesis. The feasibility of surface treatment optimization was also examined.

1.3.3. Residual stress control and new alloy design

It is known that well controlled residual stresses can benefit the fatigue performance of high strength gear and bearing steels. To fully explore the fatigue properties of Ferrium C67, a study on methods and mechanisms of producing beneficial residual stress was carried out. Feasibility of optimizing shot peening, one technique to generate compressive residual stresses, was investigated. A non-destructive method to measure residual stress distributions was developed to accelerate the study. Based on findings from residual stress study and from properties of Ferrium C67, a new ultra-hard steel alloy was then designed for better wear and contact fatigue resistance to exploit the advantages of controlled residual stresses.

1.4. Research approach

1.4.1. Residual stress control for high strength gear and bearing steels

High strength gear and bearing steels, Ferrium®C61 and C67 were successfully developed using computational tools guided by the systems approach. Superior strength and toughness over conventional gear and bearing steels were achieved [**9**]. To further explore the performance potential of these two steels, efforts were contributed to the optimization of beneficial residual stresses and corresponding processes. As reviewed in Chapter 2, shot peening and laser peening are powerful techniques to produce high compressive residual stresses in the materials. Therefore, both peening methods were first investigated for feasibility. The attainable residual stress levels in both C61 and C67 steels were then estimated according to the correlation between maximum residual stress and material hardness. After identifying appropriate peening service providers, both specimens and

gears made of C61 and C67 underwent either shot peening or laser peening with different peening conditions. Steels after peening were characterized for microstructure, residual stress and mechanical properties. Characterization for gears subject to peening treatments was conducted by Benjamin Tiemens in the General Motors Research and Development Center. As part of processing optimization, the post-peening treatment was also studied to minimize the detrimental effect of rough surfaces on gear performance.

X-ray diffraction was employed to measure surface residual stresses in specimens with various treatments. However, to obtain subsurface residual stresses, material removal is required, which is destructive and brings the need of data correction. To accelerate the optimization of residual stresses, a non-destructive technique utilizing high energy synchrotron radiation was developed. Measured residual stress depth profiles in various steels were used to assist the peening process optimization and to help interpret mechanical phenomena occurring during rolling contact fatigue.

1.4.2. Composition and process design of an ultrahigh-strength steel

From the residual stress study for Ferrium® C61 and C67 steels, it was established that the attainable surface compressive residual stress increases with hardness, which should promote more fatigue resistance. In addition, higher hardness itself allows the material to resist higher levels of contact stress. Thus with combined higher surface hardness and larger compressive residual stress, the steel should present superior wear and fatigue resistance than the current C67 steel. Therefore, composition and process design for an ultrahigh-strength steel with surface hardness of 70 Rc was proposed and carried out as a final component of the project.

After the prototype alloy was made, subsequent process optimization/development was performed to achieve the desired properties. The steel will be used to explore the achievable maximal beneficial residual stress and resulting fatigue performance. The design also helps establish the limit of surface hardness and strength that can be accomplished in steels using the secondary hardening carbide mechanism.

1.4.3. Dissertation outline

Following the introduction in Chapter 1, Chapter 2 presents the current status of high strength gear and bearing steels and residual stress study for this type of steel. Materials, processing and characterization methods involved in this research are described in Chapter 3. Feasibility of process optimization for desired residual stresses in high strength steels is investigated in Chapter 4. To effectively explore residual stress behavior, a fast, accurate and non-destructive characterization method was developed and successfully demonstrated, which is explained in Chapter 4 as well. The entire design process of the new steel alloy is elaborated in Chapters 5, 6 and 7, including design concepts for materials and processing, the predictive design of alloy compositions and characterization of the prototype alloy. Conclusions and suggestions for future work on residual stress study for high strength gear steels and on the design of next-generation ultra-hard steel are given in Chapter 8.

CHAPTER 2

Background

2.1. Gear design

Essential for power transmission systems, gear and bearing components have been under development for more than two millennia since the ancient Chinese began to use gears in "South Pointing Chariots" in 2600 B.C [**10**]. Modern gear and bearing design and materials development have been centered around the consistent improvement in component life, gearing efficiency and power density. Efforts have been made to postpone and even eliminate various failure modes. Two major fatigue modes include tooth bending fatigue and contact fatigue. For gear components, bending fatigue resistance receives relatively more attention while bearing components require contact fatigue and wear resistance.

Fatigue failure occurs when a certain area of the component is subject to a cyclic stress above its endurance limit. Therefore, estimation of applied stress has become quite meaningful for gear design. For a gear tooth, six basic types of applied stress can be found during the point or line contact between the mating teeth. These applied stresses include tensile stress (TN), compressive stress (C), slide-shear stress (S), rolling stress (R), roll-slide stress and torsion stress [**11**]. Very often two or three types of stress are simultaneously applied to a specific area of the tooth. Presented in Fig. 2.1 and Fig. 2.2 are the applied stresses for a spur gear tooth, and the stress depth distribution under contacting surfaces, respectively.

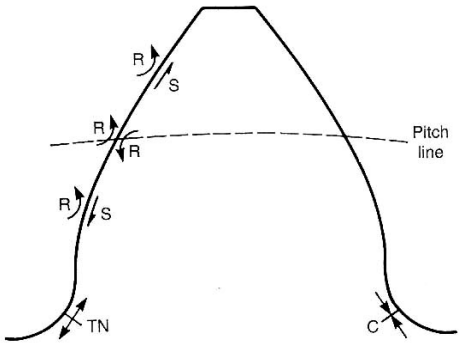

Figure 2.1. Stress areas on basic spur gear tooth [**11**]

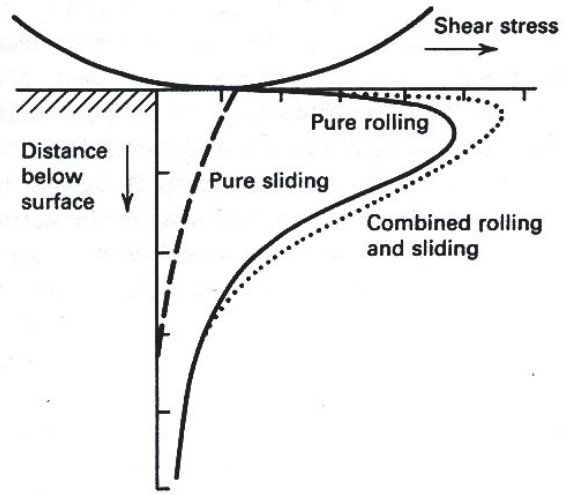

Figure 2.2. Stress depth distribution in contacting surfaces [**12**]

Dudley derived the simplified equation for surface contact stress, S_c (in psi), from rolling contact mechanics [**13, 12**].

$$S_c = C_k(KC_d)^{0.5} \tag{2.1}$$

where C_k is the geometry factor for durability, K is the index of tooth loading severity for pitting (usually called K-factor), and C_d is the overall derating factor for durability. (Values for C_k and C_d can be found in Reference [**12**] Chapter 14.)

The K-factor for spur and helical gears is:

$$K = \frac{W_t}{Fd}\left(\frac{m_G + 1}{m_G}\right) \tag{2.2}$$

where W_t is the tangential driving force (in pounds), obtained from the horsepower being transmitted by the combination of pinion and gear - P, the speed of the pinion in revolutions per minute - n_p, and the pitch diameter of the pinion - d (in inches).

$$W_t = \frac{P \times 126,050}{n_p \times d} \tag{2.3}$$

In Eq. 2.2, F is the net face width in contact (in inches), and m_G is the ratio of the number of gear teeth to the number of pinion teeth.

The bending stress, S_t, of a pinion or mating gear tooth may be estimated using the following formula derived from Lewis's cantilever model [**13, 12**]:

$$S_c = K_t U_1 K_d \tag{2.4}$$

Similarly, K_t and K_d are geometry factor and overall derating factor, respectively. U_1, the index of tooth loading severity for breakage, often called unit load, can be determined as the following for spur or helical teeth:

$$U_1 = \frac{W_t P_n}{F} \tag{2.5}$$

where P_n is the normal diametral pitch (1/inch).

Guided by the above calculation of surface contact and tooth bending stresses, gear engineers were able to preliminarily estimate the gear size, given specifications on power transmission. However, difficulty rises when there exist residual stresses at the gear tooth. Thus it is necessary to review the influence of residual stresses on the effective applied stress, which will be given in Section 2.4.

2.2. Gear and bearing steels

2.2.1. Design of gear and bearing steels

The most commonly used materials for gear and bearing components are various steel alloys because they meet most of the qualifications required by the applications, such as high allowable bending and contact stresses, good wear resistance and impact strength, good corrosion resistance, relatively low manufacturing cost and good reliability.

One of the most crucial requirements for gear and bearing steels is strength, which is frequently used to characterize the amount of stress that can be tolerated in the steel component before plastic deformation takes place. Bending fatigue performance mainly relies on the bending strength of the gear tooth, which is a function of surface hardness and surface conditions. The compressive strength of the core material in a carburized steel is another often considered factor, which indicates steel's ability to withstand surface pressure during crushing or indenting. For rolling contact bearings, shear strength is the controlling factor of failure since the initial fracture often occurs along the shear plane. One example is that a shaft subject to torsion loads finally failed along the longitudinal or transverse directions. Fig. 2.3 shows the estimated correlation between shield yield

strength and surface hardness for both high carbon steels and carburizing steels. As surface hardness increases, the alternating bending fatigue strength and contact fatigue strength also improve, as displayed in Fig. 2.4 and 2.5. Another desired property for gear and bearing steels is core toughness, which is essential to reduce the risk of catastrophic fracture failure.

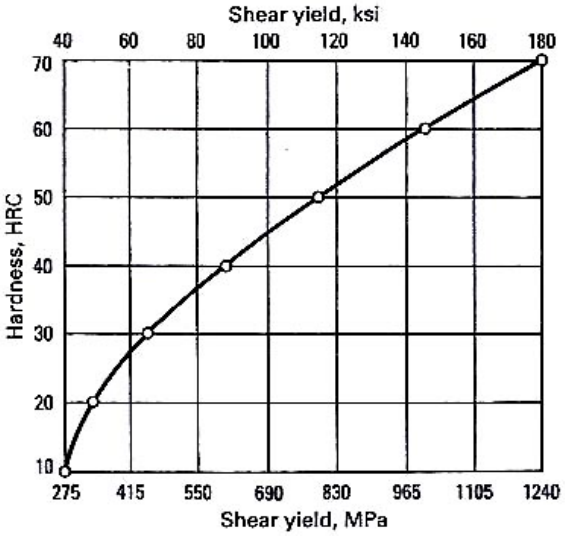

Figure 2.3. Estimated correlation between shear yield strength and hardness [**14**]

Given the above correlations between material hardness and performance, it is natural for engineers to develop new steels by seeking desired hardness profiles. Considerations on toughness, hot hardness, ductility, easy processing, are also incorporated in the steel design.

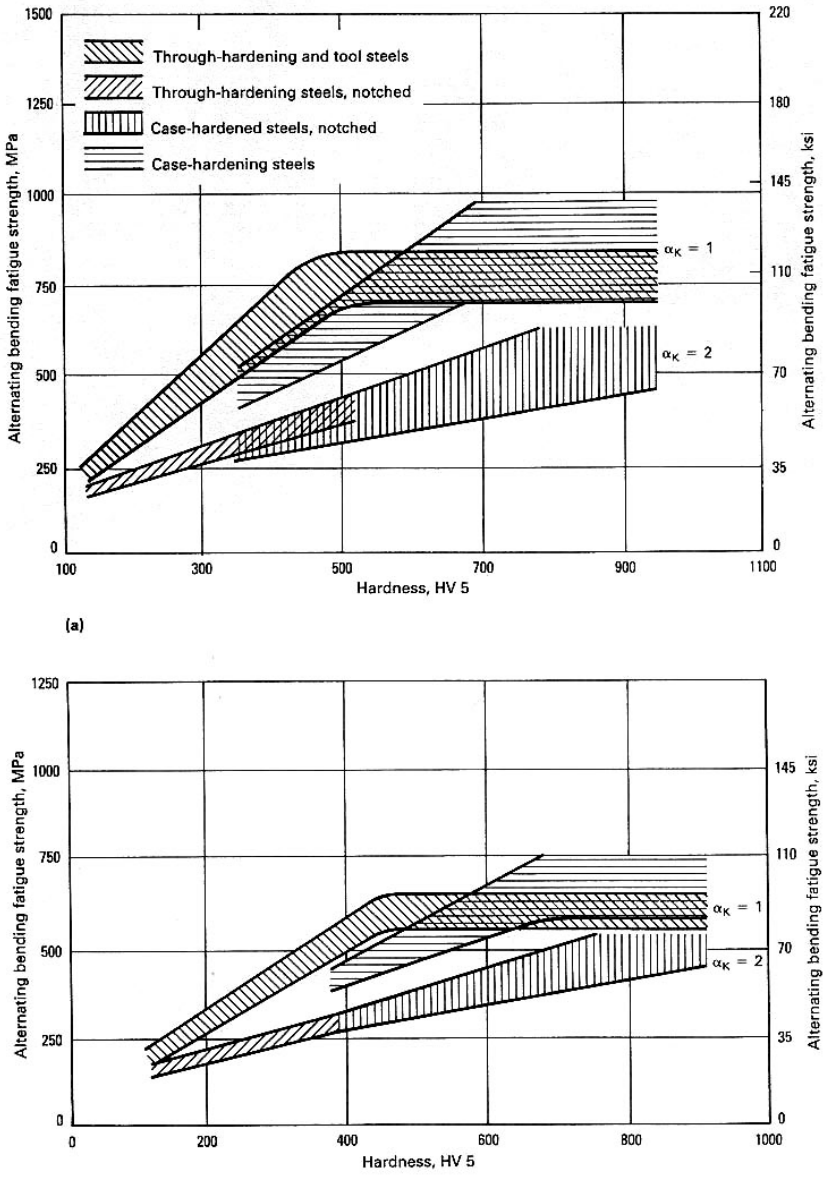

Figure 2.4. Correlation between alternating bending fatigue strength and hardness [**15**]

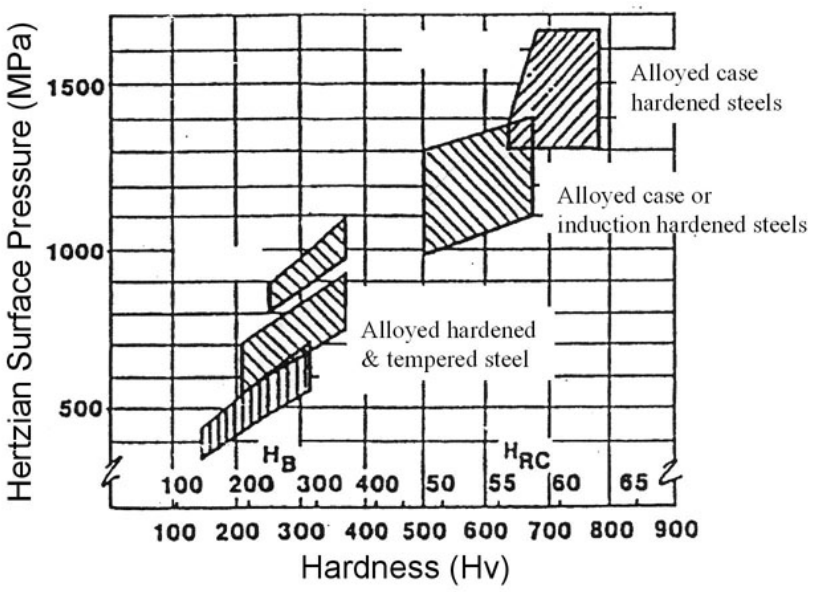

Figure 2.5. Correlation between contact fatigue strength and hardness [**16**]

2.2.2. Commercial high strength gear and bearing steels

The most widely and commonly used ferrous alloys for gear and bearing components are wrought surface hardening and through-hardening carbon and alloy steels. Other ferrous alloys used for gears include cast iron/steels, powder metallurgy iron/steels, stainless steels, tool steels and maraging steels. Surface hardening can be accomplished through carburizing and/or nitriding. Carburized steels are to date the best candidates for heavy-duty components, such as transmission gears, since they gain superior fatigue, wear resistance from hardened surface, and impact resistance from the tough core. A sufficient case depth is required to prevent case crushing in the design, and a reasonable core hardness is needed to support the case. Compressive residual stresses are usually produced in the case during the hardening process, which further help improve the fatigue resistance. Because of the combined benefits from surface hardness, interior toughness and compressive

residual stress, case-hardened steels can withstand higher load than through-hardened steels. But the latter possesses a higher core strength and its processing is much more cost effective due to the simpler heat treatment required. Compared to carburizing, nitriding offers the advantage of much less distortion and easier dimensional control since it does not involve heating to austenite phase and subsequent quenching. However, nitrided steels often lack the ability to endure possible overload since case crushing can occur due to the shallow case depth.

Carburized AISI 8620 and AISI 9310 steels serve as good representatives for advanced high performance gear and bearing steels. Alloyed with Ni, Cr, Mo, these two steels give exceptional core toughness combined with a high degree of wear resistance and surface compressive strength. They can operate with bending stresses of 483 MPa and maximum contact stresses of 1.38 GPa [**17**]. AISI 9310 is now a standard to which advanced steels are usually compared. It has a surface hardness of 60 Rc with an exceptional core toughness of 126 ksi$\sqrt{in}$ at 35 Rc. AISI 52100 is a typical through-hardened steel with hardness of 60 Rc to 64 Rc, presenting excellent contact fatigue and wear resistance for bearing applications. It has a high carbon martensite matrix with primary carbides and 5 to 10% retained austenite [**14**].

As a medium-alloy stage-I tempered steel, AISI 9310 has a limiting operation temperature of 150 °C above which hardness loss takes place. This results from the replacement of hardening epsilon carbides by cementite. Consequently, early bending fatigue, surface pitting failure or scoring will occur. Therefore, several high temperature steels were designed to meet the criterion that the accepted minimum hardness should reach 58 Rc at operating temperatures from 232 °C to 315 °C. Alloy carbide strengthened M50 has been

successfully used as bearings for temperatures up to 315 °C in aircraft and turbine engines [**17**]. Later on, M50's brittleness led to the development of case-hardened M50NiL, which displays better toughness with the addition of Ni and lower carbon content [**14**]. Two other high temperature steels are CBS600 and CBS1000M [**18**]. They are low- to medium-alloy that can be hardened to 60 Rc with a core hardness of 38 Rc. However, CBS600 has a medium fracture toughness that can cause fracture failure when a surface fatigue spall forms. Compositions of these steels are listed in Table 2.1.

Table 2.1. Compositions (wt%) of various high performance steels

Steel	C	Mn	Ni	Cr	Mo	V	Si	P	S
52100	1.04	0.35	----	1.45	----	---	0.25	----	----
8620	0.18-0.23	0.70-0.90	0.40-0.70	0.40-0.60	0.15-0.25	---	0.15-0.35	0.035max	0.04max
9310	0.08-0.13	0.45-0.65	3.00-3.50	1.00-1.40	0.08-0.15	---	0.15-0.35	0.035max	0.04max
M50	0.85	---	---	4.10	4.25	1.00	---	---	---
M50NiL	0.13	0.25	3.40	4.20	4.25	1.20	0.20	---	---
CBS600	0.19	0.60	----	1.45	1.00	---	1.10	---	---
CBS1000M	0.13	0.55	3.00	1.05	4.50	0.40	0.50	---	---

2.2.3. Computationally designed high performance steels

Utilizing the system approach and computational tools, the Steel Research Group (SRG) at Northwestern University has successfully designed several high performance gear and bearing steels, including martensitic stainless steel CS62, Ferrium®C61 steel with high core strength and toughness, high strength steel Ferrium®C67 and its variations. All steels were strengthened through efficient nano-size M_2C carbide precipitation during stage IV tempering. C61 has the surface hardness of 60-62 Rc and core hardness of 48-50 Rc, providing comparable resistance to surface fatigue and wear resistance to AISI 9310 but higher core strength. C61 was designed for alternatives to current gear materials

in applications where elevated core strength is required but component redesign is not feasible. The design of C67 was targeted for superior surface wear and contact resistance with a desired surface hardness of 67-69 Rc. It is the product of the ongoing research program with the objective of reducing gear weight by as much as 50% over conventional carburized steels. Material compositions are given in Chapter 3.

2.3. Systems design of secondary hardening carburized steels

The systems approach has been successfully applied to the design of high strength steels employing secondary carbides - M_2C as strengthening precipitates [**19, 20**]. A flow chart is first established to elaborate the relationship between processing-structure and properties-performance. Desired properties or performance requirements are prioritized to reflect the application needs. Structure describes the hierarchy of microstructural subsystems, for example, the case and core subsystems in a case hardened steel. Processing includes all sequential steps, generating the desired microstructure. Quantitative models are then devised to predict the material property or performance response to the variation in material processing or compositions. For instance, Wise has developed a secondary hardening strengthening model to predict strength from steel's compositions and processing and thus compositions can be derived from the needed strength using this strengthening model [**20**]. A brief introduction on the microstructure subsystems for secondary hardening carburized steels, such as Ferrium®C61, C67, is given below to provide basic understanding of material systems.

For the design of Ferrium®C61, C67 steels, the prioritized performance requirements include contact and bending fatigue resistance, wear resistance and fracture toughness.

Thus the alloy should possess sufficient hardness to withstand high Hertzian contact stress and bending stress. It should present general flaw tolerance as well. To satisfy these criteria, a case-core structure is selected, in which the ductile core provides flaw tolerance, and the hard case provides stress resistance.

Components in the core subsystem usually include the matrix, strengthening dispersions, grain refining dispersions and grain boundary cohesion promoters. Lath martensite with Ni, Co in solution is the matrix of the core in secondary hardening carburized steels. No retained austenite should be observed in the core matrix, i.e., full martensite transformation should be achieved after quenching. Typically, a martensite start temperature of 300 °C is required for fine lath martensite formation. Strengthening dispersions are secondary alloy carbides, M_2C, where M represents Cr, Mo, V and W. They form during stage IV tempering ($400 - 600\,^{\circ}C$) when coarse cementite is dissolved. Cementite, M_6C and $M_{23}C_6$ should be avoided since they reduce fracture toughness and strength.

A trace amount of titanium carbides are utilized to pin grain boundaries during solution treatment, thereby limiting grain growth. Grain boundary cohesion is important for steel service in a corrosive environment where chemical embrittlement may occur. The segregation of impurities, such as phosphorus and sulfur, to the grain boundaries during tempering will lower the interfacial cohesion, which can result in brittle-fracture, particularly with the influence of environmental hydrogen. Therefore, high purity is obtained through VIM and VAR processes. Rare-earth elements, such as La, are added to getter impurities. Boron is also included in the composition to enhance the grain boundary cohesion because it can increase the work of decohesion for grain boundaries [**2**].

In the case subsystem, a gradient of M_2C carbide dispersions is formed to provide desired hardness profile. Studies have shown with the optimal size of 3nm, maximum strengthening effect can be obtained [**21**]. Maximized M_2C driving force is needed to ensure the fine precipitation. Beneficial compressive residual stress is desired in the case for the improvement of fatigue, wear and corrosion resistance. It can be produced through carburizing and subsequent quenching. More effective methods to generate compressive residual stresses will be discussed in the next section.

2.4. Residual stress in gear and bearing steels

2.4.1. Influence of residual stress on fatigue life

Structural components such as gears and bearings often contain residual stresses from forming, machining and heat treatment. It is well known that compressive residual stresses are beneficial for improving fatigue endurance limit due to their ability of retarding fatigue crack initiation and propagation. In the study of Schlicht et al. [**22**], it was shown how residual stress can alter the equivalent stress distribution in rolling contact, as illustrated in Fig. 2.6. The resulting actual net shear stress from the combination of nominal shear stress and residual stress is designated by equivalent stress σ_v. Residual stresses are assumed to be biaxial (parallel to the surface in the x and y directions) and the two components, $\sigma_{x,res}$ and $\sigma_{y,res}$ are set equal. The residual stress component perpendicular to the surface is zero near the surface. All stresses were normalized to the Hertzian pressure p_0. The depth was normalized to the half width of the contact area b in the rolling direction. It was clear that the appropriate compressive residual stress could decrease

the equivalent stress while the presence of tensile residual stress caused an increase of the equivalent stress curve.

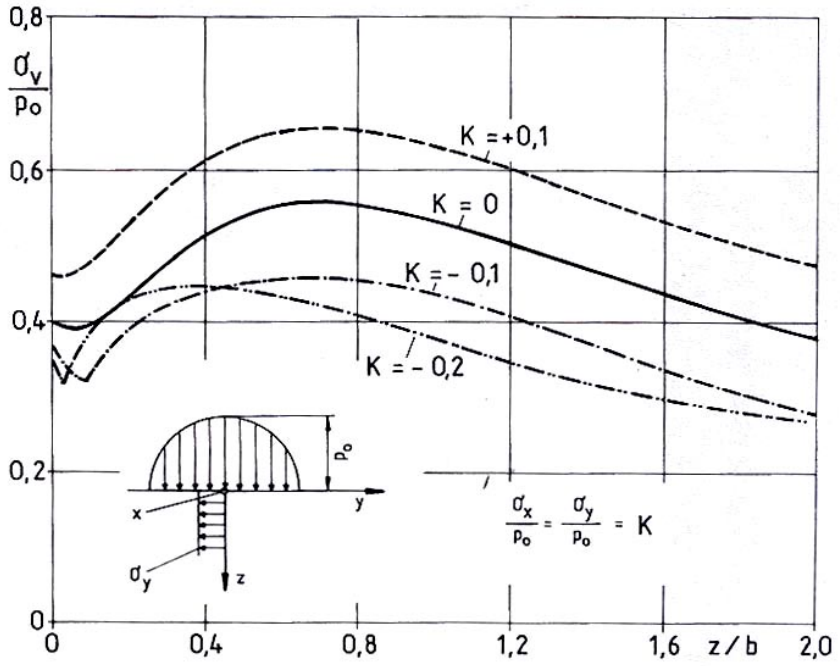

Figure 2.6. Influence of residual stress on equivalent stress distribution

Nelson reviewed the effects of compressive and tensile residual stresses on Mode I fatigue crack growth [**23**]. Two approaches for predicting the influence of residual stress on crack growth were discussed. One was the superposition of the respective stress intensity factors for the applied stress and the residual stress. The other was the simplified crack closure model. In the superposition approach, for a plate with a centering crack, an effective stress intensity was taken as $K_{eff} = K_{res} + K_{appl.}$. Fig. 2.7 schematically shows the variation of effective stress intensity for crack growth through a compressive residual stress field with constant loading amplitude at two mean stress levels. For $R = 0$, crack growth rate was correlated to the ΔK_{eff} above 0 (ΔK_a shown in Fig. 2.7) and good

predictions had been achieved. Another way was to correlate the crack growth rate to $\Delta K_{eff} = \Delta K_b$ and the effective R-ratio (given by $R_{eff} = K_{eff,min}/K_{eff,max}$). Since $\Delta K_b = \Delta K_{appl.}$, it was the influence of negative R_{eff} that slowed the growth. This correlation method also produced good predictions. However, if the applied load has a significant tensile mean stress, i.e. $R > 0$, the influence of compressive residual stress would only be to reduce R_{eff}.

K_{res} can be calculated using Kanazawa's relation [**24**]:

$$K_{res} = \int_{-a}^{a} \sigma_{res}(x) \left[\frac{2 \sin \frac{\pi(a+x)}{W}}{w \sin \frac{2a\pi}{W} \sin \frac{\pi(a-x)}{W}} \right]^{1/2} dx \tag{2.6}$$

where a is the crack half length, W is the plate width, x is the distance from the plate centerline and $\sigma_{res}(x)$ represents the residual stress. The superposition approach has been used to successfully predict the crack growth rate under constant loading amplitude in existing residual stress fields, however, with the condition that the residual stress field is not significantly changed by service load or crack growth. In many cases, crack life is consumed before it grows into the residual stress field with the opposite sign so a reasonable prediction of the total life can still be obtained.

In the crack closure model, the crack-generated residual stress or the re-distribution of residual stress caused by crack growth was taken into account to predict effects of loading sequence and mean stress on the crack growth rate. This method was proven to be effective for the case that service loadings and/or crack growth altered the residual stress field. The drawback of the crack closure model is that it requires complex elastic-plastic finite element analysis, which needs to be repeated as a crack grows. And the

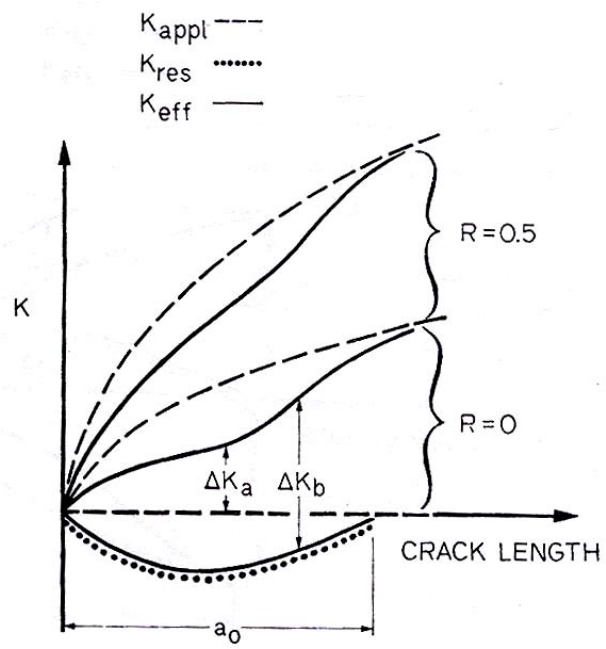

Figure 2.7. The variation of effective stress intensity for crack growth through a compressive residual stress field [**23**]

simplified models are usually used to describe cracks with simple geometries, such as the center crack in a plate.

2.4.2. Technologies to enhance beneficial residual stresses

2.4.2.1. Carburizing. Carburizing is one of the surface or case hardening techniques for steels, which introduces a carbon content gradient from the surface to the core material. Thus a gradient of M_s temperature is formed along the carbon diffusion direction in the case. Usually the high carbon case has a lower M_s temperature than the low carbon core. During quenching, martensite transformation occurs earlier in the core than in the case. The 3-4% volume expansion due to core martensite transformation deforms the case as it is still in the austenite phase. Upon further cooling, the case transforms, at a later time,

and tends to expand. However, its expansion is constrained by the strong martensite core and therefore a compressive stress state is left in the case. Of the available case hardening techniques, carburizing provides the greatest depth of hardening and compressive residual stress.

2.4.2.2. Shot peening. Shot peening is one of the most popular surface treatments used to produce compressive residual stresses, in which thousands of hard spherical shots bombard the surface or a region of surface of a part with high-velocity (Fig. 2.8) [**25**].

During shot peening, the plastically deformed surface tends to expand but is restrained by the inside material. Thus, the compressive residual stress field is generated in the surface layer. Dynamic impact test further shows how the compressive residual stress results from the superposition of residual stress produced by surrounding shots [**26**]. Generally, the depth of compressive residual stress ranges from 50 to 500μm [**25**]. This induced compressive residual stress offsets any following service-imposed tensile stress and thus delays the fatigue crack initiation and propagation and ultimately extends the fatigue life. An example of a shot peening induced residual stress field is shown in Fig. 2.9 for an AISI 4340 steel under different peening intensities [**27**].

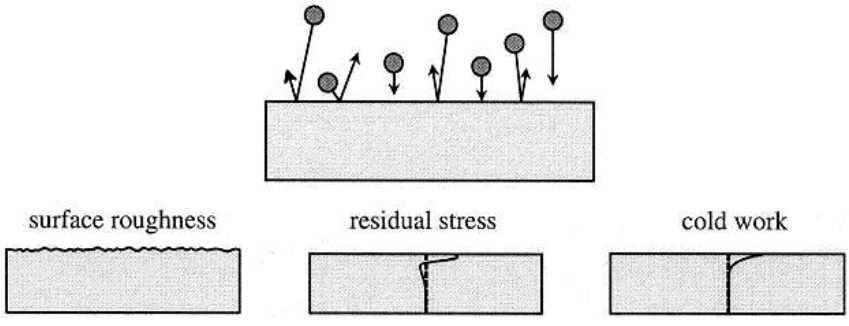

Figure 2.8. shot peening process [**25**]

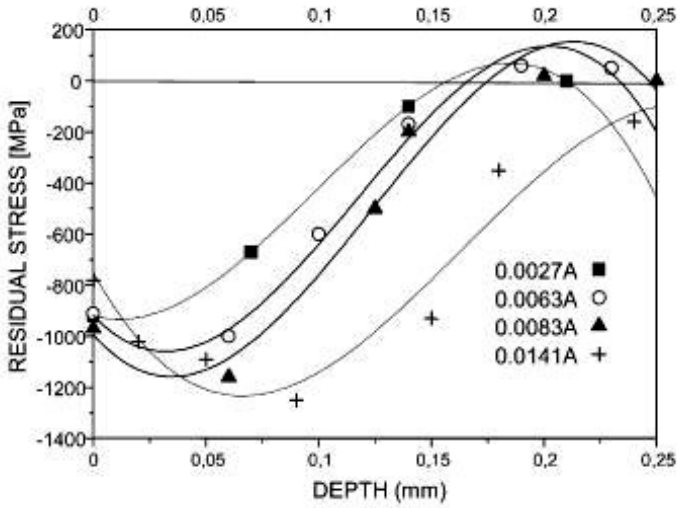

Figure 2.9. Compressive residual stress field induced by shot peening with different intensities for AISI4340 [**27**]

Consequently, the fatigue strength of 4340 steel in Fig. 2.9 was improved to various levels as presented by Fig 2.10. Another study conducted by NASA [**28**] found a 10% increase in endurance limit through shot peening in a AISI 4340 steel. Also discovered was the recovery of fatigue strength of a scratched 4340 specimen to the pristine level by shot peening. In practice shot peening has been applied to many types of mechanical components for improved fatigue life, as illustrated by Fig. 2.11.

Evidence of microstructure change by shot peening has also been reported for typical martensitic steels. X-ray diffraction has shown that the level of retained austenite prior to peening was substantially reduced through stress induced martensite transformation [**29, 30, 31**], as displayed in Fig. 2.12. TEM micrographs, in addition, confirmed this transformation [**32, 31**]. As a consequence of retained austenite reduction, the surface microhardness has presented some increase while the core hardness is maintained at the

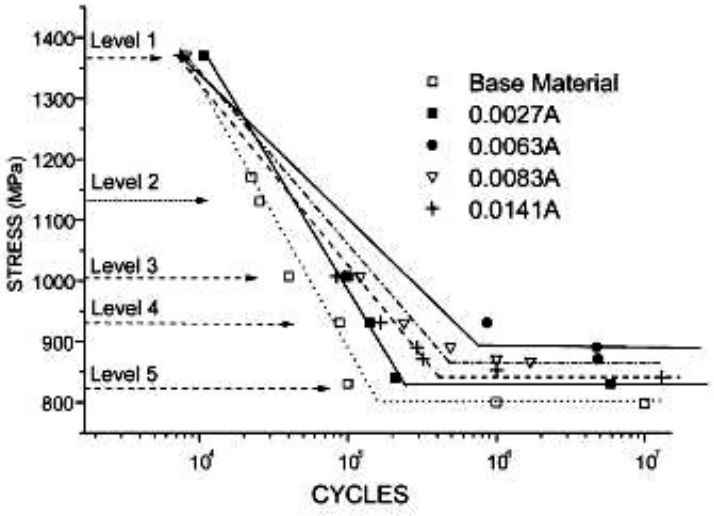

Figure 2.10. S-N comparative curves of the base 4340 and shot peening conditions [**27**]

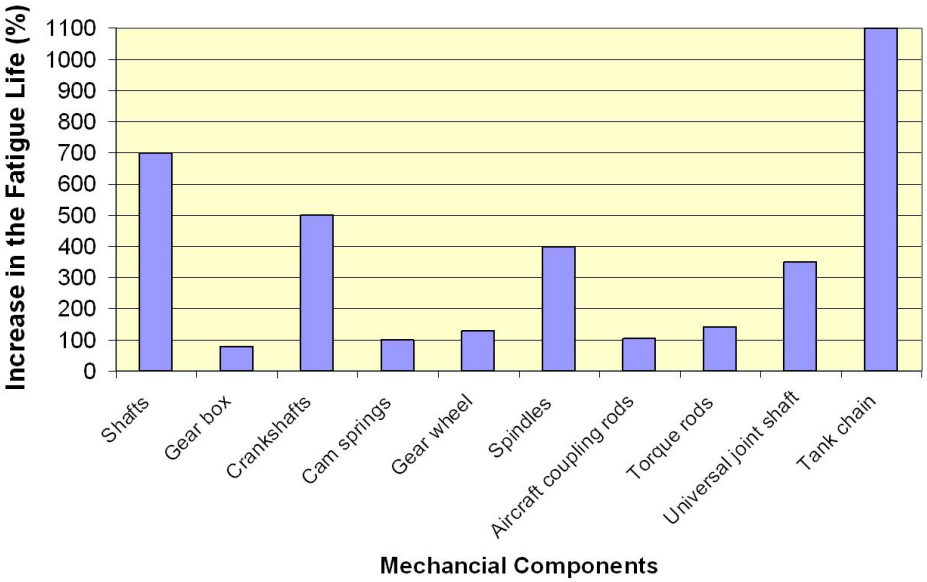

Figure 2.11. Fatigue life increase by shot peening

original level [**29, 30**]. Moreover, the plastic strain further refined the grain structure, helping improve the high cycle fatigue performance [**29, 30**].

In addition to stress induced phase transformation, high density of tangled dislocations and twin lamellae were observed after shot peening through cross sectional TEM study on normalized plain carbon steel SAE 1045 and austenitic steel AISI 304 [**33**]. The dislocation structure was believed to be associated with the large strain produced by shot peening.

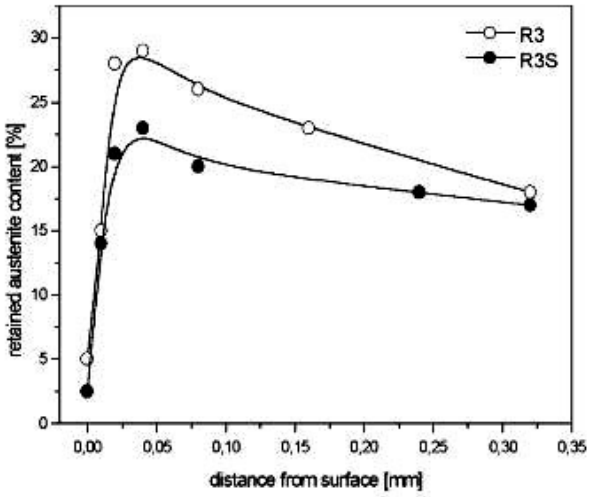

Figure 2.12. Retained austenite of unpeened (R3) and shot peened (R3S) specimen [**29**]

Shot peening generally roughens the surface, which is undesirable because the rough surface can serve as fatigue crack initiation sites. The resulted surface roughness from shot peening mainly depends on the shot size and peening intensity. A polishing step after shot peening can be used to minimize the detrimental effect of surface roughness on fatigue strength. However, the benefits from compressive residual stress normally exceed the disadvantages from surface roughness.

To further improve benefits from shot peening, double shot peening was introduced into the processing of steel gears [**30**]. A higher surface hardness, larger surface compressive residual stress and more reduction of retained austenite were achieved by using

double shot peening than single shot peening. Another variation of shot peening, *dual peening*, has also been developed and widely applied to industries. After the first pass during which larger shots with higher velocity are utilized to produce a base residual stress profile, much smaller shots with lower velocity are adopted in the second pass to increase surface residual stress and decrease surface roughness.

Ordinary peening media used in industries include cast iron and cast steel shots with hardness ranging from 48 to 60 Rc. High strength cut wire steel shots can be conditioned to the hardness of 64 Rc. When zero contamination is required, stainless steel shots are used. Small glass or ceramic shots are normally utilized for the second pass of dual peening for better surface quality. Researchers also found that enhanced peening effects (increased compressive depth, higher compressive residual stress and higher hardness) can be achieved by using Fe-based glassy alloy shots [**34**]. For materials with the surface as hard as 850-1200 Hv, Japanese inventors adopted hard metal alloy shots based on WC-Co for optimized peening effectiveness [**35**].

Finite Element Analysis (FEA) was carried out by Baragetti etal. to predict residual stress profiles with known shot peening parameters, such as shot size, shot speed, shot material density and yield strength of peened material [**36**]. Using his analysis, a reasonable maximum residual stress can be obtained, while surface residual stress was overestimated and the compressive depth underestimated. To help optimize the peening process, Baragetti also applied the *Design of Experiments* method to interpret the results obtained from numerical simulations of shot peening [**37**].

2.4.2.3. Laser peening. Laser shock peening, also called laser peening, is a novel surface processing technique to induce compressive residual stress into metals using high-power laser pulses [**38, 39**]. One note has to be made first is that laser peening is a mechanical process, not a thermal process, although inappropriate processing could cause local melting or other thermal effects.

The working principle of laser peening is schematically shown in Fig. 2.13. Prior to the treatment, the material surface is usually covered with two types of overlays. The first overlay, opaque to the laser, is spread directly onto the surface and then covered by another layer transparent to the laser. The opaque layer is also called the absorbent coating layer since it absorbs most of the laser energy. The commonly used material for opaque and transparent layers are black paint and water, respectively. When the focused laser pulse with high power density penetrates through the transparent layer and strikes the opaque layer, part of the opaque overlay is immediately vaporized. The vapor then absorbs the incoming laser energy and is heated or even ionized to produce plasma. The vapor or plasma tries to expand but is trapped by the transparent overlay and thus high pressure is accumulated during a very short time period. This sudden high pressure is against the surface of the material so a shock wave is produced and propagates into the material. The material will yield and plastically deform if the peak pressure of the shock wave exceeds the dynamic yield strength of the material. The peak stress decreases as the shock wave penetrates more material but deformation continues until the peak stress drops below the dynamic yield strength. Consequently, the material will receive strain hardening and compressive residual stresses.

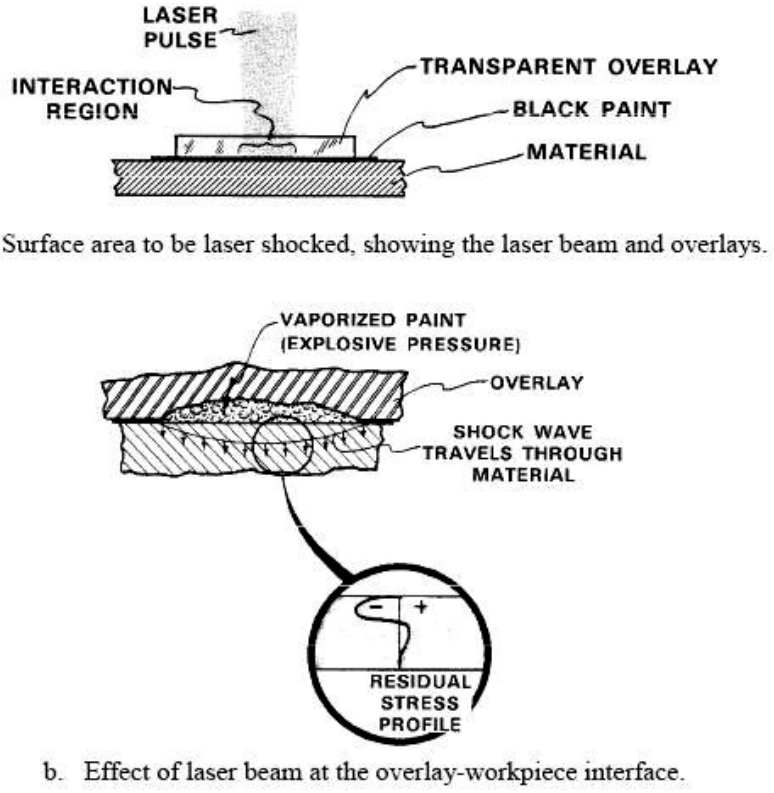

Figure 2.13. Schematics of how the laser peening works [**38**]

In Montross's review on the effects of overlays on laser peening [**39**], the transparent overlay was reported to be used to increase the shock wave intensity by preventing the plasma from expanding rapidly away from the surface. The opaque overlay was also found to increase the intensity of the shock wave in addition to its original purpose of protecting the metal surface from ablation or melting. Flat black paint is currently considered to be the most effective and practical coating among various absorbent coating systems [**40**].

A typical laser peening treatment produces a uniform biaxial in-plane residual stress field. Representative depth profiles of residual stress after laser peening are displayed in Fig. 2.14 for AF 1410 steel. One feature of the profile is that the compressive residual

stress extends to a significant depth below the surface of the material. As an outcome of this beneficial compressive residual stress, the flight hours to failure of AF 1410 was increased by approximately 60%, as shown in Fig. 2.15. The compressive residual stress can be extended to a great depth by increasing the laser peening intensity, which is associated with the incident power density. Fig.2.16 illustrates how the residual stress profile progresses in a 0.55% carbon steel as the number of shots increases from one to three. However, investigation has found that there exists a threshold for incident power density, above which the absolute value of surface residual stress starts decreasing due to the effect of surface release waves, as indicated by the example of an aluminum A356 alloy [**41**].

The laser spot size is another factor affecting the resulted residual stresses since it determines the size of the shock wave [**39**]. The small diameter shock wave propagates in a sphere mode while the large diameter shock wave behaves more like a planar front. The latter attenuates at a much slower rate and thus it can propagate deeper into the material. Therefore, a greater compressive depth is expected when a laser beam with larger spot size is utilized. An example showed 0.8 mm compressive depth for 1 mm laser spot and 1.2 mm for 6 mm spot in laser peened 55C1 medium carbon steel [**42**]. However, the surface residual stresses were approximately the same in both cases with other identical processing conditions.

Enhancement in fatigue performance was observed for a notched 55C1 steel through a four point bending fatigue test with $R = 0.1$ [**42**]. Resulted S-N curves shown in Fig. 2.17 displayed significant fatigue strength improvement in laser peened specimens compared to as-received specimens. It was also noted that with two different laser spot configurations

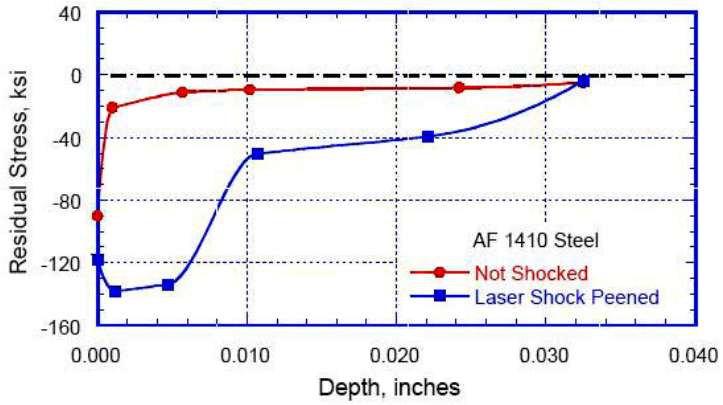

Figure 2.14. Residual stresses in AF1410 steel [**43**]

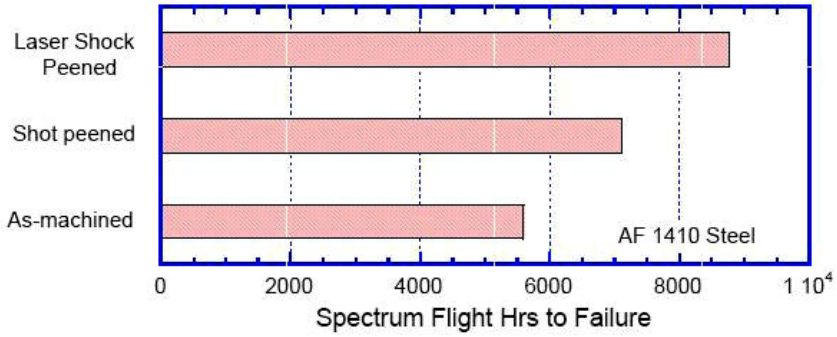

Figure 2.15. Fatigue of AF1410 Steel tested under Flight Spectrum loading conditions comparing shot peening and laser shock peening [**43**]

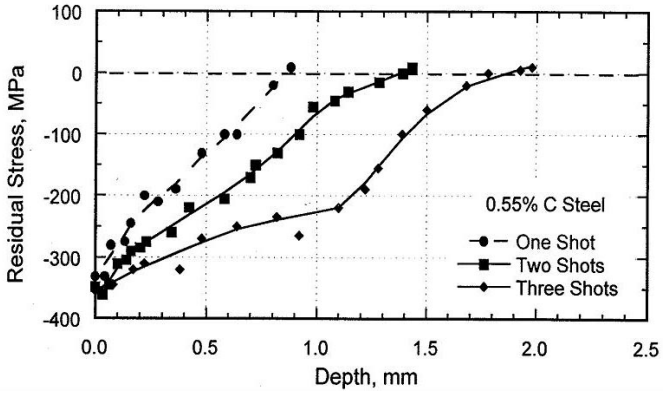

Figure 2.16. The effect of increasing laser peening intensity on the in-depth residual stress in a 0.55% carbon steel [**44**]

(1 mm and 6 mm), the steel presented approximately equivalent fatigue strength (490 MPa and 470 MPa) at the cycle of 2×10^6, although the compressive depth was greater in the steel treated with larger laser spot. This implied that surface residual stress plays a determining role in improving surface fatigue resistance. Fatigue improvement through laser peening in thin sections was also demonstrated in 4340 steel sheets [**38**]. 1.5 mm thick, 54 Rc, 4340 steel sheet was notched and then the roots of notches were laser peened with one shot. The tensile fatigue test was conducted at $R = 0.1$ with results shown in Fig. 2.18. The run-out stress was increased from 600 MPa to above 1000 MPa. Laser peening was also found to help improve fatigue strength of the weldment by 17% in 18Ni(250) maraging steel [**45**].

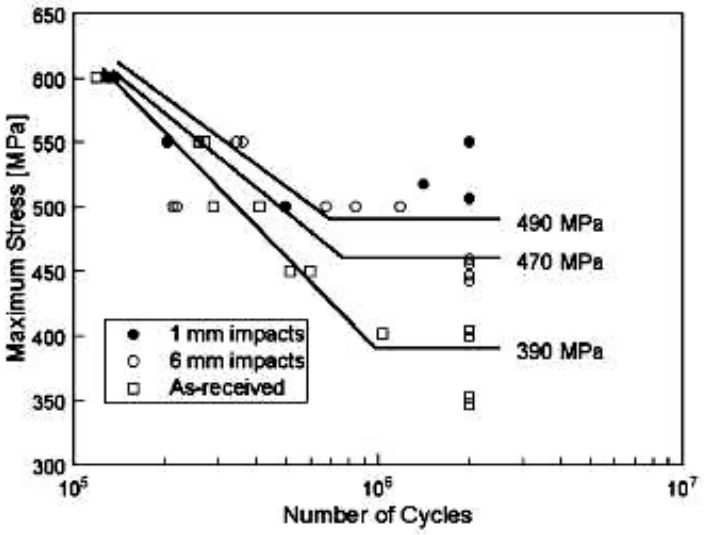

Figure 2.17. S-N curves of notched bending 55C1 steel samples treated by laser peening[**42**]

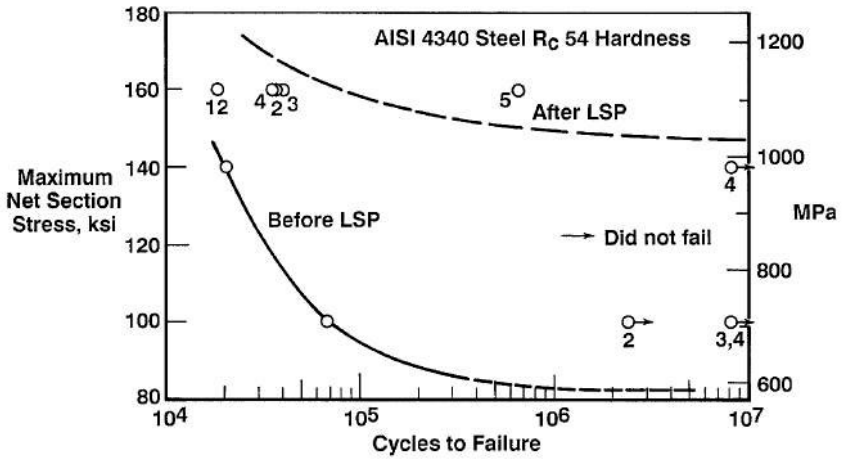

Figure 2.18. Tensile fatigue strength of 4340 steel sheet by laser peening [**38**]

An elastic-plastic model was developed to analyze the surface residual stress and the plastically affected depth after laser peening [**39, 42**]. Peyre pointed out that the laser-induced plastic deformation (ε^p) and therefore the surface stress (σ_{surf}) are linearly dependent on the ratio of laser-induced peak stress (Σ) to the material shock yield stress under uniaxial loading. The latter is usually termed as the Hugoniot Elastic Limit (HEL). The HEL is the maximum pressure a crystal can withstand before yielding in shear. The maximum plastic deformation in materials is achieved when $2HEL < \Sigma < 2.5HEL$. As $\Sigma > 2HEL$, the plastically affected depth (L) and maximum surface stress (σ_{surf}) can be calculated as follows:

$$L = \frac{\Sigma}{2HEL}\left(\frac{C_{el}C_{pl}\tau}{C_{el} - C_{pl}}\right) \tag{2.7}$$

$$\sigma_{surf} = \sigma_Y\left[1 - \frac{4\sqrt{2}}{\pi}(1 + \nu\frac{L}{r}\sqrt{2}\right] \tag{2.8}$$

where C_{el}, C_{pl} are elastic and plastic velocities (6000 and 4500 ms^{-1} for steels, respectively), τ is the pressure pulse duration (nearly 50-60 ns for a 20-25 ns laser pulse), σ_Y is

the tensile yield strength (quasi-static value) and r the radius of the impact (mm). According to Johnson's research, the HEL depends on material's compressive yield strength at high strain rate (σ_y^{dyn}) and Poisson's ratio (ν).

$$HEL = (1-\nu)/(1-2\nu)\sigma_y^{dyn} \tag{2.9}$$

During laser peening, the production of compressive residual stress is accompanied by significant microstructural and phase changes. High dislocation density ($2.6 \times 10^{11} cm^{-2}$) in a random tangled arrangement was observed in a laser peened SAE 1010 low carbon steel and in a 304 stainless steel through TEM [**46, 47**]. No dislocation cell structure was found in SAE 1010, which indicated that laser peening caused fast deformation, not allowing dislocation cross slip or long range motion. Phase transformation was also revealed through either X-ray Diffraction or TEM. In a Hadfield Manganese steel, extensive formation of ε-hcp martensite was discovered and surface hardness was increased by 130% due to the transformation [**48**]. Investigation of weld zones in a 18Ni(250) maraging steel showed that after laser peening the weldment austenite was transformed to martensite, accompanied with dislocation density increase [**45**]. Local surface melting was also observed in this steel which resulted in reverted austenite. In a laser peened 304 austenitic stainless steel, two dense sets of twins as well as α-phase embryos located at the intersections of twin sets were found [**49**]. The deformation of a laser peened Fe-Si alloy was revealed to be primarily slip plus minor twinning [**50**]. It was reported that twins were generated when the pressure was above the HEL of iron, but whether slip or twinning occurs would depend on the magnitude and duration of the shock wave pressure and possibly the resulted strain rate in the target.

The thermal stability of laser peening induced microstructure change has also been investigated. The near surface dislocation tangles in a 304 stainless steel were found to be stable up to 800 °C ($T/T_m \sim 0.6$) [**47**]. These thermally stable dislocations with high density worked as obstacles for dislocation movement and therefore help improve the resistance to fatigue crack initiation.

It was mentioned earlier that due to ϵ martensite transformation, surface hardness of a Hadfiled Manganese steel was increased by 130%. However, in most cases, it was reported that the surface hardening of metals was caused by the increased dislocation density. For instance, a 50% increase in hardness was found in SAE 1010 low carbon steel [**46**] and about 10% raise in a 18Ni(250) maraging steel weldment [**45**]. A study of 304 stainless steel also showed that increasing the number of laser shots can further increase the hardness (Fig. 2.19) as the dislocation density was raised by laser shock repetitions [**39**].

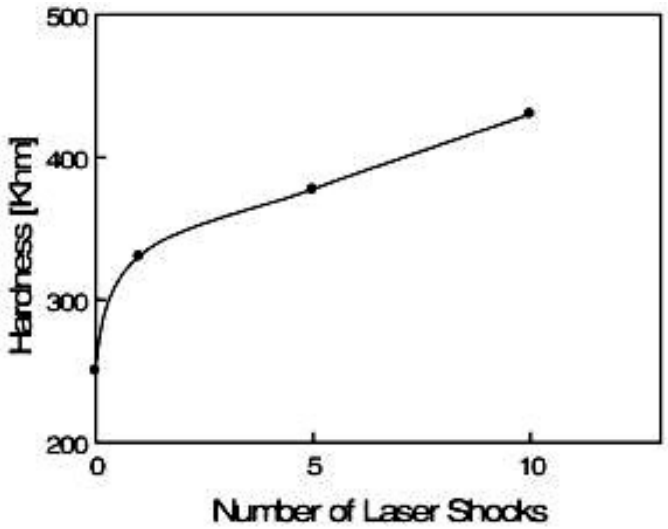

Figure 2.19. Surface hardness increase with the increasing number of laser shots [**39**]

The correlation between hardness and dislocation density was quantified by Ganin [**51**]: $H = H_0 + aGb\sqrt{p}$, where p is the average dislocation density, and H_0, a, G and b are material constants. H_0 is the hardness of an ideal material without any defects, G the shear modulus and b the scalar value of Burgers vector. In the study for a SAE 1010 low carbon steel[**46**], material constants were calculated based on results from Ganin, and the dislocation density was calculated through TEM. A reasonable agreement between experimental and calculated hardenss were obtained using this correlation. Therefore, it was concluded that the hardness increase is mainly due to the presence of high density dislocation. When twinning also occurs, a second term $k\lambda^{1/2}$ (k material constant, λ average inter-twin spacing) should be added to represent the contribution from twinning.

The tribology properties of rolling steels can also be modified by laser peening [**52**]. Study of friction coefficient evolution during rolling-sliding contact for untreated and laser peened 100Cr6 steel showed that laser peening introduced a plateau during the period of accommodation while the friction coefficient increased almost linearly in untreated steel. The duration of the period of accommodation was also shortened by laser peening. Fig. 2.20 presented the average friction coefficient tested under various applied loads for untreated and treated steels. It was noted that there was a level of applied load, above which the benefit provided by laser peening disappeared. The wear rate of the steels under different pressures were plotted in Fig. 2.21. Again it was proven that there existed a critical pressure of 100 MPa, above which the wear rate was not affected by laser peening. Under pressure lower than 100 MPa the better wear resistance was possibly because the depth of the maximum applied shear stress did not reach the depth of the extreme hardened layer ($50\mu m$). As the loading pressure increased, the depth of maximum shear

stress increased and exceeded the depth of the hardened layer. Thus the wear rate was back to the level in untreated steel.

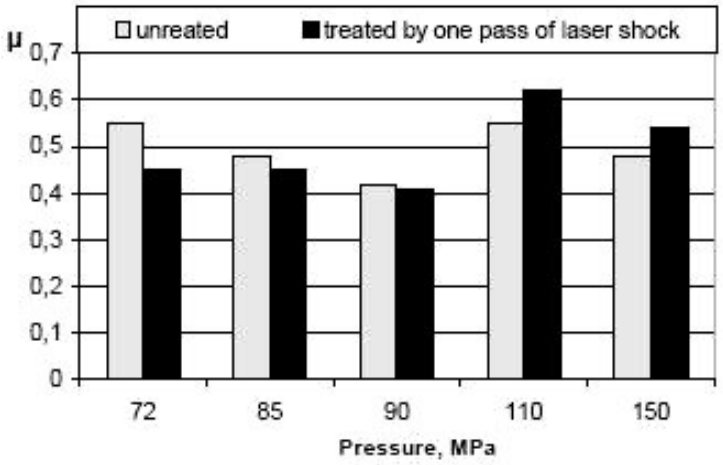

Figure 2.20. Averaged friction coefficient versus applied load[**52**]

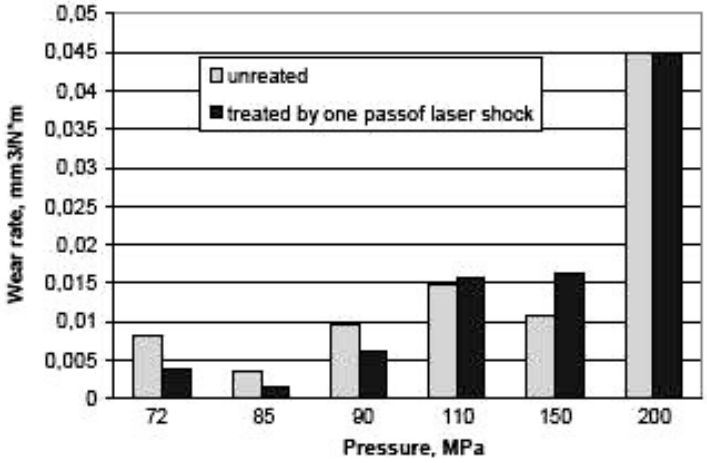

Figure 2.21. Wear rate of steels[**52**]

Effects of laser peening on stress corrosion cracking were investigated for 316L stainless steel as well [**53**]. Both untreated and treated specimens were immersed into $MgCl_2$ 44% boiling solution at 153 °C for 24 hrs. The untreated steel has a tensile residual stress near

the surface. After laser peening, compressive residual stress was developed at the surface and extended to the depth of about 1mm. Metallographic observations (Fig. 2.22) clearly showed that laser peening completely inhibited stress corrosion cracking and prevented microcracks, except very few small cracks developed locally on the surface (Fig. 2.23). No cracking was observed at the transition zone from the peened layer to unpeened core. Benefits found here were believed to be associated with the large and deep compressive residual stress on the surface.

2.4.2.4. Comparison between shot peening and laser peening. Compared to laser peening, shot peening presents the following features:

1) Shot peening is a semi-quantitative process [**39**]. The uniformity of peening intensity can not be 100% ensured since the evaluation of intensity is dependent on a metal strip or gauge, which is much smaller than the component to be treated. Difficulty still exists in precisely correlating many processing parameters to the resulted residual stresses. Peening is still optimized mainly through empiricism, although analytical tools are used to simplify and assist the optimization.

2) The compressive depth obtained from shot peening (100 to 200 μm) is usually shallower than that from laser peening. This is because a large laser spot (such as 6 mm spot) with high peening intensity is feasible for laser peening while no such big shot can be allowed in shot peening. Thus, laser peening is more suitable for subsurface fatigue resistance. Still, shot peening is quite effective in promoting resistance to surface crack initiation and propagation, which is desired for most applications.

3) The surface roughness after shot peening is usually larger than that after laser peening. However, by optimizing process parameters, surface roughening in shot peening

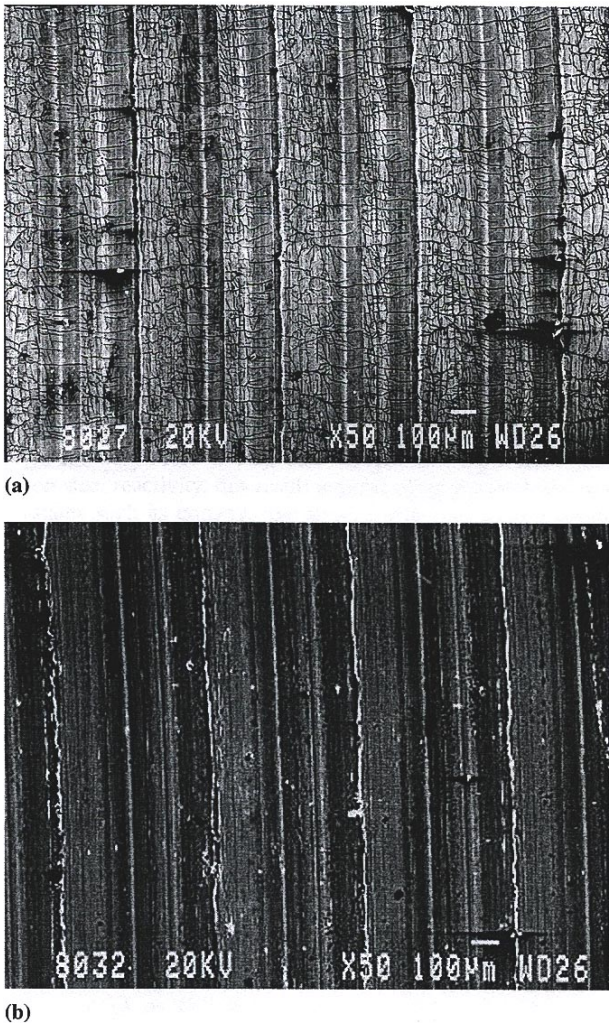

Figure 2.22. SEM graphs of 316L surfaces after SCC test[**53**] (a)non treated and (b) laser peened

can be minimized. For hard metals or alloys, the difference between shot peening and laser peening induced surface roughness is greatly reduced and so is the detrimental effect of roughness on the fatigue strength. Comparable surface roughness induced by both processes was observed in rolling steel 100Cr6 [**52**].

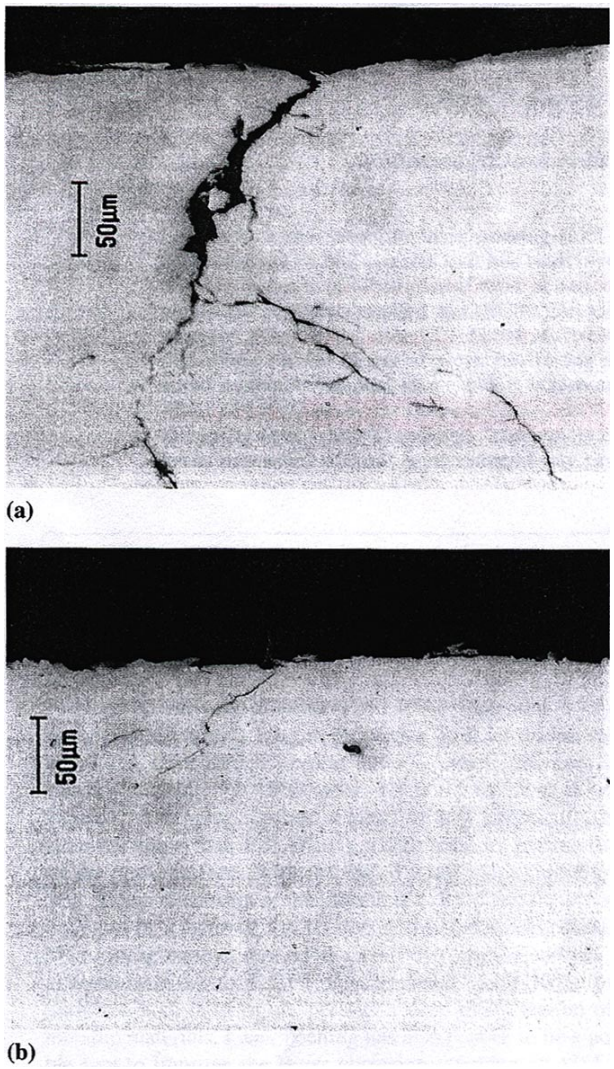

Figure 2.23. Cross section SEM image of 316L after SCC test[**53**] (a) non treated: stress corrosion cracking and (b)Laser peening: microcracks localized at the surface

4) In soft metals or alloys, the surface compressive residual stress generated by shot peening is usually lower than that by laser peening. However, comparable levels of residual stress were obtained in hard metal or alloys, such as hardened steels.

Overall, shot peening attracts more attention than laser peening due to its ease and low cost. Another significant limitation of laser peening is that large tensile stresses are

produced in the material to balance compressive residual stresses and this may cause accelerated failure of the interior material. Given the above discussion, discretion must be paid when selecting peening techniques and processing parameters for various applications.

2.4.3. Current residual stress levels in gear and bearing steels

Currently, shot peening has been widely applied to engineering components in industry, especially gear and bearing parts. Laser peening, as an emerging new technology, is starting to play its role in improving components' fatigue strength. Fig. 2.24 and 2.25 plot literature data of surface compressive residual stresses and maximum compressive residual stresses versus surface hardness for various steels. It is noted that surface and/or maximum compressive residual stresses vary a lot due to distinct processing parameters, such as shot or laser spot size, shot density and shot velocity. These processing parameters are usually integrated into and represented by one parameter, peening intensity. The determination of peening intensity could be found elsewhere [**54**]. However, a general rule is observed that the attainable surface compressive residual stress is mainly dependent on the mechanical properties of materials, i.e., the surface hardness. Correlation between residual stress and surface hardness will be established in Chapter 4. For shot peening, the correlation between the compressive depth versus peening intensity has already been developed by the shot peening industry, as shown in Fig. 2.26. By extracting data of steels from the graph, one can obtain the relationship between the compressive depth and surface hardness for steels, also given in Chapter 4.

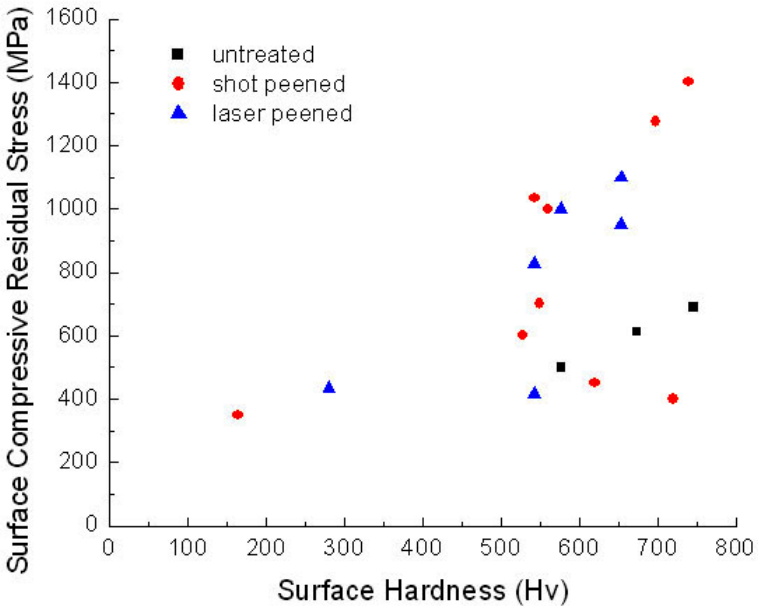

Figure 2.24. Surface compressive residual stress in various steels with different treatments

2.5. Stability of residual stress

2.5.1. Residual stress relaxation during tempering

Residual stress relief was often observed in hardened martensitic steels during tempering. A study on hardened AISI 52100 steel and a series of carbon steels discovered that stress relaxation was associated with the structure change during tempering, for example, carbide precipitation [**55**]. The kinetics of stress relaxation also followed that of structure change. Within the range of applied stresses investigated, residual stress relaxation was found insensitive to the initial applied stress. The extent of relaxation increased linearly with the increased carbon content. It was proposed that residual stress relaxation during tempering was due to the generation of a local plastic zone, which was initiated by the

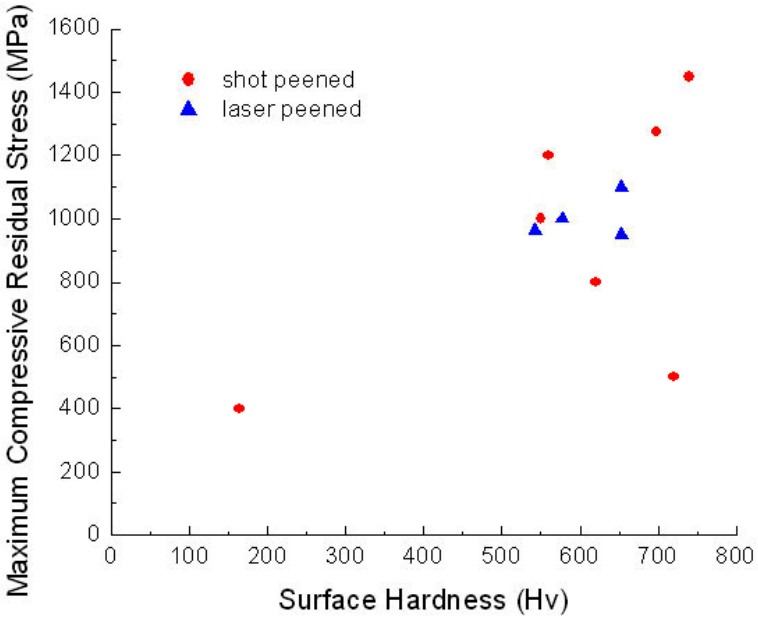

Figure 2.25. Maximum compressive residual stress in various steels with different treatments

local carbide volume change during tempering. This mechanism accounted for the strong dependence of stress relaxation on the carbon content and independence on the initial stress.

Wright [**56**] studied residual stress relaxation behavior of M50NiL alloys with two levels of carbon content using tensile tests and split-ring tests. He found that residual stress relaxation for low- or high-carbon M50NiL was also independent of the initial applied stress. Both relaxation during tempering and under cyclic load can be correlated with the volume fraction change of carbide precipitates. A linear correlation was proposed by Wright based on results from tensile and split-ring tests:

$$\Delta\%\sigma_{relaxed} = A\Delta f_v^{carbides} \tag{2.10}$$

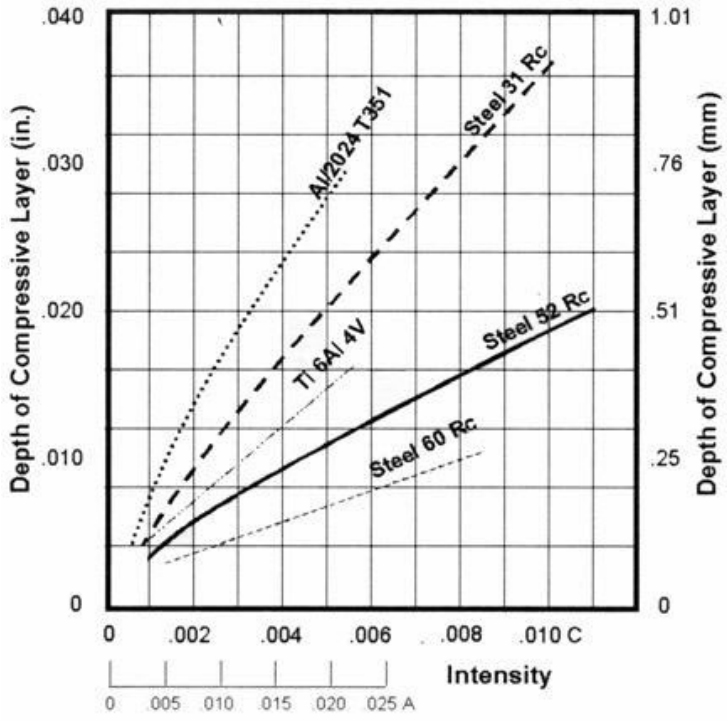

Figure 2.26. Compressive depth in various materials under different peening intensity[**54**]

where f is the volume fraction of carbides, A is a material constant, which is 2200 for M50NiL-0.38C.

2.5.2. Residual stress relaxation during annealing

Annealing temperature and time were also discovered to have effects on residual stress relaxation. Fig. 2.27 shows the kinetics of surface residual stress relaxation in a shot peened AISI 4140 steel at different temperatures [**57**]. The kinetics were described by Eq. 2.11.

$$\frac{\sigma^{rs}(T,t)}{\sigma_0^{rs}} = exp\left(-\left[Cexp\left(-\frac{\Delta H_A}{kT}\right)t\right]^m\right) \tag{2.11}$$

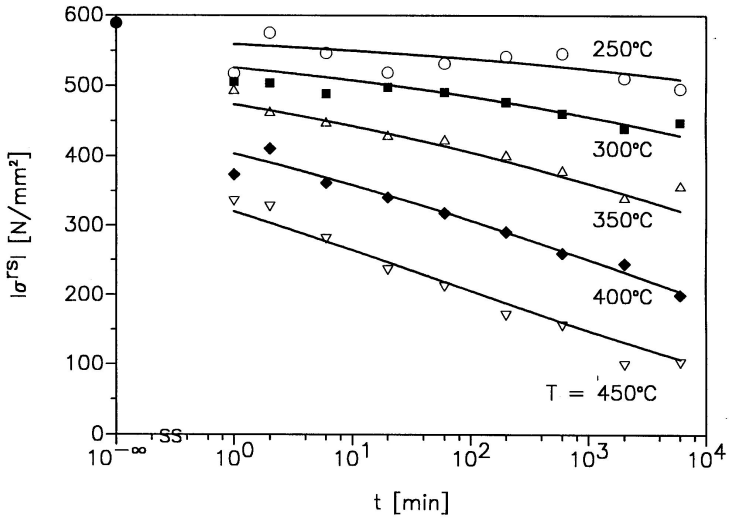

Figure 2.27. Surface residual stress relaxation of shot peened AISI 4140 steel during annealing

where σ_0^{rs} is the residual stress before annealing, $\sigma^{rs}(T,t)$ is the residual stress after annealing at temperature T for the time t, ΔH_A is the apparent activation enthalpy for the relaxation process, m an exponent, C a velocity constant and k Boltzmann constant. ΔH_A, C and m can be found from literature. The fact that the ΔH_A (3.29ev) matches the activation enthalpy for self diffusion in α-Fe led to the inerpretation that the stress relaxation rate was mainly determined by edge dislocation climbing by volume diffusion.

2.5.3. Residual stress relaxation under cyclic load

Mattson and Coleman observed residual stress relaxation in a shot peened SAE 5150 steel under cyclic load many years ago [**58**]. A linear logarithm relationship between remaining residual stress and the number of cycles was proposed by Kodama based on his measurement of surface residual stress decrease in a shot peened specimen [**59**]:

$$\sigma_N^{re} = A + mlogN \tag{2.12}$$

where σ_N^{re} is the surface residual stress after N cycles. A and m are material constants depending on the loading amplitude σ_a. From measured residual stress results, it was noted that the magnitude of compressive residual stress could drop by 50% after the first cycle, which was not described by the above relationship. Furthermore, the effect of loading ratio on residual stress relaxation was not explored in Kodama's study.

To describe residual stress relaxation in the first loading cycle, Holzapfel treated the first cycle as quasistatic tensile and compressive loading [**57**]. He conducted separate tensile and compressive loading tests to investigate residual stress relaxation behavior. It was found residual stress relaxation occurred where the equivalent von Mises stress exceeded the local yield strength and there was a critical loading stress at which the relaxation began. Due to the Bauschinger effect, the critical loading stress was much smaller during compression than during tension. After the first cycle, Kodama's relation was supported by Holzapfel's results on residual stress relaxation from alternating bending test (Fig. 2.28).

Zhuang and Halford further developed models for the residual stress relaxation mechanism by taking into account the effect of initial cold work [**60**]. They found the residual stress relaxation was also dependent on the degree of initial cold work since different levels of cold work resulted in the variation of local tensile or compressive yield strength. Generally, with the same original compressive residual stress and identical fatigue loading conditions, a larger amount of tensile cold work would cause more and faster cyclic relaxation. Integrating the concepts of cold work relaxation and cyclic loading relaxation, an

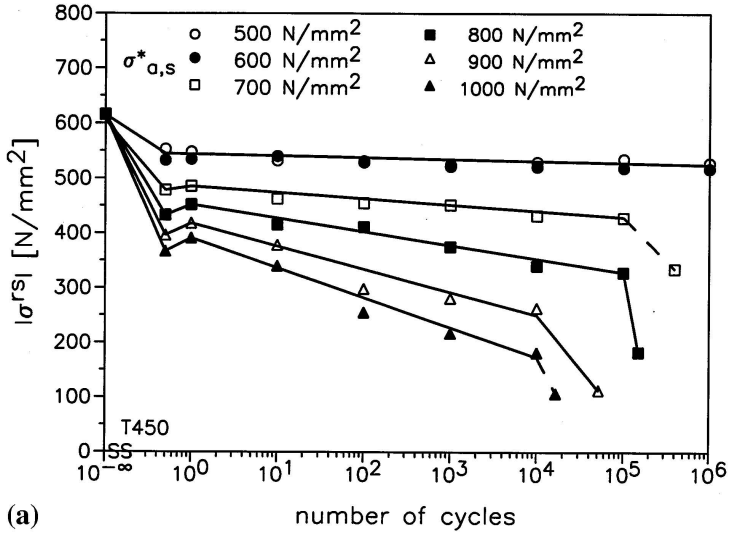

Figure 2.28. Surface residual stress relaxation of shot peened AISI 4140 during alternating bending test [**57**] ($\sigma^*_{a,s}$ is the fictitious stress amplitude at the surface)

equation to predict the residual stress relaxation was proposed:

$$\frac{\sigma_N^{re}}{|\sigma_0^{re}|} = A\left(\frac{\sigma_{max}\sigma_a}{(C_W\sigma_y)^2}\right)^m (N-1)^B - 1 \tag{2.13}$$

where σ_0^{re} is the initial residual stress, σ_N^{re} the residual stress after N cycles, σ_{max} is the maximum load, σ_a is the amplitude of the cyclic load and σ_y is material yield strength. C_W is a parameter accounting for the degree of cold work. Material constants m and A both depend on the cyclic stress and strain response. B reflects the dependence of relaxation rate on the number of cycles. In terms of the loading ratio R, Eq. 2.13 can be written into:

$$\frac{\sigma_N^{re}}{|\sigma_0^{re}|} = A\left(\frac{2\sigma_a^2}{(1-R)(C_W\sigma_y)^2}\right)^m (N-1)^B - 1 \tag{2.14}$$

The rate of residual stress relaxation increased as R increased. The relaxation slowed down as the loading amplitude was reduced.

A FEA analysis was performed to evaluate the analytical model described by Eqs. 2.13 and 2.14. Three dominating parameters were investigated, including load amplitude, load ratio and degree of initial cold work [**60**]. Comparison between the analytical model and the FEA numerical simulation demonstrated that the analytical model was robust, particulary in describing residual stress relaxation behavior during the early cycles for low cycle fatigue. This feature is crucial because residual stress relaxation mainly takes place during the early stage of cyclic loading.

CHAPTER 3

Materials and Methods

3.1. Materials

3.1.1. Ferrium®C61, Ferrium®C67 and variants

High performance gear steels, Ferrium®C61, C67 and C67 variants are computationally designed using the systems approach based on thermodynamics and strengthening models. All steels are strengthened through 3nm M_2C alloy carbide precipitation during tempering in stage IV. C61 has already been commercialized through collaboration with QuesTek Innovations, Inc. and the development of the C67 family is still ongoing. Two previous versions of C67: C69 and C69-M3B, are also involved in this research. C69 was the earliest design aimed at a high surface hardness of 69 Rc. High cobalt content was adopted for high dislocation recovery resistance to help achieve 69 Rc. However, core brittleness was found in C69 and thus C69-M3B was designed with less Co to eliminate formation of the brittle σ phase in the core. For a better combination of strength and toughness, C67 was designed with further reduced Co content and a decreased case carbon content. Fully or partially heat treated C61, C67 and variants for this research were provided by QuesTek Innovations, Inc.

For residual stress and retained austenite study, $15 \times 15 \times 6.34 mm^3$ specimens were cut from 0.25 inch (6.34 mm) thick discs, 5.25 inch (133.35 mm) in diameter. Prior to shot or laser peening, C67 steel pucks, 1 inch (25.4 mm) in diameter and 0.34 inch (8.6 mm) in

thickness were tempered either at 200 °C for 1 hr or at 482 °C for 56 hrs at Northwestern University. Shot or laser peening service was then provided by Metal Improvement Company in Addision, Illinois. Effects of peening intensity on surface residual stresses were studied.

For residual stress distribution analysis, cylindrical specimens, 3 inch (76.2 mm) in length and 0.375 inch (9.525 mm) in diameter were used. The specimens first underwent carburization/solution treatment, quenching, cryogenic treatment at liquid nitrogen temperature, tempering and fine grinding. C61 was then shot peened and C67 laser peened. Finally both C61 and C67 cylinders were subject to the NTN ball-rod rolling contact fatigue (RCF) screening test with the extreme Hertzian pressure of 5.4 GPa. Residual stress distribution was measured non-destructively using synchrotron radiation for regions away from the wear track and beneath wear tracks.

3.1.2. Pyrowear53

Pyrowear 53 is a carburized steel with good temper resistance, high case hot hardness while maintaining high core impact strength and fracture toughness. Strengthening was achieved through ϵ carbide in stage I tempering. Non-destructive measurement of residual stress distributions were also performed on shot peened and laser peened Pyrowear 53 cylinders provided by QuesTek Innovations.

Compositions of Ferrium®C61, C67 and variants, Pyrowear 53 are listed in Table 3.1.

Figure 3.1. Compositions of various high performance gear steels (wt%)

Steel	Co	Ni	Cr	Mo	V	W	C(core)	C(case)	Si	Cu	Mn	Fe
C61	18	9.5	3.5	1.1	0.08	---	0.16	0.45				Bal.
C69	28	3.1	5.1	2.5	0.02	---	0.1	0.7				Bal.
C69-M3B	19.6	2.57	4.9	2.11	0.1	---	0.071	0.6-0.7				Bal.
C67	16	4.4	4.5	1.8	0.1	0.1	0.1	0.6				Bal.
Pyrowear53	---	2.0	1.0	3.3	0.1	---	0.1		1.0	2.0	0.35	Bal.

3.1.3. CryoForm 70

CryoForm 70 steel is the new design aimed at surface hardness of 70 Rc. Like C61 and C67, it is strengthened through M_2C carbide precipitation. *CryoForm* stands for *cryogenic deformation*, a novel process developed for the achievement of the hardness goal. Details on steel composition, structure and properties are elaborated in Chapter 5-7.

3.2. Processing procedures

3.2.1. Carburizing

Carburizing is a case hardening process in which carbon is diffused into steels at temperatures between 850 °C and 1050 °C. At carburizing temperatures, austenite with high solubility of carbon is the stable phase. Hardening is accomplished when the steel is quenched from the carburizing temperature and austenite transforms into marteniste. With a carbon content gradient, a case providing good wear and fatigue resistance and a tough ductile core are formed.

3.2.1.1. Pack Carburizing. Pack carburizing is the earliest and simplest carburization method, in which parts are packed with a mixture of charcoal and carbonate compound

and then placed in a container. At carburizing temperatures, carbon monoxide is first produced which breaks down into carbon and carbon dioxide at the part surface. The nascent carbon is then diffused into the part and carbon dioxide reacts with the mixture to generate more carbon monoxide.

$$CO_2 + C_{charcoal} \rightleftharpoons 2CO \tag{3.1}$$

$$3Fe + 2CO \rightarrow 3Fe + C_{inFCC} + CO_2 \tag{3.2}$$

3.2.1.2. Vacuum Carburizing. With the same principle, an advanced carburizing technique - gas/vacuum carburizing has already been widely adopted by industry to accurately achieve desired carbon content profiles in the material, which is difficult to accomplish by using pack carburizing. Gas carburizing is normally conducted within the temperature range from 850 °C to 950 °C. Pre-oxidation is needed to prevent further material oxidation and provide a porous iron oxide surface layer for the carbon to diffuse. Vacuum carburizing is carried out at much higher temperatures, from 1050 °C to 1120 °C, at which the material can be solutionized simultaneously. After the furnace is sealed and evacuated to 10^{-4} torr (0.13Pa), a carbonaceous gas, such as propane, is introduced into the furnace with a pressure of 300 torr (3.9Pa). Carbonaceous gas breaks down into CO and then CO acts as the carbon source at the part surface. The furnace evacuation prior to gas introduction eliminates the step of pre-oxidation and thus no scale or other surface reaction occurs. The part stays clean and bright. Both gas and vacuum carburizing follows a determined carburizing procedure, as displayed schematically in 3.2. Carburization is composed of several cycles, each of which consists of a boost and a diffuse cycle. During

boost cycle, carbonaceous gas flows in with a fixed carbon potential for gas carburizing or a fixed carbon flux for vacuum carburizing. During the diffuse cycle, gas flow drops to zero and carbon starts diffusion from part surface to the interior. The intermediate diffuse between boost cycles is usually shorter than the final diffuse, which finalizes the carbon content profile. Vacuum carburizing service at 1100 °C was provided by Midwest Thermal-Vac, Inc. in Konesha, Wisconsin for the development of CryoForm 70.

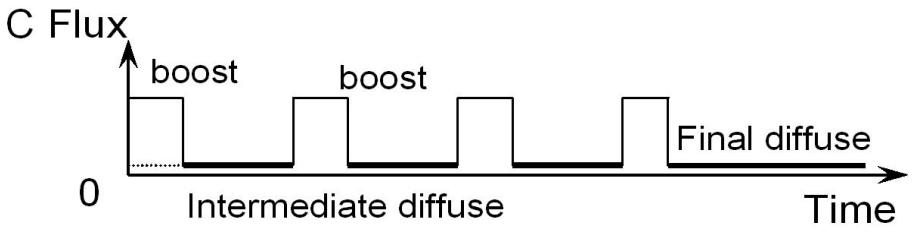

Figure 3.2. Schematic carburization process in gas or vacuum carburizing

3.2.2. Heat treatment

Pack carburized alloys were encapsulated in vacuum quartz tubes 0.75 inch in diameter and solution treated at 1100 °C for 1 hour. They were then oil quenched, treated in liquid nitrogen for 1 hour and tempered at 200 °C for 1 hour. For vacuum carburized alloys, solution treatment and carburizing was combined into the single step of carburization. After vacuum carburizing, specimens were quenched by Argon gas and cryogenic treated in liquid nitrogen for 1 hour. Subsequent tempering was completed in Northwestern University at 200 °C for 1hr or 450 °C-500 °C for prolonged hours.

3.2.3. Shot peening and laser peening

Metal Improvement Company, Inc. provided the shot peening service for C61, C67 and Pyrowear 53 alloys using their proprietary processing parameters. LSP Technologies, Inc. in Dublin, Ohio performed laser peening for C67 and Pyrowear 53 alloys with proprietary processes.

3.3. Standard characterization methods

3.3.1. Dilatometry

Alloy volume change during phase transformation is measured using an MMC Quenching and Deformation Dilatometer. 10 mm long cylindrical specimens 3 mm in diameter are placed in an induction furnace. A Pt-Pt 10% Rh thermocouple is spot-welded to the specimen for temperature measurement. Specimens are first heated up to a desired temperature and quenched by injecting helium into the vacuum chamber. The length change of specimens during thermal expansion and phase transformation is measured through an LVDT transducer connected to quartz platens on either end of the cylinder. Both specimen temperature and length change are recorded and displayed in real time by a computer system.

3.3.2. Hardness test

Alloy hardness profiles are measured using a Buehler Micromet II Micro Hardness Tester. Vickers hardness testing was performed following ASTM standard E384. A diamond pyramid Vickers indenter with face angles of 136° was used with the applied load of 300 g for 10 seconds. The lengths of indent diagonals were measured and then converted to

Vickers Hardness (Hv or VHN). With load P in kg and average diagonal length d in mm, the Vickers Hardness is expressed as

$$VickersHardness = \frac{1.854P}{d^2} \tag{3.3}$$

Prior to testing, the cross section of a carburized specimen revealing the case and core was mounted in Durofast for edge retention and polished to 1 μm. The first indent was made at least 60 μm away from the edge. Three or more measurements were performed at each depth for better statistics. A Wilson Rockwell Hardness Tester was also utilized for a quick check of surface hardness following ASTM standard E18. A "C" scale Brale diamond ball indenter was used with 10 kg preload and 150 kg test load. Parallel top and bottom faces were required for the Rockewell C test. Prior to the test, the surface was polished to 12 μm or smoother. Six or more measurements were made each time for a homogeneous surface.

3.3.3. Crystal structure and phase analysis

Crystal structure and phase relations were analyzed through X-ray Diffraction. All samples were polished to 12 μm or smoother prior to X-ray irradiation. Line focused Cu K_α radiation at 40 kV, 20 mA from a Scintag Diffractometer in the Northwestern X-ray Facility was utilized. On the source side, a 4 mm scattering slit and 2 mm divergence slit were adopted. On the detector side, a 1 mm scattering slit and 0.5 mm receiving slit was used. A good combination of high intensity and high signal-to-noise ratio was achieved with this set of slits. All phases in the alloy were identified by comparing diffraction spectrum to X-ray powder diffraction files.

Phase fractions were calculated following Eq. 3.4 [**61**]:

$$\frac{V_A}{V_B} = \frac{R_A I_A}{R_B I_B} \tag{3.4}$$

where subscripts A and B represent Phase A and Phase B, V is the volume fraction of each phase, I is the integrated intensity of the diffraction peak, R is the intensity correction factor accounting for structure factor, multiplicity, angle-dependent polarization factor and temperature factor. A NBS standard and a specimen were irradiated under identical X-ray conditions to obtain peak intensities from Pseudo-Voigt fitting. With a known $\frac{V_A}{V_B}$ ratio of the standard, the prefactor ratio $\frac{R_A}{R_B}$ was calculated. With this $\frac{R_A}{R_B}$, $\frac{V_A}{V_B}$ for the specimen was computed. This phase analysis was applied to the measurement of retained austenite level with respect to martensite phase in carburized steel alloys. X-ray diffraction was conducted with a step size of 0.05°, a counting time of 25 s for the martensite (211) peak and a 50 s counting time for the martensite (200) peak and austenite (220) peak.

Lattice parameters were calculated from finely scanned diffraction peaks with a prolonged counting time (50-100 s) and reduced step size (0.02°). d-spacing of crystal planes for a tetragonal system is calculated following Eq. 3.5.

$$\frac{1}{d} = \sqrt{(\frac{h^2+k^2}{a^2}) + (\frac{l^2}{c^2})} \tag{3.5}$$

By obtaining two sets of d, h,k,l, lattice parameters a and c are solved.

3.3.4. Microscopy

Alloy microstructures were observed by using optical microscopy and scanning electron microscopy (SEM). Matrix and precipitate phases in carburized or tempered steel alloys

were qualitatively analyzed for phase identification, phase morphology and phase fractions. Samples were mounted in Durofast or acrylic and polished to 1 μm. 2% nital etchant was used to reveal the martensite and coarse carbide phases under an optical microscope. Microstructure was also analyzed using a Hitachi S-3500 scanning electron microscope in both secondary electron and back scattering modes. Phase compositions, line element concentrations and area element map were obtained through a PGT energy dispersive X-ray analyzer attached to the S-3500.

3.3.5. Surface residual stress measurement

There are two primary types of residual stress measurement methods. Hole drilling or dissection is the common destructive method [**62**] while acoustic method, magnetic method, X-ray diffraction and neutron diffraction have been developed as non-destructive methods. Among non-destructive methods, the X-ray diffraction method is most popular for its speed, accuracy, reliability and low dependence on variations in material properties [**25**]. The X-ray diffraction method determines the residual stress by measuring the change of atomic interplanar spacing (d-spacing) to obtain the magnitude of the prevailing elastic strain, as illustrated in Fig. 3.3. In grains with different orientation, the d-spacing of the same atomic planes differs from one another due to compressive residual stress on the surface. In Fig. 3.3 (a), Bragg diffraction occurs on (hkl) planes parallel to the surface, whose d-spacing is largest. The Bragg peak is at angle 2theta. After the specimen tilts by a certain angle, in Fig. 3.3 (b), Bragg diffraction occurs at the same atomic plane but in different grains with decreased d-spacing. Therefore, the Bragg peak shifts to a higher angle. The magnitude of the peak shift is related to the residual strain, from which the

residual stress is determined. The elastic anisotropy effect on the peak shift is taken into account by using X-ray elastic constants in stress calculation.

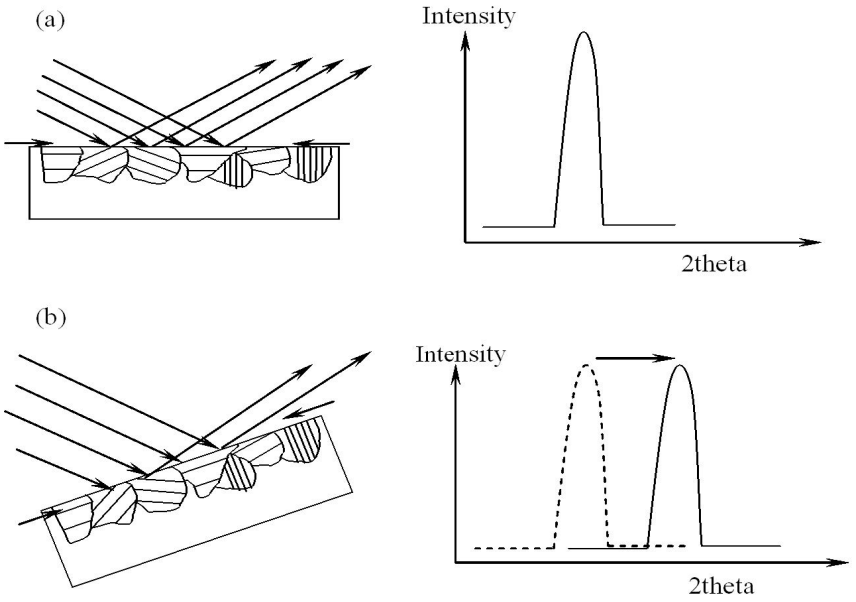

Figure 3.3. Principle of X-ray diffraction method (redraw from [**63**]

In this research, point focused Cr average K_α emission was used with a V filter to eliminate K_β emission. A typical ferrite/martensite (211) peak is selected to measure residual stress in steel alloys because the large 2θ of (211) peak (156°) helps reduce the measurement uncertainty. Detailed experimental procedure and data analysis are given in the Appendix.

3.3.6. Interferometry

Surface topography of shot or laser peened C61, C67 and Pyrowear 53 alloys was studied using light interferometry. A WYKO interferometer in the Department of Mechanical Engineering was employed with various magnifications. Specimen tilt and curvature were

corrected during the measurement whenever necessary. Surface topography was represented by surface roughness, line profiles and 2D and 3D maps. Specifically, surface roughness was expressed in various roughness values, including average roughness R_a, root mean square (rms) roughness R_q, maximum height of the profile R_t and average maximum height of the profile R_z.

3.4. Computational tools

3.4.1. $Thermo - Calc$®

Two software systems were used for the computational design of gear steels: $Thermo - Calc$® and Computational Materials Dynamics (CMD®). Developed by the Royal Institute of Technology in Stockholm, Sweden, Thermo-Calc is a widely used commercial software for the calculations of equilibrium, thermodynamic data (enthalpy, heat capacity, activity) and phase diagrams [**64**]. These calculations dramatically accelerate the development of new metals and alloys with low cost as all phase relations can be predicted without a large amount of experiments. For the design of advanced gear steels, equilibria, metastable equilibria and driving forces are calculated as a function of chemical compositions, temperature and pressure by looking for the lowest free energy state.

Thermodynamic databases compatible with the Thermo-Calc software include the compound and solution database (SSOL); steel and Fe database; specific alloys database; specific materials database etc. SSOL is developed by Scientific Group Thermodata Europe, a consortium of European research centers. It consists of Gibbs free energy data for more than 150 binary, 70 ternary and 20 higher order systems. The $SSOL + M_2C$ database was also developed at Northwestern to include data for the M_2C carbide phase.

For martensite starting temperature calculation, the Mart5 database developed by Ghosh and Olson was used since it accounts for low temperature thermodynamics of Fe-based FCC and BCC phases [**65**]. A special database developed by QuesTek Innovations LLC, Evanston, IL was used for sigma phase driving force calculation.

Thermo-Calc uses a sublattice model to describe crystal structure and thermodynamic data for the convenience of extrapolating to higher order systems [**66**]. Model parameters depend on chemical compositions, temperature and pressure. Two sublattices are described for advanced gear steel systems, a substitutional solution and an interstitial lattice.

3.4.2. Computational Materials Dynamics - $CMD^{®}$

Computational Materials Dynamics - $CMD^{®}$, developed by QuesTek Innovations LLC in Evanston, IL, consists of a collection of mechanistic models interfaced with Thermo-Calc [**67**]. Parameters and properties calculated through CMD models include hardness/strength of Ni-Co secondary hardening steels, martensite start temperature and Scheil microsegregation index. Models involved in the design of CryoForm 70 will be discussed in Chapter 5. CMD can also calculate solution treatment temperature, M_2C phase driving force and sigma phase driving force using Thermo-Calc.

3.4.3. $DICTRA^{®}$

$DICTRA^{®}$ (Diffusion Controlled Transformations), developed by the Royal Institute of Technology in Stockholm, Sweden, is used for the simulation of kinetic processes in multi-component systems [**68**]. DICTRA interfaces with Themo-Calc and numerically

solves multi-component diffusion equations with the assumption that all interfaces are at thermodynamic equilibrium. In the design of advanced gear steels, DICTRA was utilized to simulate the carburizing process in the multi-component steel alloys and predict the dependence of carbon profiles on carburizing parameters (temperature and time).

3.5. Novel synchrotron characterization of residual stress distribution

Conventional X-ray diffraction is one of the most popular techniques to analyze residual stresses due to its accuracy and convenience. However, to probe residual stress distributions at various depths, material removal is needed because X-ray can only penetrate tenths of μm in steels. It is not suitable when sample intactness is desired. Fortunately, neutron and synchrotron radiation techniques have been developed to provide non-destructive characterization of residual stress distributions three dimensionally. However, neutron strain or stress measurement is limited by slow rate data acquisition and a low spatial resolution, of the order of $1mm^3$, due to relatively low intensities of neutrons [**69**]. Modern synchrotron sources, on the other hand, can provide quite intense narrow beams of highly collimated X-ray photons with high energy [**70**], which makes high resolution strain or stress mapping very possible.

To date, three major synchrotron radiation techniques for stress measurement have been tried successfully: i) $\theta/2\theta$ scanning in either reflection or transmission geometry; ii) utilizing high energy X-rays in transmission with a two-dimensional detector; iii) using a white beam with an energy sensitive detector [**69**]. However, the non-destructive evaluation of residual stress distributions in carburized gear steels by synchrotron radiation

has not been reported before. In this research, a high-energy X-ray transmission technique was developed through collaboration with Dr. Jonathan Almer from the Advanced Photon Source, Argonne National Laboratory. This technique was employed to study the residual stress depth distributions in shot or laser peened carburized steels. A setup composed of the conical slit system [**71**], sample rotation stage [**72**] and two dimensional detector was adopted. Experimental details and new technological aspects will be fully discussed in Chapter 4.

The basic principle behind X-ray strain/stress analysis using two dimensional detectors has been developed [**73, 74, 75**]. Here only the key elements are drawn for our study. Two coordinate systems are defined, laboratory coordinate system (L_i) and sample coordinate system (S_i). L_i system is related to S_i system by angles ψ and ϕ, as illustrated in Fig. 3.4. The cylindrical specimen is orientated in such a way that the diffraction vector q, normal to diffraction planes, is along L_3 in L_i system. In the transmission mode, the incident beam makes an angle of 2θ with the diffracted beam. Diffraction rings are then recorded by a 2D detector. Define the 3 o'clock position as the origin for azimuth angle η and r as the radius of the diffraction ring. Each point on diffraction rings can then be expressed as (η, r). Diffraction rings from an unstressed polycrystalline specimen are perfect circles in which 2θ is independent of η and $2\theta = 2\theta_0$ =Bragg angle. The introduction of residual strain or stress distorts the shape of diffraction rings and thus 2θ becomes a function of η, $2\theta = 2\theta(\eta)$. This function is uniquely defined by the strain or stress tensor and the specimen orientation.

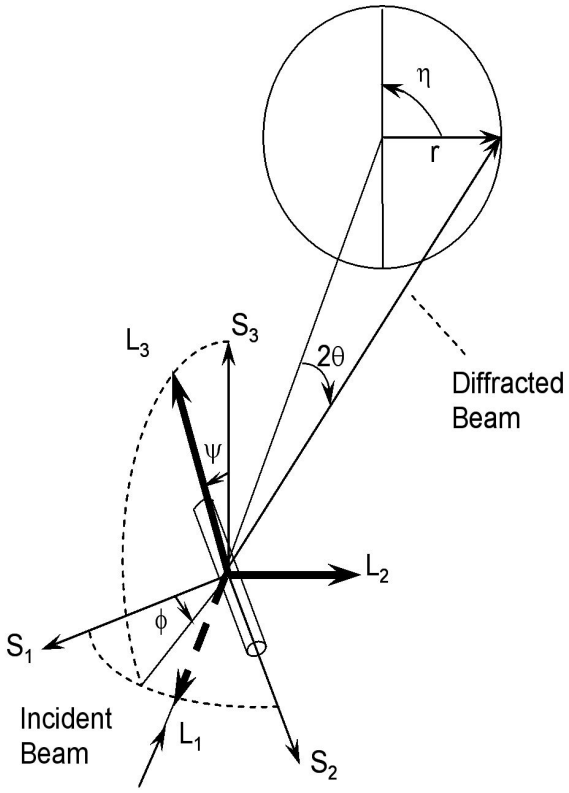

Figure 3.4. Definition of coordinate systems: Laboratory L_i, Sample S_i and Experimental geometry with a cylindrical specimen

He and Smith developed the fundamental equation of strain measurement for the 2D detector [**73**]:

$$\varepsilon_{\phi\psi} = f_{11}\varepsilon_{11} + f_{12}\varepsilon_{12} + f_{22}\varepsilon_{22} + f_{13}\varepsilon_{13} + f_{23}\varepsilon_{23} + f_{33}\varepsilon_{33} \tag{3.6}$$

where $f_{ij}s$ are strain coefficients determined by the matrix operation:

$$F = M_s(\omega, \phi, \psi) \bullet M_d(\eta, \theta) \tag{3.7}$$

$M_s(\omega, \phi, \psi)$ is the sample orientation matrix which defines the relation between the sample coordinates and the laboratory coordinates. $M_d(\eta, \theta)$ is the diffraction ring matrix defining

the orientation of each diffracted beam. He and Smith used angle χ instead of η ($\chi = \eta + 90°$) in their simplification for strain coefficients.

On the other hand, lattice strain $\varepsilon_{\phi\psi}$ can be expressed in the relative variation of d spacing for (hkl) plane:

$$\varepsilon_{\phi\psi} = \frac{d - d_0}{d_0} \tag{3.8}$$

The radius of the diffraction ring r is connected to the diffraction angle 2θ and the distance between the specimen and the detector D by

$$\theta = \frac{1}{2}\arctan(r/D) \tag{3.9}$$

Since $d = \frac{\lambda}{2\sin\theta}$,

$$d = \frac{\lambda}{2\sin\frac{1}{2}\arctan(r/D)} \tag{3.10}$$

For high energy X-rays, Bragg angles are very small ($r/D \ll 1$). Therefore the trigonometric functions can be replaced by their arguments, which resulted in the much simpler equation

$$d \approx \frac{\lambda D}{r} \tag{3.11}$$

Combining Eqs. 3.8 and 3.11, this equation yields:

$$\varepsilon_{\phi\psi} = \frac{d - d_0}{d_0} \approx \frac{r_0 - r}{r} \approx \frac{r_0 - r}{r_0} \tag{3.12}$$

So the strain is compressive when the radius increases and tensile when the radius decreases.

By combining Eq. 3.6 with Eq. 3.12, one can obtain the final equation of strain measurement:

$$\varepsilon_{\phi\psi} = \sum f_{ij}\varepsilon_{ij} \approx \frac{r_0 - r}{r_0} \tag{3.13}$$

This is a linear equation with six unknowns. Principally the strain tensor can be solved with six independent $(\eta, 2\theta)$ or (η, r) data points. With a 2D detector, thousands of data points are available. Using a least squares regression method, the strain tensor can easily be solved with very high accuracy.

CHAPTER 4

Residual stress distribution and its non-destructive analysis using synchrotron radiation for high strength gear steels

4.1. Residual stress evolution with processing

4.1.1. Effect of carburizing process on the surface residual stress in Ferrium C61, C67 steels

It is well known that the fatigue performance of engineering materials can be significantly enhanced by introducing beneficial compressive residual stresses. This fact has been incorporated into the design of new engineering materials, for instance, bearing and gear steels [**76**]. Residual stress generating processes, such as carburizing/nitriding, shot/laser peening, have also been investigated to maximize the benefits on fatigue strength [**77**]. The carburizing process is the first source of beneficial compressive residual stresses during gear steel processing. Its effect on residual stresses was investigated by analyzing surface residual stresses in specimens carburized with different procedures. Conventional X-ray diffraction techniques were employed for the analysis.

4.1.1.1. Influence of boost cycle and carburizing temperature. Ferrium C61, carburized for one cycle with various boost times, was selected to study the influence of boost cycle and carburizing temperature on surface residual stresses. After carburization, the specimen was cooled by Argon gas and cryogenically treated with liquid nitrogen. Surface residual stresses after a single boost cycle with different boost times are shown in

Fig. 4.1. At two different carburizing temperatures, surface residual stresses were found to be all compressive and displayed the same trend. As boost times increases, surface compressive residual stress climbs to a maximum at 75 s boost time and then drops with boost time. Surface carbon content was measured by Midwest Thermal-Vac, shown in Fig. 4.2. As boost time prolongs, more carbon diffuses in and surface carbon content increases.

It was expected that higher carbon content would result in higher surface compressive residual stress because the martensite transformation would be more delayed during quenching and cryogenic treatment. However, the compressive stresses decrease after reaching a maximum while the surface carbon content keeps rising. Similar trend was observed for microhardness. The microhardness test performed by Dr. Gao showed the peak hardness position moved from the surface to subsurface with increasing boost time [**78**]. This shift occurred to the boost time of 75 s, at which carbon content reached 0.5wt% approximately at both temperatures. With boost time longer than 75 s, surface hardness decreased as retained austenite began to form in connection with the increasing surface carbon content. Surface compressive residual stress was also reduced. The amount of retained austenite in four C61 specimens with different boost times were measured using X-ray diffraction. Prior to the measurement, specimens were tempered at 200 °C for 1 hour to stabilize retained austenite. Results are shown in Table 4.1. It is clear that a 30 s more boost time at 950 °C or a 25 s increase at 1000 °C doubled the level of retained austenite, which resulted in the position shift of peak hardness and reduction in surface compressive residual stress.

At a carburizing temperature of 950 °C, a larger maximum compressive residual stress was exhibited than at 1000 °C. This was attributed to the larger carbon content gradient near the surface at 950 °C. Due to the increased diffusion at the elevated temperature, hardness profiles near the surface at 1000 °C were relatively flat compared to those at 950 °C, indicating a smaller carbon content gradient. This smaller carbon gradient thus led to the lower peak residual stress value.

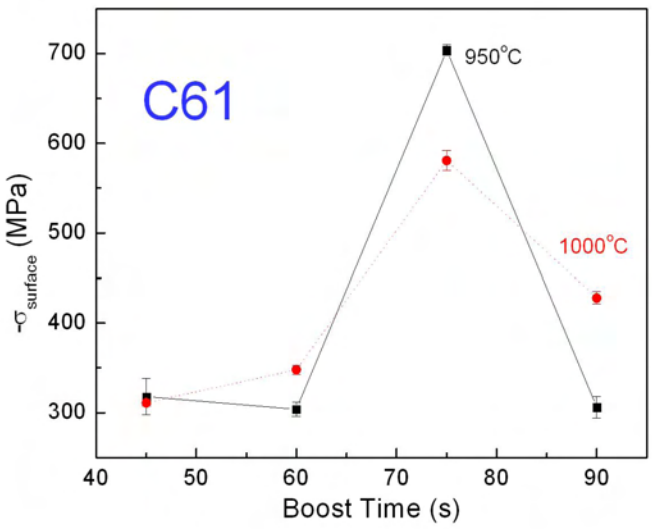

Figure 4.1. Surface residual stresses of C61 with various boost cycles

Table 4.1. Retained austenite content in C61 steels with single boost cycle

Material	Treatment			Content of Retained Austenite
	Carburizing	LN_2, 1hr	Tempering	
C61	950°C, 60s B	Y	200°C, 1hr	0.029 ± 0.005
C61	950°C, 90s B	Y	200°C, 1hr	0.065 ± 0.006
C61	1000°C,45s B	Y	200°C, 1hr	0.036 ± 0.005
C61	1000°C, 70sB	Y	200°C, 1hr	0.058 ± 0.005

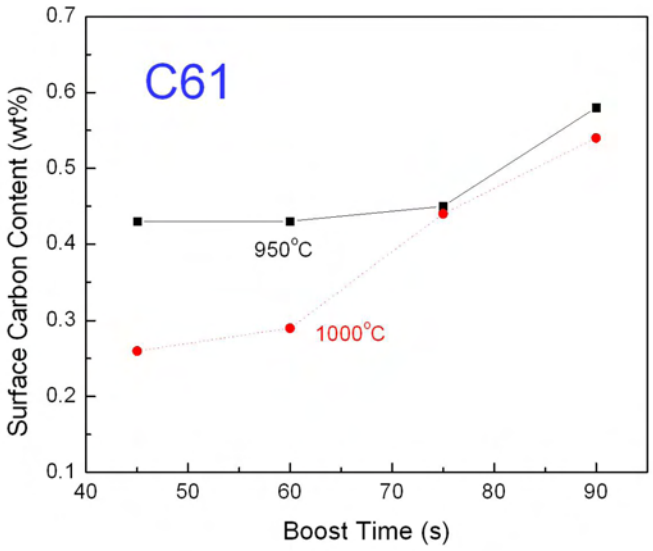

Figure 4.2. Surface carbon content of C61 with various boost cycles

4.1.1.2. Influence of diffuse cycle. Fig. 4.3 displays the influence of intermediate diffusion time on the surface residual stress. As expected, residual stress is reduced with longer diffusion time as the carbon content gradient is decreased.

Boost time, diffuse time and temperatures have been shown to affect the distribution of compressive residual stresses and the level of retained austenite. Desired compressive residual stresses and minimized retained austenite can be obtained by optimizing the carburization process. However, peening treatments have been demonstrated to be more efficient in generating higher beneficial residual stresses. Thus the exploration of carburization effects on residual stress will be utilized for fine tuning carburizing cycles after optimization of the entire processing.

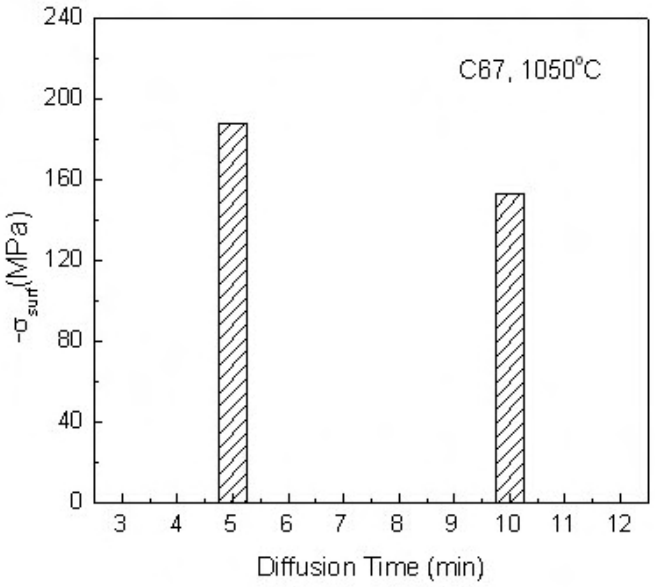

Figure 4.3. Surface residual stresses of C67 with various diffuse times

4.1.2. Evolution of surface residual stress during heat treatment and surface treatment

It is desired to maintain beneficial residual stresses as it keeps evolving with carburization, heat treatment and surface treatment. Shown in Fig. 4.4 and Fig. 4.5 is surface compressive residual stress evolution after different processes.

A surface compressive residual stress of 700 MPa was present in both C61 and C67 steels after carburizing, quenching, and cryogenic treatment. However, it relaxed by ∼480 MPa during both 200 °C and 482 °C tempering of C61. The fact that the relaxation is insensitive to tempering temperatures indicates a similar mechanism during both temperings. It is believed that residual stress relaxation is set on when the carbides start to precipitate and the extent of relaxation is linearly associated with the volume fraction

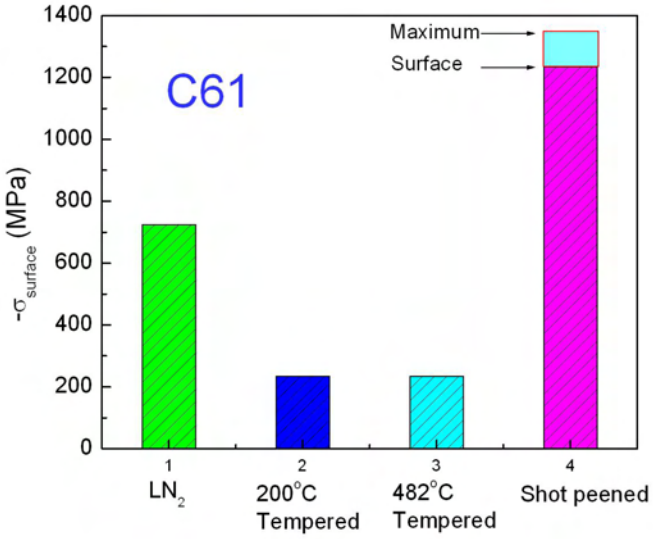

Figure 4.4. Surface residual stresses of C61 after different heat treatments and shot peening

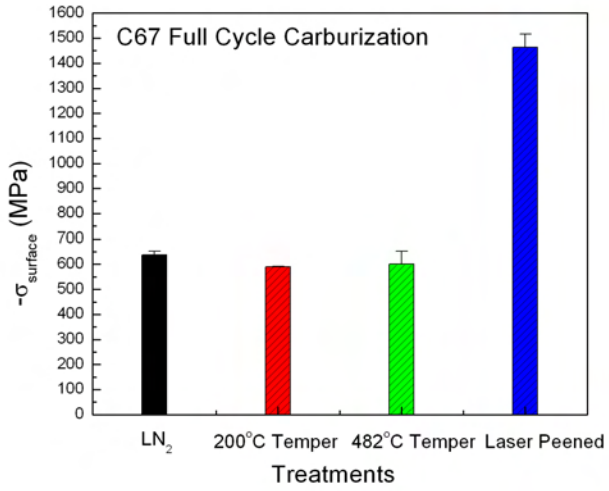

Figure 4.5. Surface residual stresses of C67 after different heat treatments and laser peening

of carbides. Howver, this relaxation did not occcur in the higher carbon case of C67. This may be associated with more gradual decomposition of retained austenite restoring residual stress levels.

Any residual stress relaxation was then compensated by the generation of large residual stresses through shot peening or laser peening. As high as 1200 MPa compressive residual stress was obtained in shot peened C61 and 1400 to 1500 MPa in laser peened C67. The effectiveness of peening in producing compressive residual stresses suggests that the optimization of peening treatment should be focused on to obtain desired residual stresses.

It is also noted that the compressive residual stress of C61 after shot peening can reach an internal maximum of 1365 MPa. Like surface residual stress, the location and the magnitude of the maximum residual stress depend on the shot peening process as well. It is desired to place this maximum where the fatigue cracks most likely initiate. For different applications, this maximum could be on the surface or at the subsurface. Thus, the peening process needs to be optimized for not only surface residual stress but also the maximum. Issues related to peening process optimization will be discussed in the next section.

4.2. Residual stress generation through peening techniques

4.2.1. Residual stress data review

Surface and maximum residual stresses in various steels are plotted in Fig. 4.6 and 4.7. In addition to literature data summarized in Section 2.4.3, residual stresses in shot peened C61 and laser peened C67 are displayed in Fig. 4.6 to better understand the correlation between residual stress and material hardness. Shot peened SKD61 was excluded from

the graphs since the outmost peened layer contained the Fe_4N white layer so SKD61 can not be treated as a metal.

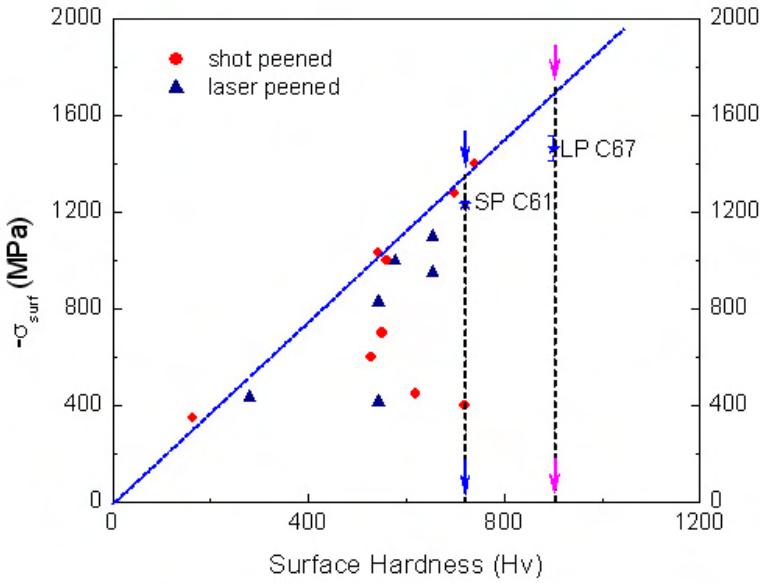

Figure 4.6. Surface compressive residual stresses of shot or laser peened steels

It is a rule of thumb in the shot peening industry that the maximum residual compressive stress is at least one half of the material yield strength when equivalently hard shots are used [**79**]. This also applies to the case of laser peening since shock waves with high energy can be treated as peening shots with sufficient hardness. Given the strong correlation between material hardness and yield strength, it is reasonable to correlate material hardness with the attainable maximum and surface compressive residual stresses. It is expected that better correlation can be obtained by using maximum residual stress data as surface values vary a lot more than the maximums as peening condition changes.

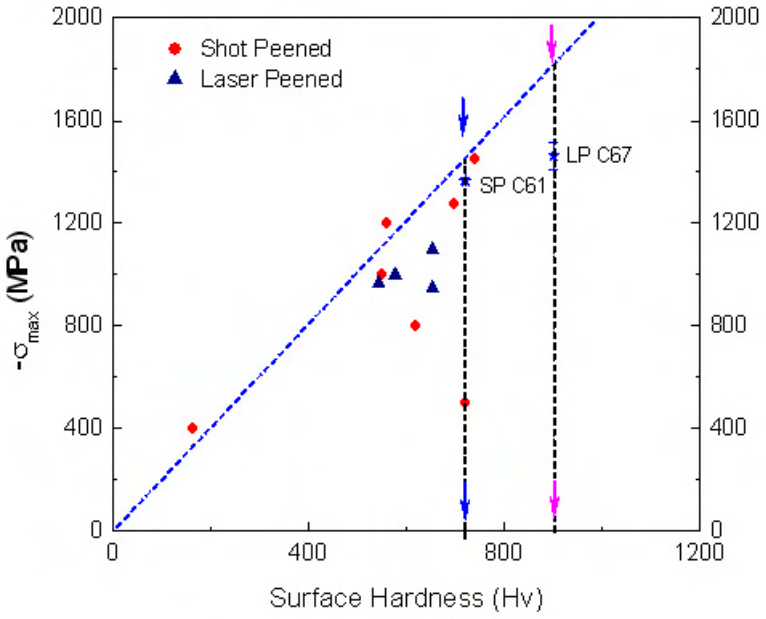

Figure 4.7. Maximum compressive residual stresses of shot or laser peened steels

Steel	max (MPa)	surf (MPa)
C61	1468	1329
C67	1835	1661

A linear relationship through (0,0) was found between the upper bounds of maximum and surface compressive residual stress and material hardness, shown by the dash lines in Fig. 4.6 and 4.7. The upper bound of maximum compressive residual stress follows: $-\sigma_{max}(MPa) = 2.03874 \times Hardness(Hv)$. For the upper bound of surface values, $-\sigma_{surf}(MPa) = 1.84546 \times Hardness(Hv)$ holds. The attainable maximum and surface compressive residual stresses in C61, C67 steels are listed above. The difference between current and attainable residual stresses indicates that the peening process needs to be optimized for higher beneficial residual stress.

4.2.2. Proposed peening intensity and media

Collaboration was established to implement peening process optimization between the Olson research group at Northwestern and the peening service industry, which includes Metal Improvement Company Inc., Laser Peening Technologies, Inc. and Research and Development at General Motors. Peening intensity and peening media are the two most important factors in the optimization. Steel shots as hard as 61 Rc with various sizes are available from the peening service industry, which enhances the optimization for C61. Unfortunately, there is no equivalently hard metal shot available for C67. No previous case of peening such a hard surface was reported. Thus peening intensity and peening media for a successful operation on C67 were explored herein.

In the Handbook of Shot Peening edited by Metal Improvement Company, Inc., the depth of compressive layer achieved from shot peening is summarized versus shot peening intensity for various kinds of materials, including steels with three different hardness levels [**54**]. Depth of compressive layer is decreased as material hardness increases if the same level of peening intensity is applied. For equivalent compressive depth, required shot peening intensity increases non-linearly with material hardness. The increasing rate also rises with material hardness. To determine the peening intensity for C67, data for steels were taken from Fig. 2.27 and replotted as peening intensity versus steel hardness for various compressive depths. Proposed peening intensity for C67 were obtained by fitting the industrial data (solid symbols in Fig. 4.8) and extrapolating fitting curves to the surface hardness of 900 Hv. The fitting process is described as follows: 1) Since surface hardness and peening intensity are positive, the function domain and range are $Hardness > 0, Int > 0$. 2) Boundary conditions were set based on the physics that

peening intensity tends toward zero or positive infinity when material hardness tends toward zero or positive infinity. 3) Provided the rate of change in the intensity increases as the hardness increases, the following corresponding rule was chosen for the function:

$$Int(AlmenC) = P_1 exp(P_2 \ln(P_3 \bullet Hardness)) \tag{4.1}$$

where P_1, P_2 and P_3 are three fitting parameters, Hardness is in Hv units. Fitting results for five compressive depths are listed in Table 4.2. Also presented are proposed peening intensity for C67 in both Almen C and Almen A units, shown as hollow symbols in Fig. 4.8. For the conversion between Almen C and Almen A please refer to [**80**]. According to desired compressive depth for C67 (0.2-0.25 mm) in the application of gears, a peening intensity of 0.040 Almen A is needed, which is much higher than that normally provided by industry.

Table 4.2. Fitting parameters and proposed peening intensity for C67

Depth (mm)	P1	P2	P3	C67 Hardness (Hv)	Proposed peening intensity (Almen C)	Proposed peening intensity (Almen A)
0.102	5.31E+09	1.757	1.28E-10	900	0.003436	0.012
0.204	5.50E+10	2.004	4.85E-10	900	0.009883	0.034
0.306	3.10E+10	1.898	3.70E-10	900	0.015839	0.054
0.408	1.15+E10	1.755	2.26E-10	900	0.020784	0.071
0.51	6.44E+09	1.669	1.65E-10	900	0.026027	0.088

A survey aboutof available shot showed that currently there is no steel shot having comparable hardness with C67. Thus the feasibility of using other harder shot, including tungsten carbide shot, ceramic shot and glass shot, was explored. Metal Improvement

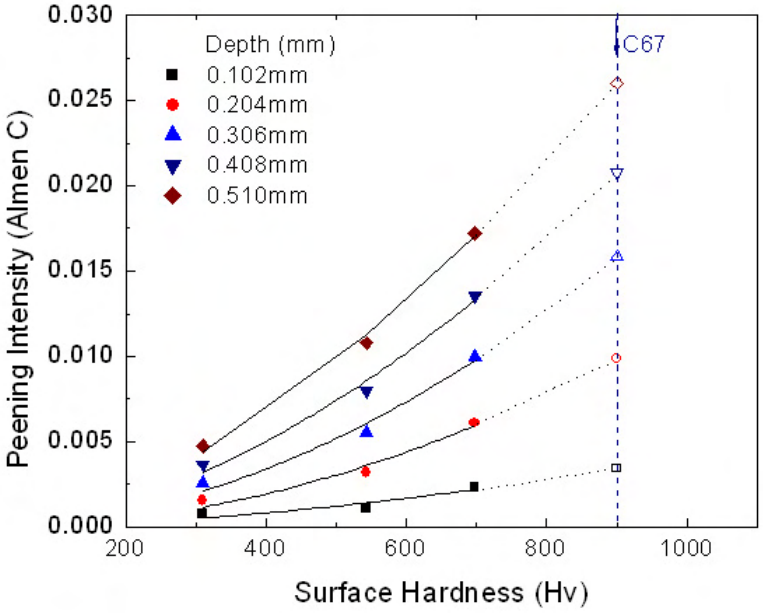

Figure 4.8. Peening intensity required for different depths in various steels

Company has glass shot with hardness of 70 Rc, but the shot are too small to produce a compressive depth of 0.2 mm. ZrO_2 with hardness of 1000 Hv can be provided by Saint-Gobain Zirpro Company in Mountainside, New Jersey. Unfortunately it is not feasible for our collaborator to modify the shot peening equipment to accommodate this special shot. Tungsten carbide shot with hardness up to 1400 Hv is the best choice since virtually no equipment modification would be needed and its very high density would provide better peening effects. However, it costs 200 dollars per lb and normal peening equipment would require a 400 lb load. Therefore, laser peening was proposed as an alternative since not only high intensity but also peening media with various sizes and virtual hardness can be obtained. The cost of laser peening is expected to be reduced as laser peening technology matures.

Besides peening techniques, *ultrasonic surface modification* will be discussed later for the possible application to C67, which employs a tungsten carbide ball to strike the material surface at an ultrasonic frequency.

4.3. Influence of peening on surface conditions

Compressive residual stress induced by peening treatment brings great benefit to fatigue strength by retarding crack initiation and propagation. However, a roughened surface due to peening acts as an adverse effect on the fatigue performance by increasing the risk of fatigue cracks initiating from the surface. Surface conditions of shot and laser peened Pyrowear 53 steel were investigated to assist the process optimization for desired residual stress and surface conditions.

4.3.1. Surface roughness

Surface roughness of shot and laser peened Pyrowear 53 cylinders was analyzed using interferometry. Sample tilt and curvature were corrected during the measurement. Before peening treatment, cylinders were ground to a RMS roughness of 4 microinch (0.1016 μm). Surface maps, line scans and 3D tomography were also carried out for Pyrowear 53, shown in Fig. 4.9 and Fig. 4.10. Crater-like 10 μm wide dimples were observed on the shot peened surface, showing the foot prints of the shots. Comparison between surface roughness before peening, after shot peening and after laser peening is shown in Table 4.3, which suggests that a worse surface condition was produced by laser peening. This was not anticipated since many researchers reported that surface roughening was alleviated by using laser peening instead of shot peening. It is implied that laser peening does not

necessarily provide a smoother surface than shot peening. For desired surface roughness, optimization is needed.

Table 4.3. Comparison of surface roughness before and after peening for Pyrowear 53

Pyrowear 53	Before Peening	After Shot Peening	After Laser Peening
RMS roughness (μm)	0.1016	0.31	0.40
Average roughness (μm)	-	0.25	0.32

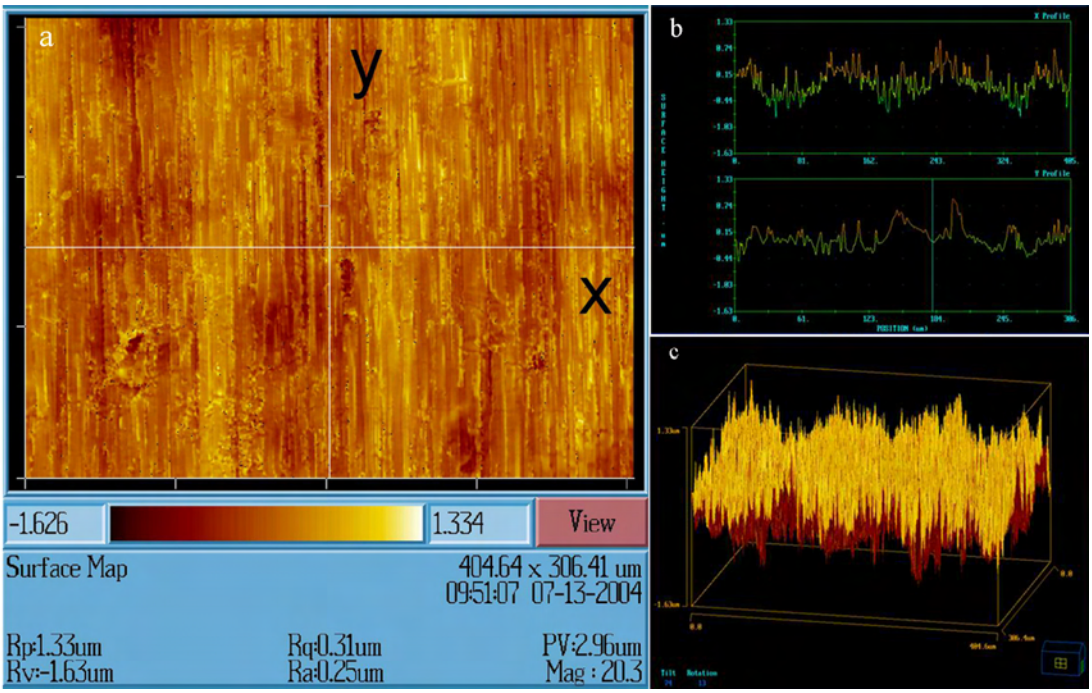

Figure 4.9. Surface conditions of shot peened Pyrowear 53 a) surface map; b) line scan along x, y axes; c) 3D tomography

4.3.2. Surface defects

Surfaces of shot and laser peened Pyrowear 53 were also observed using SEM to identify any possible defects. As displayed in Fig. 4.11, both shot and laser peened surfaces presented crossed grinding marks. Dimples due to shot bombardment were observed and

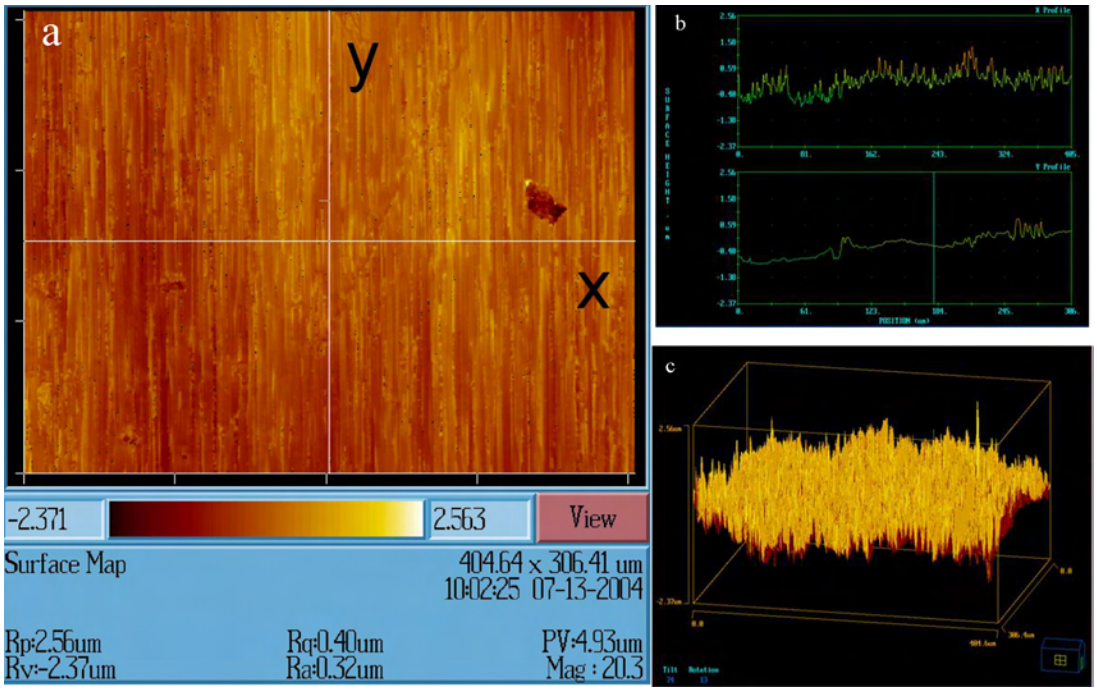

Figure 4.10. Surface conditions of laser peened Pyrowear 53 a) surface map; b) line scan along x, y axes; c) 3D tomography

a few large ones took place where horizontal and vertical grinding marks intersect. On the laser peened surface, craters linked together and formed a semi-continuous network. Most craters aligned well with the laser scanning direction (y direction), indicating they were caused by laser spot overstrike. Slight surface melting may be also involved during laser peening, promoting network formation. Undesired conditions of the laser peened surface indicated that the laser energy was set too high during the peening process.

Observation of the cross section of shot peened Pyrowear 53 revealed several micro cracks and micro notches near or on the surface, displayed in Fig. 4.12. Micro cracks were believed to initiate from the location of maximum shear stress produced during shot bombardment.

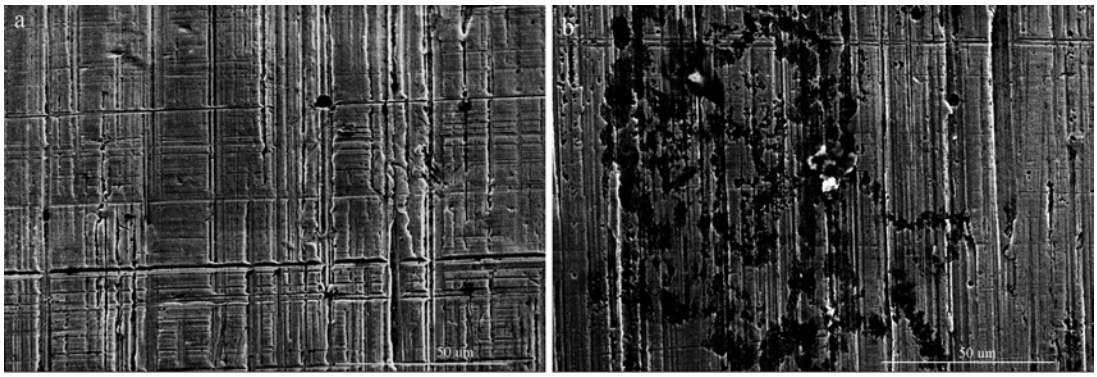

Figure 4.11. SEM images of shot and laser laser Pyrowear 53 surfaces a) shot peened; b) laser peened

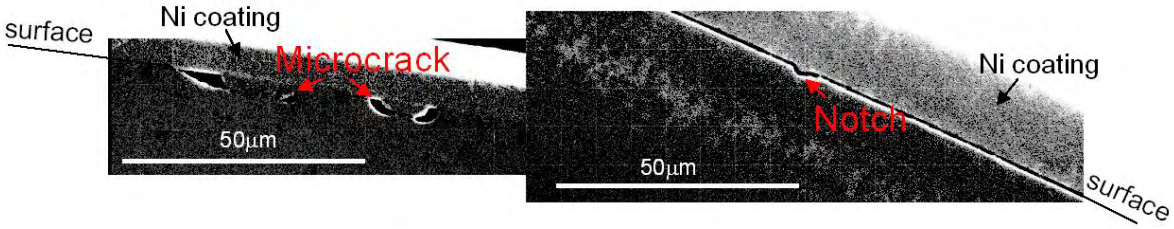

Figure 4.12. Cross section SEM images of shot peened Pyrowear 53 a) micro cracks; b) micro notch

Surface conditions were deteriorated by both shot and laser peening and thus the fatigue performance was likely downgraded. It is possible to optimize peening processes for a smoother surface with less defects. However, this objective conflicts with the goal of achieving maximum residual stresses. Thus a tradeoff must be made when applying peening treatments to improve material fatigue performance. The ultimate optimization may involve final removal of a shallow damage layer after high intensity peening.

4.4. Achieved residual stress and surface conditions in C61,C67

4.4.1. Surface residual stresses in C61, C67

Shot peening was applied to C61 steel through a proprietary process developed by Metal Improvement Company, Inc. Both experimental alloy and gear products were treated. Achieved surface residual stresses were measured using the conventional X-ray technique and results are listed in Table 4.4. Data for gears is provided by the doctoral research of Dr. Benjamin Tiemens at Northwestern University. Due to the high surface hardness of C67, it was treated by laser peening using the proprietary process provided by Laser Peening Technologies, Inc. Here, -1.3 GPa and -1.4∼-1.5 GPa are achieved on the surface of C61 and C67, respectively. Variation in surface residual stress suggests the need for further process optimization.

Table 4.4. Achieved surface residual stresses in C61, C67 steels

Steel	Treatment	Surface Residual Stress (MPa)
C67 Rod	laser peening	Axial: -1463 ± 53 Hoop: -1362 ± 4
C61 Rod	shot peening	Axial: -1309 ± 10
C61 Gear 1	shot peening	-1234 ± 14
C61 Gear 2	shot peening	-1151 ± 21
C61 Gear 3	shot peening	-1054 ± 7

In addition, to investigate the effects of shot on residual stresses, experimental C67 pucks were shot peened under three peening conditions. Peening media and intensity are tabulated in Table 4.5 as well as the resulting surface residual stresses. Peening intensities are chosen by Metal Improvement Company in Addison, Illinois, according to selected shots, desired surface residual stress and compressive depth. Two runs of single peening and one run of dual peening were performed. Comparison between results of

two single peening runs showed the effect of shot size on surface residual stress. In run I, large shots were used with higher peening intensity but lower surface residual stress resulted. That could be explained by the ball-surface contact mechanics. A large ball would lead to a greater depth of maximum shear stress, a higher maximum shear stress and a lower surface stress than a small ball. Consequently, it was expected that a lower surface residual stress, a higher maximum residual stress and a greater compressive depth were obtained by using large shot. The benefit of using dual peening is clearly shown by resulting surface residual stress, which was largest among three runs of shot peening. However, the achieved 988 ± 10 MPa compressive surface residual stress did not meet our expectation of 1400∼1500 MPa for C67. This we believe is because the shot hardness (62∼64 Rc) is lower than the surface hardness of C67. Thus laser peening is proposed instead. As dual shot peening generates a large surface residual stress and a great depth, dual laser peening is proposed for further peening optimization.

Table 4.5. Shot peening conditions for C67 and resulting surface residual stresses

Peening Method		Shot	Peening Intensity (Almen A)	Surface Residual Stress (MPa)
Single Peening		460H	0.018-0.024	-824±82
Single Peening		110H	0.006-0.010	-931±10
Dual Peening	Pass I	460H	0.018-0.024	-988±10
	Pass II	110H	0.006-0.010	

4.4.2. Surface conditions in C61, C67

Surface maps of C61 and C67 are displayed in Fig. 4.13, revealing both surface roughness and morphology. Comparison between C67 surfaces before and after laser peening showed an absolute roughness increase by laser peening. Resulting surface roughness in laser peened C67 is higher than that in shot peened C61. Noting that C67 has a higher surface hardness than C61, it can be expected that with identical laser peening processing, the laser peened C61 surface would be much rougher than shot peened C61. Thus in this case laser peening does not provide a smoother surface than shot peening.

As surface roughness of C67 was increased substantially, the case microstructures of C67 before and after laser peening were observed using scanning electron microscopy (SEM) to study the effect from laser peening (4.14, a lighter Nital etching in b)). No microstructure change was identified under SEM. Complementary hardness profiles were measured to help probe the possible change in dislocation structure and density. Results showed no detectable hardness variation, indicating a fairly stable dislocation structure and density during laser peening.

4.5. Non-destructive analysis of residual stress distributions for high strength gear steels

4.5.1. Research goals

To analyze residual stress distributions in gear steels with large composition and property gradients, a non-destructive synchrotron technique is desired for specimen intactness and measurement accuracy. The first goal of the research is to develop a non-destructive technique using synchrotron radiation and to demonstrate its effectiveness in measuring

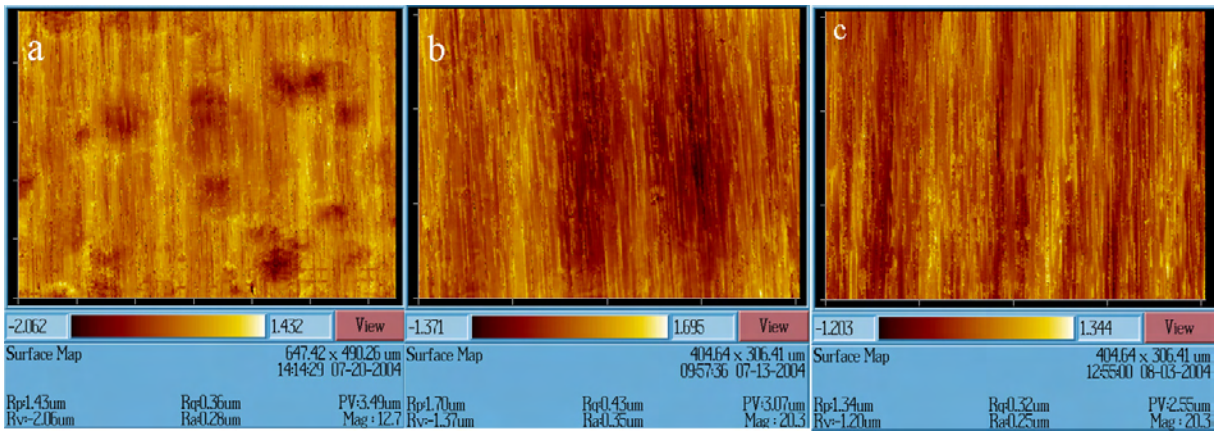

Figure 4.13. Surface maps of peening treated C61 and C67 a) shot peened C61; b) laser peened C67; c) not peened C67

residual stress distributions. The second goal is to study residual stress distribution and its evolution during an NTN rolling contact fatigue (RCF) screening test for three steels (Pyrowear 53, Ferrium C61 and C67), which were processed differently either by shot peening or by laser peening for performance enhancement. The third goal is to understand materials response in this RCF test with extreme 5.4 GPa Hertzian pressure. Finally, results are expected to illustrate issues regarding the RCF test itself and to direct the process optimization for desired residual stress and enhanced fatigue strength. Further details can be found in [**81, 82**].

4.5.2. Technological aspects

The principles of residual stress analysis using a high energy synchrotron transmission technique was briefly introduced in Chapter 3. Because the cylindrical specimen is too long (76.2 mm in length), synchrotron radiation can only penetrate the specimen perpendicularly to the cylinder axis. To determine required radiation energy, the desired penetration depth was first calculated. Since all specimens are carburized steels with a

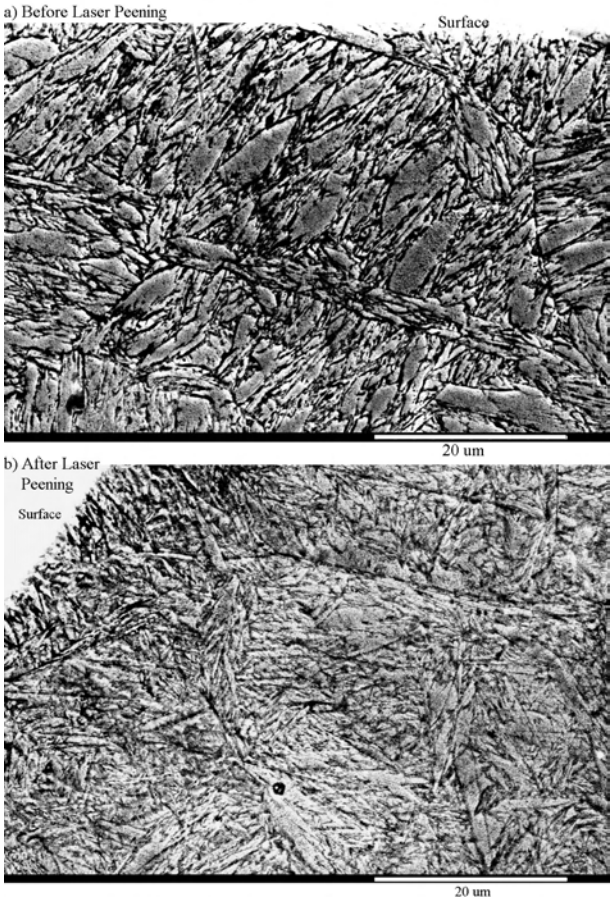

Figure 4.14. Case microstructure of C67 before and after laser peening a) before b) after laser peening

case depth of about 1 mm, it is desired to measure the residual stress at the depth of 1 mm below the cylinder surface. As illustrated in Fig. 4.15, $|AC|$ represents the greatest depth at which we would like to measure residual stress. Thus the pass length of radiation, t, equals $|BD|$. With $|AC| = 1mm$ and a diameter of 9.525 mm, the pass length of radiation $t = |BD| = 2 \times \sqrt{r^2 - (r - |AC|)^2} = 5.84mm$. For successful data collection and reading, the required transmission, T, is at least 5%. The following relation between transmission and pass length holds: $T = exp(-\mu_E \times t)$, where μ_E is element absorption

coefficient at energy E. With known T and t, μ_E can be calculated as $0.5mm^{-1}$ in this case. From μ_E, the energy level is backed out since μ_E is inversely proportional to E^3. In this study, 76 keV is needed for the radiation to pass through a length of 5.84 mm in steels.

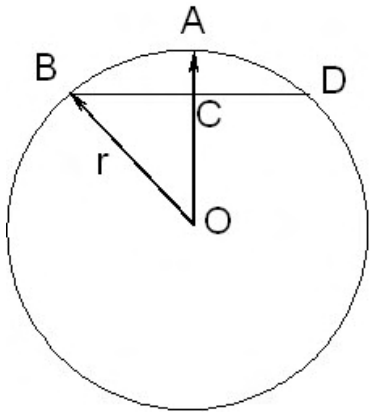

Figure 4.15. Pass length of synchrotron radiation

Along with 76 keV high energy radiation, a cryogenically cooled bent double-Laue monochromator was used to provide over ten times more flux than a flat-crystal monochromator at the same energy without increasing the energy width ($\Delta E/E \simeq 10^{-3}$) [**83**]. By using the advanced refractive X-ray lenses, the beam can finally be focused to $20 \times 20\mu m^2$ for a high spatial resolution [**84**].

Due to the existence of carbon content and strengthening dispersion gradients in the specimens, a local three dimensional gauge volume needs to be confined for the distribution analysis of residual strain or stress. In the past, slit-imaging has been used for this purpose for the bulk of polycrystalline materials, such as a shot-peened Al sample [**85**]. An imaging slit was placed behind the sample and the longitudinal spatial resolution was defined by the size of the slit. However, this usually leads to very slow data acquisition since only

one reflection from one gauge volume is recorded at a time. To be able to define a 3D gauge volume and accelerate data acquisition, a novel device, the conical slit, has been developed [**71**]. The conical slit (CS) is a two-dimensional slit, allowing simultaneous strain measurement in two directions. It is designed and positioned in such a way that Debye-Scherrer diffraction cones of a specific symmetry group at a determined energy would pass and finally reach the two-dimensional detector. Multiple reflections would be recorded simultaneously. The size of conical opening is determined from diffraction rings of an ideal powder material at a chosen energy. Higher spatial resolution can be achieved by choosing a smaller opening. In Fig. 4.17, the resolution along the z axis is determined by the projection of the gap size δ of CS according to the relation $\delta z = \delta / tan(2\theta)$. Resolutions along the other axes, δy and δx, are defined by the beam size. Thus a three dimensional gauge volume is well defined, providing an accurate locating of the irradiated volume. By utilizing the conical slit, Martins et al. successfully measured the residual strain distribution along the radius of a deformed torsion cylindrical sample [**86**]. Thus we believe it is appropriate to apply the conical slit technique to our analysis.

The combined usage of the micro-beam and the conical slit in this measurement provided a high spatial resolution. However, the resulting diffraction volume is so small that the diffracted grains could be too few to constitute valid statistics. To solve this problem, a sample oscillation method developed by Lienert et al. [**72**] was employed in this study. A specimen rotation stage was used to enable the rotation of the cylindrical polycrystalline specimens besides the x, y and z motions. At each depth, the specimen rotates continuously at a certain speed while the area detector is recording diffraction. Thus,

the number of illuminated grains increases and diffraction information averaged over a sufficiently large number of grains can be obtained.

The depth resolution of the measurement depends on the beam size as well as the eccentricity of the specimens. With zero eccentricity, the depth resolution is $\delta y_0 = 10\mu m$ since the beam size is $20x20\mu m^2$. With eccentricity δeccen, the final depth resolution is $\delta y = \sqrt{\delta {y_0}^2 + \delta eccen^2}$. The measured eccentricity and resulting dept resolution for each specimen are tabulated in Table 4.6.

Table 4.6. Eccentricity in specimens

Steels	Delta eccen (μm)	Delta y (μm)
C61 Shot Peened	12.5	16
C67 Laser Peened	10	14
C67 Ground	10	14
Pyrowear53 Shot Peened	20	22
Pyrowear53 Laser Peened	10	14

4.5.3. Experimental procedures

The non-destructive measurement of residual strain or stress depth distributions was performed at the 1-ID Beam Line at the Advanced Photon Source (APS), Argonne National Laboratory. The measurement was instructed by Dr. Jonathan Almer from APS. Dr. Benjamin Tiemens also participated in the experimentation. The schematic experimental setup in Fig. 4.16 shows the general idea of the measurement utilizing micro-size high energy radiation in transmission mode. The specimen was oriented such that the cylinder axis is perpendicular to the beam. This is because the beam can only penetrate the specimen along the z direction. With this orientation, both axial and radial strain components can be detected simultaneously.

The detailed top and side views of the experimental setup are shown in Fig. 4.17. In the top view, x is defined as the cylinder's axial direction and y points perpendicularly out of the paper plane; z is the beam direction. A $20 \times 20 \mu m^2$ micro-beam at 76 keV (wavelength $\lambda = 0.16 \mathring{A}$) in the transmission mode was adopted. The conical slit was mounted between the specimen and the area detector to define a longitudinal gauge length of $100 \mu m$, generating a diffraction volume of $20 \times 20 \times 100 \mu m^3$. The conical slit also allows diffraction over a plane encompassing (nearly) axial and normal directions to be collected simultaneously by the detector. Specimens rotated at least 360° during the exposure when diffraction was recorded. After 1s exposure, specimens moved along the y direction to the next depth position. Diffraction of standard CeO_2 powder was first taken to calibrate the position of the beam center and the distance between the specimen and the detector.

The hoop strain information will not be obtained in this setup. To collect hoop strain information, the specimen must be tilted within the xz plane and form an angle with the x axis. This could be accomplished, however, with an increased difficulty in beam alignment, data analysis and data interpretation. Given the fact that shot and laser peening induce mainly biaxial stresses, and the magnitude of hoop stress is usually equal to that of axial stress, we assume that hoop strain is equal to axial strain. Thus no specimen tilt was carried out in this study.

Diffraction from regions away from wear tracks ('untested') and under wear tracks were both collected. The X-ray beam was precisely positioned at the center of wear tracks, which could not be accomplished in the conventional X-ray lab since the beam

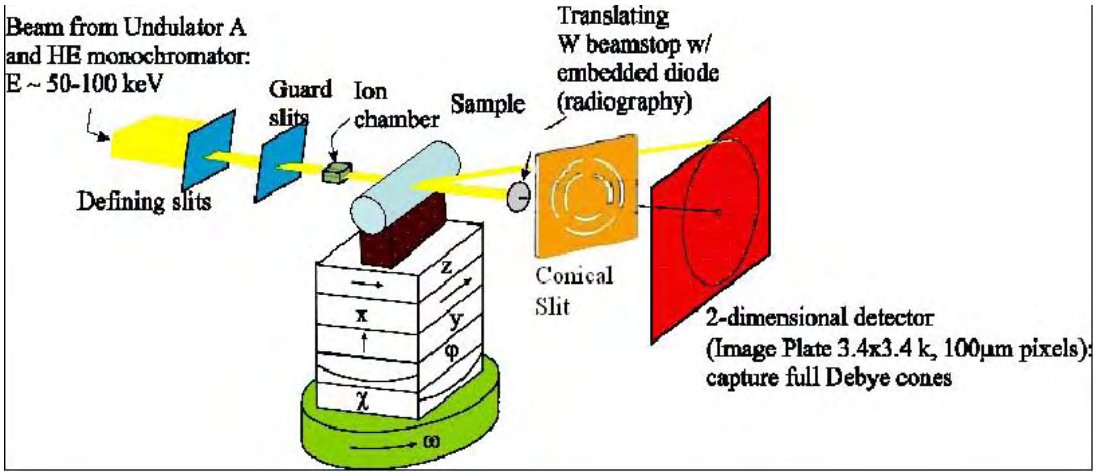

Figure 4.16. Schematic experimental setup of non-destructive residual stress distribution analysis using synchrotron radiation

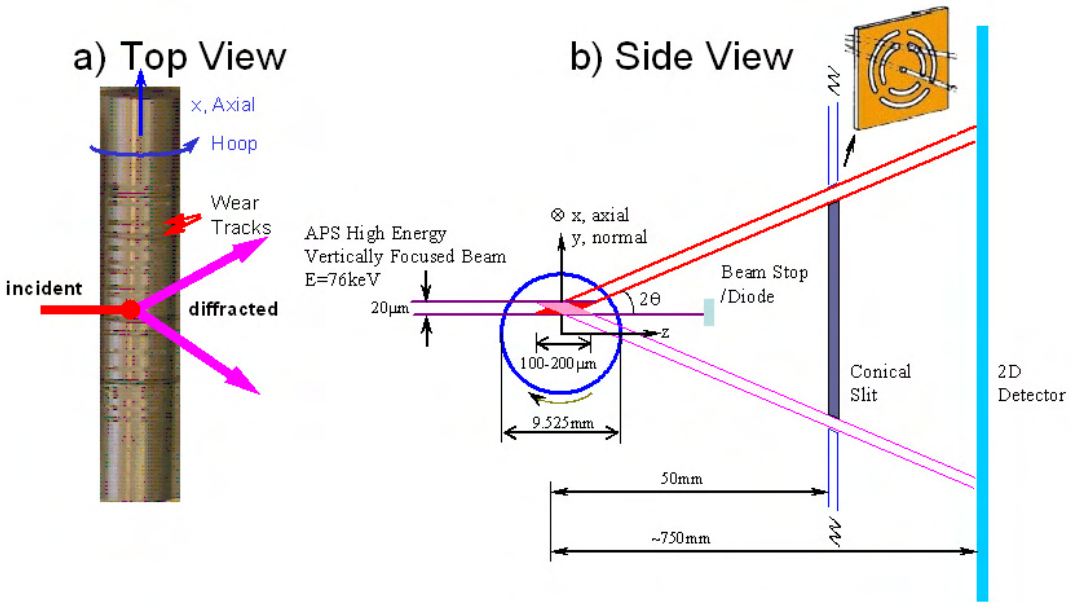

Figure 4.17. Detailed top and side views of non-destructive residual stress distribution analysis using synchrotron radiation a) top view b) side view

size itself is close to the track width. The information from wear tracks contain the averaged diffraction from both tracks and fatigue spalls located in the tracks.

4.5.4. Results and discussion

4.5.4.1. Diffraction pattern. Seven BCC reflections from the martensite matrix of three steels were first recorded without the conical slit. Shown in Fig. 4.18 is the pattern of laser peened C67 with each peak labeled. A similar pattern was observed for shot peened C61 (not shown). No austenite peak was found. Martensite peak splitting was not observed, indicating the relief of lattice distortion during tempering. With the presence of the conical slit, only four BCC peaks (200), (211), (220) and (222) were still visible. Debye diffraction rings were partially blocked by the conical slit (Fig. 4.19(a)). Diffraction rings in Fig. 4.19(a) became distorted, implying the existence of residual strain, which can be clearly observed in Fig. 4.19(b) where the lines converted from diffraction rings were not straight any more. The diffusion scattering recorded by the detector, displayed as the white regions in Fig. 4.19(b), were carefully removed in the data analysis. The (211) peak was selected for all analysis because of its least anisotropic effect on elastic constants, its second largest intensity and its relatively large radius of the diffraction ring. Analysis of multiple diffraction peaks will further improve the measurement accuracy. However, one peak analysis is more favorable herein for the simplicity and the good enough accuracy.

4.5.4.2. Residual strain. To extract strain tensors from the diffraction, angle and radial positions of each point on diffraction rings (η, r) were worked out by fitting rings to Pseudo-Voigt functions. Results of shot peened C61 and laser peened C67 are shown in Fig. 4.20. For each depth, the radial position r maximizes at $\eta = 0°, 180°$ and $360°$ while the minima occur at $\eta = 90°$ and $270°$, which indicates that the axial strain is compressive while the radial strain is tensile. This is based on the fact that larger radial position corresponds to larger 2θ and smaller d-spacing. In the first quadrant of $360°$,

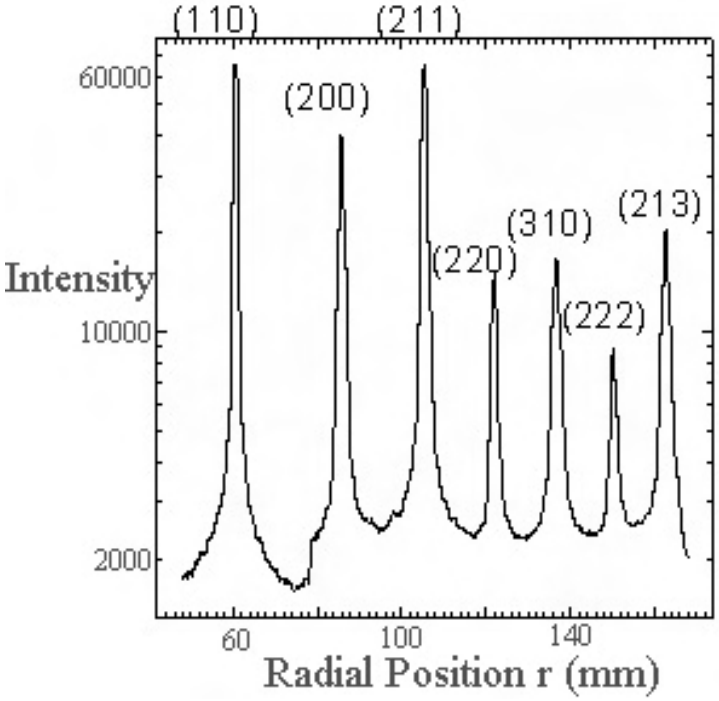

Figure 4.18. Typical diffraction pattern of laser peened C67 without the conical slit

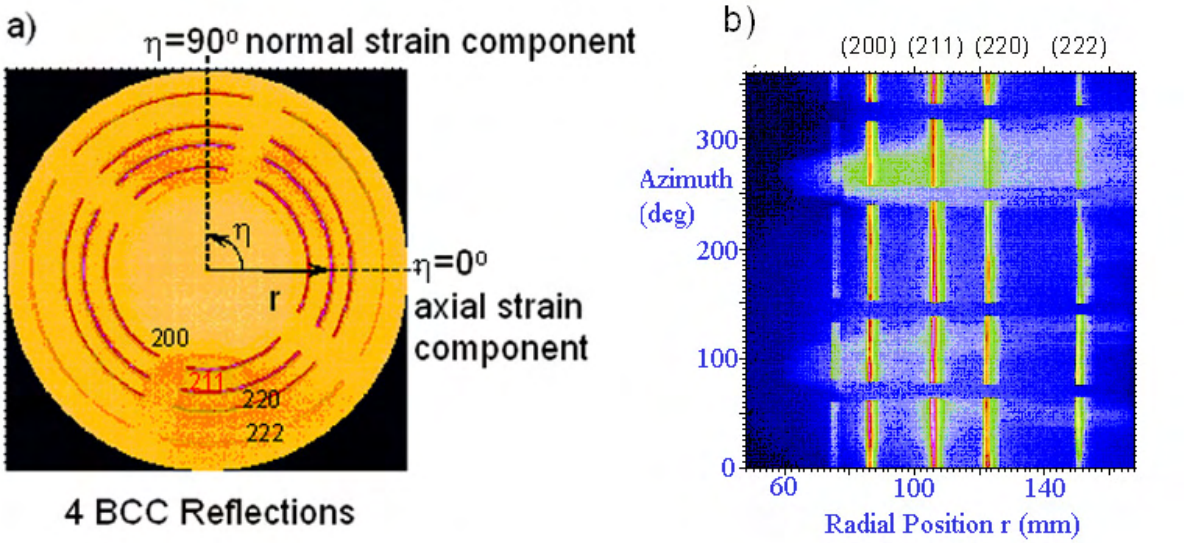

Figure 4.19. (a) Diffraction pattern with conical slit (b) Transformed diffraction pattern in azimuth and radius r Cartesian coordinate, showing the distortion caused by residual strain.

radial position at 0° reached a maximum for the depth of 0 or $25\mu m$ and then gradually damped as the depth increased, which implied that the largest axial compressive strains occurred on the surface or subsurface. Radial position at 90° first decreased as the depth varied from zero to 100μm but then rose up quickly for greater depths, which indicated that there was a maximum in radial tensile strains. For the depth greater than 1.1 mm, there was almost no difference in radial positions except small perturbations. At that point both axial and radial strains are quite small and very close to zero. Therefore, one way to determine the strain-free radial position, r_0 in Eq. 3.13, is to take the mean of the radial positions over 360° at the largest depth. However, in the case of laser peened C67, the depth where zero residual strain occurs was not reached and thus another way to determine strain-free radial position was adopted.

For laser peened C67, it is noted in Fig. 4.20 that in the first quadrant, radial position curves crossed each other at a common $(\eta*, r*)$ point. Especially at depths above 1.1 mm the curves varied around $r*$. Given that the strain status varied from pure compressive to pure tensile as η increased, there must be an azimuth value where the strains reached zero. That azimuth value was found to be $\eta*$. The corresponding radial position, $r*$ would be the strain-free value. The $r*$ has already taken into account the effect of material composition gradient on the strain-free d-spacing and should be a true representation of r_0. Analysis for laser peened C67, shot and laser peened Pyrowear 53 was based on choosing an appropriate $r*$ as r_0. For shot peened C61, both methods of determining r_0 generated similar results.

Ideally, radial position curves in the second quadrant are expected to be symmetric to those in the first quadrant about $\eta = 90°$. Curves in the third and fourth quadrants

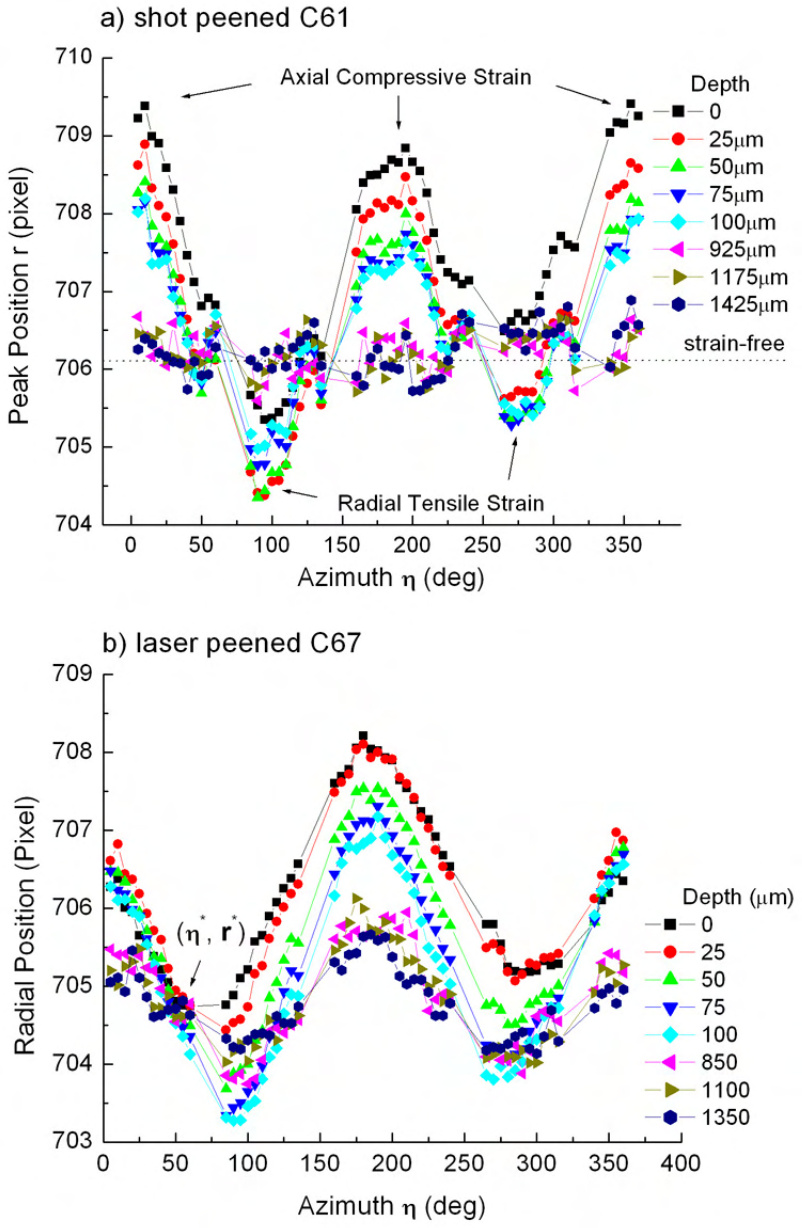

Figure 4.20. Radial positions versus azimuth in a) shot peened C61 and b) laser peened C67

should repeat patterns in the first and second quadrants. However, such symmetry is not observed in the case of laser peened C67. This is believed to be due to the differential absorption resulted from asymmetric positioning of the specimen with respect to the conical slit [**87**]. The extent of non-symmetry was alleviated as the depth increased. During strain extraction, correction was made for laser peened C67, as shown in Fig. 4.21.

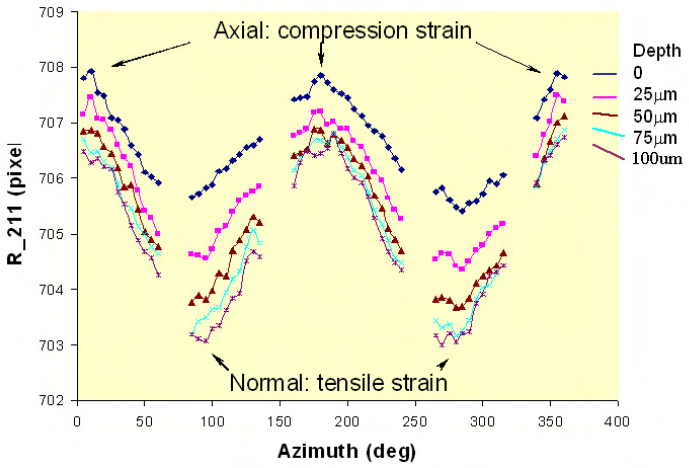

Figure 4.21. Corrected radial positions for laser peened C67

The macro-strain of the steel is represented by the micro-strain in the martensite phase measured from martensite peak (211) since the volume fraction of retained austenite is too small to be detected. Three strain components, ε_{11}(axial strain), ε_{22}(radial strain) and ε_{12}(shear in plane), were solved using Eq. 3.14 with the biaxial strain model ($\varepsilon_{13} = \varepsilon_{23} = \varepsilon_{33} = 0$). Depth distributions of three residual strain components for the untested region in shot peened C61 are shown in Fig. 4.22. Also displayed is the axial strain for the wear track. Since the measurement was performed along the principal axes, the shear strain component is negligible. Radial strain represents the extent of lattice distortion

along the radius, which is much less than the axial strain as peening mainly induces axial strain. Because the radial direction is mostly parallel to the direction of the fatigue crack propagation, the radial stress and strain are much less important than the axial and hoop stress and strain, as the direction of the latter is perpendicular to the crack propagation path. Also the assumption that the hoop strain is equal to the axial strain holds for shot peening and laser peening. Thus only axial residual strain profiles are displayed for other steels. The uncertainty in the depth caused by the eccentricity is summarized in Table 4.6. For easy graph reading, the errors in depths are not plotted.

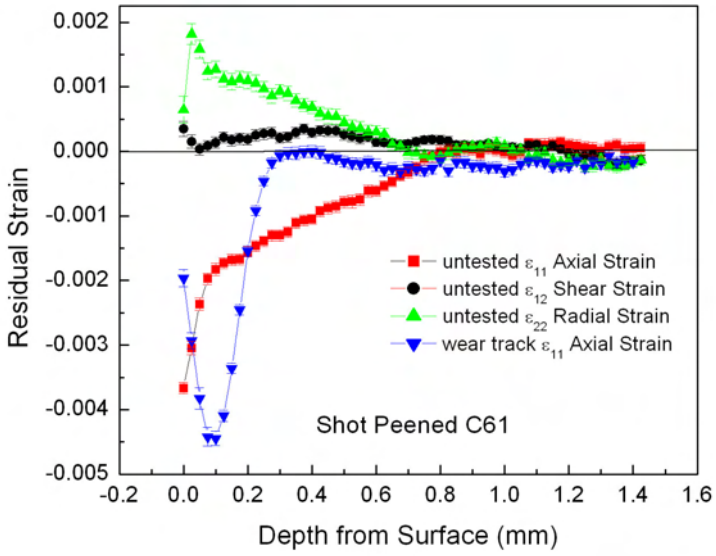

Figure 4.22. Residual strain of untested region in shot peened C61

Depth distribution of axial strains for both the untested region and wear track are plotted in Fig. 4.23 for laser peened C67, shot and laser peened Pyrowear 53. Also plotted is the axial strain for the untested region in ground C67 (unpeened). Large compressive axial strains were observed near the surface in both C61 and C67 steels, indicating the

comparable effectiveness of shot peening and laser peening. The compressive strains then gradually decrease to zero as the depth increases. However, zero strain isn't shown in laser peened C67 because our measurement didn't reach sufficient depth. In Pyrowear 53 steel, much larger axial residual strain was produced by laser peening than by shot peening, suggesting laser peening can be more effective than shot peening when appropriately conducted.

It is noted that the maximum compressive strain occurs on the surface in shot peened C61 while at the subsurface in laser peened C67. This is quite normal since the location of the maximum compressive strain can be tuned by adjusting the peening parameters. It is also evident that the compressive depth is greater in laser peened C67 than that in shot peened C61. Although the total compressive depth results from the combined effects of carburizing, heat treatment, grinding and peening, it is reasonable to deduce that the compressive depth caused by laser peening is generally greater than that by shot peening because peening is the dominating factor. The fact that C67 is harder than C61, i.e., more difficult to be peened, further supports this reasoning.

4.5.4.3. Residual stress. Residual stresses were computed using Eq. 4.2 based on the assumptions that the material is isotropic and the hoop strain is equal to axial strain ($\varepsilon_{33} = \varepsilon_{11}$). In Eq. 4.2, δ_{ij} is the Kronecker's delta function, S_1 and $S_2/2$ are X-ray elastic constants. The calculated axial residual stress profiles (σ_{11}) for untested regions and wear tracks in shot peened C61, laser peened C67, shot and laser peened Pyrowear 53 are presented in Fig. 4.24.

$$\sigma_{ij} = \frac{1}{S_2/2}\left[\varepsilon_{ij} - \frac{S_1}{S_2/2 + 3S_1}\delta_{ij}\varepsilon_{kk}\right] \tag{4.2}$$

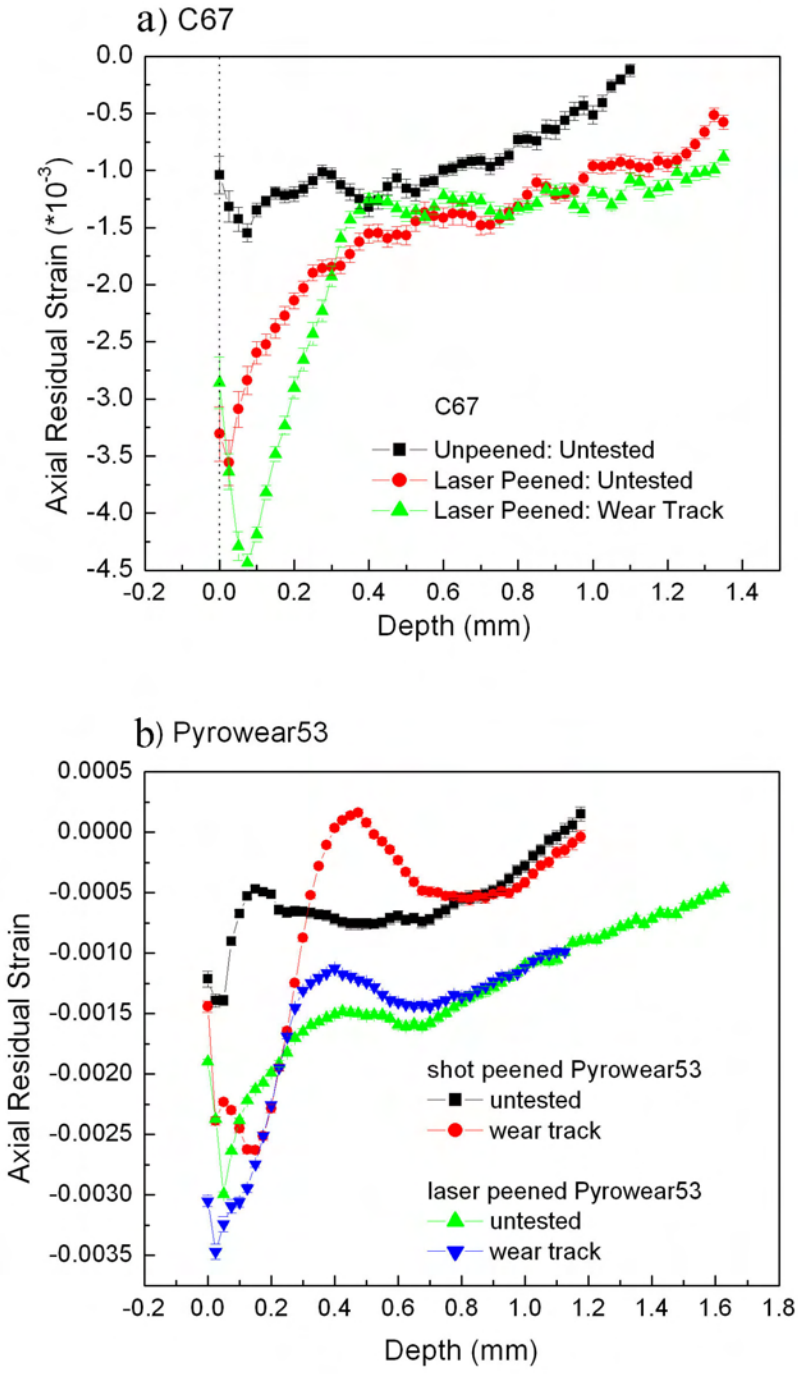

Figure 4.23. Residual strain in a) ground and laser peened C67 b) shot and laser peened Pyrowear53

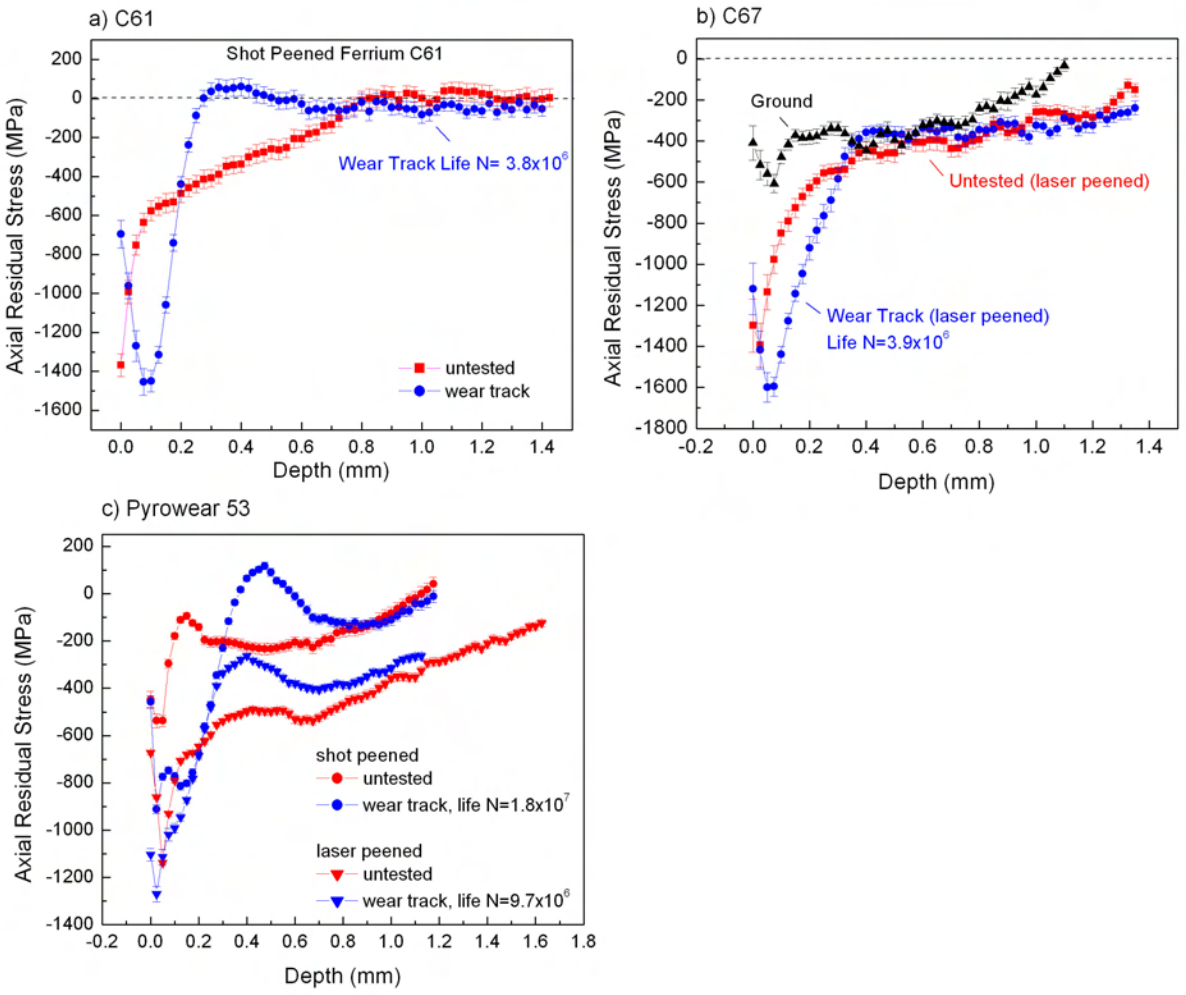

Figure 4.24. Axial residual stress distributions in a) shot peened C61 b) ground and laser peened C67 c) shot and laser peened Pyrowear53

Large compressive residual stress of -1.4 or -1.5 GPa was found near the surface in untested regions of C61 and C67 steels, suggesting the potential of the two peening techniques in generating compressive residual stresses. By optimizing the peening process, surface residual stress, maximum residual stress and its location can be fine tuned to satisfy application requirements. Measured surface axial stresses agree well with results from the conventional laboratory X-ray method (-1.31 $\sim$ -1.47 GPa). After reaching maxima,

compressive residual stresses decreased rapidly at 100 to 200μm depth and then slowly decreased to the minimum. The greater compressive depth formed in laser peening indicates that laser peening would be more favorable for subsurface fatigue resistance. Due to limited depths probed, the expected tensile residual stress in the sample center, balancing compressive residual stress in the case, was not shown in the graphs.

The response of residual stress to the extreme cyclic contact load (5.4 GPa in RCF test) were investigated by measuring the depth distribution of axial residual stress under wear tracks, shown by the blue symbols in Fig. 4.24. At cycle $N = 4 \times 10^6$, surface residual stress relaxation was observed in both the C61 and C67 steels. In shot peened C61, surface stress decreased from 1400 MPa to 700 MPa, approximately 50%. The relaxation in laser peened C67 was about 15% likely because C67 is more capable of retaining residual stresses due to its higher surface hardness. Residual stress relaxation was not observed at subsurfaces. Instead, it was maintained at the depth of 25μm in both steels and then increased until the maximum was reached. Thus a larger maximum of compressive residual stress was formed at a greater depth after cyclic contact loading. This building up of compressive residual stresses inside steels was due to the severe compression during the contact, which is supported by the fact that the position of the maximum residual stress, 100μm, agrees well with the calculated location of maximum shear stress in the contact, 98μm. The evolution of residual stress implies that the stability of beneficial compressive residual stresses under cyclic loading needs to be taken into account when considering fatigue performance.

4.5.4.4. Diffraction peak breadth. The mean of full width at half maximum (FWHM) of the martensite (211) peak over the entire diffraction ring was extracted from diffraction

and plotted versus the depth for untested regions and wear tracks in all steels, shown in Fig. 4.25.

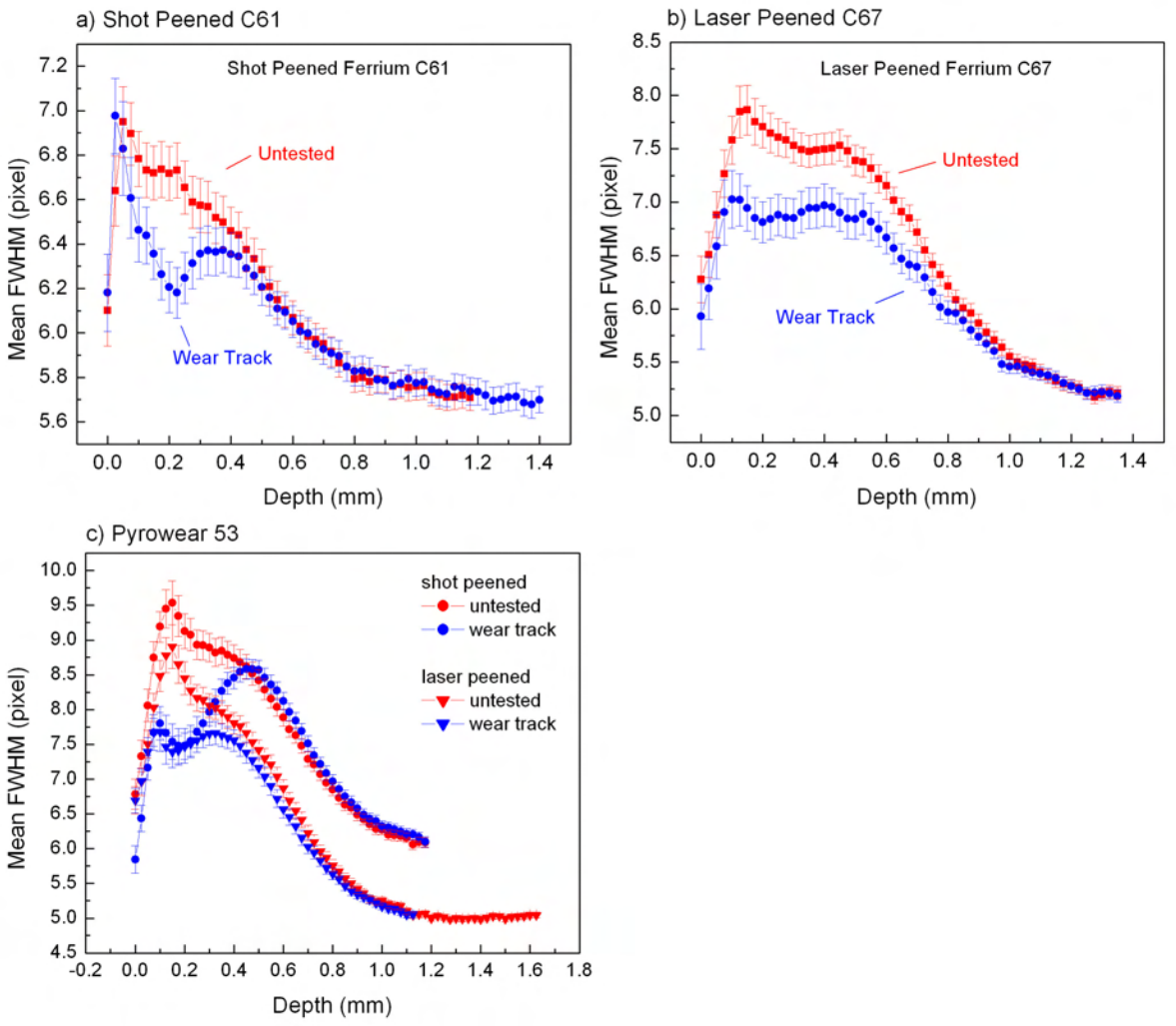

Figure 4.25. Mean (211) peak FWHM in a) shot peened C61 b) laser peened C67 c) shot and laser peened Pyrowear53

In untested regions, the martensite (211) peak broadens in the carburized and peened case (from surface to 1.2 mm depth) for all steels, which results from the combination of intrinsic martensite peak broadening and micro-strain broadening induced by peening.

The location of maximal peak breadth (75∼120μ m) for all steels matches the position of maximum shear stress produced in shot and laser peening if peening is treated as dynamic compression contact. Due to the greater compressive depth formed in laser peening than in shot peening, peak broadening took place within a wider depth range in laser peened steel (0∼700μ m) than in shot peened steel (0∼500μm). At the 10^6 cycle in the RCF test, the (211) peak sharpens significantly from the depth of 75∼100μm in all steels, shown by the blue symbols in Fig. 4.25. Provided that the RCF test and peening both generate compressive contact, it is assumed that strain broadening would not be reduced much. It was reported that in conventional hardening steels (such as Pyrowear 53), martensite could decay to ferrite under high cyclic contact loading although the transformation was not thermodynamically favorable [**88, 89**]. Thus the reduction of peak breadth in Pyrowear 53 is mainly due to the alleviation of martensite peak broadening, possibly associated with the transformation from martensite to ferrite. However, for the C61 and C67 secondary hardening steels, the tempered martensite matrix was very stable and such decay was not expected to occur. Instead, carbide dissolution was reported to be possible. Micrographs were taken to help understand the FWHM change in C61, C67 steels.

It is noted that the matrix FWHMs for shot and laser peened Pyrowear 53 do not match with each other. Although the reason has not been identified, the general trend that peak width reduces after the RCF test still holds.

4.5.4.5. Microstructure evolution. The optical images of cross sections beneath an untested region and a wear track in laser peened C67 were taken to investigate the microstructure evolution during the cyclic contact loading, shown in Fig. 4.26.

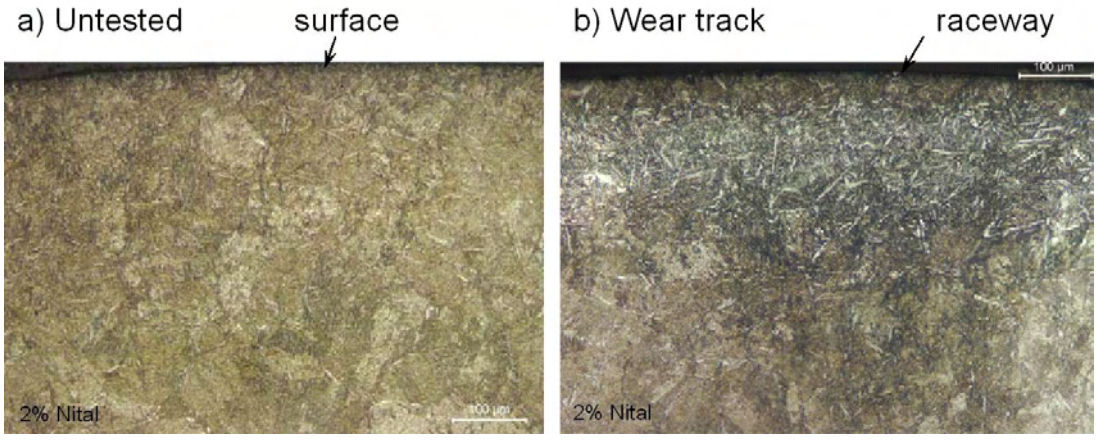

Figure 4.26. Optical micrograph of cross section under a) an untested region b) a wear track in laser peened C67

Comparison between these two optical images presents a clear microstructure change during cyclic contact loading. In the untested region, the material displays a homogeneous lath martensite structure, except a mix of lath and very fine plate martensite in the first 50μm depth. From 50μm to 200μm under a wear track, dark lath martensite was replaced by bright regions, shown in Fig. 4.26(b). This could be due to either ferrite transformed from martensite or carbide dissolution under extremely high contact load. More microstructural evidence is needed to specify the mechanism. At this point, carbide mechanical dissolution was propsed to be the reason. The fact that this zone falls within the maximum shear stress region of the RCF test (maximum shear stress depth: 98μm) indicated that the microstructure change is associated with the extreme compression in the RCF test. At greater depths, dark etching areas were observed to extend to 700μm. The depth of the entire microstructure alteration zone also matches the width of the peak sharpening region in Fig. 4.25(b). Therefore it can be concluded that it was the microstructure change displayed in Fig. 4.26(b) that caused the reduction in peak width.

4.5.5. Summary

A non-destructive synchrotron radiation technique was successfully implemented and applied for the first time to the analysis of residual stress distribution and its evolution in carburized steels with large composition and property gradients. One of the most important features in this measurement is the usage of the conical slit. It allows the confinement of a 3D gauge volume ($20 \times 20 \times 100 \mu m^3$). The longitudinal gauge length can be varied between 100 to 200μ m by adjusting the distance between the sample and CS. The combined usage of the conical slit and the area detector can accelerate data collection easily by 20 or more times.

4.5.5.1. Advantages of synchrotron radiation technique. The synchrotron and conventional X-ray techniques have reached good agreement on the measured surface residual stress values. Although the laboratory X-ray technique is much more easily accessed, the non-destructive nature of the synchrotron radiation technique makes it more favorable to measure residual stress depth profiles when the intactness of specimens is required for subsequent evaluations. This technique can be employed to assist process optimization for residual stress generation and screen out candidates for contact and bending fatigue testing. Moreover, the non-destructive nature enables the unique ability to precisely evaluate residual stress profiles under wear tracks, which is not possible using conventional laboratory X-ray techniques. The synchrotron radiation measurement is much faster than the laboratory X-ray method since multiple reflections can be recorded in seconds by using an area detector and the material removal step can be eliminated. Without layer removal correction, the accuracy is also improved. Moreover, a high depth

resolution of 25μm was achieved in our measurement by utilizing the $20 \times 20\mu m^2$ microbeam. High spatial resolution also enables us to investigate possible gradients in the strain and microstructure.

4.5.5.2. Conclusions to non-destructive residual stress distribution analysis. The non-destructive residual stress analysis using synchrotron radiation was successfully implemented and performed for shot or laser peened high strength gear steels. The measurement demonstrated that the high energy X-ray transmission technique is suitable and efficient in exploring residual strain/stress and microstructure non-destructively. It is also quite effective to investigate in-situ material response to the cyclic loading by probing strain/stress and microstructure under wear tracks. Large residual stresses of -1.4$\sim$-1.5 GPa near the surface in C61 and C67 steels show that shot and laser peening are both effective in producing beneficial residual stresses. The greater compressive depth obtained in laser peening indicates that laser peening is more favorable for subsurface fatigue resistance. Surface residual stresses relax in both C61 and C67 steels after the RCF screening test, which needs to be taken into account when considering fatigue life from the combined effect of applied stress and residual stress. The material microstructure also significantly alters during cyclic contact loading, which is supported by the peak sharpening after the RCF test and cross section micrographs under wear tracks. Carbide mechanical dissolution is proposed for this microstructure change under extremely high Hertzian contact stress. Residual stress relaxation and microstructure change under extremely high contact load of 5.4 GPa suggest that this extreme RCF test is not a good indicator for the normal service life.

These results, together with measurements on other processed specimens, can guide and accelerate process optimization to achieve the most suitable residual stresses for selected applications.

CHAPTER 5

Conceptual material and process design for an ultrahigh-strength gear steel - CryoForm 70

5.1. Design background and motivation

Several Ni-Co secondary hardening steels have been successfully designed using the systems approach, including Ferrium C67. The achievement of 67 Rc surface hardness endows the steel with excellent contact fatigue strength and wear resistance. C67 was demonstrated to be one of the best performing steels in auto racing applications [**90**]. However, a surface hardness of 69 Rc was desired when the design was initiated. Since higher surface hardness enables the further increase in contact and bending fatigue strength, redesigning an ultrahigh-strength gear steel with surface hardness of 69-70 Rc was brought forward. Moreover, as shown in Chapter 4, higher hardness allows higher compressive residual stress to be obtained, which further benefits the fatigue performance. We can also assess the feasibility of utilizing current hardening theory for the design, and explore the theoretical limit of achievable surface hardness. This design was also motivated by the gear industry vision of reaching surface hardness of 70 Rc in the near future. During the design, C67 steel and its variations will be referred to when setting design objectives and parameters.

Utilizing secondary carbides M_2C for strengthening, the design requires high carbon and alloying element concentrations. A low case M_s is anticipated for the desired case

hardness. However, mechanical deformation has been demonstrated to effectively transform retained austenite to martensite in low M_s high alloy steels. More transformation is expected with simultaneous cryogenic treatment due to the combination of mechanical and thermal martensite transformation driving force. A novel process of *Cryogenic Deformation* is proposed to promote martensite transformation in low M_s high alloy steels. Thus the other goal of this design is to evaluate the feasibility and effectiveness of cryogenic deformation process. Designed for higher surface hardness and for the exploitation of cryogenic deformation process, the new steel is named *CryoForm 70*, where *70* specifies the desired case hardness of 70 Rc and *CryoForm* stands for *Cryogenic Deformation*. Details regarding this process development are given in Chapter 7.

5.2. Design objectives

As the design goal is to improve the surface hardness from current 67 Rc to 69-70 Rc, the design objectives of the new steel is determined based on the achieved steel properties in Ferrium C67. Properties of Ferrium C61 are also compared.

5.2.1. Case property objectives

The top two performance attributes desired in CryoForm 70 include fatigue and wear resistance. Bending and contact fatigue failure are dominating failure modes in gears. Under high pressure gears wear out rapidly. Both contact fatigue strength and wear resistance improve as the surface hardness increases. Thus a surface hardness of 70 Rc (1076 Hv) is desired. With this hardness, the steel is expected to present a contact fatigue strength of 1800 $\sim$ 2200 MPa, according to the extrapolation made to the hardness of

1076 Hv, as shown in Fig. 5.1. In addition, a surface or maximum compressive residual stress of 1.9 to 2.1 GPa is anticipated based on the correlation between residual stress and hardness (explained in Chapter 4). Associated with this hardness objective, it is desired the driving force of M_2C carbide strengthening dispersion be maximized. A martensite matrix is also required to provide the desired dislocation structure on which M_2C carbides nucleate.

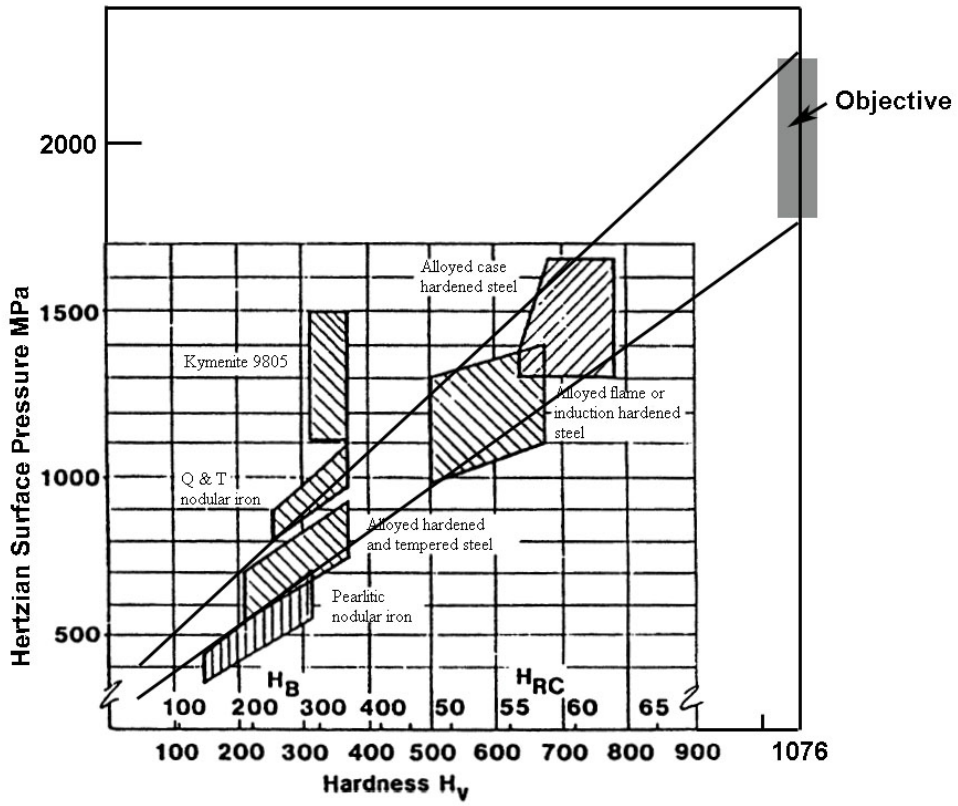

Figure 5.1. Desired contact strength for CryoForm 70

Ferrium C67 has shown an excellent hot hardness at elevated temperatures. Since the same hardening mechanism is applied in the CryoForm 70 design, this new steel is expected to possess a high hot hardness as well.

5.2.2. Core property objectives

An appropriate hardness gradient in secondary hardening steels is desired for a smooth transition in structure and properties. A core hardness of 500 Hv is needed to support the case, prevent core crushing under high load and provide necessary toughness. A fracture toughness of 50∼75 $ksi\sqrt{in}$ is required to tolerate an acceptable critical flaw size at this core hardness. A M_s of 350 °C or higher is desired for lath martensite formation. The brittle sigma phase was observed in the C69 core. Thus it is desired to limit the driving force of sigma phase to avoid its precipitation during tempering. Design objectives for CryoForm 70 are summarized in Table 5.1.

Table 5.1. Design objectives for CryoForm 70

	C61	C67	CryoForm70
Hardness Case (Hv)	720	901	**1076**
Hardness Core (Hv)	500	500	500
Max Contact Fatigue Strength (MPa)	1300-1600	1600-2000	**1800-2200**
Surf/Max Residual Stress (MPa)	-1400	-1600	**-1900/2100**
Core Fracture Toughness (ksi√in)	50-75	50-75	50-75

5.3. Design approach

Compared to the conventional strengthening mechanism utilizing transition $Fe_{2.4}C$ ϵ carbides, secondary hardening mechanism can provide higher efficiency. With only 0.5wt% carbon, a 60 Rc hardness can be obtained with secondary hardening, while 0.9wt% carbon is needed for comparable hardness using the conventional strengthening mechanism.

Based on the relationships between process/structure and property/performance of secondary hardening gear steels, a system design chart was prepared to guide the material and process design of CryoForm 70.

5.3.1. System design chart

The system design chart for CryoForm 70 is presented in Fig. 5.2. From the left to the right, this chart itemizes each process step, the hierarchial subsystems of material structure and prioritized properties and performances. Arrows indicating cause-effect relations are drawn from process steps to material structure and to properties and performances. In most cases, a cause results in multiple effects and an effect results from several causes. Thus the system design chart shows the network of all cause-effect links. A brief introduction to the processing will be given below. Material structure will be elaborated in the next section.

For the easy commercialization of CryoForm 70, a standard industry processing line is adopted. The processing starts with the ingot or other forms of core material, followed by simultaneous carburization and solution treatment. Quenching and cryogenic treatment are performed subsequently to form the case martensite matrix. Final tempering allows the strengthening dispersion to precipitate. To allow use of compositions that can not be fully transformed to martensite by cooling alone, a unique process of *cryogenic deformation* between cryogenic treatment and tempering is developed for CryoForm 70 to achieve the desired martensite matrix for maximized strengthening effect. After tempering, a shot peening step is conducted to enhance beneficial residual stresses.

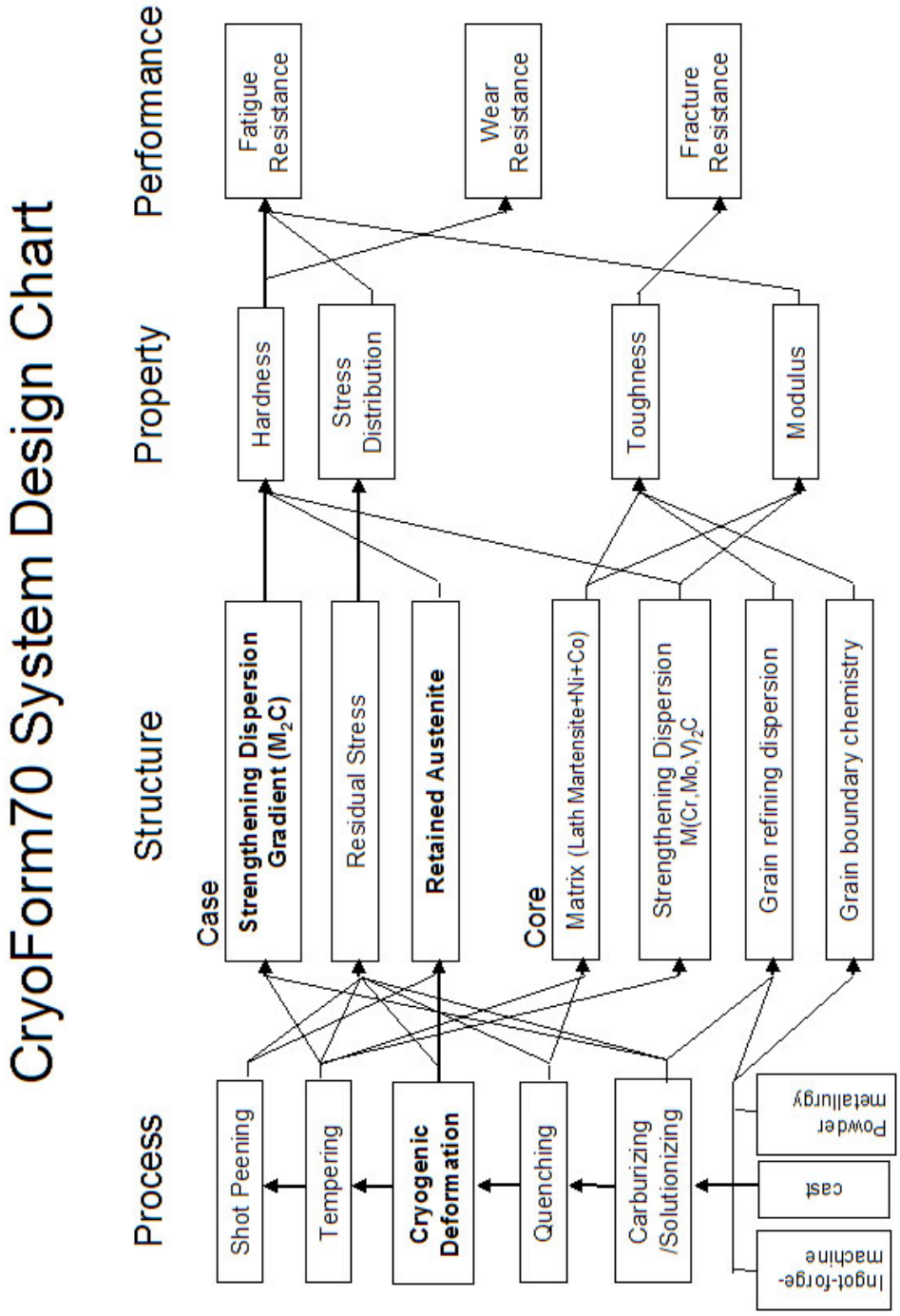

Figure 5.2. System design chart for CryoForm 70

5.3.2. Core microstructure

5.3.2.1. Matrix. Ni-Co secondary hardening steel systems were selected for the design of CryoForm 70 due to their superior strength, toughness and extraordinary fatigue performance. The matrix of a Ni-Co secondary hardening steel is composed of tempered lath martensite with Ni and Co in solid solution. The martensite structure is generated when the steel is quenched from the parent austenite phase. Along with martensite transformation, a high density dislocation is produced and provides high strength and resistance to crack propagation. Among two morphologies of martensite, lath martensite provides higher strength and toughness than plate martensite and thus is more desirable. To maximize the formation of lath martensite, a M_s temperature of at least 300 °C is required. Past research has shown that a higher M_s has already been realized in Ferrium C61 and C67 steels. Thus to promote lath martensite formation in the core, the core M_s for CryoForm 70 is desired to be 350 °C.

Ni helps improve cleavage resistance in the martensite matrix. Tempered martensite matrix has a distorted BCC structure with c axis elongated and tends to fracture on (100) planes. Using quantum mechanical methods, it was reported by Krasko and Olson that the presence of Ni at or near the surface increases the surface energy of Fe on (100) planes [**91**]. This surface energy increase results from the increase of the ferromagnetic term contributing to the total surface energy. Thus the energy for the brittle separation on (100) planes rises.

Co is the element hindering dislocation recovery in the matrix [**92**]. Dislocation density and structure are quite important for the precipitation of fine M_2C strengthening carbides. A fine carbide dispersion not only strengthens the matrix efficiently but also

promotes higher toughness. M_2C carbides nucleate heterogeneously on dislocations, grain boundaries and ferrite/martensite interfaces. To ensure a fine carbide dispersion, a high dislocation density is needed at early tempering times to provide a large concentration of nucleation sites. However, self-diffusion of Fe leads to dislocation climb, which aids dislocation recovery. The addition of Co can increase the short-range ordering, which reduces the self-diffusion of Fe. Thus Co acts as an inhibitor to dislocation recovery and promotes the fine precipitation of M_2C carbides.

5.3.2.2. Strengthening dispersion. The strengthening dispersion employed in Ni-Co secondary hardening steels are M_2C carbides. As W is a slow diffusing element, it will not be considered in our design. M_2C carbides precipitate during stage IV tempering in the temperature range of $400 \sim 600\,^{\circ}\mathrm{C}$. Before they precipitate, most of the carbon is partitioned in the cementite phase Fe_3C, a coarse dispersion detrimental to fracture toughness and limiting the achievable strength. Fe_3C is kinetically favorable as only carbon diffusion is needed for its formation. Fortunately, it is less stable compared to M_2C carbides. As M_2C precipitation continues, Fe_3C gradually dissolves. More stable carbides M_6C and $M_{23}C_6$ will precipitate when tempering is extremely prolonged. The presence of these carbides causes toughness loss as they precipitate incoherently on interfaces. Thus an optimum tempering time is desired to fully dissolve the cementite phase but form only M_2C carbides.

The mechanism of strengthening relies on how these particles interact with dislocations in the matrix. When a dislocation meets with a particle, it will either shear through the particle or bypass it by bowing. When the particle is small so it still keeps its coherency with the matrix or the particle is soft - having a low elastic modulus, the shear mode

dominates. As the particle grows, the possible loss of coherency and the increase in size make the shearing more difficult. At a critical size, the dislocation can not shear the particle any more and it will bypass the particle by bowing around it, which is called *Orowan bypass*. During the bypassing, the central part of the dislocation is pinned by the particle but the two end segments are free to glide continuously and they combine with each other after circumventing the particle. The combined two segments become one, leaving a dislocation loop around the particle. The Orowan bypass becomes easier as the particle continues to grow at a constant volume fraction. Thus, as a precipitate grows, the strength first increases since shearing becomes more difficult with particle size increasing. At the critical size where the transition from shearing to Orowan bypass occurs, the strength reaches its maximum. Afterwards, the strength begins to decrease as the precipitates coarsen. This two-stage strength evolution during particle growth is illustrated in Fig. 5.3 [**20**]. Past research has shown that for Ni-Co secondary hardening steels, peak hardness occurs at a particle radius of 1.5 nm [**21**]. Thus it is desired to optimize precipitate driving force to achieve this optimal size for maximum strength.

5.3.2.3. Grain refining dispersion. Grain refining dispersions are particles undissolved during the solutionizing process, including carbides, nitrides and carbonitrides. With a size scale of $0.1\mu m$, they pin the grain boundaries to prevent grain growth during high temperature processing and thus help promote strength and toughness. However, one disadvantage of having these dispersions is that they can nucleate microvoids similar to primary inclusions. Primary inclusions are usually oxides and sulfides and some rare earth compounds. They are on the scale of $1\mu m$, weakly bonded to the matrix and easily

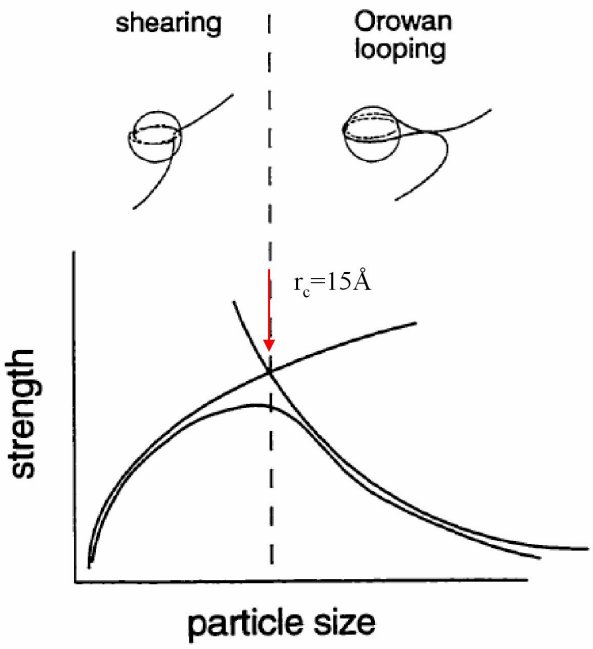

Figure 5.3. Strength evolution during precipitation as a function of particle size with a constant volume fraction [**20**]

nucleate voids. Under both monotonic and cyclic loading, the existence of primary inclusions accelerates the coalescence of microvoids and the ductile fracture. With clean steel technology, primary inclusions are greatly diminished and thus grain refining dispersions play a more important role in affecting fracture toughness. Fortunately, the grain refining dispersions are strongly bonded to the matrix and a much greater strain is needed for them to debond and generate microvoids. It has been reported that fine dispersions are less likely to produce microvoids [**93**]. Thus fine submicrion grain refining dispersions are desired in the design of CryoForm 70. Trace amount of titanium carbides are utilized for this purpose.

5.3.2.4. Grain boundary chemistry. Intergranular fracture is one of the common failure modes for high temperature materials due to the breaking of atomic bonds at

grain boundaries. After a crack is initiated whether within the grains or along grain boundaries, it finds its propagating route with lowest energy. If the energy to break atomic bonds at grain boundaries is lower than to emit dislocations within grains, the crack will propagate along grain boundaries and finally lead to the intergranular fracture. For high strength steels, embrittlement is often associated with tempering because element diffusion toward and away from grain boundaries during tempering can significantly alter local compositions and the fracture characteristics at grain boundaries.

The energy needed for atomic bonds to break and grain boundary to cleave is usually denoted as 2γ, *work of separation*, accounting for the energy change of two sides of the interface. With the introduction of solute atoms to the grain boundary, the work of separation is affected because this particular solute has the affinity of either residing at an interface or staying at a free surface. Thus the free energy of segregation to a grain boundary, Δg_{gb}, and to a surface, Δg_s, influence the work of separation according to:

$$2\gamma = 2\gamma_0 - (\Delta g_{gb} - \Delta g_s)\Gamma \tag{5.1}$$

$2\gamma_0$ is the work of separation for a solute-free grain boundary, Γ is the impurity composition at the grain boundary. If an element has the affinity of staying at the surface, meaning $\Delta g_{gb} - \Delta g_s > 0$, the work of separation will be decreased. Thus grain boundary debonding becomes easier and the material toughness is reduced.

Denote $\Delta E = \Delta g_{gb} - \Delta g_s$. Measuring ΔE for various solute elements experimentally has had limited success. To study effects of P, S, C and B on grain boundary cohesion, Wu determined ΔE for these elements using first principle calculations by the full potential linearized augmented plane wave (FLAPW) method [**94**]. It was found that P and S

produce positive ΔE and are grain boundary embrittlers, while C and B increase 2γ by generating a negative ΔE and help improve grain boundary cohesion. This finding agrees well with the experimental data of embrittlement sensitivity, which was measured as the change in intergranular ductile-brittle transition temperature resulting from the solute segregation to the grain boundary. Fig. 5.4 shows the correlation between theoretical calculations and experimental results.

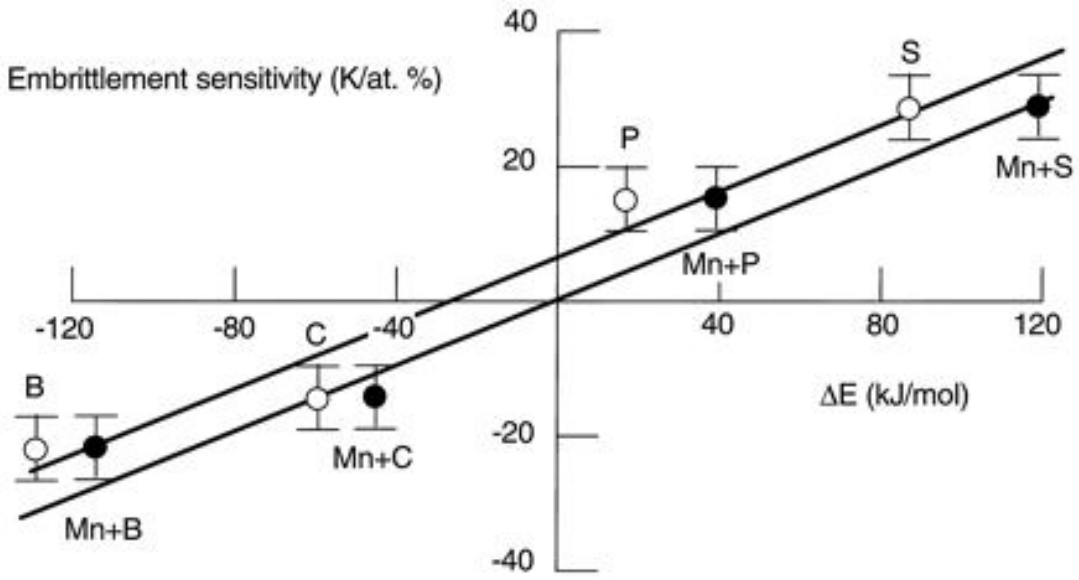

Figure 5.4. Embrittlement sensitivity of solute atoms

For many years, the addition of a small amount of B is known by empiricism to help improve fracture toughness. Clean steel technology is developed to reduce the levels of P and S. Elements La and Ce are also added to getter P and S in steels.

5.3.3. Case microstructure

5.3.3.1. Dispersion gradient. As the carbon content gradually decreases from the case surface to the core, a gradient of strengthening dispersion is generated. The surface carbon

content is constrained to maintain the stoichiometry with the carbide formers to ensure only M_2C carbides can form. Excess carbon results in the formation of coarse cementite and leads to the reduction in fatigue strength [**20**].

The introduction of carbon drives the case M_s temperature down. The addition of alloying elements often affect the case M_s as well. One way to increase case M_s is to reduce the amount of Ni, which conflicts with the objective of improving core toughness. To ensure a lath martensite structure in the case, a M_s of 150 °C is normally required for high strength gear steels. However, to achieve 70 Rc surface hardness, a large amount of carbon is needed. To allow this, the CryoForm 70 design lets the case M_s be reduced to $50 \sim 100$ °C. The high carbon content not only results in a mixed case matrix of lath and plate martensite but also retains a significant amount of austenite after quenching. Unfortunately, there is no other alternative of utilizing less carbon to achieve that high surface hardness. Thus in the design of CryoForm 70, the key concept is to employ novel processing is to promote martensite in the case. A special process of cryogenic deformation is developed to minimize the retained austenite level prior to tempering.

5.3.3.2. Residual stress. Besides generating a strengthening dispersion gradient in the case, carburizing also imparts compressive residual stress at the surface, which benefits the case fatigue strength. The amount of this beneficial compressive residual stress is limited by relaxation during tempering. Thus shot peening is applied to produce residual stresses at both surfaces and subsurfaces. Compressive residual stresses help enhance fatigue performance by retarding the fatigue crack initiation and propagation. Carburizing needs optimization to avoid quench cracking due to improper residual stress. The optimization of shot peening is desired to obtain beneficial residual stresses.

5.3.3.3. Retained austenite. Retained austenite is not desired in the case since its presence reduces the strengthening dispersion nucleation sites and decreases the achievable strength. However, it is expected to exist in the case of CryoForm 70 even after cryogenic treatment due to the high carbon content. Fortunately, it is established that the amount retained austenite in high strength gear steels can be reduced by shot peening [**29, 30, 31, 32**]. One example is shown in Fig. 2.12. The reduction in retained austenite is due to the high Hertzian stress produced through the dynamic compressive loading during shot peening. With sufficient shear stress applied to the habit planes, austenite is transformed to martensite since this transformation is diffusionless. This behavior provides an alternative way of taking advantage of mechanical stress to induce martensite transformation. An appropriate deformation process, such as shot peening, can help minimize the retained austenite level in the case of CryoForm 70. If the deformation is combined with cryogenic treatment, more reduction in retained austenite is anticipated. Thus the process of *cryogenic deformation* is proposed prior to tempering to promote the case martensite structure in highly alloyed compositions.

5.4. Design models

5.4.1. Driving force and martensite transformation kinetics

To promote the case martensite structure, it is necessary to look into the driving force of martensite transformation and to explore how much martensite can be obtained with certain amount of driving force. Two major driving forces, thermal driving force and mechanical driving force, are discussed herein. Theoretical predictions for resulting martensite volume fraction is also presented.

5.4.1.1. Thermal driving force. The thermal driving force for martensite transformation is the chemical free energy difference between martensite phase and the parent austenite phase. This driving force is denoted as ΔG_{chem}. With defined steel compositions, the free energy of martensite and austenite phases can be calculated based on thermodynamic principles.

$$\Delta G_{chem} = G_{BCC} - G_{FCC} \tag{5.2}$$

Effort has been made to predict the volume fraction of martensite from the temperature difference between quenchant and M_s. Harris and Cohen, Koistinen and Marburger estimated the martensite level for athermal transformation according to the temperature interval below M_s, ΔT [**95, 96**].

$$f = 1 - 6.956 \times 10^{-15}[455 - \Delta T]^{5.32} \tag{5.3}$$

$$f = 1 - exp(-(1.10 \times 10^{-2}\Delta T)) \tag{5.4}$$

where ΔT is in °C. Both relationships focused on the alloys with $M_s > 100\,°C$. Harris and Cohen's equation is valid for carbon and low alloy steels, with carbon contents up to 1%. Thus it is not intended for high alloy steels. Koistinen and Marburger's expression was derived from data on the amount of retained austenite in a number of carbon steels and has not been examined over a wide range of compositions. Since CryoForm 70 is designed for $M_s < 100\,°C$, transformation kinetics for low M_s alloys were reviewed. According to Magee [**97**], the volume fraction of martensite depends on the driving force gain over the critical driving force. The critical driving force is the ΔG_{chem} at M_s, at which martensite just starts forming and the volume fraction of martensite is very close to 0. Simplifying

Magee's expression of martensite volume fraction gives:

$$f_{mar} = 1 - exp(k(\Delta G - \Delta G_{crit})) \tag{5.5}$$

where k is a material constant. This relationship is used to predict the martensite level after different processes and assist the process design.

5.4.1.2. Mechanical driving force. Mechanical stress is the second source for martensite transformation. Olson, Tsuzaki and Cohen investigated the mechanical driving force distribution for the transformation with applied stress [**98**]. It was derived that under a uniaxial stress σ, the mechanical driving force Δg^{σ}, is dependent on orientation and can be expressed by:

$$\Delta g^{\sigma} = \frac{\sigma}{2}[\gamma_0 \sin 2\theta \cos \alpha + \varepsilon_0(1 + \cos 2\theta)] \tag{5.6}$$

where γ_0 and ε_0 are the transformation shear and normal strains, θ is the angle between the stress axis and the habit normal, α is the angle between transformation shear direction and the maximum shear stress direction on the habit plane. For a random orientation distribution they derived the relation [**99**]:

$$\Delta g^{\sigma} = -[0.7183\sigma + 6.85\Delta V/V\sigma_h - 185.3(1 - exp(-0.003043\sigma))] \tag{5.7}$$

where $\sigma_h = 1/3\sigma$ for uniaxial stress and $\sigma_h = 2/3\sigma$ for biaxial stress.

The additional martensite transformation resulted from the applied mechanical stress can also be predicted using Eq. 5.5. Thus the expected total volume fraction of martensite can be theoretically calculated.

5.4.2. Precipitation strengthening

The strengthening efficiency of precipitation depends on various factors, including particle size, precipitate volume fraction, the chemical and mechanical properties of particles and their coherency with the matrix.

5.4.2.1. M_2C precipitation strengthening. At the early stage of tempering, the shearing mechanism dominates the interaction between particles and dislocations. Surface energy, coherency strain, modulus misfit, stacking fault and ordering all contribute to the strengthening. When the particle is sheared, additional surface area is exposed. Dislocation movement is hindered as the elastic strain field from the coherency with the matrix interacts with the strain field of dislocation. In response to modulus misfit, the line energy of dislocation changes. After reviewing several quantitative models for shearing strengthening, Wise recommended Nembach's model for coherency strengthening and Hornbogen's model for modulus strengthening [**20**].

At the late stage of tempering, M_2C precipitates grow bigger than the critical size and the Orowan bypass mechanism dominates, which is often the case when a long tempering time is applied to fully dissolve the coarse cementite. The Orowan bypass strengthening model takes into account: 1) the energy needed for dislocation bending which depends on dislocation line tension and spatial distribution of obstacles; 2) the influence from neighboring dislocations, including both edge and screw dislocations; 3) the effect of particle size on the particle spacing. The final model is [**20**]:

$$\Delta\tau = K\frac{Gb}{2\pi\sqrt{1-\nu}(L-2r)}\ln\frac{2r}{r_0} \tag{5.8}$$

where L is center to center distance between obstacles and $L = r(\frac{2}{f})^{1/2}$. f is the volume fraction of precipitates which depends on the carbon content of steels, r is the obstacle radius, G is the matrix modulus, b is the dislocation Burger's vector in the matrix, ν is Poisson's ratio, and r_0 is dislocation core radius. K is a prefactor.

Wise studied the strengthening effect in the model 1605 alloys under overaged condition [**20**]. With the substitution of calculated solid solution strengthening and cementite strengthening, he found a prefactor of 1.71 by correlating experimental strength gain from M_2C precipitates with theoretical values. By combining terms, the Orowan model yields:

$$\Delta\tau = K\frac{Gb}{2\pi\sqrt{1-\nu}(L-2r)}\ln\frac{2r}{r_0} = (0.8-1.0)\frac{Gb}{L-2r} \tag{5.9}$$

where the new prefactor $0.8 - 1.0$ describes the overaged condition corresponding to an average particle radius r equal to or larger than 1.5 nm.

5.4.2.2. Total strength in Ni-Co secondary hardening steels. The total strength of Ni-Co secondary hardening steels consists of strength from precipitates (τ_p) and strength from the matrix. The matrix strength is composed of solid solution strengthening (τ_{ss}), dislocation strengthening (τ_D) and strength from lath martensite matrix ($\tau_{\alpha'}$). After reviewing available strengthening models and finding material constants and prefactors from the experimental data of model 1605 alloys, Wise expressed the total strength as the linear superposition of all four components [**20**]:

$$\tau = \tau_p + \tau_{ss} + \tau_D + \tau_{\alpha'} \tag{5.10}$$

Since $\tau \propto \Delta H$, we have

$$\Delta H_{p,shear} = 0.65 \frac{Gb}{L-2r}\left(\frac{G_p r}{2\pi Gb}\right) \tag{5.11}$$

$$\Delta H_{p,Orowan}(M_2C, Fe_3C) = 1.68 \frac{Gb}{2\pi\sqrt{1-\nu}(L-2r)} \ln\frac{2r}{r_0} \tag{5.12}$$

$$\Delta H_{ss} = 0.0078G(|\varepsilon'_G| + 2|\varepsilon_a|)^{4/3} c^{2/3} \tag{5.13}$$

$$\Delta H_D = 0.38Gb\sqrt{\rho} \approx 145 - 60(V/V_f)_{M_2C}(VHN) \tag{5.14}$$

$$\Delta H_{\alpha'} = \tau_\alpha + kd^{-1/2} \approx 65(VHN) \tag{5.15}$$

The solid solution strengthening originates from the size and elastic modulus misfit between solutes and the matrix. It also depends on the concentration of solute atoms, such as Co, Ni, Cr and Mo. In the equation, c is the solute concentration, ε'_G and ε_a are modulus and size misfit parameters, respectively. Dislocation strengthening is determined mainly by dislocation density ρ. 145 VHN is the initial strength from dislocation substructure, estimated from data on model 1650 alloys. As dislocations recover during tempering, the total dislocation strengthening decreases. The reduction in dislocation strengthening can be expressed as the recovery rate constant (60) correlated to the precipitation state index - V/V_f. V/V_f is the ratio of current precipitate volume fraction over final volume fraction at equilibrium. With known V/V_f, the total dislocation strengthening can be estimated. Finally, the tempered martensite strength increases as grain size decreases and is estimated to be 65 VHN for typical secondary hardening lath martensitic steels.

Compared to precipitate strengthening, strength from the matrix is only a minor contributor. Total strength can be computed as analytical curves versus carbon content,

as shown in Fig. 5.5 [**20**]. Precipitate diameter and volume fraction which depends on the carbon content are the two major factors controlling the total strength. Ideally, peak hardness is reached as the particle diameter is at the optimum of 3 nm. However, typical commercial steel alloys all present a precipitate larger than 3 nm and thus a drop in the total strength is observed. Thus in the design of CryoForm 70, precipitate size is a critical parameter to be determined.

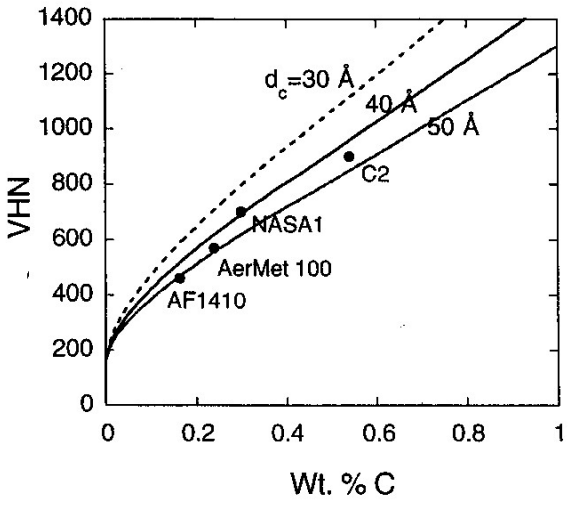

Figure 5.5. Total strength versus carbon content for Ni-Co secondary hardening steels [**20**]

5.4.3. Driving force for sigma-phase precipitation

Doctoral research of J. Wright showed that C69 steel suffered core brittleness after prolonged tempering. APFIM study was performed to investigate core microstructure and the σ-phase was identified to be the root cause of core brittleness [**9**].

The sigma-phase typically forms after long aging times at lower temperatures. Its chemical formula is $(Fe, Ni)_3(Cr, Mo)_2$, with the composition of 61at% Fe, 26at% Cr,

7at% Mo and 5at% Ni. It belongs to the intermetallic phase family with a complex structure (space group No. 136, P42/mnm) [**100**]. The unit cell contains 30 atoms, which are distributed into five inequivalent sublattices. This phase is very brittle and stable once it forms. It deteriorates mechanical properties by providing more crack initiation sites [**100**] and corrosion resistance by removing Cr and Mo from the matrix [**101**].

A high concentration of Cr and Mo promotes the precipitation of sigma-phase [**100, 101**] and thus it is often observed in duplex stainless steels and austenitic stainless steels. The sigma-phase preferentially nucleates at the pre-formed $M_{23}C_6$ carbides [**102**] and thus the existence of $M_{23}C_6$ strongly accelerates its precipitation. Similar effects were also found with Cr_7C_3 carbides [**103**]. Study on a W-containing duplex stainless steel revealed that the substitution of W to Mo delayed the sigma-phase precipitation by reducing its driving force [**104**]. Analysis of sigma-phase kinetics also shows its formation depends on the availability of high energy nucleation sites as well as on the driving force [**105**].

To eliminate the possible formation of sigma-phase in CryoForm 70, the driving force of sigma-phase must be calculated and limited. Besides Cr, Mo in the steel, Co also acts as a promoter for sigma-phase precipitation. The calculation can be performed using Thermo-Calc with an appropriate database. QuesTek Innovations, Inc. has developed a proprietary database for the control of sigma-phase. Through collaboration with QuesTek, sigma-phase driving force was successfully calculated for Ferrium C67 steel and designed CryoForm 70 prototypes.

5.4.4. Simulation aided carburizing process design

Controlling the carburizing process is essential for the design of case hardened steels. A proper carbon content profile and strengthening gradient in the case directly determines the success of the design. Heat treaters often rely on empiricism to develop carburizing cycles as large amount of carburizing data exists for ordinary steels. Simulation aided carburizing process design has been utilized to assist the achievement of desired carbon content profiles and steel properties in new steels. High temperature carburizing (above 1000 °C) is desired so the carburization and solution treatment can be combined into one step. The carburizing temperature is raised to shorten the total carburizing time for cost reduction.

The simulation starts with solving Fick's second law for cabon diffusion.

$$\frac{\partial C_c}{\partial t} = \frac{\partial}{\partial x}(-J_c) \tag{5.16}$$

where C_c is carbon concentration, J_c is the flux of carbon. In a multicomponent system, J_c follows Fick's first law:

$$J_c = -\sum_{j=1}^{n-1} D_{1j} \frac{\partial C_j}{\partial x} \tag{5.17}$$

where j is the index of component, 1 is carbon and 2 to n-1 represents other substitutional alloying elements. The effect of interstitial elements on the flux of carbon is negligible and thus interstitial element terms are not included in the sum. When carbon only diffuses in the FCC phase, the concentration gradient of substitutional elements can be assumed to be zero because long range diffusion of these elements hardly occurs with a small carbon

gradient. Thus, Eq. 5.17 can be simplified to:

$$J_c = -D_{11}\frac{\partial C_c}{\partial x} \tag{5.18}$$

where D_{11} strongly depends on the carbon concentration.

On the other hand, carbon diffuses more slowly as the amount of Co increases in the steel. This effect appears more prominent in Ni-Co secondary hardening steels as much Co is included in the alloy to retard dislocation recovery. To accurately simulate carbon diffusion, Wise studied the carbon diffusion in Fe-Ni-Co alloys and extracted carbon diffusion coefficients from the experimental carbon profiles in 20Co-10Ni model alloys [**20**]. He then modified the carbon-cobalt binary interaction parameters in the DICTRA kinetic database. The final carbon diffusivity in the database was adjusted down to the experimental level. The general trend of carbon diffusivity increasing with increased carbon content was still maintained.

To investigate the response of C61 and C67 steels to high-temperature carburizing, Gao used the CBPWIN2 code (ECM-USA) for one dimensional carbon diffusion with temperature dependent diffusion coefficients [**7**]. He also simulated 2D and 3D diffusion using DEFORM HT (Scientific Forming Technologies Corporation) with diffusion coefficients dependent on both temperature and composition. The carbon diffusivity used in DEFORM HT as well as the activation energy and pre-exponential diffusion coefficient (D_0) used in CBPWIN2 were calculated using DICTRA. Compared to CBPWIN2 and DEFORM HT, DICTRA can not only account for the temperature and composition dependence of carbon diffusivity but also simulate the variable carbon flux with time. Thus DICTRA is the major tool employed to design the carburizing process for CryoForm 70.

In practice, to avoid the formation of primary carbide networks during the boost cycle of carburization, a carbon content of 3wt% was set to be the maximum. An average carbon flux was utilized as the boundary condition to simplify the simulation without sacrificing too much accuracy. Both FCC and carbide phases were taken into account during carburization. Compositions of FCC and carbide phases were calculated using Thermo-Calc and imported into DICTRA. Since the prototype has a simple puck geometry, 1D diffusion cells were used in the simulation. It is assumed that carbon was the only diffusing element and the diffusion only occurred within the FCC phase.

CHAPTER 6

Design Synthesis

6.1. Design parameters

Design parameters are established to accomplish desired steel structure and properties with acceptable processes. In Chapter 5, design objectives for the case and core materials have been specified. To achieve the hardness goal, case M_2C driving force needs to be maximized to obtain fine strengthening dispersions. A lath martensite matrix is desired to provide M_2C nucleation sites. Although a case M_s temperature as high as possible is normally wanted, it is planned that the case M_s in CryoForm 70 could be pushed down to 50 °C to accommodate the high carbon and alloy content for extreme case hardness. Thus the case M_s of $50 - 100$ °C is desired for the design. A diffusional rate constant for carbide precipitate is used to control fast precipitation. Finally, the case solution treatment temperature, above which the steel system is fully austenite, should not be higher than 1100 °C for easy processing and reasonable cost.

A Core M_s greater than 300 °C is desired to form a lath martensite matrix for core toughness. To avoid core embrittlement, the sigma-phase driving force in the core should not be greater than that in sigma-phase-free C67 prototype. Overall, limited segregation should occur during solidification. Thus the fraction of microsegregation for each element in CryoForm 70 should be below the level in C67 steel. Design parameters are listed in Table 6.1.

Table 6.1. Design parameters for CryoForm 70

	C61	C67	**CryoForm 70**
M_2C DF Case (kJ/mol)	29	29	**Max**
M_s Case (^{o}C)	137	146	**>50**
M_s Core (^{o}C)	279	400	>300
Sigma DF Core (kJ/mol)	----	2.8	<2.8
Precipitation Rate Constant (s/(m^2*(J/mole)))	----	4.5E-28	4.5E-28
T_s Case (^{o}C)	1000	1050	1100

6.2. CryoForm70 composition design

Computational composition design for CryoForm 70 was carried out following four steps. First, the desired carbon content for 70 Rc case hardness was set based on the total strength model in which total hardness is quantitatively correlated to carbon content. Second, after preliminarily setting carbide former concentrations according to the M_2C stoichiometry, the concentrations of Ni, Co substitutional elements were determined for a combination of high case M_s temperature and low core sigma-phase driving force. Third, the relative concentrations of Cr, Mo and V carbide formers were refined to achieve the maximum M_2C driving force with the constraint of reasonable solution treatment temperature. Phase status was also studied using Cr-Mo-V pseudo-ternary phase diagram to ensure that no phase other than FCC is present at the solution treatment temperature. Finally, the Ni, Co contents were re-optimized to accommodate the change in carbide former concentrations. Iterating through this sequence defines an overall composition balancing all design parameters for optimal performance. This composition design process is described in the flow chart below. (Fig. 6.1)

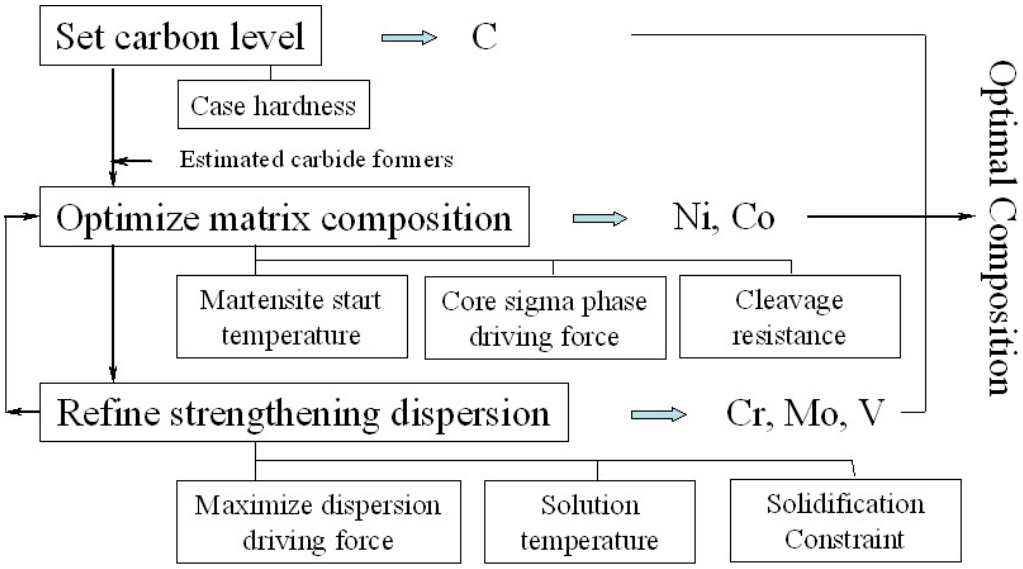

Figure 6.1. Composition design flow chart for CryoForm 70

6.2.1. Carbon content

From the total hardness dependence on carbon content, principally the carbon content for both the case and the core can be determined according to the hardness goals. In Wise's total strength model, it was assumed that the volume fraction of strengthening dispersions was the volume fraction at the final equilibrium. However, the kinetics of M_2C precipitation showed that it takes 100 hours or longer for the precipitation to reach final equilibrium. With practical tempering time, about 80% M_2C of the final volume fraction forms. Thus the total hardness was re-calculated with $V/V_f = 0.8$ and computed versus carbon content in Fig. 6.2.

It is apparent that peak hardness occurs with optimal particle radius of 1.5 nm. However, Wise had shown in Fig. 5.5 that typical secondary hardening steels (AF1410, AerMet 100, NASA1 and experimental alloy C2) obtained a precipitate radius of 2 nm or larger at a high precipitation level of $V/V_f = 0.8$, and thus total hardness reduction was observed.

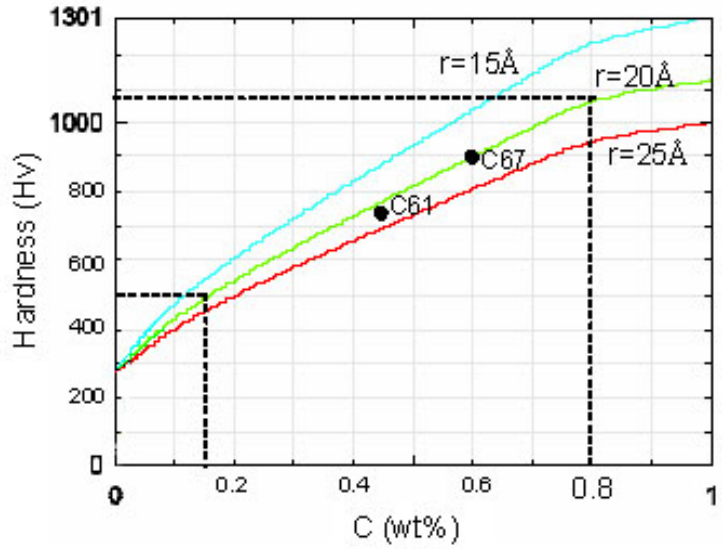

Figure 6.2. Total hardness versus carbon content plot showing desired case and core carbon content for CryoForm 70

Different levels of total hardness with various particle sizes are also plotted in Fig. 6.2 to reflect this trend. To obtain desired case carbon content in CryoForm 70, particle size needs to be calibrated. Compositions and processing parameters of C61 and C67 were input into the strengthening model and the particle size of each was calibrated, as displayed in Fig. 6.2. In the design for CryoForm 70, a similar M_2C particle radius of 2 nm is assumed.

The hardness goal for CryoForm 70 is 1076 Hv (70 Rc) for the case and 500 Hv for the core. Thus from the calibrated strengthening model (Fig. 6.2), a case carbon content of 0.8wt% and a core carbon content of 0.15wt% are needed with a particle radius of 2 nm or smaller. In comparison to C61, C67, an extremely high case carbon content is required. The resulted M_s is expected to be very low and thus special treatment is designed for the processing.

6.2.2. Optimization of matrix

With desired carbon content, Ni and Co concentrations were optimized to achieve required case, core M_s temperatures and sigma-phase driving force. Initially, a rough estimation of carbide former (Cr, Mo, V) concentrations was made for subsequent calculations. According to the stoichiometry of M_2C, the total atomic fraction of carbide formers should be twice the carbon atomic fraction to allow M_2C precipitation only. Experience from the design of C67 families suggested a starting composition of Fe-xNi-yCo-5.2Cr-2.5Mo-0.15V-0.8C for the case.

The first step was to optimize Ni and Co concentrations for a case M_s of $50 \sim 100\,^{\circ}\mathrm{C}$. To calculate M_s for multi-component system, the Ghosh-Olson model for martensite transformation was employed, where systems with low temperature M_s were taken into account. Using the Mart5 database in CMD, the case M_s contours versus Ni and Co concentrations are plotted in Fig. 6.3. For a high M_s, high Co and low Ni concentrations are favored, as shown by the arrow. Approximately 15wt% Co and 3wt%Ni are needed for a M_s of $90\,^{\circ}\mathrm{C}$.

Limiting sigma-phase driving force in the core is another criterion for Ni-Co content optimization. The sensitivity of sigma-phase driving force to element concentrations was first investigated. Fig. 6.4 and 6.5 depicted the dependence of sigma-phase driving force on concentrations of C and all alloying elements in C69M3B model alloy (Fe-Ni-Co-4.9Cr-2.11Mo-0.1V-0.071C) with the tempering temperature of $510\,^{\circ}\mathrm{C}$. C69M3B was chosen as a reference alloy due to its borderline resistance to core brittleness. As sigma-phase is an intermetallic compound composed of Fe, Cr, Mo and Ni, richer carbon decreases sigma-phase driving force by combining more alloying elements to form carbides. High Cr and

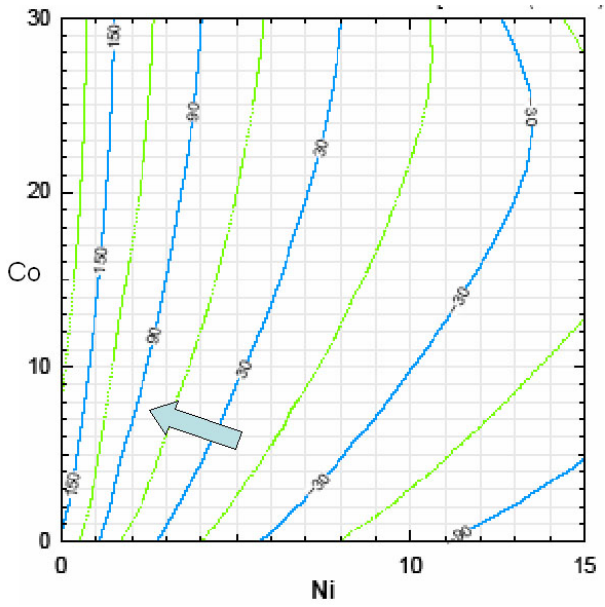

Figure 6.3. M_s contours for Fe-xNi-yCo-5.2Cr-2.5Mo-0.15V-0.8C alloy

Mo concentrations raise the driving force for sigma-phase formation. The addition of Ni and Co increases sigma-phase driving force as well but their effect is weaker. The driving force, however, is quite insensitive to V. There is little room to reduce the amount of Cr and Mo as they are demanded for desired hardness, and the core C level is restricted by core hardness. Thus the minimization of sigma-phase driving force is mainly accomplished through the optimization of Co and Ni concentrations.

Fig. 6.4 b) shows that low Co and Ni concentrations are desired for sigma-phase driving force reduction. However, this conflicts with the goal of case M_s, for which a high Co level is needed. A tradeoff must be made to balance these two requirements and thus a medium Co concentration was selected to meet both criteria.

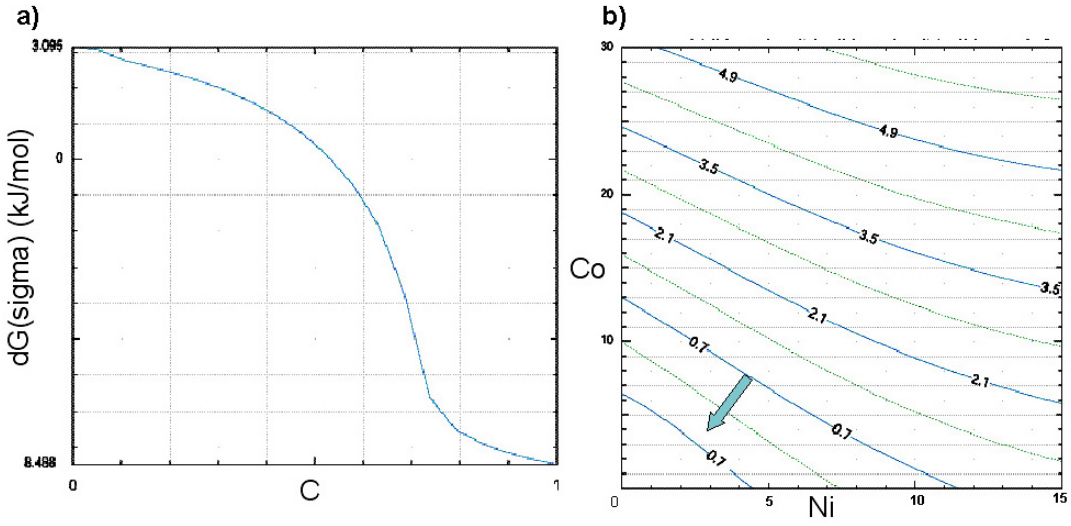

Figure 6.4. Sigma-phase driving force dependence on a)C b)Co and Ni for Fe-Ni-Co-4.9Cr-2.11Mo-0.1V-0.071C alloy

6.2.3. Optimization of strengthening dispersions

The optimization of strengthening dispersions - Cr, Mo and V is aimed at the possible maximum M_2C driving force, possible highest case M_s and a solution treatment temperature lower than 1100 °C. The starting composition for this step is an alloy with medium Co concentration.

Contours of case M_2C driving force, case M_s and solution treatment temperature were calculated and plotted versus element concentrations to explore the effects of Cr, Mo and V. The M_2C driving force was calculated for incoherent M_2C precipitation from a fully supersaturated BCC matrix. An example is shown in Fig. 6.6. M_2C driving force increases toward the Mo-rich corner. Case M_s decreases as Cr increases and it is not sensitive to Mo concentration. Both Cr and Mo raise the solution treatment temperature. To ensure the stoichiometry in the design, a dash line was superimposed in the graph to mark the stoichiometric Cr-Mo content for 0.8wt% C. With the constraint of solution treatment

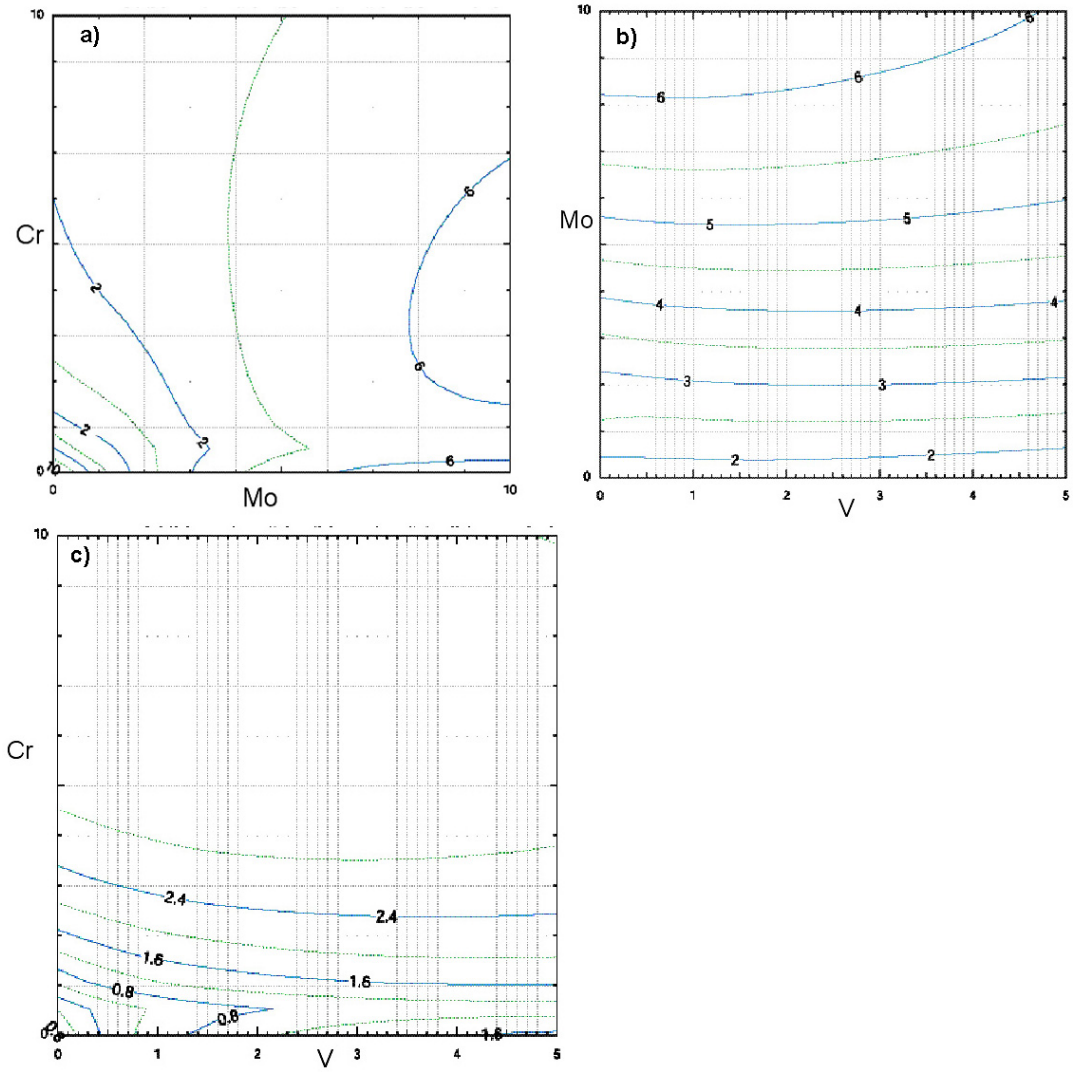

Figure 6.5. Sigma-phase driving force contours versus a)Cr and Mo b)Mo and V c)Cr and V for Fe-Ni-Co-4.9Cr-2.11Mo-0.1V-0.071C alloy

temperature, the circled region along the stoichiometric line was found to provide a M_2C driving force of 28 kJ/mol. To enlarge the area satisfying solution treatment temperature requirement, the concentration of V needs to be decreased as the addition of V greatly increases the solution treatment temperature. That means the concentrations of Cr and Mo should be increased to maintain the stoichiometry. However, the raise in the Cr level

is limited by case M_s and the Mo concentration should not exceed the limit set for alloy's castability. Several iterations were carried out at this step to balance conflicting design criteria. Similar analysis was performed for element pairs of Mo, V and Cr, V.

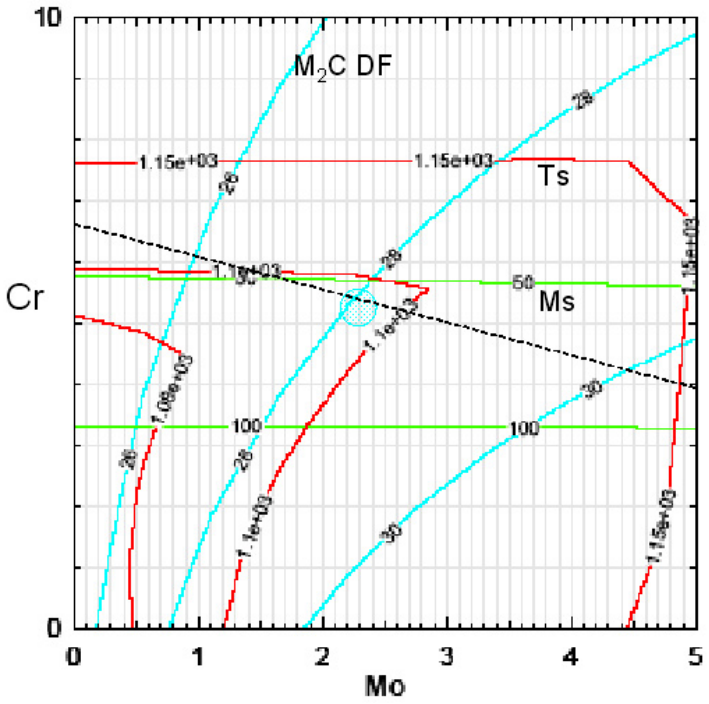

Figure 6.6. M_2C driving force, M_s and solution treatment temperature for Fe-3.7Ni-10Co-xCr-yMo-0.15V-0.8C alloy

Candidate compositions must be examined for their phase status at solution treatment temperature to avoid primary carbides. A pseudo-ternary phase diagram of Cr-Mo-V was plotted at 1100 °C (Fig. 6.7). The diagram is called *pseudo* because the equilibrium tie line compositions can not be determined from the phase boundaries although the phase regions can be identified. The sum of Cr, Mo and V concentrations are set to satisfy the stoichiometry in this diagram. Candidate compositions must fall into the $FCCA1\sharp1$ phase

region. After optimizing concentrations of strengthening dispersions, two good candidates were labeled in the phase diagram to illustrate its validity.

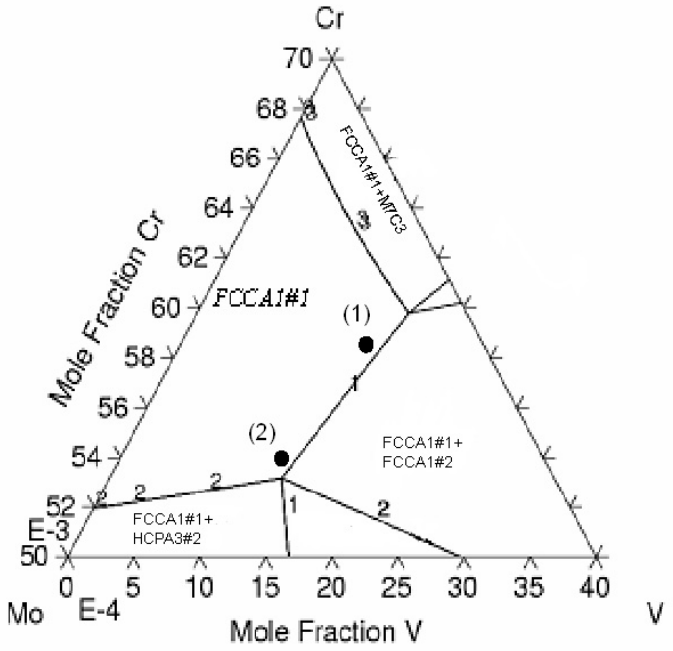

Figure 6.7. pseudo-ternary phase diagram for Fe-3.7Ni-10Co-xCr-yMo-zV-0.8C alloy at 1100 °C

6.2.4. Iterative optimization

Finally, Ni and Co concentrations were re-optimized for case M_s and sigma-phase driving force. If significant composition modification is needed, iterative optimizations are also conducted to refine the strengthening dispersion. Ultimately, we evaluate the overall composition against all design parameters to achieve well balanced properties. Several iterations were performed to achieve the design objectives.

Table 6.2. Compositions and calculated properties of two CryoForm 70 alloys

Compositions

Wt%	Co	Ni	Cr	Mo	V	C-core	C-case
390-1	10	2.57	5.86	1.45	0.27	0.1	0.8
390-2	10	3.73	5.34	2.52	0.21	0.1	0.8

Calculated Properties

	M_2C DF (479°C, kJ/mol)	Hardness –case (Hv)	Hardness –core (Hv)	Ms-case (°C)	Ms-core (°C)	Ts-case (°C)
390-1	27	1047	415	73	378	1100
390-2	28	1067	423	58	350	1098

In addition, the precipitation rate constant was calculated to ensure reasonably fast kinetics of precipitation at desired tempering temperatures. Solidification microsegregation was also checked for each element using the Sheil microsegregation model.

6.3. Summary of designs

The final compositions of two designs, performed in collaboration with an undergraduate MSE 390 Materials Design project team, are listed in Table 6.2. Also tabulated are calculated properties.

Among two compositions, 390-1 presents higher case M_s while 390-2 displays a higher M_2C driving force for a higher case hardness. A case hardness of 1067 Hv and a core hardness of 423 Hv are predicted for 390-2, which meets the hardness goals for this design. However, 390-2 has an extremely low case M_s, which makes the formation of a full martensite matrix more difficult. The weight fraction of microsegregation amplitude in the designed alloys were also calculated and compared to that of the C69M3B reference alloy, shown in Table 6.3. Both designed compositions show a comparable fraction of segregation to that in C69M3B alloy, indicating acceptable microsegregation during solidification.

Table 6.3. Microsegregation of designed CryoForm 70 alloys

	Weight Fraction of Microsegregation Amplitude			
	Cr	Mo	Ni	Co
C69M3B	0.0076781	0.0060108	0.0013812	0.0033780
390-1	0.0096329	0.0048529	0.0024014	0.0067529
390-2	0.0092954	0.0082847	0.0027723	0.0051293

CHAPTER 7

Process Optimization and Characterization of CryoForm 70

Two candidate compositions for CryoForm 70 have been computationally designed based on thermodynamics and strengthening models. They both have higher carbon level and higher concentration of strengthening precipitate formers compared to compositions of C67 steels. To avoid possible core brittleness, the concentration of Co was reduced to 10wt% in CryoForm 70. Due to the higher amount of several M_s reducers, CryoForm 70 presents a much lower case M_s than that in C67. Between the two candidate compositions 390-1 and 390-2, the latter was chosen for prototype because of its relatively higher M_2C driving force, higher predicted case hardness and less solidification microsegregation.

Prototype alloys were processed following the proposed processing in the system design chart in Chapter 5. Three processes need to be optimized for desired properties: carburization, cryogenic deformation and tempering. An optimal carburizing procedure was first determined with the assistance from DICTRA simulation for the desired 0.8wt% surface carbon. The cryogenic deformation process was designed and optimized for improved case martensite structure. With theoretical prediction on attainable case martensite volume fraction, several means of cryogenic deformation were explored experimentally and one was employed for the final implementation. A cyclic tempering procedure was developed to maintain the martensite matrix promoted through cryogenic deformation. Microstructure characterization and hardness tests were performed after process optimization.

7.1. Prototype fabrication

Prototype CryoForm 70 core material was produced following a typical commercial processing route for high strength gear steels. Two 15-pound ingots were first cast using combined Vacuum Induction Melting (VIM) and Vacuum Arc Re-melting (VAR) with high purity materials at Special Metals Corporation in New Hartford, New York. Trace amounts of Ti (0.015wt%) and La (0.030wt%) were added to refine grains and getter impurities such as P and S, respectively. Ingots were then shaped into appropriate geometries for easy specimen sectioning at the Technology Processing Center of Special Metals in Huntington, West Virginia (also known as Huntington Alloys). There ingots were first homogenized at 1250 °C for 12 hours, hot rolled to 0.6" thick plate at 1050 °C and air cooled to room temperature. The plates were then normalized at 1050 °C for 1 hour and aired cooled again to room temperature. Finally, the plates were annealed at 700 °C for 2 hours to relieve residual stress and soften the plate for machining.

7.2. Core martensite start temperature

The core M_s temperature of the CryoForm 70 prototype was first measured using dilatometry. As shown in Fig. 7.1, a core M_s of 350 °C was obtained, which is very consistent with the theoretical prediction (350 °C). This validates the Ms design and supports feasibility for further process optimization.

7.3. Carburization

With the validation from core M_s measurement for the design, carburization optimization was first performed to achieve the desired 0.8wt% surface carbon content. Both pack

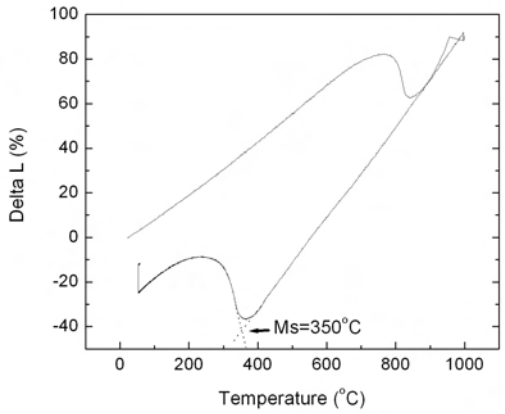

Figure 7.1. Dilatometry measurement showing core M_s for CryoForm 70 prototype

and vacuum carburizing were tested and vacuum carburizing was finally chosen for full optimization because of its controllable accurate carbon profiles produced.

7.3.1. Pack carburizing

Preliminary pack carburizing was carried out at Northwestern University to initially assess the feasibility of the CryoForm 70 prototype. DICTRA was utilized to simulate the process and resulting carbon content from DICTRA was compared with experimental results.

Prototype alloys were sectioned into small rectangular bars ($12 \times 12 \times 6mm^3$) and pre-oxidized at 900 °C for half an hour to form a thin porous iron oxide layer. Air cooled samples were packed into a mixture of 85% charcoal and 15% Calcium Carbonate in stainless steel bags. The bags were then closed with an open slit for gas venting. Samples were pack carburized at 975 °C, 1025 °C and 1075 °C for various times (0.5 hour, 1 hour, 1.5 hours, 2 hours and 3 hours). After bags containing samples were air cooled, samples were taken out and cleaned. Since it is impossible to directly quench samples from pack

carburization, they were subsequently encapsulated and solutionized at 1100 °C for 0.5 to 1 hour, followed by oil quenching and cryogenic treatment in liquid nitrogen for 1 hour. An Argon furnace was used for solutionizing if samples were larger than the size of encapsulating tube. This step dissolved primary carbides that formed during carburization as the carburizing temperature was far below the designed solutionizing temperature. A final tempering at 200 °C for 1 hour was subsequently performed before microstructure observation and preliminary hardness testing.

Hardness profiles under various carburizing conditions are plotted in Fig. 7.2. As carburizing temperature increased, an increase in peak hardness was first observed, followed by a drop. The increase results from increased dissolved carbon content and the drop was due to the formation of large amount of retained austenite. Also noted is that the variation in peak hardness is not so sensitive to the temperature increase and peak hardness varies around an average value of 750 Hv. As carburizing time was prolonged, maximum hardness evolved in a similar manner. At 1025 °C, hardness at depths up to 1000μm was first raised and then dropped to the original level. The hardened case depth, however, was increased monotonically with longer carburization. Among all conditions, carburization at 1025 °C for 1.5 hours seems to produce the highest maximum hardness. Due to the presence of retained austenite, it is difficult to select the best condition according to just peak hardness.

To better assess carburizing conditions, carbon content was both estimated based on the experimental correlation between hardness and carbon content [**106**] and measured using Optical Emission Spectroscopy (OES) by Bodycote Materials Testing in Skokie, Illinois. Results are shown in Fig. 7.3. Also plotted are simulated carbon content profiles

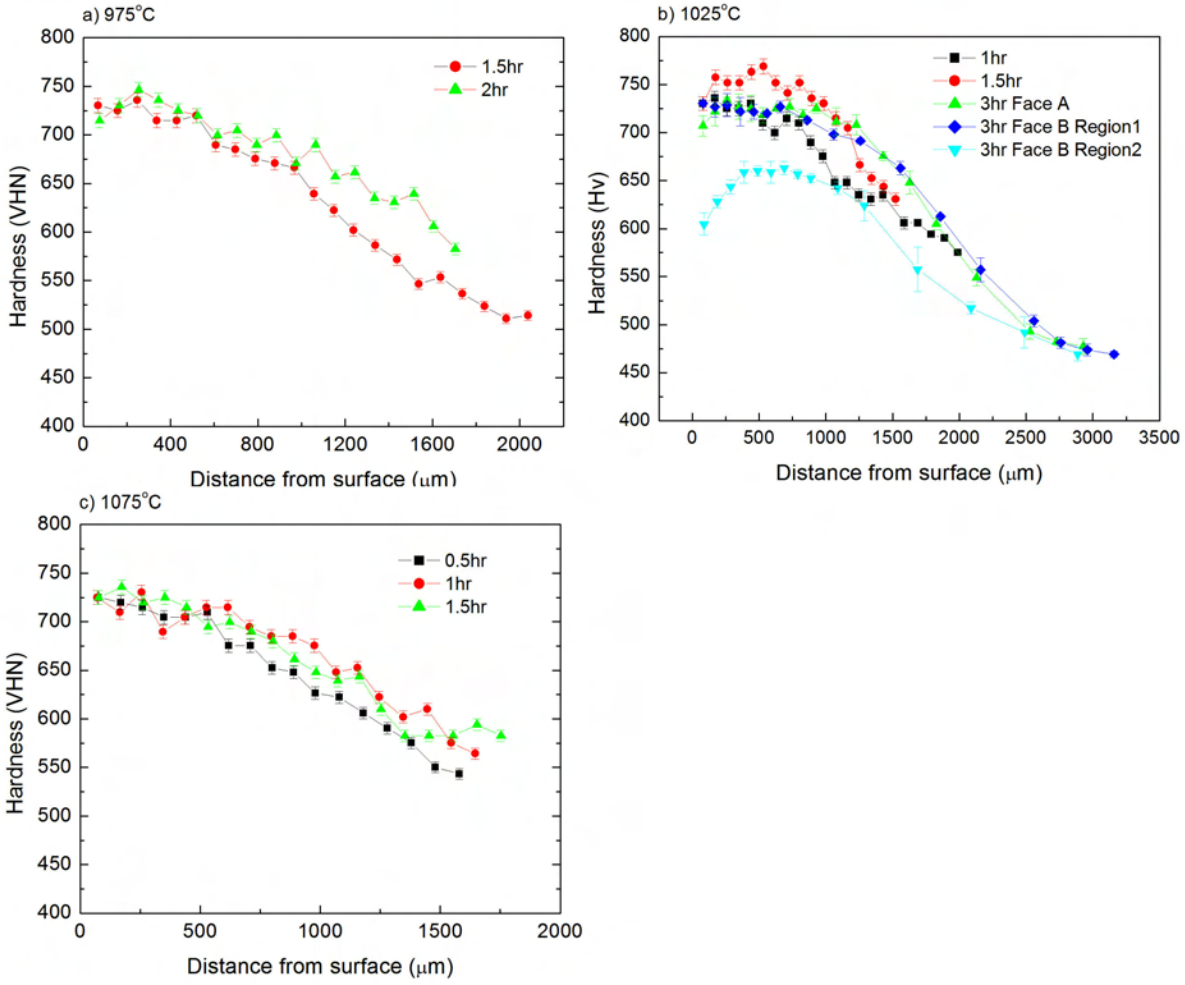

Figure 7.2. CryoForm 70 prototype Hardness profiles after a)975 °C b)1025 °C and c)1075 °C carburizing

from DICTRA. Carburization at 1025 °C for 1.5 hours and 3 hours produced a surface carbon content of 0.6wt% and 0.76wt%, respectively. But the carbon content decreased rapidly as the depth increased, indicating that carbon diffusion from the surface to the core was delayed. With longer time more carbon was diffused into the case but the hardness was not necessarily raised because of retained austenite. Comparison between experimental and simulated carbon content profiles shows there is a good match on the

surface carbon content but disagreement is observed for subsurface carbon content. Lower experimental values are possibly due to the formation of a Cr primary carbide film as excess surface carbon does not diffuse quickly enough to the inside. This phenomenon, however, is not taken into account in DICTRA simulation. It is also noticed that estimated or measured carbon content profiles of two faces for one sample do not match with each other, indicating the inhomogeneity of pack carburization.

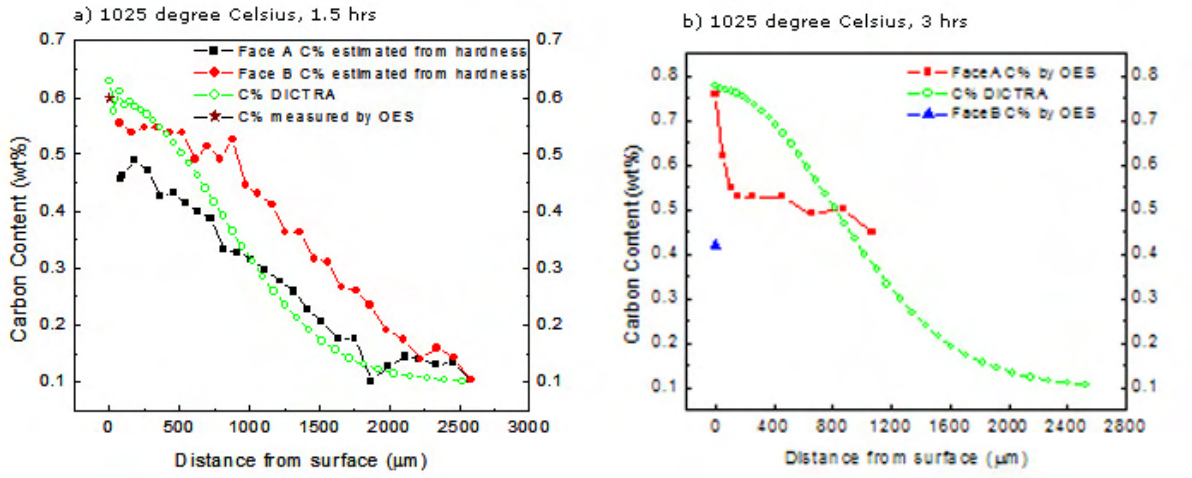

Figure 7.3. CryoForm 70 prototype carbon content profiles carburized at 1025 °C for a)1.5 hours b)3 hours

The case microstructure of a sample with 0.76wt% surface carbon content was further studied. X-ray diffraction shows prominent austenite peaks (labeled as A) coexisting with distorted martensite (labeled as M) after 200 °C tempering (Fig. 7.4). An austenite volume fraction of 55% at 10μm depth was obtained through quantitative analysis. Optical and scanning electron microscopy (SEM) were both employed to reveal the case microstructure (Fig. 7.5 and 7.6). 2% nital was used to etch the cross section to display the case microstructure. Both optical and SEM images confirmed that a large amount of

retained austenite was present at or near surface. Due to the high surface carbon content, plate martensite also formed at or near surface.

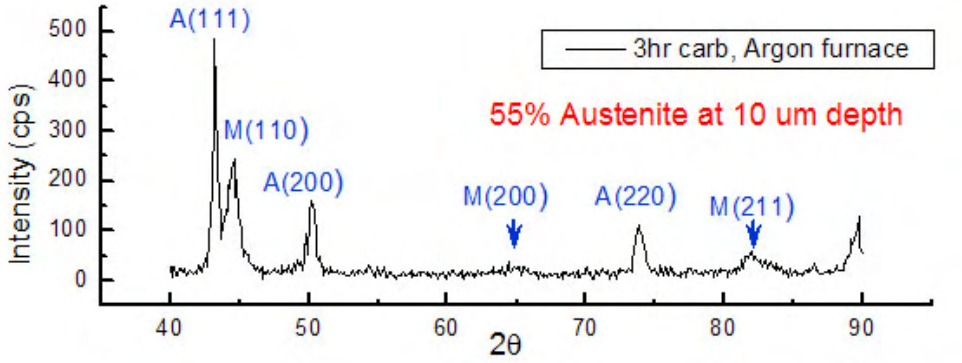

Figure 7.4. Phase analysis of CryoForm 70 prototype using X-ray diffraction

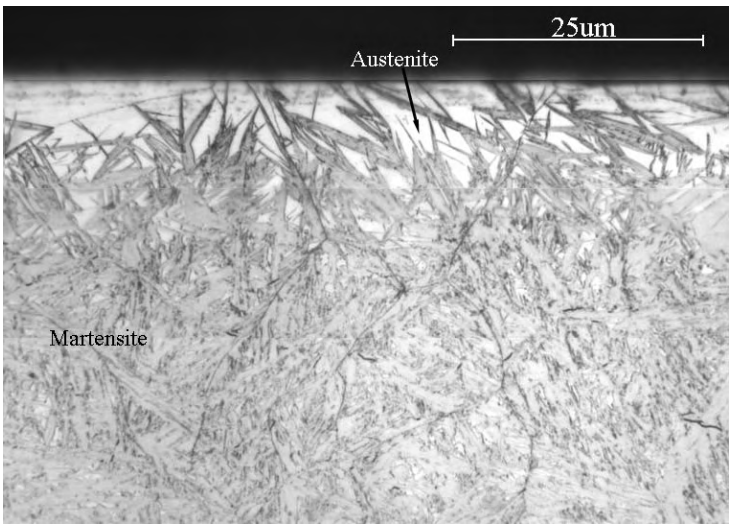

Figure 7.5. Case microstructure of CryoForm 70 prototype through optical observation

Through pack carburizing, a surface carbon content of 0.76wt% was achieved but the resulted steep carbon gradient was not desired. With increased carburizing temperature or time, no rise in surface carbon content was found, suggesting the limitation of pack

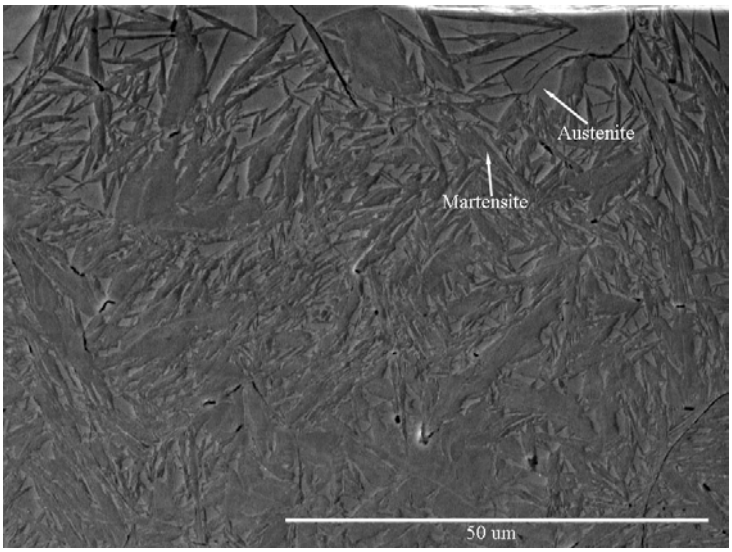

Figure 7.6. SEM image of the case microstructure in CryoForm 70 prototype

carburizing in achieving high carbon content and appropriate carbon profiles. Microstructure analysis revealed 55% retained austenite at the depth of $10\mu m$, which may be too much for the subsequent austenite reduction. Moreover, the non-uniformity presented in pack carburizing makes this practice not favorable for further carburizing optimization. It does appear that DICTRA is effective for simulating surface carbon content.

7.3.2. Vacuum carburizing

For a better controlled process and carbon content profile, vacuum carburizing was selected for further carburizing optimization. After developing carburizing cycles through simulation, two batches of carburization were performed by Midwest Thermal-Vac in Kenosha, Wisconsin. Hardness, carbon content profiles and microstructure were studied to illustrate the efficiency of vacuum carburizaiton. Simulated carbon content profiles were compared with experimental results.

High temperature is desired for fast carburization and elimination of primary carbides. Thus the designed solution treatment temperature, 1100 °C, was adopted as carburizing temperature. The same carbon flux as that for C67 was chosen by the vendor for the ease of processing. The effective carbon flux for CryoForm 70 was determined by extracting the effective carbon flux from experimental C67 carburization data. Required by the vendor equipment, the boost and diffusion time must be multiples of five and sixty seconds, respectively. Other restrictions include that the carbon content after any boost cycle should not exceed 3 wt% to prevent carbide networks from forming.

The carburizing cycles for the fist batch implementation was developed using the CBPWIN2 code due to its friendly interface and ease to use. In CBPWIN2, the activation energy and pre-exponential diffusion coefficient (D_0) was calculated using DICTRA with known effective carbon flux. With the input of temperature and combinations of boost and diffusion times, carbon content profiles after each boost and diffusion cycle were generated. According to the restriction on maximal carbon content, the surface carbon content and case depth, the combinations of boost and diffusion times were further adjusted and a final recipe was selected. Simulated carbon content profiles are depicted in Fig. 7.7. The surface carbon content after final boost and diffusion is 2.64% and 0.9%, respectively. To accommodate further machining, a surface carbon content higher than the designed 0.8% was accepted.

DICTRA was utilized to develop the carburizing cycles for the second batch implementation for its ability of taking into account the carbon diffusivity dependence on carbon content. To accelerate simulation, the $Carb^{©}$ optimization program previously developed by Dr. Gao [**8**] for QuesTek Innovations, Inc. was first used to narrow down the suitable

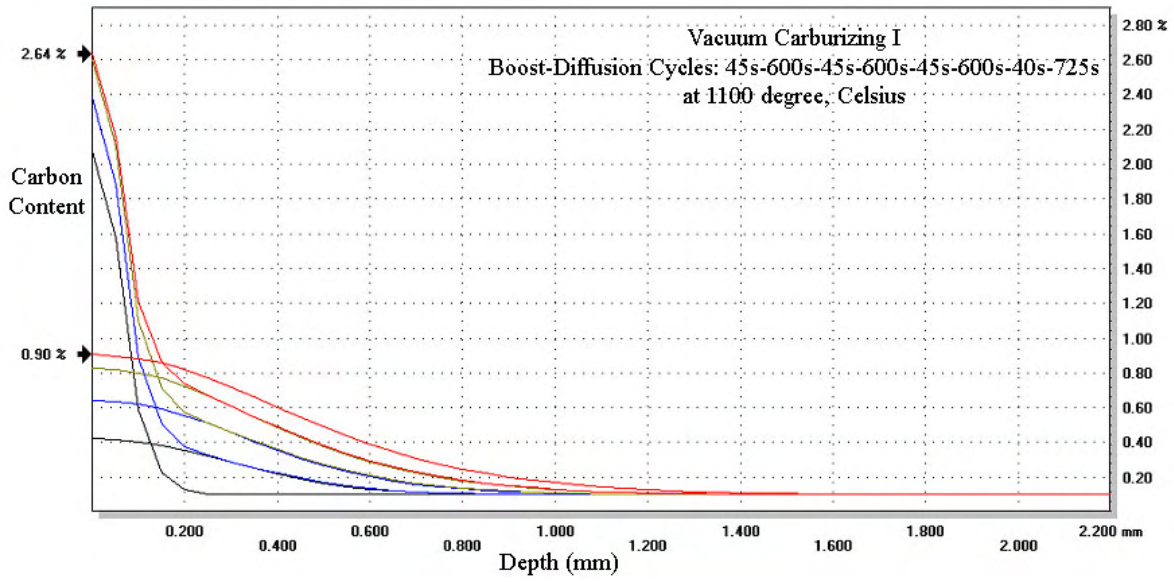

Figure 7.7. Simulated carbon content profiles by CBPWIN2 for the first practice

time range for boost and diffusion cycles. Further adjustment was then made using DICTRA. Simulated carbon content profiles for the second recipe are displayed in Fig. 7.8 as hollow symbols, labeled *Vac II*.

With provided carburizing cycles, vacuum carburizing was performed, followed by Argon gas cooling and one hour freeze in liquid nitrogen. Measured carbon content profiles using the OES technique are also plotted in Fig. 7.8, shown as solid symbols. 1.2% and 0.9% surface carbon content were obtained for the first and second batch carburization, respectively. A 0.8% carbon content was detected at the depth of $50\mu m$ in Batch Two. The 1.2% experimental surface carbon content from the first batch is much higher than the simulated value from CBPWIN2 (0.9%) because CBPWIN2 underestimated the carbon diffusivity with increasing carbon content. Fortunately, the experimental value agreed with the prediction by DICTRA, suggesting that DICTRA is more suitable for the system

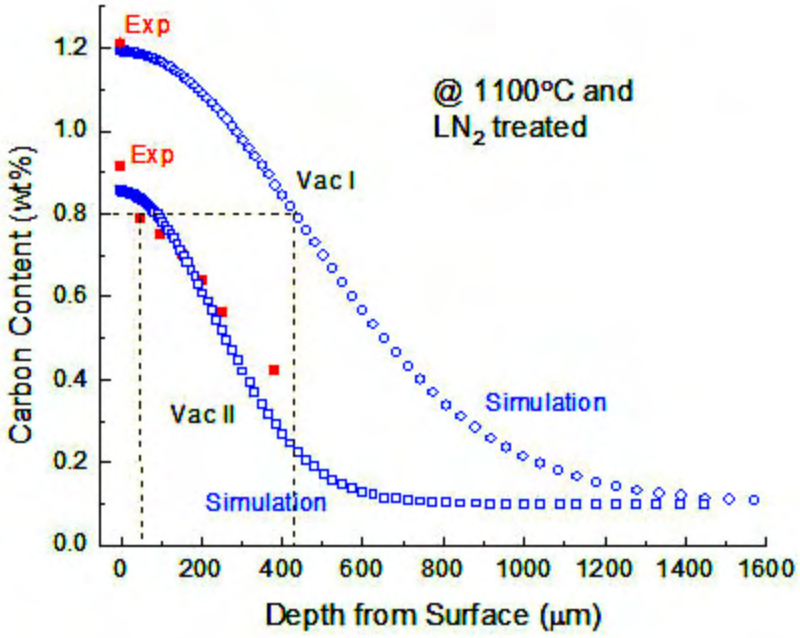

Figure 7.8. Simulated carbon content profiles by DICTRA for the first and second practice. Recipe for the second practice: 40s-180s-25s-295s

with variable carbon content. Comparison between simulated and experimental carbon content profiles for Batch Two also supports this point.

Hardness profiles after liquid nitrogen treatment were measured for both batches (Fig. 7.9). Peak hardness occurs at a substantial depth below surface in both batches, supporting the presence of a large amount of retained austenite at or near the surface. Although the surface carbon content in Batch Two is much lower than that in batch one, the peak hardness is higher due to the effect of much less retained austenite, possibly associated with the sharper composition gradient. With the total number of boost and diffusion cycles decreased from four to two, the total amount of carbon absorbed was reduced and thus Batch Two alloy displays a case depth half of that in batch one.

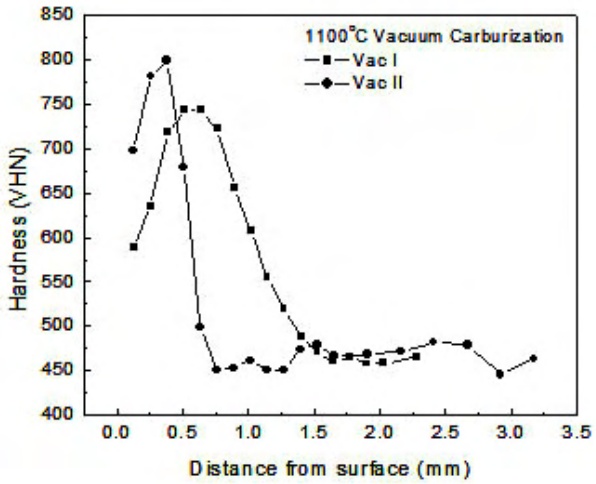

Figure 7.9. Measured hardness profiles for both vacuum carburization batches

To measure the amount of retained austenite at the carbon level of 0.8%, samples from batch one were ground to the depth of about $400\mu m$, where the carbon content reached 0.8% according to DICTRA simulation. Similarly, the subsurface at $50\mu m$ depth of a batch two sample was exposed for phase analysis. From the X-ray diffraction spectrum (Fig. 7.10), a two phase structure - austenite and martensite- is present in the matrix but the austenite peak is greatly diminished compared to that in pack carburization, indicating lower austenite volume fraction. Retained austenite profiles for both batches are presented in Fig. 7.11. At the carbon level of 0.8%, 22∼24% retained austenite was found in both batches. This was confirmed by the optical observation (Fig. 7.12), where light regions are austenite phase and dark areas are martensite.

7.4. Cryogenic deformation

In the CryoForm 70 prototype, a fully martensite matrix is ultimately desired for maximized strengthening efficiency. However, at the desired 0.8% carbon level, 22∼24%

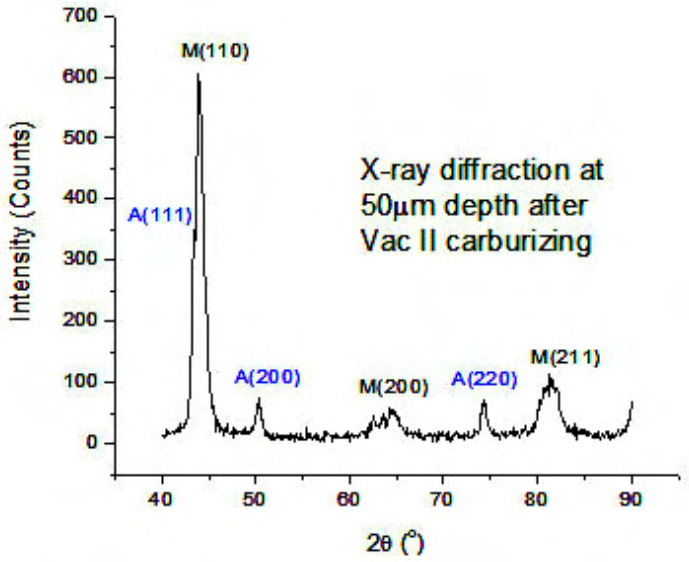

Figure 7.10. X-ray diffraction spectrums from batch two, showing peaks from austenite

retained austenite was identified, meaning the volume fraction of martensite is only about 76%. Before tempering can be carried out, retained austenite needs to be minimized. Cryogenic deformation was thus developed to fulfill this goal. Theoretical calculation based on driving force and kinetics of martensite transformation was first conducted to predict the final martensite volume fraction that could be achieved from cryogenic deformation. Cryogenic shot peening was first explored for austenite reduction. Other methods including cryogenic ultrasonic surface modification and cryogenic compression were explored later. Cryogenic compression was proven to be most effective in reducing the amount of retained austenite.

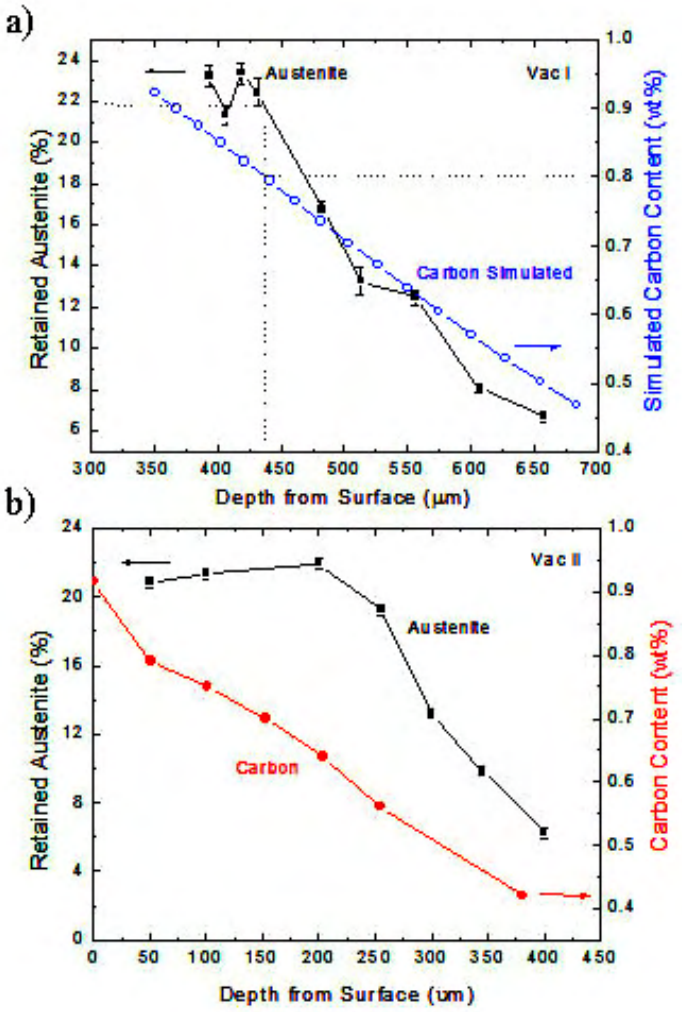

Figure 7.11. Retained austenite profiles for a)batch one b)batch two

7.4.1. Driving force and kinetics of martensite transformation

Following the principles introduced in Chapter 5, the thermal driving force for martensite transformation in the CryoForm 70 prototype was calculated and plotted in Fig. 7.13. About 2500 J/mol gain over the critical driving force at M_s (-2423 J/mol) can be obtained by quenching the alloy to the liquid nitrogen temperature ($-196\,^{\circ}C$). With applied stress

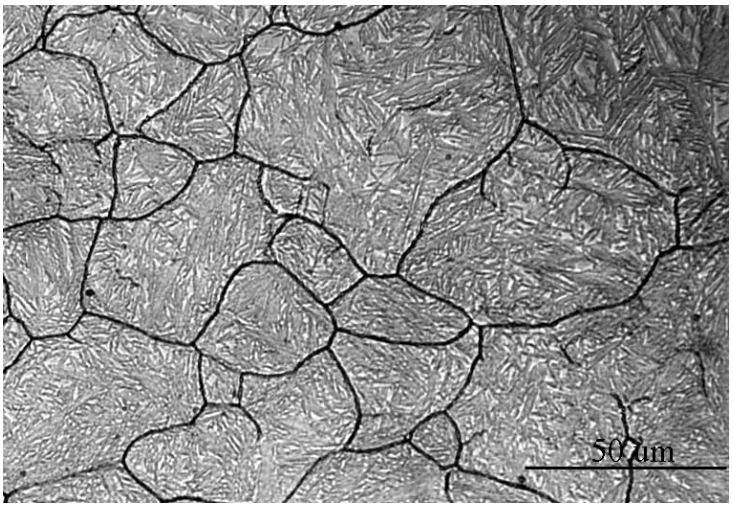

Figure 7.12. Optical image showing the microstructure containing 22∼24% austenite

that deforms the CryoForm 70 prototype, an additional 1200 J/mol driving force can be obtained (Fig. 7.14). Fig. 7.15 displays the total driving force versus temperature together with the thermal driving force, which illustrates the additional driving force gain resulting from the mechanical deformation (by arrow). At LN_2 temperature, this gain is about half of the thermal driving force. However, at room temperature, the total driving force is less than the thermal driving force at LN_2. That means mechanical deformation at room temperature does not benefit martensite transformation more than cryogenic treatment only. Thus for maximized benefit, mechanical deformation needs to be performed at the LN_2 temperature, which gives this process the name *Cryogenic Deformation*.

To predict the final volume fraction of martensite after cryogenic deformation, the material constant k in Magee's single-parameter transformation kinetic model was fitted based on the experimental observation that 76% martensite was formed after quenching the alloy to liquid nitrogen. With the calibrated $k = 0.00061 mol/J$, a final volume fraction of 90% was then predicted for combined cryogenic treatment and mechanical

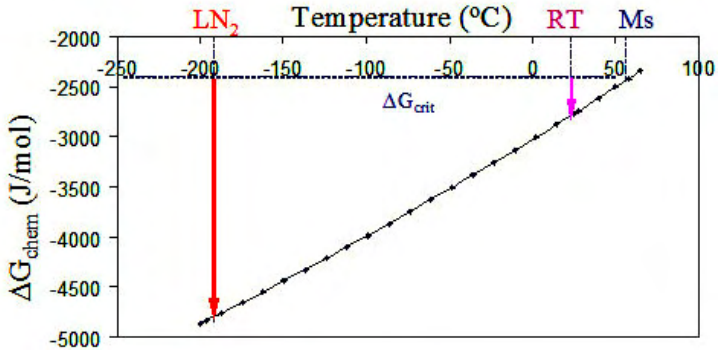

Figure 7.13. Thermal driving force for martensite transformation in CryoForm 70 prototype at 0.8% C

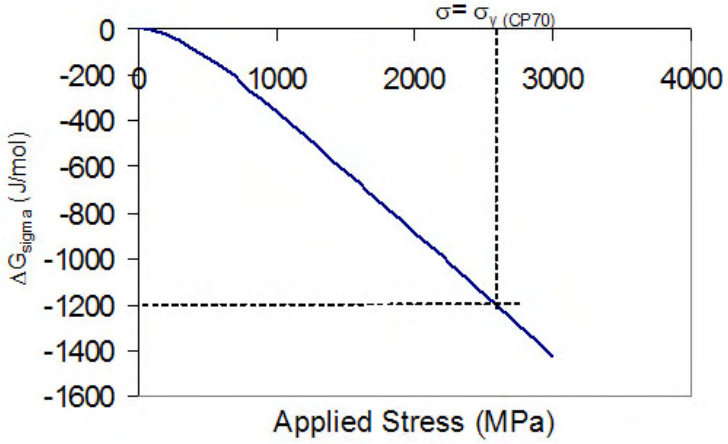

Figure 7.14. Mechanical driving force for martensite transformation

deformation (*cryogenic deformation*), shown as the red or solid line in Fig. 7.16). For comparison, also plotted are a 80% martensite line (magenta or dotted line) resulting from liquid nitrogen treatment and a 20% martensite line (blue or dashed line) from quenching to room temperature.

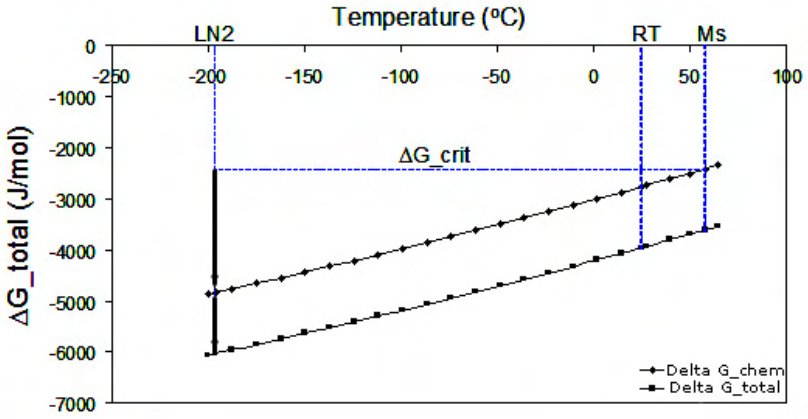

Figure 7.15. Total driving force for martensite transformation in CryoForm 70 prototype

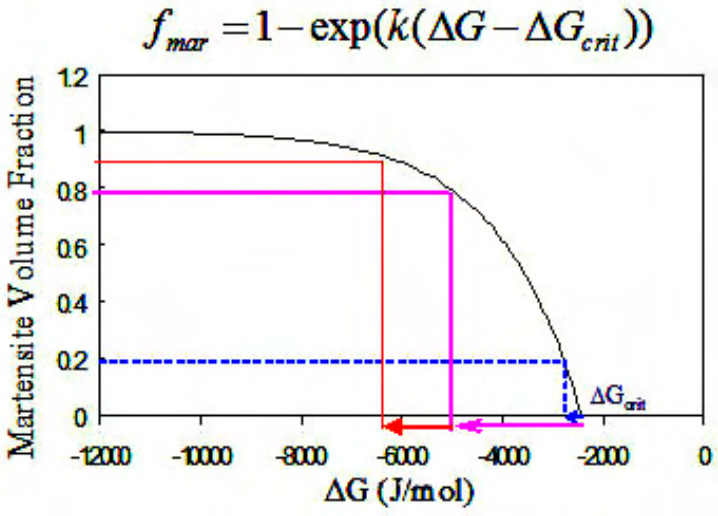

Figure 7.16. Predicted volume fraction of martensite transformation in CryoForm 70 carburized case

7.4.2. Cryogenic shot peening

The predicted 90% martensite volume fraction means the austenite level would be reduced to 10% or lower in a martensite-austenite two phase structure. Shot peening was

chosen first to implement the mechanical deformation for its reported ability of decreasing austenite content and for its potential availability within gear industries.

7.4.2.1. Preliminary study. A preliminary study was conducted to explore the effect of room temperature shot peening on the austenite content. Core CryoForm prototype was pack carburized to contain 0.6% C on the surface and then shot peened at room temperature by Metal Improvement Company, Inc. in Addison, Illinois. Austenite measurement using X-ray diffraction before and after shot peening showed an austenite reduction from 18% to 10% , indicating the feasibility of applying shot peening to the vacuum carburized prototype.

7.4.2.2. Shot peening at $-112\,^{\circ}$C. Collaboration was established between Northwestern University and Purdue University to carry out cryogenic shot peening utilizing the equipment at Purdue. Graduate student Jeremy Hahn from Purdue participated in this project. The experimental setup is shown in Fig. 7.17. Inside the chamber, the circular table serves as the base for the sample holder. The sample was attached to the holder by a magnet. Thermocouple wires were welded to a side of sample through a steel pipe for real-time temperature recording. The entire holder with the sample was then screwed onto the circular table. The position and orientation of the nozzle can be adjusted to perform a customized peening at any angle with variable shot travel distance. In Fig. 7.17 b), the nozzle was orientated to allow vertical shot travel. The circular table can rotate at a certain speed if needed. It was set to be immobile in this study. Conditioned extra-hard cut wire shots with 0.032 inch diameter made of carbon steel were employed for their high hardness of 62$\sim$64 Rc. Shot was provided by Premier Shot Company.

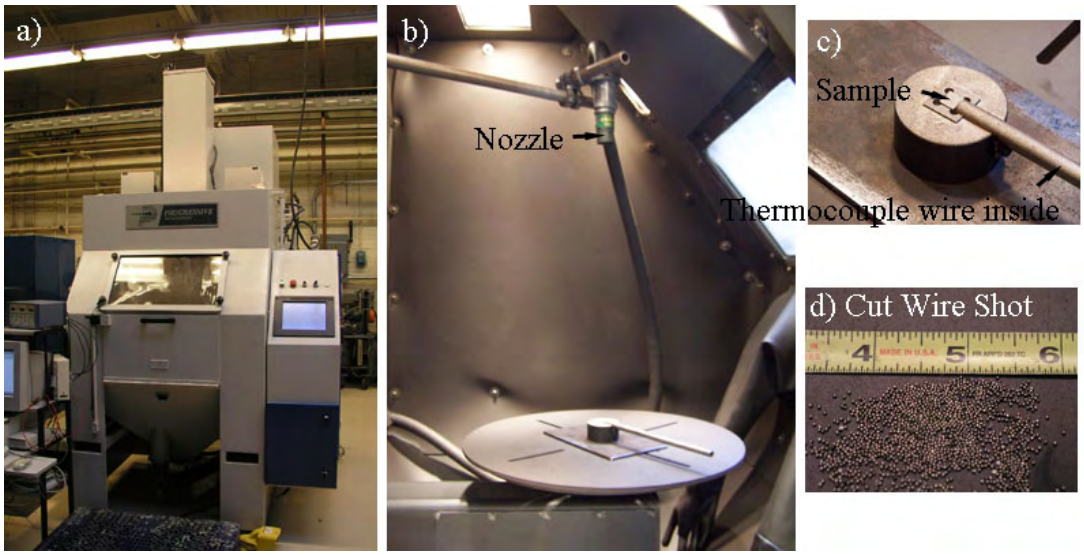

Figure 7.17. Cryogenic shot peening setup a)Shot Peener b)Inside the chamber c) sample and sample holder d)Shots

To ensure mechanical deformation in the targeted prototype, a high applied stress and thus a high peening intensity is desired in this process. A standard Almen strip was used to measure shot peening intensity. This procedure is illustrated in Fig. 7.18. Peening intensity is represented by the extent of strip warping (Fig. 7.18 b)). There are three types of Almen strips with different thickness, among which type A with the medium thickness is used mostly in industry and the intensity measured is recorded as *inch A*. The maximal deviation that an A strip can measure is 0.025 inch so the measurement of any more severe deformation needs the usage of the thicker C strip. As shot peening intensity increases from zero to low (0.0074 inch A) to medium (0.0255 inch A), surface roughness prominently increases. Combining the effect of various factors on the peening intensity (including shot propelling force - air pressure, shot flow rate and peening time), an intensity of 0.0075 inch C was identified to be the maximum that could be achieved using the Shot Peener. Three levels of peening intensity, low (0.0044 inch C), medium

(0.0064 inch C) and high (0.0075 inch C) were selected for the peening at cryogenic temperature.

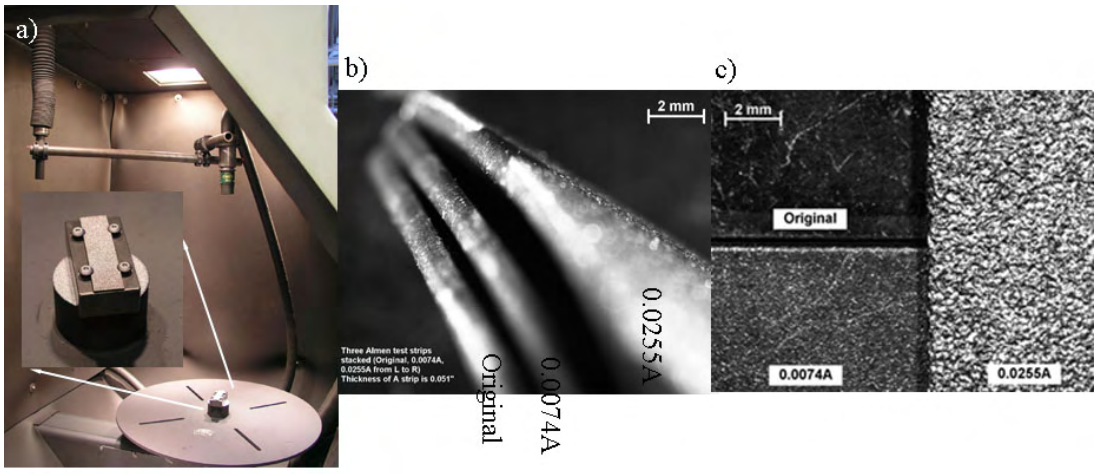

Figure 7.18. Almen strip test for intensity selection a)setup b)Almen strips deformed with 0, 0.0074A and 0.0255A peening intensity c)Almen strip surface conditions under different peening intensity

Several attempts showed that the temperature of samples rose rapidly during peening, despite both the sample and sample holder being submerged into liquid nitrogen for 20 minutes to reach $-190\,^{\circ}\mathrm{C}$. To maintain the sample temperature as low as possible, a cyclic peening procedure was developed, as shown in Fig. 7.19. During the interval between 10 seconds peening, liquid nitrogen was poured over the sample and holder for another freeze. This step was repeated every 10 seconds till a total peening time of 2 minutes was reached. Temperature evolution of the sample during peening was displayed in Fig. 7.20 for three levels of intensity. The sample temperature started around $-190\,^{\circ}\mathrm{C}$ and rose up to $-84 \sim -112\,^{\circ}\mathrm{C}$ after 10s peening depending on the peening intensity. It was brought down to the original level when the sample was cooled again. A 10s peening then started over. The lowest average temperature after 10s peening was obtained with

the low peening intensity, which indicated that it was easier to maintain low temperature with decreased peening intensity.

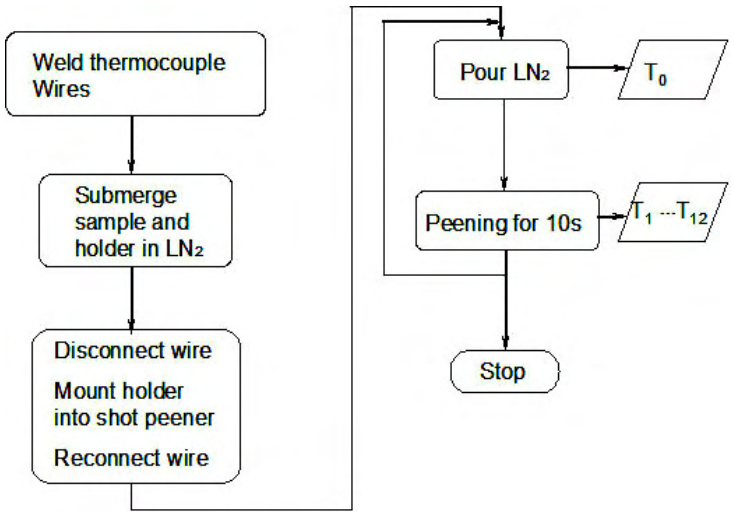

Figure 7.19. Cryogenic shot peening procedure

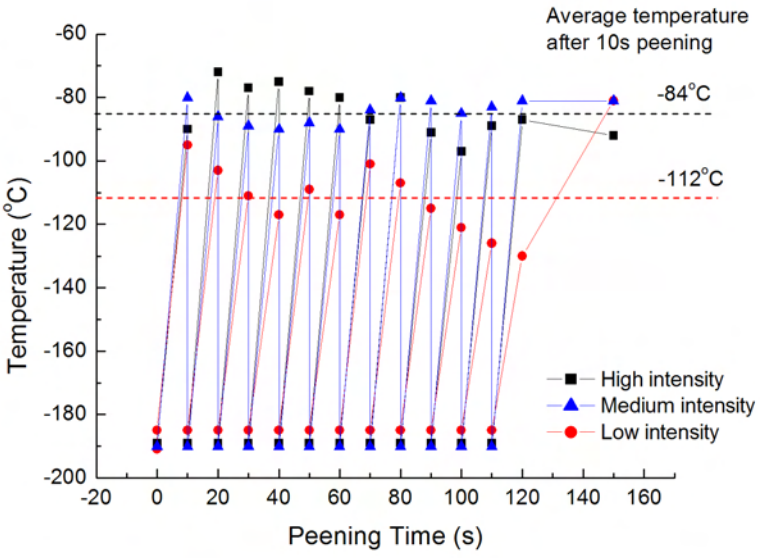

Figure 7.20. Temperature evolution during cryogenic shot peening

For each peening condition, two samples were treated following the above procedure. A retained austenite level of 24% was confirmed in these samples before cryogenic peening. Similar analysis after peening showed only under the low peening intensity was the amount of retained austenite slightly reduced (Fig. 7.21). The integrated intensity of both austenite (220) and martensite (200) peaks were almost not changed, although the austenite (220) peak was depressed and broadened. This indicates that the austenite was deformed by peening but not transformed to martensite. No reduction in austenite level was found in samples peened with medium and high intensities. Sample temperature rise was proposed to be the reason. With temperature raised to $-112\,^{\circ}\mathrm{C}$ or higher, about 900 J/mol or more was lost in the driving force of martensite transformation, which greatly counteracted the effect from the applied stress. Consequently, no or slight reduction in the retained austenite level was observed.

7.4.3. Ultrasonic surface modification at cryogenic temperature

Another means of mechanical deformation process, ultrasonic surface modification (UNSM) was tried at liquid nitrogen temperature due to its potential suitability for large scale products. UNSM was reported to improve fatigue strength, wear resistance and friction loss, and to retard stress crack corrosion [**107**]. In UNSM, a tungsten carbide ball constantly strikes the surface of materials at an ultrasonic frequency (20,000∼40,000 impacts per second). The coverage of UNSM treatment can be customized by controlling the position and motion of the ball, which is attached to a rigid arm that moves freely. This treatment can produce 1000 to 10,000 shots per square mm on the work surface. Surface finish, hardness and the magnitude of compressive residual stress can be improved through UNSM

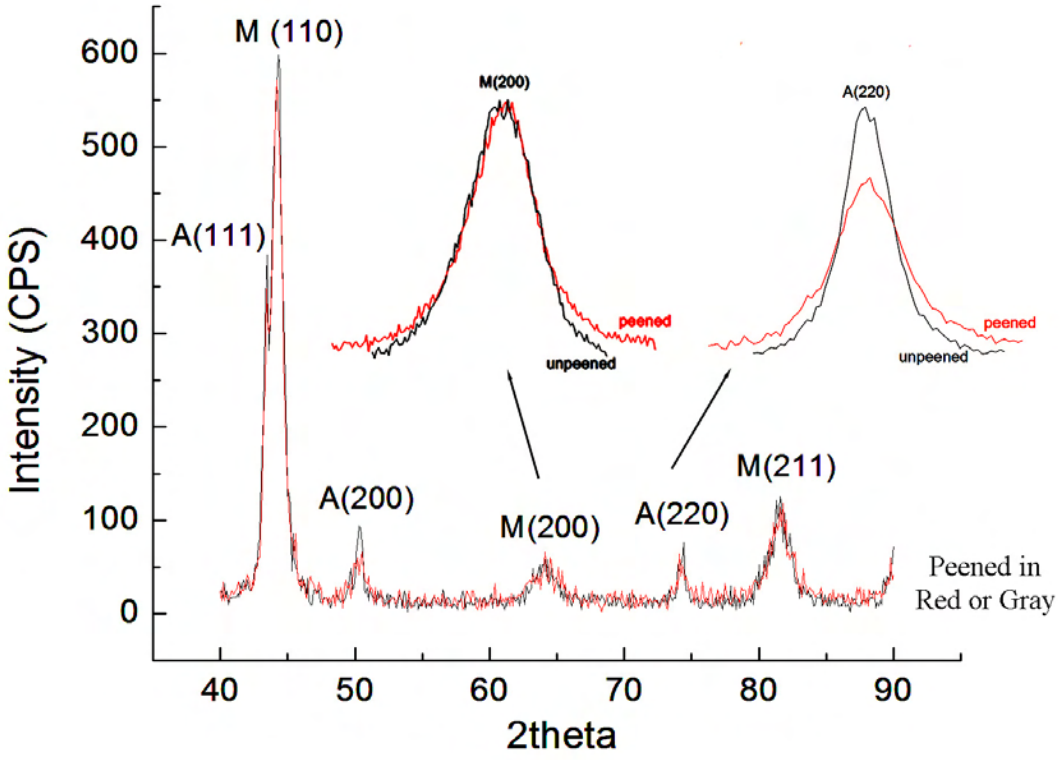

Figure 7.21. X-ray diffraction showing slight reduction in retained austenite content treated with low intensity cryogenic peening

treatment. This treatment also employs mechanical stress to obtain the similar effect to that resulted from shot peening. The operating temperature can be controlled by cooling the specimen with a constant liquid nitrogen blast. Thus it is a good alternative for cryogenic deformation process.

The core prototype was machined into cylinders with 16mm in diameter and 89mm in length and vacuum carburized with batch two recipe. The surface of cylinders was then turned to the roughness of $R_a = 23\mu inch = 0.6\mu m$. During turning, a layer of 50 μm was removed to expose the surface with 0.8% carbon. A 60° 3mm center hole was drilled on

each end of the cylinder so the specimen can rotate on a machining center during UNSM treatment. The experimental setup is illustrated by Fig. 7.22.

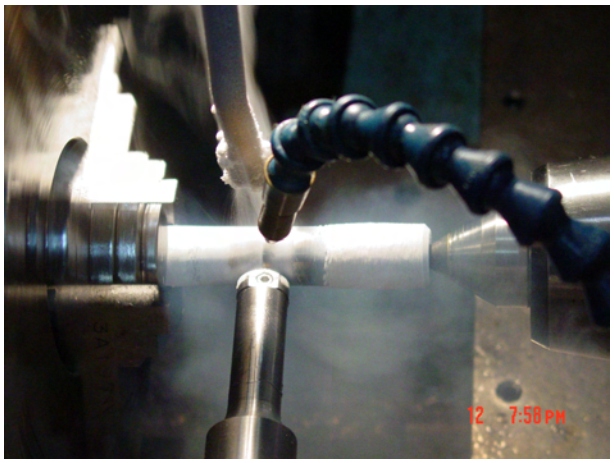

Figure 7.22. Experimental setup for ultrasonic surface modification at cryogenic temperature

The UNSM treatment was performed by DesignMecha Co., Ltd. in Asan, ChungNam, South Korea. Through the processing the surface hardness was increased from 61 Rc to 63 Rc. However, not much reduction in the integrated intensity of austenite peak was found. Given that a super hard (1400 Hv) tungsten carbide ball acts as the peening media and the liquid nitrogen temperature can be obtained, it is believed that further optimization of this process should be able to reduce the level of retained austenite significantly.

7.4.4. Cryogenic compression

A more static cryogenic deformation process, cryogenic compression was chosen for its ability of maintaining liquid nitrogen temperature and reaching higher stress than cryogenic shot peening. Olson and Azrin studied the transformation curves for a 220 ksi yield strength 0.27C TRIP steel and obtained the correlation between the resulting martensite

volume fraction and the true strain by applying mechanical stress at various temperatures [**108**]. Typical transformation curves were shown in Fig. 7.23. However, their study focused on low carbon alloys so experimental design is still needed to find out the appropriate plastic strain level at cryogenic temperature for high carbon alloys. Prior to experiments, required plastic strain at $-196\,^{\circ}\mathrm{C}$ for martensite fraction of 0.24 was estimated from Olson's curves as a starting point (shown as the dash line in Fig. 7.23). According to the transformation curve at $-196\,^{\circ}\mathrm{C}$, a 0.025 true strain was needed for additional 24% martensite.

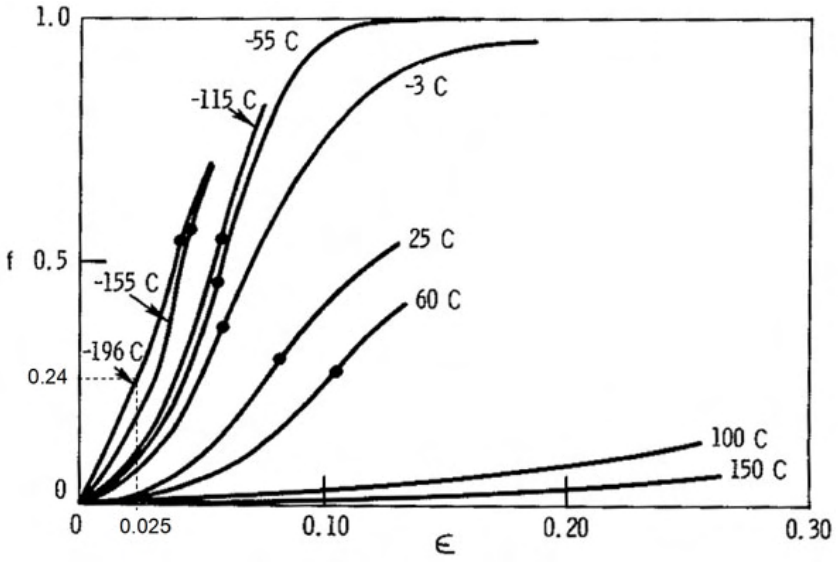

Figure 7.23. Transformation curves for 0.27C TRIP steel [**108**]

Rectangular bars ($3 \times 3 \times 6mm^3$ and $4 \times 4 \times 7mm^3$) were cut from the case of vacuum carburized specimens, Batch No. 2. For easy X-ray examination, $50\mu m$ was ground off from the case so the subsurface of 0.8% carbon was exposed. Before cryogenic compression, 24% retained austenite was confirmed at the 0.8% carbon level. The experiment setup is presented in Fig. 7.24. Compressive stress was applied onto the specimen through

a pair of tungsten carbide platens. The specimen was cooled in liquid nitrogen for 20 minutes before the test was started. A thin layer of plastic containing liquid nitrogen was placed between the specimen and the upper and bottom platens. Liquid nitrogen was continuously filled into the container to maintain the low specimen temperature. The specimen was aligned in the way that the interface between the case and the core was parallel to the compression axis so that both the case and the core were subject to the compressive strain simultaneously. Although the core would yield earlier than the case, the distortion was minimized through this alignment. A compliance test was performed first before any specimen was tested.

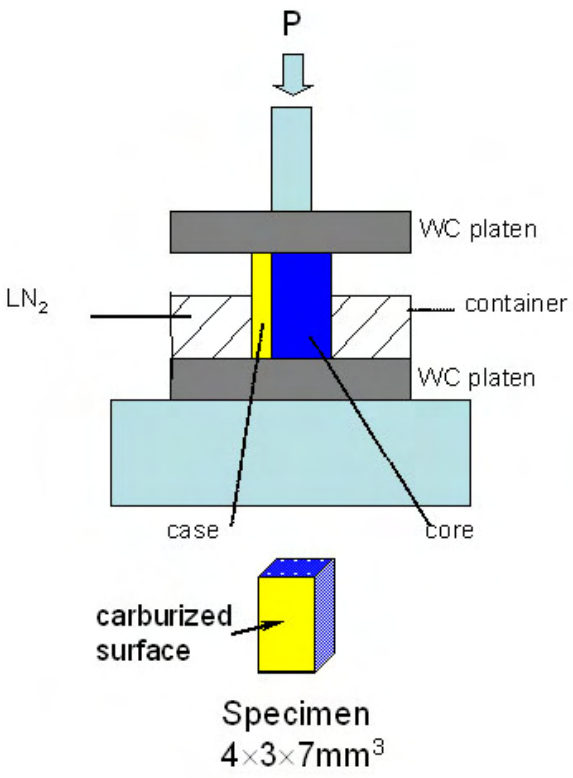

Figure 7.24. Schematic experimental setup for cryogenic compression

The specimens were taken to the total engineering strain of 5%, 7%, 8% and 9%, respectively. The stress-strain curves of these tests are shown in Fig. 7.25. The obtained plastic strain for test 1 to 4 was calculated to be 2%, 5%, 6% and 7%, respectively. The serration on Curve 2 or 3 is attributed to the breaking of the plastic containing liquid nitrogen during compression, which does not affect the continuity of the test. The agreement between yield points of four curves indicated that the constant low temperature was well maintained during the test although very small fluctuation was observed. The setup could be improved by attaching a low temperature thermocouple wire to the specimen so the temperature could be monitored. Neither material failure nor cracking at the core-case interface was observed during or after the compression. However, slight distortion occurred due to the friction on the upper and bottom surfaces of the specimen. The distortion could be reduced with the application of a low temperature lubricant. Different levels of strain rates (0.5mm/min, 0.1mm/min and 0.05mm/min) were employed in the test. It was found that the strain rate lower than 0.05mm/min was so slow that it was quite difficult to maintain the low specimen temperature since the testing time was dramatically increased. Among three levels of strain rates, 0.05mm/min was the one inducing minimal specimen distortion as the friction rate was reduced with the small strain rate. Thus the rate of 0.05mm/min was chosen as the optimum for cryogenic compression.

X-ray diffraction was used to measure the austenite level after cryogenic compression with different strain levels. Typical diffraction spectra were displayed in Fig. 7.26 where a) is the case for 2% plastic strain and b) for 5% and higher plastic strain. A 18% austenite was still remained in the steel for case a). In case b) only about 8% austenite was detected, which is a quite significant reduction from the original level of 24%. Thus an

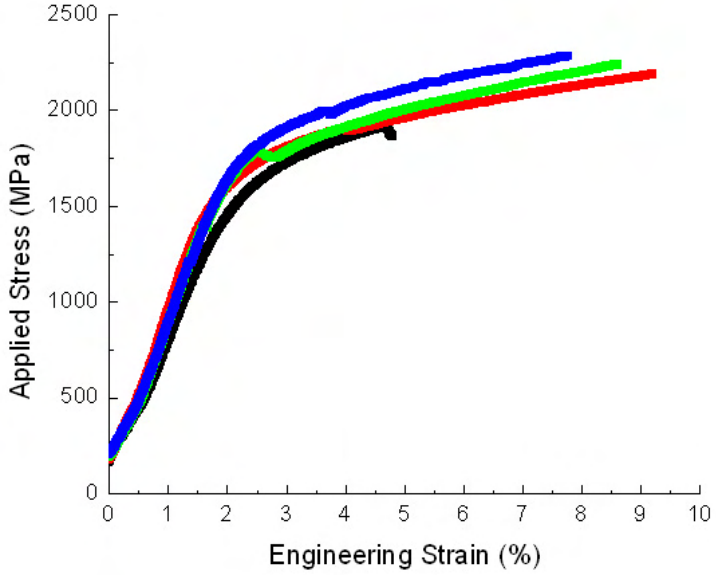

Figure 7.25. Typical stress-strain curves of cryogenic compression

appropriate strain level was identified for successful martensite transformation under high pressure at liquid nitrogen temperature. A summary of all successful tests can be found in Table. 7.1. The actual specimen temperature was not recorded during the test as it was believed to be very close to the liquid nitrogen temperature. A plastic strain higher than 3% is essential for significant austenite reduction. 5% plastic strain or larger ensures the martensite transformation even with the uncertainty in specimen temperatures. However, slightly less reduction in austenite was observed in test 6 with the strain level of 4.1%, which was believed to be due to the higher specimen temperature (lower yield point) than those in other tests. The temperature effect can be observed by comparing the yield points of the specimens under different tests since the decrease in temperature leads to the increase in steel's yield point. The reduction in retained austenite was proven to be

insensitive to the strain rate. However, the 0.05mm/min was chosen as the optimal strain rate for the minimized specimen distortion.

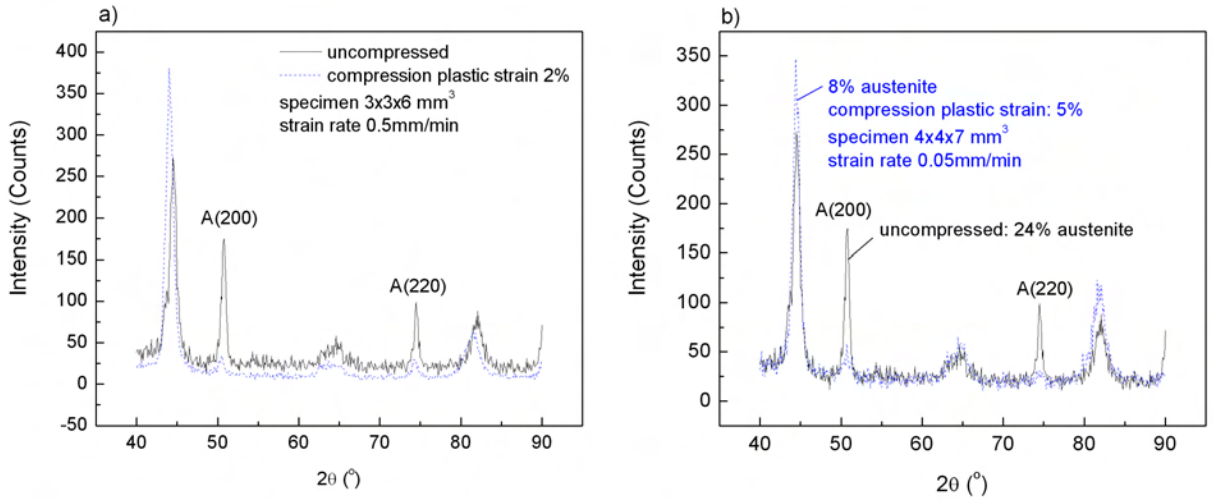

Figure 7.26. Crystal structure after cryogenic compression

Table 7.1. Summary of cryogenic compression test

Test ID	Specimen (mm^3)	Test Strain Rate (mm/min)	Plastic Strain (%)	Yield Point (MPa)	Resulting Austenite Level (%)
2	4x4x7	0.05	5.2%	1863 ± 25	7.6±0.5
3	4x4x7	0.1	6%	1780 ± 25	7.8±0.6
4	4x4x7	0.05	6.9%	1754 ± 25	7.9±0.6
5	3x3x6	0.5	3%	1771 ± 25	7.8±0.4
6	3x3x6	0.5	4.1%	1670 ± 25	10.2±0.4

7.5. Tempering response

Subsequent to cryogenic deformation through which the martensite structure in the vacuum carburized prototype was improved, tempering was carried out to enable the

precipitation of strengthening M_2C carbides. Two parameters are to be determined, tempering temperature and tempering time.

The M_2C driving force increases as the tempering temperature decreases. However, the lower the temperature, the lower the precipitation rate. By balancing the needs of high driving force and fast kinetics, a tempering temperature of $479 \sim 482\,^{\circ}\mathrm{C}$ was chosen for CryoForm 70 based on experience with the related C61, C67 steels.

To maintain the low level of retained austenite during tempering, a cyclic tempering procedure was developed, as shown in Fig. 7.27. After encapsulated, the specimen containing 8% austenite was treated at $482\,^{\circ}\mathrm{C}$ for 8 hours. The specimen was then oil quenched from the tempering temperature and cooled in liquid nitrogen for 1 hour or longer. These treatments were then repeated until a peak hardness was found. Evolution of case hardness at $80\mu m$ and complete hardness profiles with prolonged tempering are presented in Fig. 7.28. With this cyclic tempering-quenching-cryogenic treatment procedure, the case hardness started to pick up around 32 hour tempering and then reached a maximum of 975 ± 10 Hv at 56 hour tempering. Reduction in case hardness was seen with continued tempering. Because there is a steep gradient in case carbon content and the hardness was measured at $80\mu m$, the carbon content corresponding to $80\mu m$ depth was estimated to be $0.72\% \pm 0.2\%$ from the experimental carbon content profile (Fig. 7.29). Thus it can be concluded that a case hardness of 975 ± 10 Hv was achieved at the carbon content of $0.72\% \pm 0.2\%$. From the measured hardness profiles, a core hardness of 512 ± 2 Hv was accomplished, providing the necessary toughness for the application.

With the cyclic tempering procedure, the level of retained austenite was successfully controlled. A very low austenite level of 1.3 ± 0.2 after 48 hour tempering at $482\,^{\circ}\mathrm{C}$ was

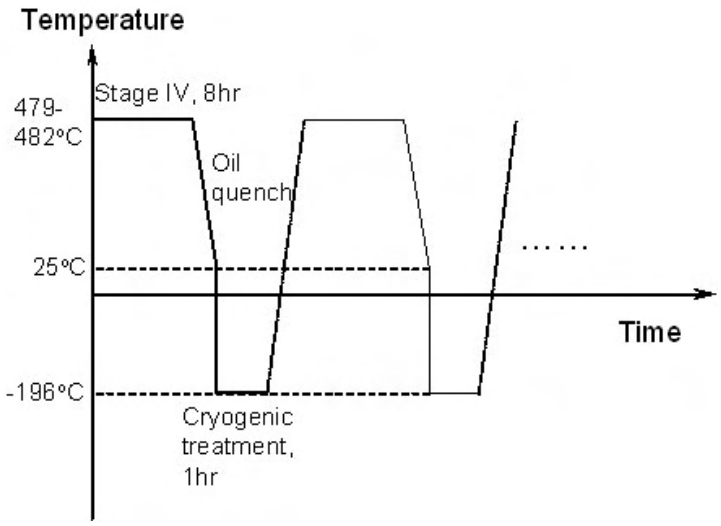

Figure 7.27. Cyclic tempering procedure for CryoForm 70

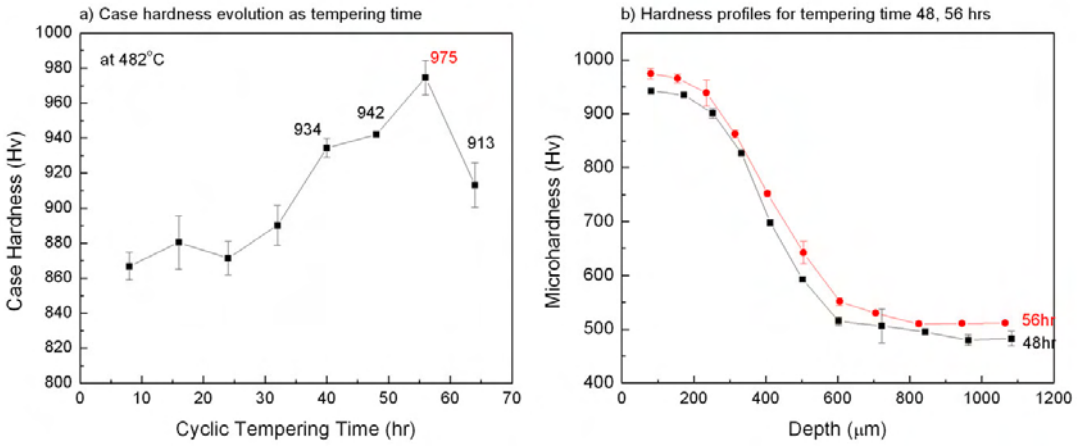

Figure 7.28. CryoForm 70 a) case hardness evolution with tempering time b) complete hardness profiles after tempering cyclicly for 48 and 56 hours

found. Optical micrographs were taken to observe the constitution of the matrix, shown in Fig. 7.30. Mixed plate and lath martensite was observed from the surface to the depth of $80 \sim 100\mu m$; as the depth increases the amount of lath martensite increases. No austenite regions are visible from this micrograph. At the condition for peak hardness, a similar microstructure was observed (not shown).

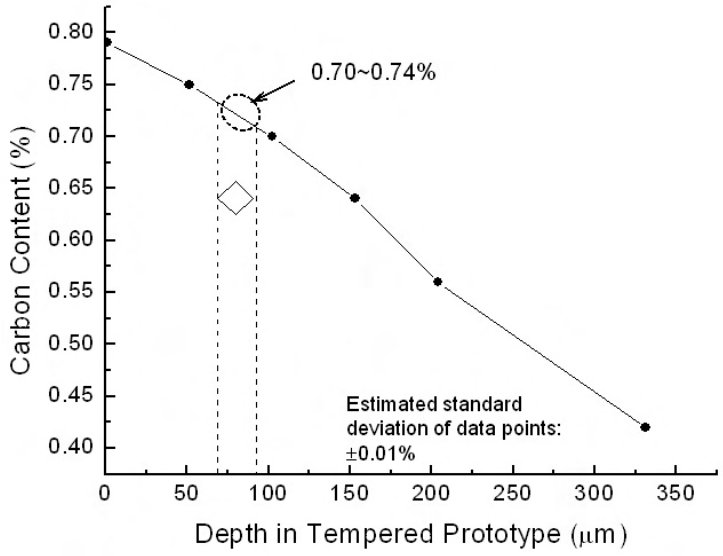

Figure 7.29. Estimation of case carbon content of CryoForm 70

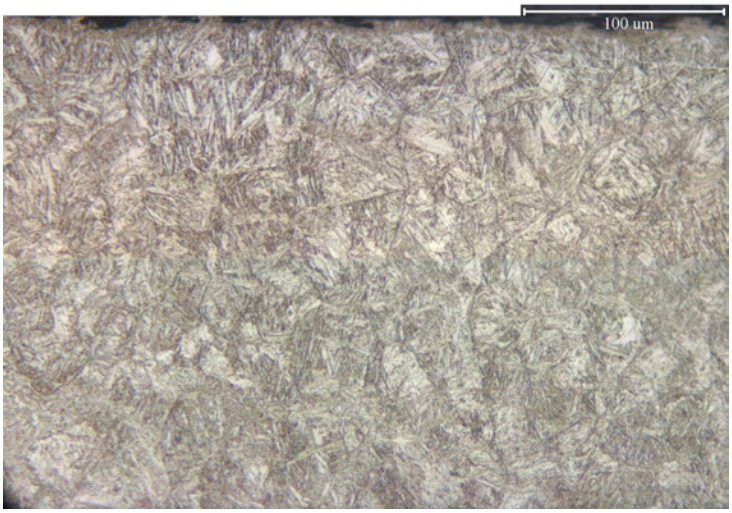

Figure 7.30. CryoForm 70 microstructure after tempering cyclicly for 48 hours

The number of density of M_2C carbides in the case of CryoForm 70 after 56 hour cyclic tempering can be estimated by using the calculated M_2C phase fraction and estimated M_2C particle size from the strengthening model. Thermodynamic computation shows that the M_2C phase fraction is 0.10266 at 479 °C with a carbon content of 0.8%. Comparison

between predicted and achieved case hardness shows a particle radius of 2nm is the best estimation of the precipitate size. Thus the number of density of M_2C carbides is: $N_v = \frac{PhaseFraction}{ParticleVolume} = \frac{0.10266}{4/3*\pi*(2*10^{-9})^3} = 3.06 * 10^{24} m^{-3}$ The order of magnitude is 10^{24}, agreeing with the experimental data from LEAP analysis of C61 steel.

7.6. Surface carbon content validation using X-ray diffraction

Currently 0.79wt% C was achieved at the depth of 50μm in the vacuum carburized prototypes. For the subsequent processing, 50μm was first removed from the case so that the surface with 0.79wt% C was exposed to cryogenic compression and cyclic tempering. However, the true surface carbon content might be slightly lower since more material is possibly removed during machining. Thus the validation of surface carbon content in cryo-compressed prototype is needed to achieve the correlation between case hardness and case carbon content. The surface was too small to apply the Optical Emission Spectroscopy to measure the carbon content. As an alternative, X-ray diffraction analysis was performed to probe the crystal structure of the surface. Past research has shown that the diffraction peak splitting of martensite phase is strongly correlated to the carbon content as a and c axes became distorted with increased carbon content [**109**]. By measuring the ratio of c over a, the carbon content can be estimated.

The (200), (400) series of martensite peaks are good candidates for the measurement of lattice parameters, c and a, as strong peak splitting presents between (200) and (002) or (400) and (004). Higher order diffraction peaks are recommended for the analysis to obtain more accurate c/a. However, due to the limitation of the diffractometer, only low angle (200) and (002) peaks can be detected. The surface crystal structure of a cryogenic

compressed specimen was measured first and 8% retained austenite was confirmed from the measurement. Then with a fine scan of peaks (200) and (002), the d spacings were calculated using pseudo-voigt peak fitting function. Since $c = 2d_{002}$ and $a = 2d_{200}$, $c/a = d_{002}/d_{200} = 1.028$ from the diffraction. Referring to the correlation between c/a and carbon content in steels, the carbon content is estimated to be 0.68 using experimental data in [**110**] or 0.64 with [**111**].

7.7. Summary

Compared with the carbon content estimation using the experimental carbon content profile, the estimation using X-ray diffraction resulted in the larger uncertainty. Thus it is summarized that the final hardness was achieved with the corresponding carbon content of 0.72%±0.2%. Plotted in Fig. 7.31 are achieved case and core hardness with corresponding carbon contents. The current case hardness and carbon content combination agrees well with the 2nm- radius precipitate strengthening model, demonstrating the validity of the selected model. With the uncertainty in the case carbon content, a good agreement has been achieved, demonstrating the effectiveness of computational composition design and the efficiency of cryogenic deformation in improving material microstructure. With increased case carbon content to 0.8%, it is shown that the hardness goal can be reached.

The comparison between theoretical and experimental prototype properties is summarized in Table. 7.2. Agreement between calculated and experimental core M_s clearly validates the design. The achieved case hardness of 975 ± 10 Hv is a 39% improvement if compared to current commercial case hardness of 720 Hv. Substantial progress has been made in increasing the case hardness with respect to C67 steel.

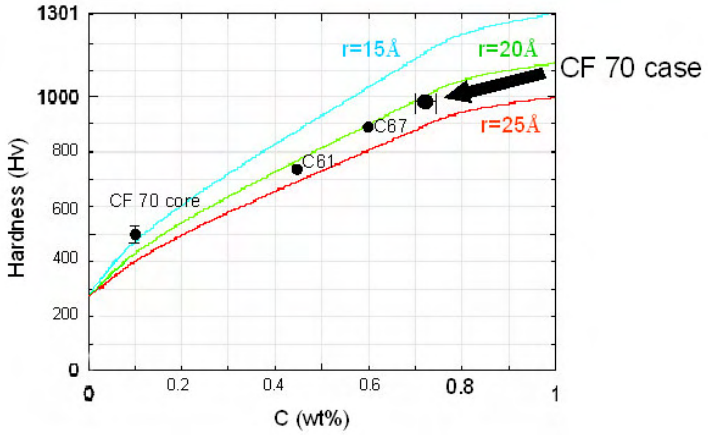

Figure 7.31. Summary of case and core hardness with carbon contents in CryoForm 70 prototype

Table 7.2. Summary of CryoForm 70 design

	Goal	Theory	Exp.
Hardness Case (Hv)	1076	1067	**975 ±10**
Hardness Core (Hv)	500	423	**512 ± 2**
Max Residual Stress (MPa)	-1700	-1700	**----**
M_2C DF Case (kJ/mol)	Max	28	**----**
Sigma DF Core (kJ/mol)	<2.8	2	**----**
M_s Case (^oC)	50~100	58	**----**
M_s Core (^oC)	350	350	**350**
T_s Case (^oC)	1100	1098	**1100**

The successful design of CryoForm 70 demonstrated the effectiveness of cryogenic deformation process in promoting case martensite transformation and the effectiveness of computational design approach. The difficulty encountered in achieving a full martensite matrix with high carbon content also indicates the design is approaching the theoretical limit of surface hardness for Ni-Co secondary hardening steels.

7.8. Next step process optimization

The potential of CryoForm 70 in possessing ultrahigh surface hardness has been demonstrated through the achieved case hardness and microstructure. For continuous improvement in case hardness and fatigue performance, further process optimization is proposed herein, including the future optimization of carburization, cryogenic UNSM, cyclic tempering and final peening.

7.8.1. Carburization

Although it is claimed that a 0.79wt% C was achieved at the surface exposed to cryogenic compression and cyclic tempering, the estimated surface carbon content from tetragonality was 0.68% C. Although further validation with higher accuracy is needed, it is plausible to conclude that there is the possibility that the surface carbon content is below the desired 0.8wt%. To avoid this uncertainty, further optimization of vacuum carburization is needed.

7.8.2. Cryogenic ultrasonic surface modification

The ultrasonic surface modification (UNSM) treatment at cryogenic temperature has demonstrated its ability of increasing surface hardness but not the ability of reducing the level of retained austenite. However, it shows strong potential of being utilized for large scale products. Thus another run of optimization aiming at improving microstructure is desired. The pressure transmitted to the steel surface and the frequency of the pointer vibration are the two major factors to be optimized.

7.8.3. Cyclic Tempering

To demonstrate CryoForm 70's ability of achieving higher case hardness than 975 Hv, it is desired to further increase the M_2C driving force during tempering. Thermodynamic calculation performed through CMD and Thermo-Calc has shown that decreasing tempering temperature brings higher M_2C driving force but slower kinetics. Previous practice demonstrated that 482 °C is an optimal tempering temperature for C61 and C67 steels. It is presented in Fig. 7.32 that M_2C driving force in CryoForm 70 could be increased to about 30kJ/mol with a tempering temperature of 455 °C. Not to sacrifice precipitation kinetics too much, a combined cyclic tempering procedure at two temperatures is proposed: 482 °C tempering for the first 40 hours to keep a fast kinetics and 455 °C tempering for the rest of time to increase M_2C driving force.

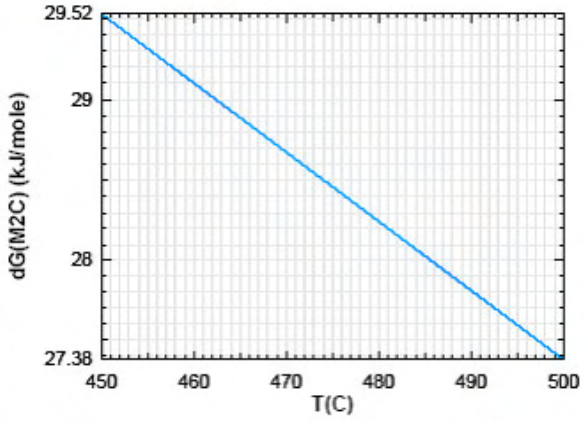

Figure 7.32. Effect of temperature on M_2C driving force for CryoForm 70

7.8.4. Final UNSM or Laser Peening

For improved fatigue performance, the final peening process producing beneficial compressive residual stress needs to be optimized. In this design, the extremely high hardness at the surface challenges the current shot peening technique, in which cost-effective metal/alloy shot harder than 64 Rc is not available. As the UNSM treatment is essentially shot peening, it is an alternative since the tungsten carbide ball is hard enough to deform CryoForm 70. Thus it is desired to optimize this process at room temperature for the purpose of generating possibly larger compressive residual stress. Laser peening is another option for the fulfillment of this task because of its ability of producing large and deep compressive residual stresses with high intensity.

CHAPTER 8

Conclusions and suggestions for future work

8.1. Conclusions

A system approach has been applied to investigate the hierarchial material structures and guide the new materials and process design for advanced secondary hardening gear steels. Residual stress and its distribution, an indispensable link in material structures, have been analyzed to understand its evolution during processing, its generation through process optimization and the non-destructive measurement of its distribution using synchrotron radiation. Results from residual stress study gives direction to the future process optimization for desired residual stress distribution and improved fatigue performance in high strength gear steels. Motivated by the advantages from beneficial residual stress and from cryogenic deformation process, and by the demands for ultra-hard steels in gear industry, a gear steel with enhanced surface hardness and low case M_s was successfully designed. Process development or optimization was subsequently performed to achieve desired properties. Combined materials and process design confirmed the feasibility of designing a super hard steel through secondary hardening mechanism and cryogenic deformation process. The design also shows the potential of achieving higher surface hardness.

8.1.1. Residual stress in secondary hardening gear steels

As large compressive residual stresses are desired in Ferrium C61 and C67 secondary hardening gear steels, residual stress evolution during carburizing, heat treatment and peening treatment was investigated. An optimal boost time during carburization was found for largest surface residual stress resulting from the combined effects of carbon content gradient and the level of retained austenite. Elevated carburizing temperature and prolonged diffusion both reduce the surface compressive residual stress as the carbon content gradient is decreased. Compressive residual stress obtained from carburizing and subsequent quenching relaxes during tempering with increased volume fraction of precipitates. This relaxation, however, is insensitive to tempering temperatures as long as carbide precipitation occurs. Fortunately, the loss of compressive residual stress can be re-introduced through peening processes, which affect residual stress much more significantly than carburization.

Correlation between attainable residual stress and material surface hardness was established. Estimated from this correlation, a -1.3 or -1.7 GPa surface residual stress was expected for C61 and C67 steels through shot peening, respectively. With shot peening provided by the third party, -1.4 GPa surface residual stress was achieved in C61 steel, suggesting further potential of shot peening in generating desired residual stress. A peening intensity of 0.034 inch A (0.010 inch C) was proposed for C67 steel to obtain a 0.2 mm compressive depth. However, due to the lack of equally hard or harder shot media, laser peening was instead applied and -1.5 GPa residual stress was achieved on the surface. There is still room for further process optimization for higher compressive residual stress.

Surface conditions in shot and laser peened Pyrowear 53 was studied to illustrate surface roughening and possible surface defects that occurred during shot and laser peening. Both processes cause surface roughening. Surprisingly, surface roughness of laser peened Pyrowear 53 was higher than that of its shot peened counterpart, which was believed to be due to the inappropriate high power density adopted in laser peening. Similarly, surface roughness in laser peened C67 was higher than that in shot peened C61. However, microcracks or micro-notches or surface pitting were not revealed in C61 and C67 steels as they were in Pyrowear 53, indicating the suitability of both shot and laser peening for C61 and C67 steels. When optimizing both processes, a tradeoff must be made between achieving large residual stresses and obtaining high surface roughness.

A novel non-destructive synchrotron radiation technique was implemented and applied to the analysis of residual stress distribution in carburized steels for the first time through collaboration with the Advanced Photon Source, Argonne National Laboratory. Residual stress depth profiles in shot peened C61, ground and laser peened C67, shot and laser peened Pyrowear 53 were successfully measured. Large residual stresses of -1.4∼-1.5 GPa near the surface in C61 and C67 steels show that shot and laser peening are both effective in producing beneficial residual stresses. The greater compressive depth obtained in laser peening indicates laser peening is more favorable for subsurface fatigue resistance. Residual stress profiles in Pyrowear 53 assisted the root cause identification of material behavior in RCF testing. The rougher surface with pitting in laser peened Pyrowear 53 counteracted the benefits from larger and deeper compressive residual stress and thus led to the earlier failure in laser peened steel than in its shot peened counterpart.

By probing residual stress distribution under wear tracks, surface residual stress relaxation was discovered in both C61 and C67 steels after the RCF screening test with 5.4 GPa Hertzian pressure. Diffraction peak sharpening after the RCF test indicates significant material alteration during cyclic contact loading, supported by the microstructural change observed in the material's cross sectional images. Residual stress relaxation needs to be taken into account when considering fatigue life from the combined effect of applied stress and residual stress. The fact that residual stress and microstructure both change under such a high contact load suggests that the RCF test with 5.4 GPa Hertzian pressure is not a good indicator for the normal material service life.

8.1.2. Design of the ultra-hard gear steel: CryoForm 70

An ultra-hard gear steel, CryoForm 70, aiming at super high surface hardness of 70 Rc and at the demonstration of the effective cryogenic deformation process, was designed utilizing the system approach. Based on thermodynamics and strengthening models in Ni-Co secondary hardening steels, two candidate compositions were designed, meeting the hardness goals for both case and core materials. Other design parameters include case and core M_s, case solutionizing temperature and core sigma phase driving force. A surface carbon content of 0.8wt% was first set to achieve desired surface hardness. To maximize the strengthening effect from M_2C carbides, concentrations of carbide formers (Cr, Mo and V) were balanced for efficient carbon consumption during tempering. Co concentration was reduced greatly to decrease the core sigma phase driving force. A core carbon content of 0.1wt% was determined for required core strength and toughness. One candidate composition was chosen for prototype fabrication with higher predicted

case hardness and lower solidification microsegregation. Trace amount of Ti and La were added when fabricating prototypes for grain refining and impurity gettering.

The high carbon and alloy content necessary for high hardness resulted in expected dramatic reduction in case M_s (58 °C in CryoForm 70 prototype), which verifies the CryoForm 70 prototype is a good candidate for the assessment of the novel cryogenic deformation process. The process combining mechanical deformation and cryogenic treatment was developed to improve the volume fraction of martensite in the case prior to tempering. Calculations regarding theoretical thermal and mechanical driving force for martensite transformation and transformation kinetics predicted 90% martensite volume fraction through cryogenic deformation treatment. Three means of cryogenic deformation, cryogenic shot peening, cryogenic ultrasonic surface modification (UNSM) and cryogenic compression, were attempted. Cryogenic compression was demonstrated to be the best candidate for promoting case martensite volume fraction from 76% to 92%.

A cyclic tempering procedure involving intermediate quenching and cryogenic treatment was developed to further enhance the martensite volume fraction resulting from cryogenic compression treatment. Peak case hardness of 975 ± 10 Hv (68.5 ± 0.1 Rc) at $0.74 \pm 0.5\%$ carbon content was achieved after 56 hour cyclic tempering at 482 °C. A core hardness of 512 ± 2 Hv was obtained, promoting sufficient core toughness. Other processes optimized include simulation aided carburization, through which the vacuum carburizing recipe was developed and optimized. Desired 0.8wt% carbon was achieved at the depth of 50μm in the prototype.

The measured core M_s of 350 °C for the prototype agrees with the theoretical prediction very well, validating this computational design. The fact that the achieved case

hardness is only 8% below predicted value suggests that the system approach is quite effective for the design of unusual secondary hardening steels. A 39% improvement in hardness was obtained if compared to current commercial steel hardness value of 720 Hv, and 8% increase in hardness with respect to Ferrium C67 steel.

8.2. Suggestions for future work

8.2.1. Residual stress in high strength gear steels

Further process optimization for higher compressive residual stresses is desired for Ferrium C67 steel since current residual stress levels are still below the predicted attainable values. To achieve large compressive residual stress without inducing high surface roughness, dual laser peening is proposed based on the study of dual shot peening. In dual laser peening, the first pass employs a high power density laser with a large laser spot to provide a large surface compressive residual stress and a great compressive depth. The second pass operating at a much lower power density with a smaller laser spot further increases the surface residual stress level and smooths the surface. It is suggested that the practice of dual laser peening and its optimization should be accomplished through collaboration with a laser peening service provider, such as Metal Improvement Company, Inc. in Livermore, California. Alternatively, desired residual stresses in C67 can be achieved by taking advantage of ultrasonic surface modification (UNSM) treatment. The tungsten carbide ball with super high hardness (about 1400 Hv) used in UNSM is an ideal peening medium for residual stress production in hard steel alloys. The peening intensity can be adjusted by modifying the ball striking pressure and its vibrating frequency. Collaboration can be established with DesignMecha Co. Ltd. in South Korea. The proposed two means

of generating compressive residual stress are suitable for the newly designed CryoForm 70 as well.

Based on the non-destructive synchrotron technique for residual stress distribution analysis, a modified experimental setup is desired for the measurement in a real gear with complex geometry. In the case that the tooth root is too thick for the high energy beam to penetrate, the thinner tooth tip may be considered as substitute. The orientation of the gear with respect to the beam can also be adjusted to find the shortest path for radiation.

8.2.2. Design of the ultra-hard gear steel: CryoForm 70

With the available CryoForm 70 prototype, further process optimization is desired to achieve better material properties. First, vacuum carburization needs to be optimized for accurate surface carbon content. For cryogenic deformation process, cryogenic ultrasonic surface modification (UNSM) shows its potential as the candidate for the application in large scale products. Thus a second run of cryogenic UNSM should be performed, targeting the improvement in case martensite volume fraction. Two stage cyclic tempering with two temperatures is expected to further enhance the M_2C carbide driving force without sacrificing precipitation rate. For final residual stress generation, the development of dual laser peening or optimization of UNSM is proposed.

Preliminary microstructure validation can be performed using Atom Probe Microanalysis with the current tempered CryoForm 70 prototype. A thin slice could be cut from the case of the prototype and made into an atom probe tip for data collection. A detailed atom probe analysis is desired after the accomplishment of enhanced surface hardness through further process optimization.

References

[1] Erwin V. Zaretsky. Bearing and gear steels for aerospace applications. Technical report 102529, NASA, March 1990.

[2] G. B. Olson. Computational design of hierarchically structured materials. *Science*, 277:1237, August 1997.

[3] Energetics Inc. Gear industry vision - a vision of the gear industry in 2025, developed by the gear community. Technical report, AGMA, ASME, GM Powertrain etc., September 2004.

[4] G. M. Jenkins. *The systems approach*. University Press, 1972.

[5] C. S. Smith. *A search for structure*. The MIT Press: Cambridge, 1981.

[6] Gregory B. Olson. Designing a new material world. *Science*, 288(5468):993, May 2000.

[7] X. Jay Gao and Gregory B. Olson. Process design and optimization for high-temperature vacuum carburizing. In *Proceedings, the 2003 Spring Meeting of CHTE, the Center for Heat Treating Excellence of WPI, Worcester*, 2003.

[8] X. Jay Gao. Unpublished research. 2005.

[9] QuesTek Innovations. Data sheet for *Ferrium® C61 and C69*. Technical report, 2004.

[10] Darle W. Dudley. *The evolution of the gear art*. Washington,American Gear Manufacturers Association, 1969.

[11] L.E. Alban. *Systematic analysis of gear failures*. American Society for Metals, 1985.

[12] J.R. Davis, editor. *Gear materials,properties, and manufacture*. ASM International, 2005.

[13] Darle W. Dudley. *Handbook of practical gear design*. New York : McGraw-Hill, 1984.

[14] Harold Burrier. Bearing steels. Technical report, AMS International Handbook, 1989.

[15] W.F. Burd. A carburizing gear steel for elevated temperatures. *Met. Prog.*, May 1985.

[16] G. B. Olson. *Materials Design* course material, 2003.

[17] John J. Coy. Gearing. Technical report, NASA Lewis Research Center, NASA reference publication 1152, 1985.

[18] Chester F. Jatczak. Specialty carburizing steels for elevated temperature service. *Metal Progress*, April 1978.

[19] Charles J. Kuehmann and Gregory B. Olson. Gear steels designed by computer. *Advanced Materials and Processes*, 5:40–43, 1998.

[20] John P. Wise. *Systems design of advanced gear steels*. PhD thesis, Northwestern University, June 1998.

[21] C. E. Campbell and G. B. Olson. Systems designs of high performance stainless steels i. conceptual and computational designs. *Journal of Computer-Aided Materials Design*, 7:145–170, 2001.

[22] Hans Schlicht, Eckehard Schreiber, and Oskar Zwirlein. Effects of material properties on bearing steel fatigue strength. *ASTM STP*, 987:81, 1988.

[23] D. V. Nelson. Effects of residual stress on fatigue crack propagation. *ASTM STP*, 776:172, 1982.

[24] T. Kanazawa, H. Oba, and S. Mahida. *Society of Naval Architects of Japan Journal*, 109:359, 1961.

[25] H. Carreon, P. B. Nagy, and M. P. Blodgett. Thermoelectric nondestructive evaluation of residual stress in shot-peened metals. *Res Nondestr Eval*, 14:59, June 2002.

[26] M. Kobayashi and T. Matsui et al. Mechanism of creation of compressive residual stress by shot peening. *International Journal of Fatigue*, 20(5):351, 1998.

[27] M.A.S. Torres. An evaluation of shot peening, residual stress and stress relaxation on the fatigue life of aisi 4340 steel. *International Journal of Fatigue*, 24:877, 2002.

[28] R. A. Everett, W. T. Matthews, and et al. The effects of shot and laser peening on fatigue life and crack growth in 2024 aluminum alloy and 4340 steel. Technical report, U.S. Army Research Laboratory, 2001.

[29] M. Benedetti, V. Fontanari, and et al. Influence of shot peening on bending tooth fatigue limit of case hardnened gears. *International Journal of Fatigue*, 24:1127, 2002.

[30] Katsuyuki Matsui, Hirohito ETO, and et al. Increase in fatigue limit of gears by compound surface refining using vacuum carburizing, contour induction hardening and double shot peening. *JSME International Journal, Series A*, 45(2):290, 2002.

[31] A. Nakonieczny, W. Szyrle, and J. Suwalski. Residual stresses, microstructure and fatigue behaviour of carburized layers before and after shot peening. *Acta Physica Polonica A*, 89(3):357, 1996.

[32] Hongbin Xiao, Qing Chen, Eryu Shao, and et al. The effect of shot peening on rolling contact fatigue behaviour and its crack initiation and propagation in carburized steel. *Wear*, 151:77, 1991.

[33] Ulrich Martin, Igor Altenberger, and et al. Characterization of the microstructure-depth profile of shot peened steels. *Prakt. Metallogr.*, 35(6):327, 1998.

[34] Akihisa Inoue, Isamu Yoshii, and et al. Enhanced shot peening effect for steels by fe-based glassy alloy shots. *Materials Transactions*, 44(11):2391, 2003.

[35] Hitoshi Rokutanda, Toru Takahashi, and et al. Hardened metal product produced by shot peening with shot having high hardness. Technical Report 6,153,023, United States Patent, 2000.

[36] S. Baragetti, M. Guagliano, and L. Vergani. A numerical procedure for shot peening optimization by means of non-dimensional factors. *Int. J. of Materials and Product Technology*, 15(1/2):91, 2000.

[37] S. Baragetti and A. Terranova. Non-dimensional analysis of shot peening by means of doe. *Int. J. of Materials and Product Technology*, 15(1/2):131, 2000.

[38] Allan H. Clauer. Laser shock peening for fatigue resistance. Technical report, LSP Technologies, Inc., 1996.

[39] Charles S. Montross, Tao Wei, and et al. Laser shock processing and its effect on microstructure and properties of metal alloys: a review. *International Journal of Fatigue*, 24:1021, 2002.

[40] CS Montross, V. Florea, and et al. Influence of coatings on subsurface mechanical properties of laser peened 2011-t3 aluminum. *Journal of Materials Science,*, 36:1801, 2001.

[41] P. Peyre, R. Fabbro, and et al. Laser shock processing of aluminium alloys. application to high cycle fatigue behavior. *Materials Science and Engineering A*, A210:102, 1996.

[42] P. Peyre, L. Berthe, and et al. Laser-shock processing of aluminium-coated 55c1 steel in water-confinement regime, characterization and application to high-cycle fatigue behaviour. *Journal of Materials Science*, 33:1421, 1998.

[43] LSP. Laser shock peening. Technical bulletin, LSP Technologies, Inc.

[44] J.-E. Masse and G. Barreau. Surface modification by laser induced shock waves. *Surface Engineering*, 11(2):131, 1995.

[45] G. Banas, H.E. Elsayed-Ali, and et al. Laser shock-induced mechanical and microstructural modification of welded maraging steel. *J. Appl. Phys.*, 67(5):2380, March 1990.

[46] J.P. Chu, J.M. Rigsbee, and et al. Laser-shock processing effects on surface microstructure and mechanical properties of low carbon steel. *Materials Science and Engineering A*, A260:260, 1999.

[47] I. Altenberger, E.A. Stach, and et al. An in situ transmission electron microscope study of the thermal stability of near -surface microstructures induced by deep rolling and laser-shock peening. *Scripta Materialia*, 48:1593, 2003.

[48] J.P. Chu, J.M. Rigsbee, and et al. Effects of laser-shock processing on the microstructure and surface mechanical properties of hadfield manganese steel. *Metallurgical and Materials Transactions A*, 26A:1507, 1995.

[49] M. Gerland and M. Hallouin. Effect of pressure on the microstructure of an austenitic stainless steel shock-loaded by very short laser pulses. *Journal of Materials Science*, 29:345, 1994.

[50] A. H. Clauer, B. P. Fairand, and et al. Pulsed laser induced deformation in an *Fe-3Si* alloy. *Metallurgical Transactions A*, 8A:119, 1977.

[51] E. Ganin, Y. Komen, and A. Rosen. Shock induced hardness in α-iron. *Materials Science and Engineering*, 33:1, 1978.

[52] Iryna Yakimets, Caroline Richard, and et al. Laser peening processing effect on mechanical and tribological properties of rolling steel 100cr6. *Wear*, 256:311, 2004.

[53] P. Peyre, C. Braham, and et al. Corrosion reactivity of laser-peened steel surfaces. *JMEPEG*, 9(6):656, December 2000.

[54] Metal Improvement Company. Shot peening technology bulletin. Technical report, Metal Improvement Company, 2001.

[55] R.L. Brown, H.J. Rack, and M. Cohen. Stress relaxation during the tempering of hardened steel. *Materials Science and Engineering*, 21:25, 1975.

[56] James A. Wright. *Design principles for advanced carburized bearing steels*. PhD thesis, Northwestern University, 2003.

[57] H. Holzapfel, V. Schulze, O. Vohringer, and E. Macherauch. Residual stress relaxation in an aisi 4140 steel due to quasistatic and cyclic loading at higher temperatures. *Materials Science and Engineering A*, A248:9, 1998.

[58] RL Mattson and WS Coleman. Effect of shot peening variables and residual stresses on fatigue life of leaf spring specimens. *Transactions, Society of Automotive Engineers*, 62:546, 1954.

[59] S Kodama. The behavior of residual stress during fatigue stress cycles. *Proceedings of the International Conference on Mechanical Behavior of Metals II*, 2:111, 1972.

[60] Wyman Z. Zhuang and Gary R. Halford. Investigation of residual stress relaxation under cyclic load. *International Journal of Fatigue*, 23:S31, 2001.

[61] B. D. Cullity and S. R. Stock. *Elements of X-ray Diffraction*. Upper Saddle River, NJ : Prentice Hall, third edition edition, 2001.

[62] K. Heindlhofer. *Evaluation of Residual Stresses*. McGraw-Hill, New York, 1948.

[63] I. C. Noyan and J. B. Cohen. *Residual Stress Measurement by Diffraction and Interpretation*. Springer-Verlag New York Inc., 1987.

[64] B. Sundman, B. Jansson, and J. O. Andersson. The thermo-calc databank system. *Calphad-Computer Coupling of Phase Diagrams and Thermochemistry*, 9(2):153–190, 1985.

[65] G. Ghosh and G. B. Olson. Kinetics of fcc-bcc heterogeneous martensitic nucleation -1. the critical driving-force for athermal nucleation. *Acta Metallurgica et Materialia*, 42(10):3361C3370, 1994.

[66] M. Hillert, B. Jansson, B. Sundman, and J. Agren. A 2-sublattice model for molten solutions with different tendency for ionization. *Metallurgical Transactions A - Physical Metallurgy and Materials Science*, 16(2):261–266, 1985.

[67] C. J. Kuehmann H.J. Jou, L. Li and G. B. Olson. *User Guide for CMDTM (Computational Materials Dynamics) Software*. QuesTek Innovations LLC, Evanston, IL, 3/31/03 edition, March 2003.

[68] J. O. Andersson and J. Agren. Models for numerical treatments of multicomponent diffusion in simple phases. *Journal of Applied Physics*, 72:1350–1355, 1992.

[69] P.J. Withers. *Use of synchrotron X-ray radiation for stress measurement.*

[70] M.E. Fitzpatrick and A. Lodini, editors. *Analysis of residual stress by diffraction using neutron and synchrotron radiation*. London : Taylor and Francis, 2003.

[71] S. F. Nielsen, A. Wolf, H. F. Poulsen, M. Ohler, U. Lienert, and R. A. Owen. A conical slit for three-dimensional xrd mapping. *Journal of Synchrotron Radiation*, 7:103–109, 2000.

[72] U. Lienert, J. Almer, D. Haeffner, Y. Gao, and W. Carter. Nondestructive strain tensor scanning within samples of cylindrical symmetry. *AIP Conference Proceedings, SYNCHROTRON RADIATION INSTRUMENTATION*, 705:1074–1077, 2004.

[73] B. B. He and K. L. Smith. Fundamental equation of strain and stress measurement using 2d detector. *Proceedings of the SEM Spring Conference on Experimental and Applied Mechanics and Experimental/Numerical Mechanics in Electronic Packaging III*, 1998.

[74] J. Almer and U. Lienert. Strain and textue analysis of coatings using high-energy x-rays. *Journal of Applied Physics*, 94:697–702, 2003.

[75] A. Wanner and D. C. Dunand. Synchrotron x-ray study of bulk lattice strains in externally loaded *Cu-Mo* composite. *Metallurgical and Materials Transactions A*, 31A, 2000.

[76] H.-J. Bohmer. Residual stresses and material behavior of m50nil and rbd. *ASTM STP*, 1195:34–48, 1993.

[77] B.A. Shaw, C. Aylott, P. O'Hara, and K. Brimble. The role of residual stress on the fatigue strength of high performance gearing. *International Journal of Fatigue*, 25:1279–1283, 2003.

[78] Xiujie Gao, Benjamin L. Tiemens, Yana Qian, and et al. Optimization of high-temperature vacuum carburizing - process simulation, experiment and validation. *manuscript in preparation*.

[79] Jack Champaigne. Shot peening overview. Technical report, Electronics, Inc., January 2001.

[80] ASM Handbook. Shot peening. 1989.

[81] Y. Qian, J. Almer, U. Lienert, B. Tiemens, and G. B. Olson. Non-destructive residual stress distribution measurement in nano-structured ultra-high strength gear steels. *Proceedings, the Fifth International Conference on Synchrotron Radiation in Materials Science*, 2006.

[82] Y. Qian, J. Almer, U. Lienert, and G. B. Olson. Residual strain/stress analysis for advanced gear steels utilizing synchrotron radiation. *manuscript in preparation*, 2007.

[83] S. D. Shastri, K. Fezzaa, and et al. Cryogenically cooled bent double-laue monochromator for high-energy undulator x-rays (50-200 kev). *Journal of Synchrotron Radiation*, 9:317–322, 2002.

[84] Bjorn Cederstrom and Mats Lundqvist. Multi-prism x-ray lens. *Applied Physics Letters*, 81(8):1399–1401, August 2002.

[85] U. Lienert, R. Martins, and et al. High spatial resolution strain measurements with-ing bulk materials by slit-imaging. *Proceedings of Materials Research Society Symposium*, 590:241–246, 2000.

[86] R. V. Martins, U. Lienert, and et al. Residual strain tensor determination within highly plastically deformed torsion samples using high energy synchrotron radiation. *Journal of Neutron Research*, 9:249–254, 2001.

[87] J. Almer. unpublished research. 2005.

[88] A. P. Voskamp, R. Osterlund, P. C. Becker, and O. Vingsbo. Gradual changes in residual stress and microstructure during contact fatigue in ball bearings. *Metals Technology*, page 14, January 1980.

[89] H. Swahn, P. C. Becker, and et al. Martensite decay during rolling contact fatigue in ball bearings. *Metallurgical transactions A*, 7A:1099–1110, 1976.

[90] Brian Tufts and et al. Proprietary research. Technical report, QuesTek Innovations, Evanston, IL, March 2006.

[91] G. L. Krasko and G. B. Olson. Evaluation of decohesion mechanisms in iron by *LMTO-ASA-Stoner* cohesive energy calculations. *Sagamore Army Materials Research Conference Proceedings, Innovations in Ultrahigh-Strength Steel Technology*, 34:677–704, 1987.

[92] I. Aslinidis. Softening and recovery resistance in *Fe, Fe-Co, Fe-Al, Fe-Ni and Fe-Ni-Co* alloys. Technical report, MIT, 1989.

[93] M. J. Gore, G. B. Olson, and M. Cohen. Grain-refining dispersions and properties in ultrahigh-strength steels. *Sagamore Army Materials Research Conference Proceedings, Innovations in Ultrahigh-Strength Steel Technology*, 34:425–441, 1987.

[94] R. Wu, A. J. Freeman, and G. B. Olson. First principles determination of the effects of phosphrous and boron on iron grain boundary cohesion. *Science*, 265:376–380, 1994.

[95] W. J. Harris and M. Cohen. *Trans. AIME*, 180:447–470, 1949.

[96] D.P. Koistinen and R. E. Marburger. *Acta Met.*, 7:59–60, 1959.

[97] C. L. Magee. *Phase transformation*. the American Society for Metals, 1970.

[98] G. B. Olson, K. Tsuzaki, and M. Cohen. Statistical aspects of martensite nucleation. *Turnbull symposium: Phase Transactions in Condensed Systems, MRS*, 1987.

[99] Blastalloy design team. Materials design course project. Technical report, Northwestern University, 2005.

[100] J. Houserova, M. Friak, M. Sob, and J. Vrestal. Ab initio calculations of lattice stability of sigma-phase and phase diagram in the *Cr-Fe* system. *Computational Materials Science*, 25:562–569, 2002.

[101] M.Schwind, J. Kallqvist, J.-O. Nilsson, J. Agren, and H.-O. Andren. σ-phase precipitation in stabilized austenitic stainless steels. *Acta Materialia*, 48:2473–2481, 2000.

[102] T. H. Chen and J. R. Yang. Effects of solution treatment and continuous cooling on σ-phase precipitation in a 2205 duplex stainless steel. *Materials Science and Engineering A*, A311:28–41, 2001.

[103] G. Restrepo Garces, J. Le Coze, J. L. Garin, and R. L. Mannheim. σ-phase precipitation in two heat-resistant steels-influence of carbides and microstructure. *Scripta Materialia*, 50:651–654, 2004.

[104] Sang-Beom Kim, Kyung-Wook Paik, and Young-Gil Kim. Effect of mo substitution by w on high temperature embrittlement characteristics in duplex stainless steels. *Materials Science and Engineering A*, A247:67–74, 1998.

[105] T. Sourmail and H.K.D.H. Bhadeshia. Modeling simultaneous precipitation reactions in austenitic stainless steels. *Computer Coupling of Phase Diagrams and Thermochemistry*, 27:169–175, 2003.

[106] SL Semiatin and David E Stutz. *Induction Heat Treatment of Steel*. Metals Park, Ohio : American Society for Metals, 1986.

[107] Young-Shik Pyoun. Nano technology improves fatigue strength, wear resistance and friction loss and retard scc (stress crack corrosion) drastically. Technical report, Sun Moon University / DesignMecha, September 2006.

[108] G. B. Olson and M. Azrin. Transformation behavior of trip steels. *Metallurgical Transactions A*, 9A:713–721, May 1978.

[109] George Krauss. *Principles of heat treatment of steel*. Metals Park, Ohio : American Society for Metals, 1980.

[110] Jozef Mazur. Lattice parameters of martensite and of austenite. *Nature*, 166:828, November 1950.

[111] Liu Xiao, Zhong Fan, and Zhang Jinxiu. Lattice-parameter variation with carbon content of martensite. i. x-ray diffraction experimental study. *Physical Review B*, 52(14):9970–9978, October 1995.

[112] Robert A. Winholtz. *Microstresses and macrostresses in the fatigue of steel*. Phd dissertation, Northwestern University, 1991.

APPENDIX

Surface residual stress analysis by conventional X-ray

1. X-ray facility and operation parameters

Surface residual stress was analyzed using the Orange diffractometer in J. B. Cohen X-ray Laboratory at Northwestern University (Fig. .1). Detailed operation parameters were displayed in Table .1.

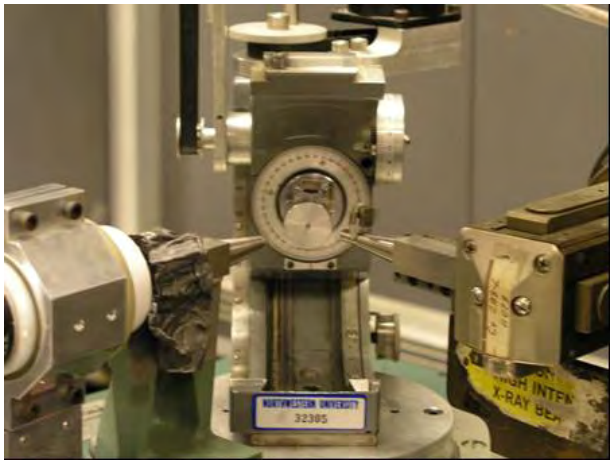

Figure .1. Diffractometer for surface residual stress analysis at Northwestern University

2. Experimental procedure of residual stress measurement

2.1. Beam alignment

The optics of the diffractometer should be checked before the measurement. Zero positions of theta, two theta and chi are of most importance. First, use the level to set the chi to

Table .1. Operation parameters of Orange diffractometer

Cr, K_α average	λ=2.291Angstrom
Filter in incident arm	Vanadium
Point source size	1 mm
Collomator size	1 mm
Slit in incident arm	1 mm
Slit in detector arm	2 mm (near), 3 mm (far)

zero. Second, scan in theta-two theta mode without sample around 0 deg at low energy to find the position of the two theta peak. That position is zero two theta. Third, bring the sample in, cutting the beam in half. Fourth, scan in theta mode around 0 deg and determine the peak position, which is the zero of theta. Repeat Steps Three and Four until the zero position of theta doesn't change any more. During this process, the statistical effect of counting should be taken into account.

2.2. Sample alignment

Instrument misalignment can lead to large deviation in experimental results. Among several causes of misalignment, sample position is the most significant. The peak shift it causes can even change the sign of the measured residual stress. If the diffracting volume is not located at the center of the diffractometer, there is a relative peak shift between $chi = 0$ and chi. This effect is shown in Fig. .2.

According to Noyan, Cohen [**63**] and Cullity [**61**], for cubic materials and small angles, the following equation holds:

$$\frac{a_{hkl} - a_0}{a_0} = -\frac{\Delta x}{R_{GC}} \bullet \left(\frac{\cos\theta^2}{\sin\theta} + \frac{\cos\theta^2}{\theta} \right) \qquad (.1)$$

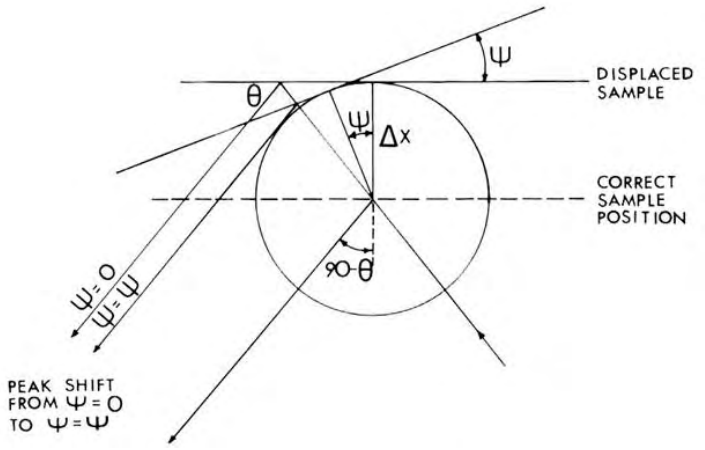

Figure .2. The effect of the sample displacement on the peak shift when sample is tilted

where a_{hkl} is the lattice parameter calculated from peak (hkl), a_0 is the true lattice parameter by extrapolation, Δx is the sample displacement from the center, R_{GC} is the radius of the diffractometer, $\frac{\cos\theta^2}{\sin\theta} + \frac{\cos\theta^2}{\theta}$ is called the Nelson-Riley function.

Eq. .1 can be used to measure Δx by X-ray diffraction. Determine a_{hkl} for various reflections at $chi = 0$ and plot the data versus the Nelson-Riley function. The slope of this line is equal to $-\frac{\Delta x}{R_{GC}}$, which directly leads to the determination of sample displacement. The extrapolated value of a at $\theta = 90°$ is considered as the true lattice parameter, a_0. If the slope is positive, the sample displacement is negative, which means the sample is behind the center of the diffractometer, away from the X-ray source and the detector. If the slope is negative, the sample is in front of the center. With the assistance of a dial indicator, the diffracting volume of the sample can be accurately located at the center of diffractometer.

Three Bragg peaks, (110) (200) and (211), are used to determine the lattice parameter. Therefore, the deviation of the sample off the diffractometer center is obtained. The accuracy of the alignment can reach 0.0005 inch.

2.3. Data collection and analysis

Data of $\theta/2\theta$ scan at Bragg peak (211) at six *chi* positions were collected: $chi = 0, 18.43°$, 26.57°, 33.21°, 39.23°, 45°. Choosing high angle peak (211) is because the measurement of residual stress is more accurate at high angles than low angles [**63**]. A biaxial stress condition without shear components is assumed on the surface. Therefore, the *chi* tilting toward the opposite direction is not necessary. On the other hand, the current diffractometer configuration does not allow the opposite *chi* tilting. A typical (211) peak is shown in .3 below. Due to the 2θ limit (158°) of the diffractometer, a 3/4 peak is obtained. To increase the statistical accuracy, a small step size and long counting time are adopted.

Peak position is determined using a Gaussian fit provided by data analysis software - Origin. Several functions can be utilized to fit the data, such as Gaussian, Modified Lorentzian, Pearson VII and Pseudo-Voigt function. A parabola fit to the top 85% of a peak can also be used to find the peak. Past studies have shown that a Pseudo-Voigt function performs best overall. It converges reliably and gives more flexibility in peak shape than the Gaussian. The program PEAKFIT by Robert Winholtz [**112**] is a good tool to fit data with Pseudo-Voigt function. However, the background line needed for the Pseudo-Voigt fit can not be determined by this program since the peak is incomplete.

Therefore, a Gaussian fit (smooth curve in Fig. .3) with a flat background is taken to determine the peak position.

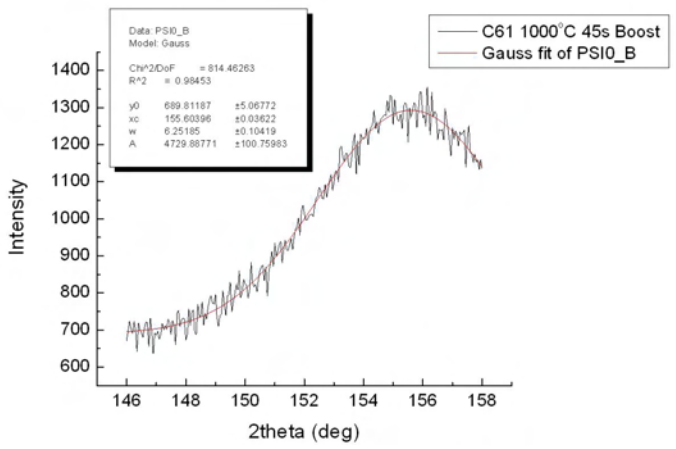

Figure .3. (211) peak used to measure residual stress, step size 0.05 deg, counting time 20s

After the determination of peak position, curves d versus $\sin\psi^2$ and $\frac{d-d_0}{d_0}$ versus $\sin\psi^2$ are worked out, in which d_0 is assumed as d-spacing at $\psi = 0$ obtained from d versus $\sin\psi^2$ data. The uncertainty in results caused by taking d-spacing at $\psi = 0$ as the unstressed value d_0 is neglected here [**63**]. According to Eq. .2, the macro-residual stress is obtained by multiplying the slope of $\frac{d-d_0}{d_0}$ versus $\sin\psi^2$ curve with $\frac{E}{1+\nu}$. The error is calculated from the error of peak position and the linear fit deviation. A worked out example is given in next section.

$$\frac{d-d_0}{d_0} = \sigma \sin\psi^2 - \frac{\nu}{E}(\sigma_{11}+\sigma_{22}) \tag{.2}$$

where σ is the angular combination of σ_{11} and σ_{22}.

2.4. An example of diffraction data analysis

Sample: C61 after quenching and liquid nitrogen treatment

Step1: Determine peak position from the diffraction data by a Gaussian fit function in the Origin software. Results are shown in Table .2.

Table .2. Peak positions at different psi angles

Psi (deg)	2 theta (deg)
0	154.60261 ± 0.04454
18.43	154.71181 ± 0.04728
26.57	155.02045 ± 0.05530
33.21	155.21635 ± 0.05502
39.23	155.50586 ± 0.06365
45	155.67886 ± 0.07293

Step2: Calculate d-spacing of peak (211) at each *psi* angle using Bragg's Law. The error is given by Eq. .3. Results are presented in Table .3. Fit the data linearly and get the d-spacing at $\psi = 0$ (Fig. .4). Use that value as d_0 which is proven by Noyan and Cohen to be feasible. In this case, $d_0 = 1.17365 \pm 5.38474E - 5$ from Fig. .4. The good linear fit indicates that there is no shear stress component.

$$\Delta d = \frac{\lambda \cos_\theta}{2 \sin^2_\theta} \Delta\theta \tag{.3}$$

Step3: Calculate $\frac{d-d_0}{d_0}$ for each value of $\sin\psi^2$. Results are displayed in Table .4. The error is given by Eq. .4. Plot $\frac{d-d_0}{d_0}$ versus $\sin\psi^2$, shown in Fig. .5. A linear relationship presents between $\frac{d-d_0}{d_0}$ and $\sin\psi^2$. From Eq. .2, the slope of this line is related to the macro stress.

$$\Delta\frac{d-d_0}{d_0} = \Delta\frac{d}{d_0} = \frac{\Delta d}{d_0} - \frac{d(\Delta d_0)}{d_0^2} \tag{.4}$$

Table .3. d-spacing versus $\sin\psi^2$

$\sin^2\psi$	d-spacing	Error of d-spacing
0	1.17356	1.02785E-4
0.10	1.17330	1.08601E-4
0.20	1.17260	1.25346E-4
0.30	1.17216	1.23655E-4
0.40	1.17151	1.41250E-4
0.50	1.17113	1.60613E-4

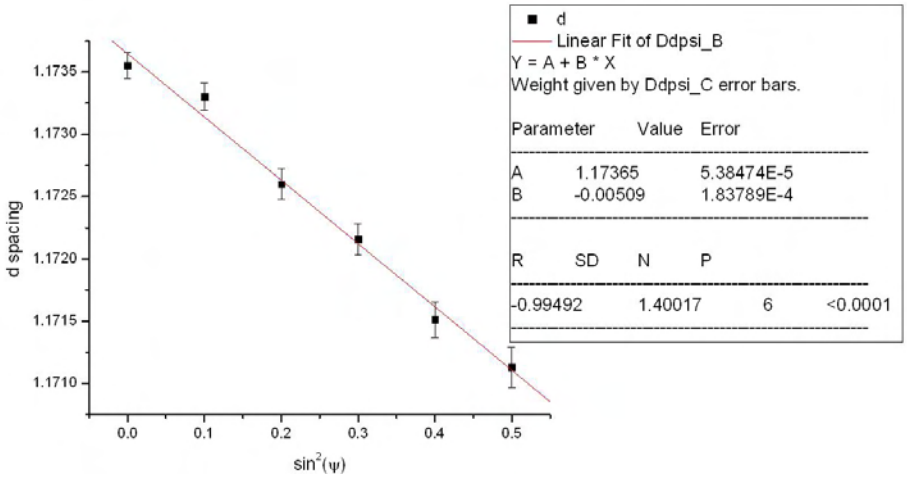

Figure .4. d-spacing versus $\sin\psi^2$

Table .4. $\frac{d-d_0}{d_0}$ versus $\sin\psi^2$

$\sin^2\psi$	$(d-d_0)/d_0$	Error
0	-8.035E-5	4.170E-5
0.10	-2.946E-4	4.667E-5
0.20	-8.946E-4	6.096E-5
0.30	-1.271E-3	5.954E-5
0.40	-1.822E-3	7.455E-5
0.50	-2.148E-3	9.107E-5

Step4: The macro stress is calculated by using Eq. .5, where B is the slope of the line $\frac{d-d_0}{d_0}$ versus $\sin\psi^2$, E is Young's modulus and ν is Poisson's ratio. The error is calculated

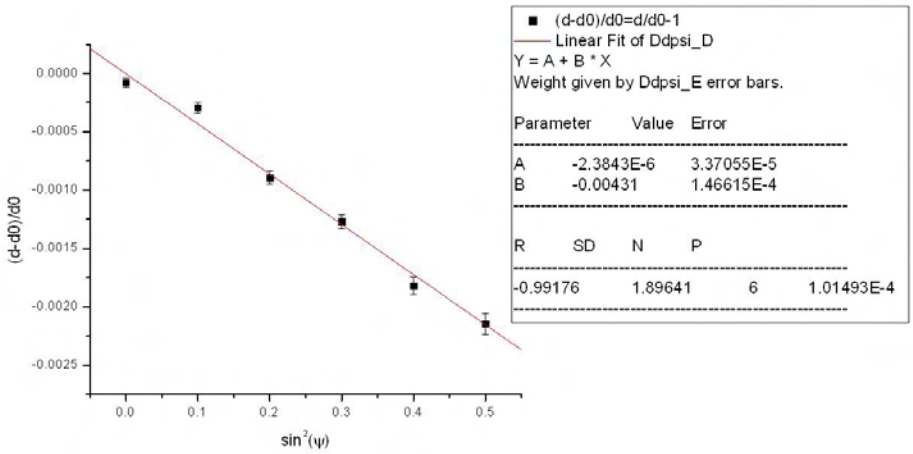

Figure .5. $\frac{d-d_0}{d_0}$ versus $\sin\psi^2$

from the error of the slope. In this case, $B = -0.00431 \pm 1.46615E-4$ and we assume $\frac{E}{1+\nu}$ is 168GPa for steels. Therefore, the macro stress of this sample is -724 ± 24.6 MPa.

$$\sigma = B \bullet \frac{E}{1+\nu} \tag{.5}$$